The Influence of Stoichiometry and Cure Conditions on Surface and Interfacial Properties of Epoxy Resin Barrier Coatings

CALLUM CRAIG BANNISTER

BANNISTER, CALLUM CRAIG (2023) The Influence of Stoichiometry and Cure Conditions on Surface and Interfacial Properties of Epoxy Resin Barrier Coatings. Doctoral thesis, Durham University.

The Influence of Stoichiometry and Cure Conditions on Surface and Interfacial Properties of Epoxy Resin Barrier Coatings

Callum Bannister

Department of Chemistry

Durham University

2023

A thesis presented for the degree of Doctor of Philosophy

Abstract

In the transport of corrosive, small molecule cargoes, ship-tanker holds are often covered with (2+ layer) amine-cured epoxy resin coatings to prevent damage to the tanker steel. However, over time these coatings can experience interlayer delamination or adhesion failure, and while the associated financial implications can be large, ultimately, relatively little is known about the causes of these adhesion failures. This thesis addresses the potential causes of interlayer adhesion failure in 2-layer epoxy systems by characterising and comparing system properties as a function of stoichiometry and cure condition.

Variation in cure conditions (temperature, relative humidity (RH) and delay time between epoxy component mixing and film casting, "induction time") and stoichiometry significantly altered the surface properties of the ambient-cured, first coat of the epoxy resin system (Dow Epoxy Novolac, (D.E.N. 431), resorcinol diglycidyl ether (RDGE), and 4,4-diaminodicyclohexylmethane (PAC-M)). Gravimetric analysis showed that increasing induction time significantly reduced surface layer formation (carbamation) of cured epoxy resin coatings at 80% RH, but had no measurable effect at 40% RH and below. At lower RH, the likelihood of carbamate formation decreases as water catalyses carbamation. Therefore, to reduce carbamation, it is advised that films are cured at lower RH (<40%). RMS surface roughness increased with increasing RH and decreased with increasing induction time and ambient cure temperature, at two stoichiometric extremes. However, the net change in surface area arising from these conditions was not sufficient to significantly alter the equilibrium contact angles or wetting regime. The variation in surface wettability appears to be predominantly influenced by variations in surface chemistry rather than roughness. Stoichiometry emerged as the most influencial factor affecting surface wettability, average void volume and fractional free volume, while cure temperature significantly influenced the extent of cure at both stoichiometries. Off-stoichiometry formulation and elevated ambient cure temperature significantly increased system average void volume, while fractional free volume decreased.

Interlayer diffusion, and the formation of an interphase, was shown to occur in bilayer ambient cured epoxy resins systems and is likely to be significant regarding interlayer adhesion. This was achieved by mapping the ingress of probe molecules into ambient cured epoxy resins after overcoating, using Raman spectroscopy. This process was shown to occur over tens of microns during a 3-day period. Extent of diffusion depth was significantly increased by decreasing ambient cure temperature,

overcoating interval and RH. Most impactfully, high carbamate formation almost completely suppressed second coat ingress suggesting that carbamate contributes to adhesion failure by inhibiting the interdiffusion of sequential layers.

Novel approaches, using micron-resolution, spatially-resolved solvent ingress measurements (Raman mapping; PIXE), were developed, and showed that the crosslink density homogeneity of films polymerised using predominantly amine addition was increased when the cure temperature was increased from 25 °C to 35 °C. However, little difference was observed between bulk and interphase crosslink densities. Moreover, neutron reflectometry (nanometre-resolution), showed that cure temperature, stoichiometry and overcoating interval all affected film crosslink density at the nanometre scale. In particular, increasing the cure temperature from 25 to 35 °C generally increased crosslink density homogeneity, as regions of increased crosslink density were observed near the surface of films cured at 25 °C. This temperature-dependent effect is likely attributed to the accelerated reaction kinetics at higher temperatures, promoting more uniform crosslinking throughout the material and reducing the formation of localised high-density regions observed at lower cure temperatures. However, throughout all films, no obvious signs of early-stage adhesion failure were observed. Given delamination is a fatigue associated issue, this result may imply that obvious signs of delamination are not intrinsically present in the film from synthesis, and instead are caused by the repetitive cycles of solvent exposure, followed by film drying, in industrial application.

Solvent ingress studies showed that epoxy resin system stoichiometry significantly affected ultimate ingress more than cure temperature. The time-dependence of solvent ingress indicated a behaviour neither purely Fickian (linear dependence of penetration of diffusant with the square root of time) nor Case II (linear dependence with the time), but appeared to be intermediate between these extremes.

“Your ancestors called it magic, and you call it science, well I come from a place where they’re one and the same thing.”

Thor Odinson

Contents

Statement of Copyright

List of Symbols and Abbreviations

1-MI	1-methylimidazole
2-E-4-MI	2-ethyl-4-methylimidazole
AFM	Atomic Force Microscopy
AHEW	Active Hydrogen Equivalent Weight
ATR FT-IR	Attenuated Total Reflectance Fourier-Transform Infrared Spectroscopy
AVV	Average Void Volume
CD_3OD	Deuterated Methanol
CT	Cure Temperature
D	Diffusion Coefficient
D.E.N. 431	Dow Epoxy Novalac 431
D_2O	Deuterated Water
DGEBA	Bisphenol A Diglycidyl Ether
DMA	Dynamic Mechanical Analysis
DMP-30	2,4,6-tris(dimethylaminomethyl)phenol
DSC	Differential Scanning Calorimetry
EEW	Epoxide Equivalent Weight
FFV	Fractional Free Volume
FT-IR	Fourier Transform Infrared
G	Shear Modulus
G'	Shear Storage Modulus

G''	Shear Loss Modulus
GA	Gravimetric Analysis
G^{mix}	Free Energy of Mixing
H^{mix}	Enthalpy of Mixing
m	Mass
M_w	Weight-Average Molecular Weight
NMR	Nuclear Magnetic Resonance
NR	Neutron reflectometry
PAC-M	4,4'-Diaminodicyclohexylmethane
PALS	Positron Annihilation Lifetime Spectroscopy
PGE	Phenyl Glycidyl Ether
PIXE	Proton Induced X-Ray Emission
QNM	Quantitative Nanomechanical Mapping
R	Reflectivity (NR)
RDGE	Resorcinol Diglycidyl Ether
RH	Relative Humidity
R_q	Root Mean Square Roughness
SCA	Solvent Contact Angle
SFE	Surface Free Energy
SLD	Scattering Length Density
S^{mix}	Entropy of Mixing
T	Temperature
t	Time
T_1	p-Ps Lifetime

T_2	Free Positron Lifetime
T_3	o-Ps lifetime
T_g	Glass Transition Temperature
TGDDM	N,N’-tetraglycidyl diaminodiphenylmethane
T_m	Melting Temperature
v	Velocity
VOC	Volatile Organic Compound
WCA	Water Contact Angle

ΔG	Gibbs Free Energy Change
γ	Surface Tension
δ_d	Dispersive Component of Material Cohesive Energy
δ_h	Hydrogen Bonding Component of Material Cohesive Energy
δ_p	Polar Component of Material Cohesive Energy
θ	Contact Angle
λ	Wavelength
ρ	Scattering Length Density / Complex Reflectance Ratio
τ	Stress
ϕ_i	Volume Fraction
χ	Flory-Huggins Interaction Parameter

Acknowledgements

My uppermost gratitude must go to my supervisor, Dr. Richard Thompson whose knowledge, ideas, kindness, and patience were endless, and who allowed me to achieve more than I ever thought possible! In addition, a huge thank you to my external supervisors, Alan Guy and Ralitsa Mihaylova who were always insightful, enthusiastic, and very welcoming. También, me gustaría agradecer a Dr. Mirela Cuculescu-Santana who sparked my passion for research with our turtle endeavours and opened my eyes to the possibility of PhD research. I'd also like to thank the Safinah Group, the European Regional Development Fund, and the Intensive Industrial Innovation Programme for funding the project.

Thank you to Purneema, Ste, Lucy, and Josie for all the help, discussions, and good times along the way! Also, shout out to the boy, PG, and of course, up the Bohs!

I will be eternally grateful for my wonderful family. Thank you to my girlfriend, Beth, and to my sister, Aimée, who never fails to make me feel better in times of stress with our conversations and jokes! Finally, thank you to my parents, my biggest inspirations, without whom I'd have never achieved any of what I have today. To my mum, my best friend, and to my dad, the man I've always aspired to be like; your efforts were never lost on me, and I (your favourite son) will be forever grateful.

Dedication

To Mum and Dad

Chapter 1

Overview

Amine-cured, multi-layer, epoxy coatings are used to line chemical tankers, which transport methanol and other small molecule cargoes, but can undergo interlayer adhesion failure or delamination over time. Throughout this thesis, the surface, bulk, and interface properties of bilayer, amine-cured epoxy systems were investigated as a function of stoichiometry and cure condition (cure temperature, relative humidity, time duration prior to second layer application) to better understand the impact of these variables on interlayer adhesion.

Initially, context regarding the project directions, aims and underpinning science are introduced in Chapter 2, followed by a description of the materials and methods used in Chapter 3. Sequently, Chapter 4 describes how the components that constitute the cured epoxy resin systems were characterised to enable accurate stoichiometric calculations of said resin systems.

In bilayer epoxy systems, the first coat acts as a substrate for the second coat and so the physicochemical properties of this layer are hypothesised to influence the adhesion between layers. Therefore, Chapter 5 discusses the characterisation of the first coat of the 2-layer resin system, prior to overcoating with the second coat as a function of stoichiometry and cure condition. Chapter 6 then goes onto determine the mechanism of interface formation before directly characterising the physicochemical properties of the interphase. Relationships will then be drawn between the first coat properties described in Chapter 5 and the physicochemical properties of the interface.

Chapter 7 describes investigation of the post cured, 2-layer samples (final form) function as a barrier anticorrosive *via* solvent studies. Relationships will be drawn between chemical performance and stoichiometry / cure conditions.

Finally, in chapter 8, all key findings of this research are revisited, drawing final conclusions utilising all collected data. Directions for future work are suggested.

Chapter 2

Introduction

2.1 Maritime Transport

2.1.1 Commercial Coatings and Liquid Cargo Transport

Within maritime transport, coating application is crucial in maintaining aesthetic, structural, and functional integrity, as surface coatings are expected to protect substrate from weather, physical abrasion, and corrosion. In the transport of liquid cargo, cargo tanks are considered revenue-earning spaces and to maintain tank viability various practical and economic factors regarding the application of a protective coating must be considered, including simple and economic application, minimal operational restrictions, chemical resistance to carried cargoes, low cargo absorption and retention, short conditioning /cleaning time and long service life. With the continued increase in world maritime trade over the last decade, the demand for larger chemical tankers has never been higher.[1]This demand is also estimated to increase as the United Nations Conference on Trade and Development (UNCTAD) project an increased annual average growth rate of 2.4% over the period 2022 to 2026, further highlighting the importance of using suitable coatings to protect these assets.[2]

Liquid bulk cargoes, such as oil, oil products and various chemicals, are transported in specialised, protectively coated tankers and transport scheduling is dictated by customer demand, ship location and coating capabilities. Subsequently tankers can be used to transport a variety of liquid cargoes ranging from large and complex molecules (crude oil and petroleum products) to relatively small (acetone, hexane, toluene, benzene, paraxylene, xylene, methanol, *etc*).

2.1.2 Chemical Resistance and Degradation of Commercial Coatings

Coating regime (number of coats, drying time, etc) is decided upon by manufacturers based on a variety of factors, including cost, chemical composition, cure conditions and intended purpose. A single coat (~ 160 microns) system could leave defects such as pinholes or pores that reach down to the steel substrate, leading to corrosion.[3] Because pinholes only constitute a small fraction of the total area, overcoating with a second layer should reduce the risk of uncoated steel substrate. However, two coat systems can be susceptible to intercoat adhesion failure caused by the adverse effects of solvent ingress. Small molecule cargoes are capable of diffusing into the coating free volume where they can be retained, causing swelling and potentially blistering, amongst other failure modes. This can result in contamination of subsequent cargoes (leaching) if an insufficient egress interval is applied. In addition, absorption and desorption of small molecule cargoes from the coating, caused by the cycling of cargoes upon delivery, increases internal coating stresses. This can lead to the coating cracking, delaminating, or detaching, incurring large financial implications. The cost for full tank coating refurbishment on chemical tankers can often reach in excess of $3 million per vessel.[4]

2.2 Epoxy Resin Coatings

2.2.1 Epoxy Resins and Curing Agents

Epoxy coating systems are thermoset polymers produced by the ring-opening of epoxy resin containing more than one epoxy (oxirane) ring (Figure 2.1) *via* reaction with curing agents. Epoxy functional groups are receptive to a broad range of curing agents (amines, polyamides, anhydrides, etc) due to their high reactivity towards nucleophilic and electrophilic species, which is attributed to the strained structure of the oxirane ring.[5,6] Curing agents can be divided into two subgroups: co-reactive and catalytic.[5,7] Catalytic curing agents initiate homopolymerisation through anionic chain-growth polymerisation of epoxide groups, which ultimately leads to low average degrees of polymerisation due to frequent chain transfer reactions and termination.[8,9] Co-reactive curing agents act as a co-monomer, undergoing step-growth addition. The choice of co-reactive curing agent is dictated by cure conditions, cost, practicality, and the chemical and physical properties required of the cured resin. Polyamino compounds, such as diamines, are the most used co-reactive curing agent as they are relatively cheap, can react at ambient conditions and offer property versatility *via* backbone variation.[10]

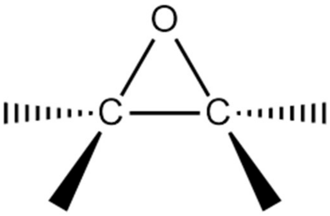

Figure 2.1: Epoxy Functional group.

Amines are organic compounds containing one or more amino groups and are classified as primary, secondary, or tertiary, dependent on the number of hydrogen atom(s) substituted for hydrocarbon(s) within ammonia (NH_3).[11] Further classification can be assigned according to the hydrocarbon backbone: aliphatic, aromatic, or cycloaliphatic amines.[12] The cured resins from these amines exhibit excellent physicochemical properties and heat resistance. While aromatic amines do achieve greater heat and chemical resistance than aliphatic amines under optimal cure conditions,[13] they react more slowly at ambient conditions due to the steric hinderance of the aromatic ring.[11] In addition, as the aromatic ring is electron withdrawing, the amine is therefore less nucleophilic, and as such increased energy would be required to carry out amine-epoxy reactions as they are typically nucleophilic.[14]

Therefore, when cured under ambient conditions, such as in marine coating application, the properties exhibited in aliphatic amine-cured resins can be superior to that of aromatic amine-cured resins. In addition, some aromatic amines are potent carcinogens, which renders them less attractive.

2.2.2 Epoxy-Amine Reaction

Epoxy resins react with amine-based curing agents *via* step-growth addition; each independent step involves the reaction of two separate functional sites leading to the formation of new covalent bonds. Figure 2.2 shows that primary amines react with the epoxy ring to form a secondary amine and a hydroxyl group.[11,15,16] The secondary amine can react again with another epoxide group to form a tertiary amine, with the hydroxyl groups generated acting as a catalyst for further reactions.[17,18] To achieve crosslinking of these networks, average functionality must be greater than 2.

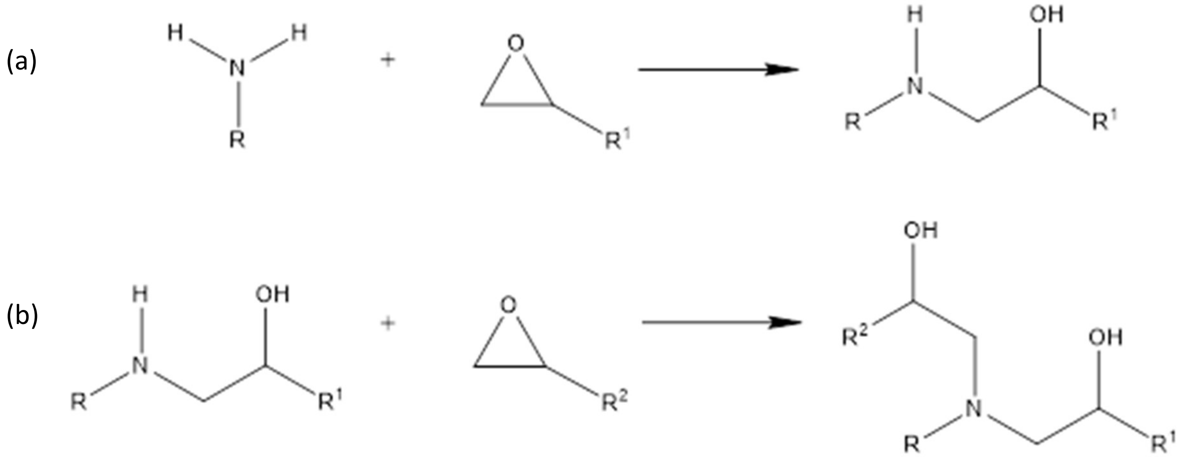

Figure 2.2: a) Primary amine reacts with epoxy forming secondary amine. (b) Secondary amine reacts with epoxy to from tertiary amine.

2.2.3 Epoxy Network Formation

The curing of epoxy resins can be simplified into three stages. Initially, linear growth occurs, increasing molecular weight. Next, the chains begin to branch, eventually reaching the gel point where there is sufficient interconnection between branches forming a continuous, insoluble three-dimensional network. Supported within this network remains the sol fraction: extractable material that has not yet reacted with the network. The final stage, usually but not necessarily requiring elevated temperatures and often incomplete in industrial application, involves the incorporation of the remaining sol fraction into the network.[8]

As well as crosslinking achieved *via* step-growth amine addition, network formation can also be achieved through anionic and cationic chain-growth polymerisation of epoxide groups.[19,20] This is typically done by utilising a “post-cure” (additional elevated cure temperature) step in the presence of suitable catalytic curing agents. Within this work, Lewis bases such as imidazoles or tertiary amines, were used as catalytic curing agents. As Lewis bases initiate anionic polymerisation rather than cationic polymerisation,[20] only anionic polymerisation will be discussed. The reaction mechanism of anionic epoxy polymerisation has not yet been fully established, but two initiation processes have been proposed. The first (pathway 1) involves the formation of an alkoxide adduct through the reaction of an epoxy group and a tertiary amine, Figure 2.3.[17,21] From here, propagation can occur, in which the negatively charged oxygen of the alkoxide zwitterion can react with another epoxy group leading to chain growth.[9,20,21]

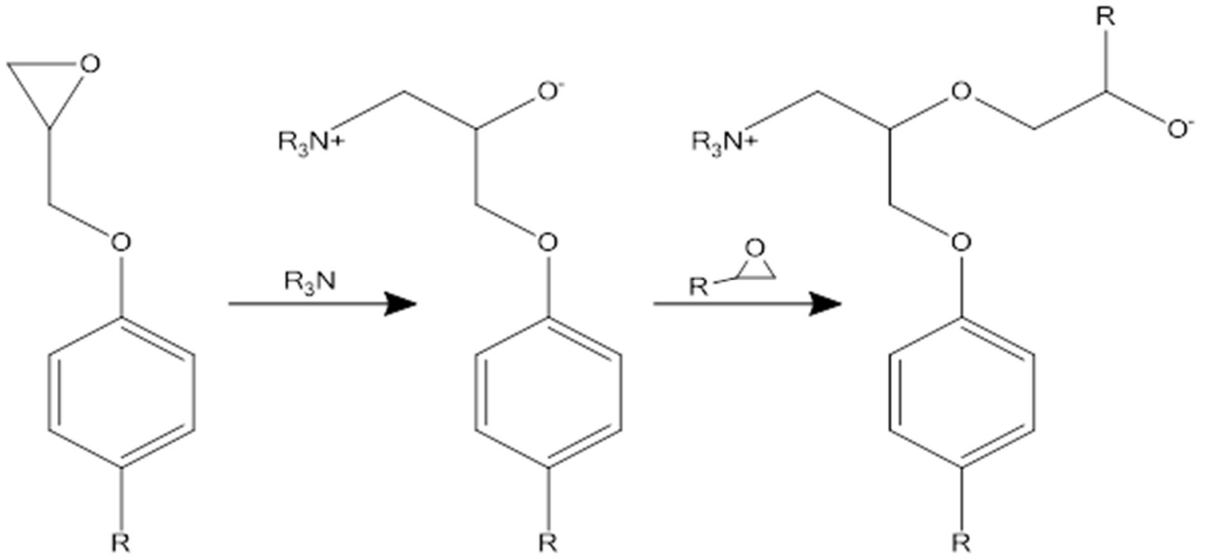

Figure 2.3: Initiation and propagation of epoxy homopolymerisation (pathway 1).

This reaction pathway was adopted by Farkas and Strohm who proposed a two-step initiation mechanism for the polymerisation of monofunctional phenyl glycidyl ether (PGE), and 2-ethyl-4-methylimidazole (2-E-4-MI), Figure 2.4, through which the pyrrole-type nitrogen (N1) of 2-E-4-MI attacks the terminal epoxy carbon of the PGE to generate an adduct.[22] This adduct was then free to propagate further reaction with PGE epoxies *via* etherification, thus allowing the 2-E-4-MI to act as an initiator for polymerisation.[22] This mechanism was later revised by Barton and Shepherd who concluded that the other nitrogen (N3) was the reactive species.[23]

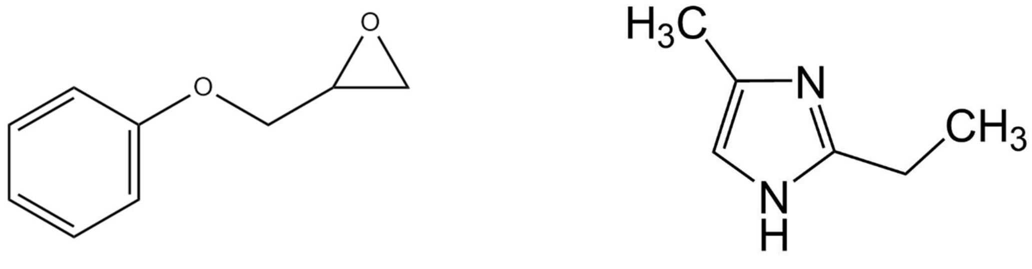

Figure 2.4: The structure of phenyl glycidyl ether (left) and 2-ethyl-4methylimidazole (right).

The second proposed initiation process (pathway 2) involves the formation of a quaternary ammonium alcoholate counterion to the propagating anion (Figure 2.5). The propagating anion is then free to react with epoxy groups, leading to chain growth.[20] Therefore, in principle the polymeric product is free of nitrogen.

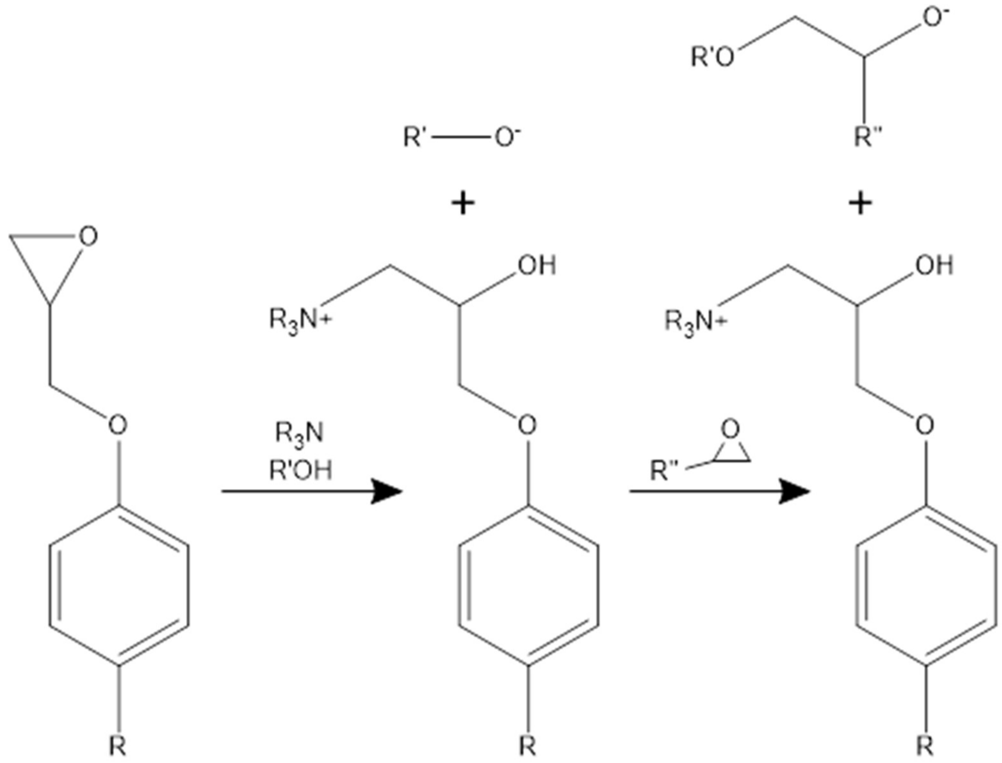

Figure 2.5: Initiation and propagation of epoxy homopolymerisation (pathway 2).

Termination of both pathways 1 and 2 are alike. Due to the extensive source of protons in the reaction mixture from active-hydrogen species, and the polar nature of the active alkoxide, chain transfer of the propagating anion from non-epoxy sources can be frequent. Ultimately this transfer reaction leads to termination, limiting chain length at any stage. [17,24] Unlike free radical polymerization of acrylic monomers, propagation in epoxy anionic polymerization does not lead to high chain lengths. Typically, low degrees of polymerization (<10, commonly 3-6) are observed.[17]

Tertiary amine catalysts can be regenerated by several mechanisms, such as *via* elimination or substitution reactions as shown in Figure 2.6.

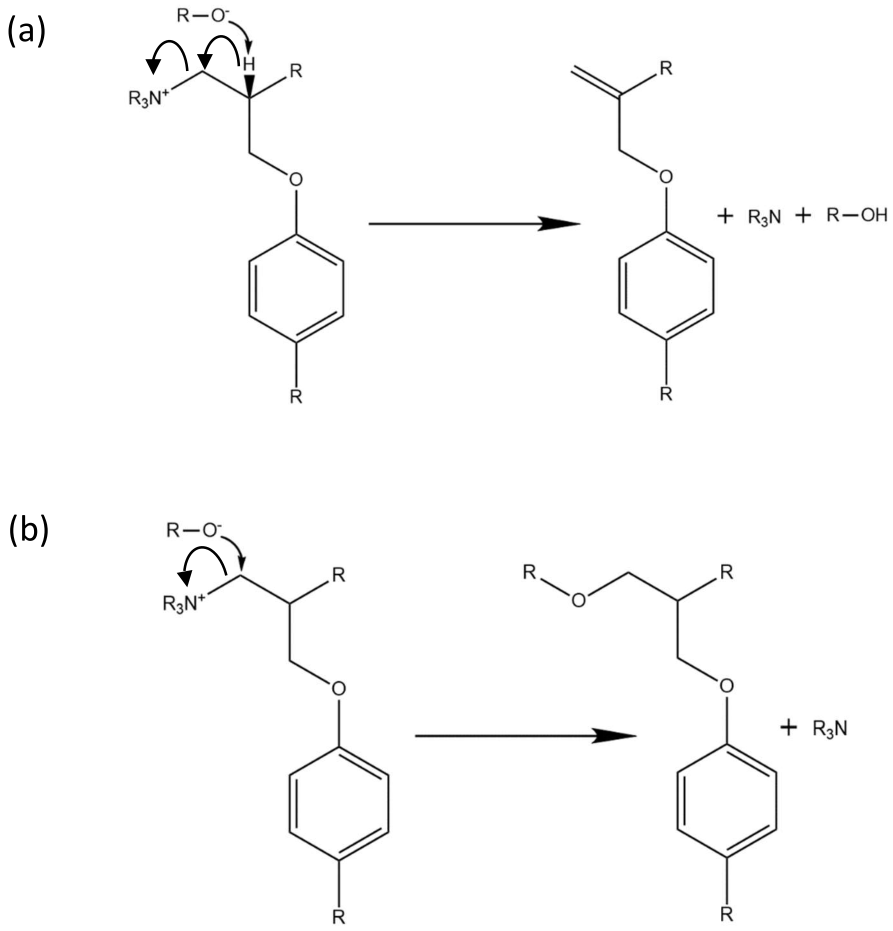

Figure 2.6: The reaction pathway for catalyst regeneration via elimination (a) or substitution (b).

2.2.4 Properties and Applications of Epoxy Resin Coatings

Epoxy thermosets remain one of the most widely used high-performance polymeric materials due to their ease of processing, excellent physicochemical properties, and the extensive understanding regarding their chemistry and cure kinetics.[25,26] As coatings, epoxy resins are often primarily applied for protective or aesthetic purposes, but commonly have more specialised functions such as an anti-corrosion for ship steel or as a high-level insulator in electronic application.[27] As such, epoxy resin coatings have found application in a variety of sectors and remain the most widely used technology for protecting steel.

Within industry, the processing of epoxy resins is convenient as viscosity is inherently low and can be further reduced *via* the inclusion of a compatible organic solvent, allowing for spray coating application. This can also increase coating flexibility, quality of finish, and polymer into substrate permeability.[28,29] However, Trinidad *et al.* showed that if residual solvent is included, and remains in a cured resin coating, the thermal and mechanical properties can be negatively impacted.[30] Yi *et al.* reported that degree of cure and tensile strength of the cured resin decreased with the addition of solvent.[28] In addition, Shackleton reported that system T_g decreased and free volume increased in solvated epoxy systems.[31] While the inclusion of solvent is widely reported and enables easier processing, it can be concluded that as well as the environmental consideration of additional VOCs, there are often undesirable consequences for the finished coating properties.

Alternatively, the processing requirements (viscosity, application method, pot life and cure temperature), and resultant resin properties (chemical and thermal resistance, toughness, tensile strength) can be varied through the use of different curing agents, as the molecular composition of the curing agent (and epoxy) determine the type of chemical bonds that will occur.[12,13,32] Marks and Snelgrove found that fracture toughness of amine-cured thermosets was influenced by curing agent structure,[25] while Wang *et al.* showed that the curing behaviour and resultant properties (chemical resistance, thermal stability, tensile strength, modulus, swelling ratio, *etc*) of amine-cured bioepoxy resins was significantly varied through the use of different curing agents.[33]

The stoichiometry of a formulation, defined by the ratio of curing agent active hydrogens to epoxy functional groups, has also been identified as a variable which influences material properties, as it can be used to control the distribution of polymerisation mechanisms (step-growth amine addition, anionic chain-growth polymerisation), as well as the extent of cure.[34–37] For example, step-growth addition (Figure 2.2) promotes the formation of polar hydroxyl groups, while in the case of anionic polymerisation (Figure 2.3 and Figure 2.5), less polar ether groups are formed. Therefore, the resultant polymer polarity, attributed to variation in stoichiometry, will impact compatibility with other materials / solvents. Both Meyer *et al.* and Gupta *et al.* observed variation in the thermal and mechanical properties of epoxy resins cured at varying epoxy-hardener ratios.[34,38] The extent of cure (or conversion achieved) of an epoxy system, rarely complete in practical coating applications, is thought to be important for barrier properties, flexibility, and surface properties.[39] In practical application, often processing time is favoured over completeness of functional group conversion if the resultant properties are sufficient.[25] The cure temperature and duration has also been identified as a parameter which influences extent of cure, as previous studies have shown how increasing the cure temperature / duration leads to increased conversion.[40,41] Within polymer chemistry, conversion achieved can be indirectly estimated using the Miller Macosko theory, which provides a mathematical, network modelling approach for the prediction of the sol fraction in polymer networks formed by step-growth polymerisation.[42] Put simply, the theory considers the length and site distribution of polymer chains and employs a recursive probability methodology to predict the outcome of different events occurring during the polymerisation process, which is then used to estimate sol fraction.

2.3 Epoxy Resin Coating Production

Processability, intended coating properties, and the demands of coating performance dictate the required production process of epoxy resin coatings. Therefore, to ensure coating success, it is essential that prior to coating application, manufacturers must consider a plethora of variables such as stoichiometry, cure conditions, and cure regime.

2.3.1 Stoichiometry and Formulation Strategies in Epoxy-Amine Coatings

Stoichiometry defines the ratio of two different functional group types in a reacting system. Systems defined as on-stoichiometry have a 1:1 ratio of component functional groups. As explained in Section 2.2.4, previous studies have shown how variation in stoichiometry can influence the properties of the cured resin system.[34,36–38] Often, coating manufacturers will utilise off-stoichiometry, epoxide-excess formulations, in the presence of accelerators, to promote homopolymerisation of epoxide groups. This allows for the formation of highly crosslinked networks in systems with less curing agent, thus reducing environmental impact and cost as typically curing agents are more expensive than epoxies.[24]

Within epoxy-amine systems, stoichiometry is calculated using epoxide equivalent weight (EEW) and active hydrogen equivalent weight (AHEW). Equivalent weight is simply the mass of material required to give 1 equivalent of functional groups. The nominal epoxy resin equivalent weight (Equation 2.1) or active hydrogen equivalent weight (Equation 2.2) can be determined using the following equations:

$$EEW = \frac{M_w}{Epoxy\ functionality}. \tag{2.1}$$

$$AHEW = \frac{M_w}{Amine\ functionality}. \tag{2.2}$$

For systems in epoxide excess, stoichiometry can be calculated using the following equation:

$$Stoichiometry = \frac{wt\ amine}{AHEW} \div \frac{wt\ epoxy}{EEW}. \tag{2.3}$$

2.3.2 Managing Induction Time to Mitigate Carbamation in Epoxy-Amine Systems

Induction time refers to the amount of time between reactant mixing and coating application, and influences mixture compatibility and viscosity. The amine component of epoxy-amine systems is often only partially compatible with epoxy components and so tends to migrate to the film surface during the liquid cure phase.[43] As amines are characteristically hygroscopic and efficient carbon dioxide scavengers, at the surface they can react with carbon dioxide and moisture in the air (Figure 2.7). This leads to a disproportionate fraction of amine groups consumed near the sample surface and sometimes manifests as a white surface layer salt, termed carbamate. While all systems cured under ambient conditions can be expected to experience some degree of carbamation (due to the CO_2 in the atmosphere), sufficient carbamate formation at the surface of the first coat can lead to the formation of a weak boundary layer in bilayer epoxy resins, upon overcoating with a sequential layer.[3,44–47] This decreases interlayer adhesion, which can eventually lead to interlayer delamination (the separation or detachment of layers of epoxy, resulting from a loss of adhesion), if compounded with other issues (which will be discussed later in Section 2.5.3). However, while carbamation is recognised as a potential source of a weak boundary layer in epoxy-epoxy interfaces, the intricate mechanisms and interactions governing this phenomenon have yet to be fully elucidated and require further investigation.

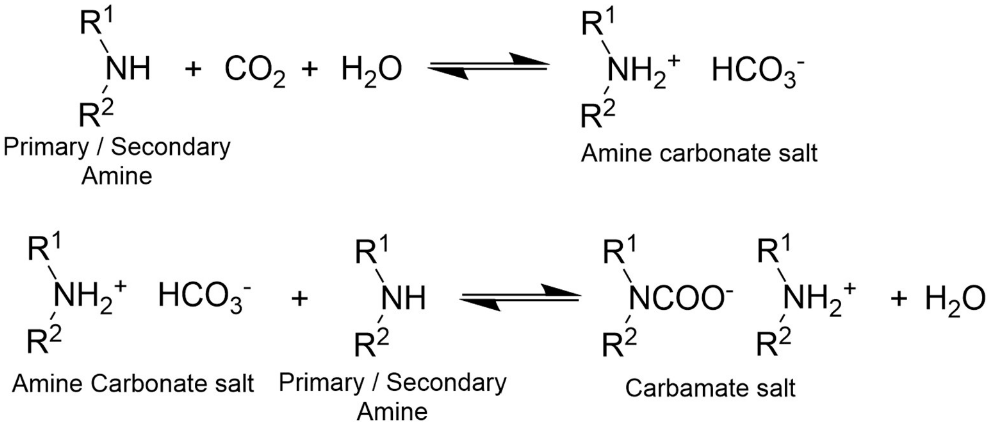

Figure 2.7: Reaction scheme of primary / secondary amine and CO_2.[206]

The inclusion of an induction time prior to coating application allows free, low molecular weight amine hardener to pre-react with epoxies to produce oligomeric molecules. This improves amine-epoxy compatibility and increases bulk viscosity. Pre-reaction slows down any migration of amine and consequently reduces the opportunity for carbamate to form. While this is understood, and some authors have shown that increased exposure time and reactant chemistry are amongst the variables which can increase carbamation in epoxy-amine systems, this area remains less studied. Consequently, data quantifying the amount of surface layer formed, and the subsequent impact on film surface properties could not be found.

2.3.3 Epoxy Resin Ambient Cure Stage, Gelation and T_g

Post mixing and casting, some systems, especially those using aliphatic amines, are left to cure under ambient temperature and relative humidity, RH, forming the ambient cure stage. This allows the formation of fully soluble branched clusters up to the gel point, at which point the system changes state from a liquid to more solid like material as the bulk material is no longer fully soluble.[25] Gelation is defined as the point where a single, covalently bonded molecule percolates through the entire volume of the sample, forming a three-dimensional network. Gelation rapidly increases system viscosity, increasing glass transition temperature, T_g. T_g corresponds to the temperature at which there is a shift in the properties of the polymer, changing from that of a rigid, glassy state to a more flexible rubbery state. This occurs when there is sufficient energy to induce rapid chain segmental motion about single bonds, thus reducing crosslink rigidity.[48,49]

Within epoxy resin chemistry, system T_g can give an indication of the conversion achieved, in same stoichiometry systems where the number of competing reactions is consistent.[50] Therefore, an increase in T_g is indicative of advancing cure or epoxy ring consumption. The extent of epoxy conversion (extent of cure) can be measured in real time using Fourier-transform infrared (FTIR) spectroscopy by tracking the intensity of one of the peaks associated with the epoxy ring, over time. At ~ 4530 cm^{-1} there is a signal which corresponds to the secondary overtone of the CH_2 vibrations of the epoxy ring (fundamental C-H stretching at 2725 cm^{-1}). Figure 2.8 shows that the intensity of this peak decreases over time indicating that the epoxy ring concentration within the sample decreases as cure advances *via* ring opening. Transmittance data (Figure 2.8) can then be converted into concentration (Figure 2.9) using the Beer-Lambert law. It should be noted that there is some error in the associated figures arising from uncertainties from the choice of peak area and the assumption that the baseline would be flat at zero concentration.

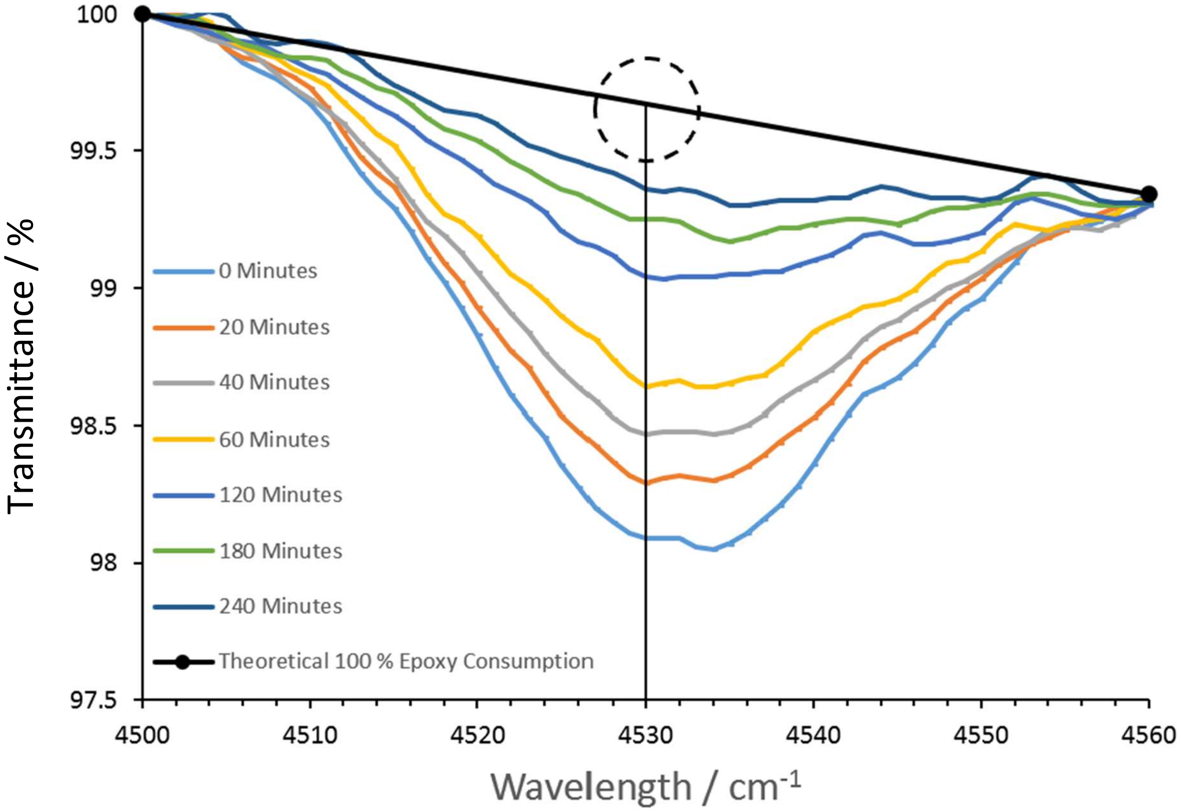

Figure 2.8: Transmission FTIR spectrum (4500-4600 cm^{-1}) of a model epoxy system (phenyl glycidyl ether and 4-methylcyclohexylamine) focused on the NIR epoxy ring combination band (4530 cm^{-1}) during curing. The theoretical point of 100% epoxy conversion has been circled. Methods provided in Section 3.7.

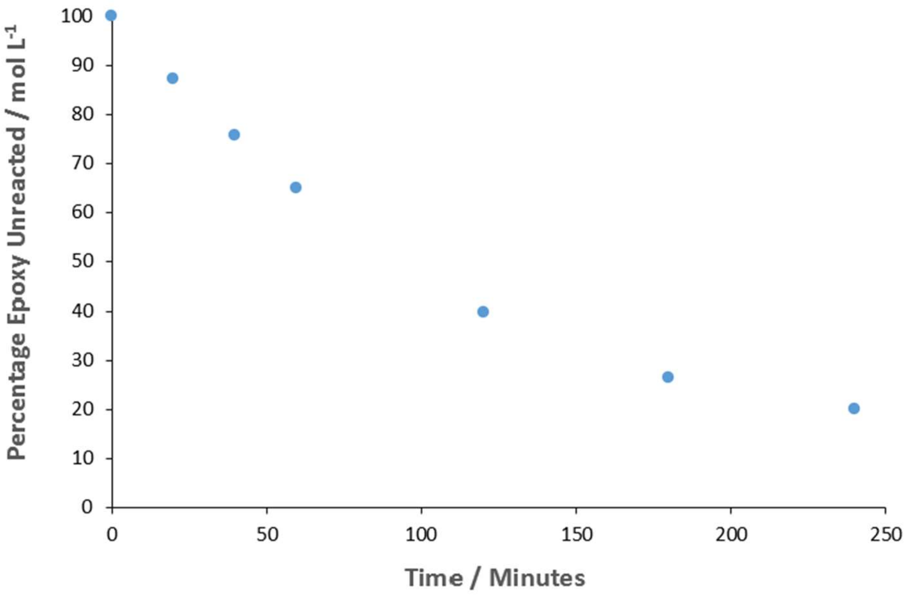

Figure 2.9: Scaled epoxy concentration of curing model system over time.

2.3.3.1 Ambient Cure Condition Variability

Seasonal and geographical variation means ambient cure RH and temperature are variable. In industrial environments, RH should be maintained within the limits specified by the coating manufacturers (often <50% RH for tank linings) and ambient temperature usually falls between 25 – 35 °C. It is well known that increasing the cure temperature advances cure by increasing the rate of reaction. Lapique and Redford even showed that increasing the cure temperature from 23 to 45 °C significantly impacted the viscoelastic properties of a two-component epoxy resin system during curing.[40] However, it has not been reported how variation within the ambient ranges influences first coat surface and bulk properties, and in turn, interface formation and adhesion.

2.3.4 Overcoating Interval in Multilayer Epoxy Resin Coatings

The duration of time allocated to first coat cure, prior to second coat application is termed the overcoating interval. Most coating manufacturers advise overcoating is carried out within a critical time window.[3] A sufficient minimum interval should be observed to allow the first coat time to gel and therefore prevent the coat sagging and running upon application of the second coat. Conversely, an excessive interval may lead to elevated crosslink density in the first coat, theoretically decreasing the ease of interdiffusion of the second, top layer into the first, base layer, thus forming a smaller boundary layer more susceptible to adhesion failure. Figure 2.10 displays a schematic of two epoxy resin matrices allowing for the visualisation of low and high crosslink density. Currently the quantitative impact of variation in overcoating interval on interface formation have not, to the author's knowledge, been reported and as such its impact on adhesion failure not understood.

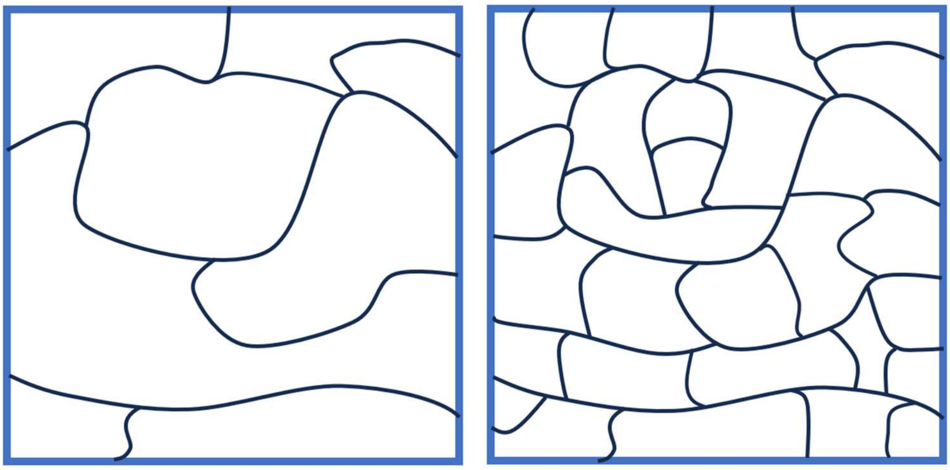

Figure 2.10: A schematic of a crosslinked epoxy resin matrix at low (left) and high (right) crosslink density.

Post second coat application, the system is allowed to cure under ambient conditions. Following this, many dry film thickness readings are taken in which film thickness must fall within a recommended range. Low thickness areas correspond to decreased coverage and protection, while excessive thickness areas may have elevated internal stress, increasing the potential for coating cracking.

2.3.5 The Influence of Post Cure Step on Coating Properties

As the cure progresses and the network continues to form, system T_g also increases. While the cure temperature is above the system T_g (like in the ambient cure stage), the rate of reaction and extent of epoxy conversion achieved is kinetically controlled. Eventually the system T_g increases to the point of cure temperature, and at which point rate of reaction slows dramatically as it is now limited by the rate of diffusion of the functional groups. This is termed vitrification and post this point; further reaction can become limited. Large fractions of sol can have a negative effect on the desired properties of the cured resin. Therefore, in order to complete the cure, and unlock the full potential of the resin properties, an elevated cure temperature step above T_g, termed the “post cure”, is often employed. In addition, catalytic curing agents which promote epoxy homopolymerisation typically have high activation temperatures which require the application of a post cure step.

As post-curing increases film crosslink density, and epoxy-epoxy interfaces are thought to form *via* interdiffusion, entanglement and subsequent crosslinking between layers, post-curing should be conducted after overcoating. This to ensure first coat crosslink density is not too high and inhibits second coat ingress.

2.4 Interface Formation of Multilayer Epoxy Resin Coatings

2.4.1 Formation Mechanism

While the interface formation mechanism of epoxy-substrates[51–56] and epoxy-thermoplastics[57–63] has been previously documented, bilayer epoxy interface chemistry remains less studied and further understanding as to the formation mechanism is an aim of this thesis. For strong adhesion between layers of epoxy, it is thought that some interdiffusion and entanglement between the propagating structures of the first and second layers must occur, so that the cross-linked structure propagates across the interface, forming an interphase. [64–67] An interface is defined as the two-dimensional surface whereby two bulk phases meet, whereas an interphase is defined as the three-dimensional region encompassing the interface and a zone of finite thickness either side of the interface where physicochemical properties vary from that of the bulk.[68,69] If adhesion between layers is low, delamination can occur.[70]

Jones and Richards state that for truly miscible polymers there is no equilibrium interface width and that the practically achieved interface width is solely determined by the kinetics of the interface formation and the time available.[71] This can be described by equation 2.4, which describes the growth in interfacial width, *w*, by Fickian diffusion (linear dependence of penetration of diffusant with the square root of time).[72] In this case, interface width grows indefinitely.

$$w = \sqrt{4D \times t} \tag{2.4}$$

where *D* is the diffusion coefficient and *t* is time (Figure 2.11).[73] However, the situation is not so simple for thermoset polymers. While equation 2.4 may provide a reasonable description of the early stages of interdiffusion, it is clear that the interface width cannot grow indefinitely, because the topological constraints of the cured resin would restrict long range interdiffusion. Instead, it could be hypothesised that interdiffusion is influenced by the first coat surface (surface roughness, wettability, surface free energy) and bulk properties (extent of conversion, free volume) of the cured resin.

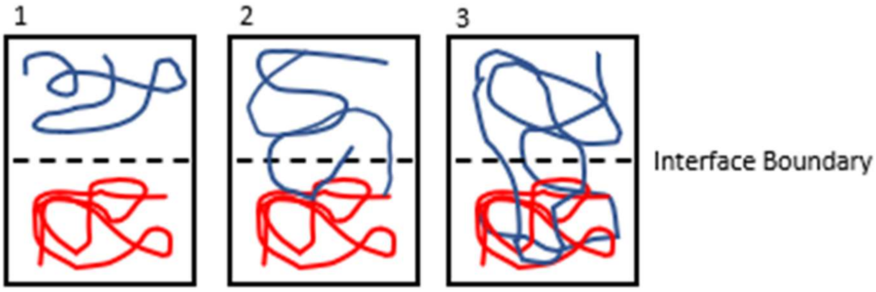

Figure 2.11: A schematic of a second layer polymer chains (blue) diffusing into the first layer (red).

2.4.2 The Role of First Coat Properties in Interface Formation

The physicochemical properties hypothesised to influence interface formation in 2-layer epoxy systems are of interest within this thesis as this remains an unexplored area within academic epoxy literature. When considering the adhesion of two surfaces, some authors suggest that substrate roughness and surface free energy (SFE) are important, [70,74–77] while others regard the impact of SFE on intercoat adhesion as less important, particularly in polymers where the SFE is already low (typically <60 mJ/m^2) compared to the energy required to fracture an interface.[78] Instead, surface chemistry and the ability to form an interpenetrating network are proposed as more relevant factors.[79,80] The following sections will outline the first coat surface and bulk properties hypothesised to influence second coat interdiffusion.

2.4.2.1 Surface Properties

The idea of macroscopic material interlocking attributed to mechanical keying, often depicted as mortise and tension joints, has been refuted at the nanometre level; Kendall discusses the theories and laws of molecular adhesion stating that atomically smooth surfaces adhere best of all.[79] However, while others have shown that increasing the surface roughness can lead to increased adhesion by increasing the surface area available for chemical bonding, these studies were performed on epoxy-metal substrate complexes where the extent of interdiffusion is negligible.[81,82] If 2-layer epoxy systems are to form *via* interdiffusion, the practical impact of increasing roughness in these systems is likely to be insignificant. In theory, doubling the surface area should double the adhesion from surface energy. However, surface energy alone is a relatively trivial effect, increasing surface energy from approximately 0.1 J/m^2 (~ 0.03 J/m^2 reported by Minisini, *et al*. for a TGDDM / 4,4′-methylenebis(2-methylcyclohexylamine) epoxy system[83]) to 0.2 J/m^2 compared to the several hundred J/m^2 required to fracture an interface, (343 J/m^2 reported by Quan and Ivankovic for a DGEBA-dicyandiamide-fenuron epoxy system).[84]

SFE is a characteristic, thermodynamic property which describes the excess energy (or unrealised bonding) at the surface of a material.[85] The consideration of surface free energy has been described as fundamental to understanding adhesion,[86] as previously authors have shown a correlation between interface adhesion and SFE.[76] Arslanov and Ogarev varied the surface free energy of an aluminium substrate *via* anodization or chemical oxidation and showed a linear correlation between substrate SFE and the magnitude of adhesive strength between a polymeric acrylic varnish and the aluminium substrate.[76,87] Following a similar rationale, considering the negligible interdiffusion in epoxy-metal systems,[81,82] higher SFE of the metal ship tanker substrate, to which epoxy is bound, is likely to result in greater adhesion. However, when considering epoxy-epoxy interactions, should interdiffusion occur, the impact of SFE on adhesion may be less significant. Nevertheless, the characterisation of SFE remains an important surface property as variation in SFE between different systems can indicate differences in surface chemistry, and therefore the ability to react and form strong bonds across an interface.

Surface wettability is a physicochemical parameter linked to surface energy as it describes how well a liquid can spread upon a substrate. Therefore, for epoxy-epoxy interface formation, surface wettability limits interdiffusion as it concerns the ability of the second coat of epoxy (liquid) to spread upon the first coat (solid) during application and permeate any cracks that may be present in the first coat. Herczeg *et al.* stated that improved adhesion can be expected through improved wetting and better interfacial contact.[43] Therefore, it can be hypothesised that an increase in surface wettability would increase the surface area available for interdiffusion, which is more favourable for interphase formation.

2.4.2.2 Bulk Properties

Within epoxy resin chemistry, once significant conversion has been achieved during curing, a crosslinked network may be formed, depending on the system. Given that two-coat epoxy system adhesion is thought to form through interdiffusion,[64–67] it is hypothesised that elevated crosslink density in the first coat would be expected to decrease second coat diffusion potential, thus decreasing interfacial width, forming a smaller boundary layer.

Free volume is linked to extent of cure and crosslink density as first coat free volume represents the space available for the second coat to diffuse into upon overcoating. Previous studies have shown a correlation between increased epoxy free volume and increased rate / extent of solvent ingress.[31] Therefore, it is hypothesised that increased free volume (void volume and total volume) in the first coat would increase the rate and extent of second coat diffusion. Currently, no literature has explored the impact of first coat epoxy resin free volume on extent of second coat interdiffusion.

2.5 Interactions of Epoxy Resin Coatings with Solvents

The industrial application of the epoxy coatings studied in this research is as a barrier anticorrosive used to line the inside of chemical tankers in the transport of reactive and corrosive liquid cargoes and chemicals. Subsequently, solvent-coating interaction is inevitable, and these interactions are influenced by a variety of parameters, such as thermodynamics, epoxy network structure and solvent molecular size.

2.5.1 Solvent Ingress

Solvent ingress is the action of solvent entering a material. Rate and extent of ingress is determined by material permeability, which is a measure of the ease of flow of a liquid or gas through a medium. Polymer permeability depends on diffusion and solubility as,[88]

$$\text{Permeability (cm}^2\text{/s)} = \text{Diffusion (cm}^2\text{/s)} \times \text{Solubility (g/g)}. \qquad 2.5$$

Diffusion encapsulates several factors relating to absorption kinetics (T_g, crosslink density, chain packing and density, film morphology and penetrant molecular dimensions),[72] while solubility concerns the miscibility of the polymer network with the penetrant, reflecting the relative thermodynamic interactions between the two.

2.5.1.1 Solvent Diffusion in Polymers

Diffusion is the movement of particles down a gradient in chemical potential enabled by thermal energy.[89] The diffusion of solvent into polymers or resins is a complex process due to the physical properties of polymeric materials and consequently a single theoretical framework or mathematical model has yet to describe the process.[72] Several diffusion models have been proposed, including Fickian (Case I), Non-Fickian (Case II), sigmoidal, and two-step diffusion.[90]

Fickian diffusion, in which the mobility of the diffusing species is independent of its concentration, is characterised by a linear dependence of penetration of diffusant with the square root of time. Fick's first law (Equation 2.6) assumes that the flux (*J*) through a material of distance x is proportional to the concentration (*c*) gradient measured normal to the system with a known proportionally, termed the diffusion coefficient (*D*). Fick's second law (2.7) relates the concentration change as a function of time, to the flux relative to position.[72]

$$J = -D\frac{\delta c}{\delta x}, \qquad 2.6$$

$$\frac{\delta c}{\delta t} = \frac{\delta J}{\delta x}, \qquad 2.7$$

For Fickian diffusion to occur, upon change in conditions, the surface concentration must immediately attain equilibrium value and remain constant through the sorption process. In addition, the mobility of the diffusing species must be independent of its concentration, *i.e.*, ingress must not have any plasticising effect on the polymer matrix. For most polymer-solvent systems, these requirements are too simplistic and not accurate.

Whereas Fickian diffusion fronts propagate a distance through a material that is proportional to $t^{1/2}$, Case II diffusion is observed to be linear with t.[91] Case II diffusion is usually associated with a sharp penetrant front propagating through the polymer at constant velocity, and thus total sorption is linear with respect to time.[73,92]

2.5.1.1.1 Measuring Small Molecule Diffusion in Polymers

The diffusion of small molecules into polymers has been investigated for a variety of systems and applications. Typically, the penetration of small molecules into glassy polymers exhibits Case II diffusion,[93,94] whereby diffusion is predominantly controlled by three factors: polymer free volume, solvent molecular size, and polymer-solvent interaction.[92] Previously, various analytical techniques have been used to quantify solvent ingress into polymers, including gravimetric analysis,[10,31,95,96] ion beam analysis,[97] and neutron reflectometry.[92]

Within epoxy ingress studies, predominantly gravimetric analysis has been used to quantify solvent mass uptake over time due to its relative simplicity. However, it is important to note that gravimetric analysis has inherent limitations. This method solely measures the overall change in mass attributed to solvent uptake without providing insights into the specific interactions occurring at the molecular level. For instance, upon ingress the solvent may induce plasticisation of the epoxy matrix, resulting in further solvent uptake. Didsbury used gravimetric analysis to quantify solvent ingress into amine-cured epoxy resins produced from bis(epoxide) monomers based on either catechol, resorcinol, or hydroquinone.[10] He concluded that the system cured from the resorcinol-synthesised monomer exhibited the greatest chemical resistance compared to those cured from the other bisepoxide monomers. He then went on to quantify the free volume of these systems stating that average void volume (AVV) measured by PALS was inversely proportional to crosslink density.[10]

The work of Didsbury correlated with the work of Jackson *et al.* who utilised PALS to probe the AVV of morphologically different epoxy resin systems and used gravimetric analysis to monitor solvent uptake as a function of said morphology.[96] It was observed that solvent uptake kinetics had a strong dependence on AVV as uptake decreased as solvent molecular volume approached AVV; gravimetric analysis (0.1 mg / 300 mg sample) showed that methyl ethyl ketone (~88 Å^3) was excluded from post-cured epoxy networks with an average void volume of ~59 Å^3. This highlights that polymer free volume and penetrant molecule volume are essentially two different aspects of the same situation and are both important regarding diffusion. Therefore, it was concluded that reducing the AVV is a reasonable approach to exclude solvents from epoxy resins.[96] In a similar study, Frank *et al.* used PALS and gravimetric analysis to investigate the impact of stoichiometry on solvent ingress.[95] They reported that systems in epoxide excess had a smaller AVV and fractional free volume (FFV), which decreased the ingress of water and methyl ethyl ketone. The decrease in AVV and FFV was hypothesised to be due to enhanced chain packing caused by etherification.[95]

2.5.1.2 Flory-Huggins Solution Theory

While the kinetics of solvent migration through a polymer network is concerned with diffusion, thermodynamic parameters such as solubility also influence ingress as increased compatibility increases ingress potential. When considering the solubility and compatibility of a polymer and solvent, Flory-Huggins (FH) theory is a useful starting point.[98,99] The theory describes the thermodynamics of polymer blends and solutions using a 2-dimensional lattice model whereby all sites within the lattice are fully occupied by components of the system (Figure 2.12).

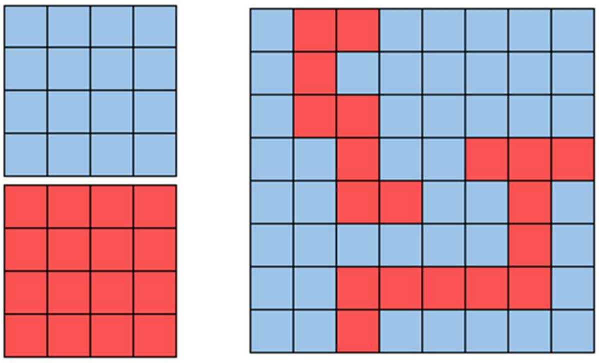

Figure 2.12: Illustration of a 2-D lattice model of polymer (red) and solvent (blue) mixing: unmixed (left) and mixed (right).

Entropy of mixing is the total increase in entropy (or disorder), when initially separate components of different composition are mixed without chemical reaction leading to a new internal thermodynamic state of equilibrium. The FH theory accounts for entropy of mixing by including molecular component sizes. The overall Gibbs free energy change, ΔG^{mix}, (Equation 2.8) for the mixing of a polymer and a solvent can be written as:

$$\Delta G^{mix} = \Delta H^{mix} - T\Delta S^{mix}, \qquad 2.8$$

where ΔH^{mix} is the enthalpy of mixing and ΔS^{mix} is entropy of mixing. ΔH^{mix} can be obtained by considering the first neighbour intermolecular interactions in the system: solvent-solvent, solvent-monomer, monomer-monomer (ω_{11}, ω_{12}, and ω_{22} respectively). From these, the energy increment per solvent-monomer contact constituting the enthalpic part of the Gibbs free energy change, $\Delta\omega_{12}$, can be given as

$$\Delta\omega_{12} = \omega_{12} - \tfrac{1}{2}(\omega_{11} + \omega_{22})\,. \qquad 2.9$$

By determining the number of solvent-monomer contacts in the solution, and defining the solvent and polymer volume fractions (ϕ_1, ϕ_2 respectively) using equations 2.10 and 2.11, where N_1 is the number of solvent molecules and N_2 is the number of polymer molecules with x degree of polymerisation

$$\phi_1 = \frac{N_1}{N_1 + xN_2} \qquad 2.10$$

$$\phi_2 = \frac{xN_2}{N_1 + xN_2} \qquad 2.11$$

the enthalpy of mixing can be expressed as

$$\Delta H^{mix} = (z - 2)N_1\phi_2\Delta\omega_{12}\,, \qquad 2.12$$

where z is the number of nearest cell neighbours. Given $\Delta\omega_{12}$ and the lattice parameter are not easily accessible, they are replaced by the Flory Huggins polymer-solvent interaction parameter, χ

$$\chi = (z - 2)\tfrac{\Delta\omega_{12}}{kT}\,, \qquad 2.13$$

simplifying ΔH^{mix} to

$$\Delta H^{mix} = kTN_1\phi_2\chi\,. \qquad 2.14$$

As ΔS^{mix} can be expressed as

$$\Delta S^{mix} = -R[n_1 ln\phi_1 + n_2 ln\phi_2] \qquad 2.15$$

where n_1 and n_2 are the number of solvent and polymer moles respectively, the expressions for the enthalpy and entropy of mixing can be combined, yielding the Flory-Huggins equation for the Gibbs free energy of mixing,

$$\Delta G_m = RT[n_1 ln\phi_1 + n_2 ln\phi_2 + n_1\phi_2\chi]\,. \qquad 2.16$$

Entropy of mixing decreases as the molecular weight builds up, and so compatibility may decrease. It is worth noting that in the case of epoxy networks, as the epoxy component becomes extremely large, its contribution to the entropy of mixing tends to approach zero. This is an important consideration in the context of epoxy resins and their behaviour in polymer blends and solutions, as it implies that the entropy-driven aspects of mixing become less significant with increasing epoxy content.

2.5.1.3 Solubility Parameters

Generally, the miscibility of penetrant and polymer network is governed by their respective chemical structure as usually chemical similarity favours solubility.[100] The Hansen solubility parameters (HSP) provide a quantitative framework for understanding and predicting the solubility and compatibility of different materials. HSP estimate the proportion of different interactive forces responsible for the compatibility between materials by accounting for respective chemical functionality.[101] This parameter system fundamentally divides the cohesive energy, which concerns molecular interactions, into three distinct components: dispersive (δ_d), polar (δ_p), and hydrogen bonding (δ_h), Equation 2.17.

$$\delta_t^2 = \delta_d^2 + \delta_p^2 + \delta_h^2 \qquad 2.17$$

where δ_t^2 is a measure of the cohesive energy density. A material can then be thought of having a position in HSP space based on these contributions. The likelihood of two materials being compatible or miscible depends on how far apart they are in HSP space, which is what is calculated by equation 2.17. This approach can be more favourable than others (such as the Hildebrand solubility parameter) as it allows for the distinction between materials of similar overall cohesive energy density but differing polarity, thus allowing for more accurate prediction of polar component miscibility.[102]

2.5.2 Polymer-Solvent Swelling

Crosslinked polymers do not dissolve; they instead absorb solvent and swell. The Flory-Rehner equation correlates crosslink density and swell stating that swell decreases as crosslink density increases.[103] When a coating is adhered well to a rigid planar surface, the ingress of solvent can lead to swelling normal to this surface.[104] As the coating is unable to swell in the xy plane of the surface due to adhesive constraints, this leads to compressive coating stress, and if it exceeds the adhesive strength, fracture may occur.

2.5.3 Methanol Ingress into Epoxy Resin Coatings

Small molecule solvents, capable of diffusing into epoxy coating free volume, are typically problematic as they can cause increased internal stress, swelling, blistering, cracking, and delamination. Previous studies have quantified the ingress of a variety of different liquids and organic solvents into epoxy resins.[10,31,96,105,106] Within this research, methanol is of particular interest as it is a common solvent transported by chemical tankers and it has been identified as a key solvent carried by ships whose coatings later experience intercoat adhesion failure.[105] This is due to its small, polar, single carbon structure (M_r 32.04 g/mol), low molecular volume (~ 67 $Å^3$) and high compatibility with epoxy resins allowing for rapid ingress. Table 2.1 displays the HSP of some commonly used epoxy resins, methanol, and water showing that the epoxies are more similar, regarding HSP, to that of methanol than water. This is likely a contributing factor to why previously it has been reported that the rate and extent of ingress of methanol into epoxy resins is greater than that of water.[10]

Previously, authors have quantified methanol uptake into a variety of different epoxy systems. Unthank *et al.* investigated the percentage mass uptake of problematic organic solvents into epoxy-amine (D.E.N. 431 and PAC-M) and epoxy-amine-borate (EAB) hybrid systems showing that mass uptake was lower in the hybrid material at ~ 10%, compared to ~ 14% in the epoxy-amine system.[105] Similarly, Jackson *et al.* investigated methanol uptake as a function of morphology reporting mass uptake percentages between 5% - 15% depending on the system.[96] Even larger uptakes were reported by Didsbury who saw methanol uptake vary from 16% - 23%, depending on the bisepoxide monomer precursor used, compared to <7% uptake of water, ethanol, propan-2-ol or tert-butanol.[10]

Table 2.1: HSP values of resorcinol diglycidyl ether, D.E.N. 431, methanol, and water.

Compound	δ_d / MPa$^{1/2}$	δ_p / MPa$^{1/2}$	δ_h / MPa$^{1/2}$
resorcinol diglycidyl ether	19.0	8.8	7.0
D.E.N. 431	20.5	7.0	5.8
methanol	14.7	12.3	22.3
water	15.5	16.0	42.3

2.6 Project Aims

Over time, the repeated absorption and desorption of solvent into 2 (+) layer epoxy resin systems can lead to fatigue-based intercoat adhesion failure, and ultimately cause blistering, cracking and delamination. However, currently there is no published literature exploring epoxy-epoxy interface formation, and consequently the reasons behind these adhesion failures are not well understood. In particular, often the stoichiometry and environmental conditions during the ambient cure phase are varied, and the impact on interphase formation not documented.

This thesis seeks to provide insight into the impact of stoichiometry, cure conditions and the interplay of cure conditions on the surface and bulk properties of the first coat prior to overcoating, to determine the likely impact on interface formation. Following on from this it will be determined if the diffusion of sequential layers is possible, thus leading to an area of bonding between the topcoat and basecoat, termed the interphase. Investigation will then be carried out to understand the dimensions and physicochemical properties of this region as well as the factors which govern this. This will provide greater understanding into what factors influence interphase strength and therefore impact adhesion failure.

The aims are addressed in the next five chapters as follows:

- *Chapter 3: Methodology*

An outline of all materials and experimental procedures carried out within this research. The approach involved utilising a diverse range of analytical methods, chosen deliberately over a more detailed yet restricted range, given the challenge of limited reporting and understanding of epoxy-epoxy interfaces in published literature.

- *Chapter 4: Material Characterisation*

The characterisation of resin system components prior to coating synthesis and analysis to ensure component chemistry and accuracy of stoichiometric calculations.

- *Chapter 5: The Influence of Cure Conditions and Stoichiometry on the Surface and Bulk Properties of Epoxy Resin Coatings*

One-layer coatings were produced and characterised as a function of stoichiometry and ambient cure condition to determine the impact of these variables on the first coat surface properties.

- *Chapter 6: Bilayer Epoxy Interface Characterisation*

Two-layer samples were produced, and the 2-layer interface physicochemical properties characterised as a function of stoichiometry and cure condition. Results obtained here were compared to those reported in Chapter 5 to develop relationships between the first coat properties exhibited due to stoichiometry / cure conditions, and the physicochemical properties of the interface.

- *Chapter 7: Solvent Ingress and Egress Studies in Epoxy Resins*

A series of 2-layer samples, produced as a function of stoichiometry and ambient cure conditions, were immersed in solvent, mimicking their function application as a barrier anticorrosive. Relationships were drawn between chemical performance and stoichiometry / cure conditions.

- *Chapter 8: Conclusions and Future Work*

The key findings of this research were revisited, drawing final conclusions.

Chapter 3

Methods

3.1 Materials

3.1.1 Epoxies, Curing Agents and Accelerators

The following epoxies, curing agents and accelerators were obtained and used as received (Table 3.1). Their respective suppliers and nominal structures have been detailed.

Table 3.1: Details of epoxy, curing agents and accelerator providers.

Name	Identifier	Supplier, Location	Structure
resorcinol diglycidyl ether (RDGE)	Epoxy	OLIN, Missouri United States	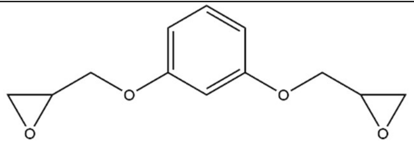
Dow Epoxy Novolac 431 (D.E.N. 431, n ~ 0.8)	Epoxy	OLIN, Missouri United States	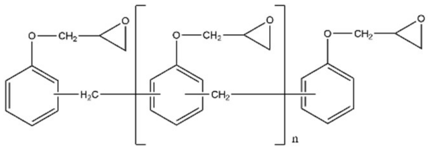

Name	Identifier	Supplier, Location	Structure
4,4-diaminodicyclohexylmethane (PAC-M), >99%	Curing Agent	Evonik Industries, Essen Germany	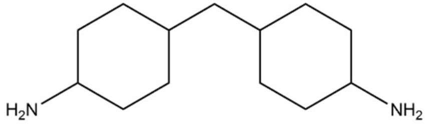
2,4,6-tris(dimethylaminomethyl)phenol (DMP-30), 95%	Accelerator	Merck, Darmstadt Germany	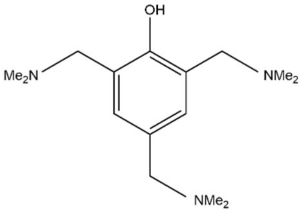
1-methylimidazole (1-MI), 99%	Accelerator	Merck, Darmstadt Germany	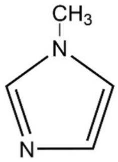
2-ethyl-4-methylimidazole (2-E-4-MI), 95%	Accelerator	Merck, Darmstadt Germany	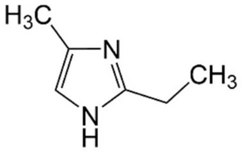

3.1.2 Other Materials

The following materials were also used throughout this research and have been listed alongside their respective suppliers.

Table 3.2: Details of other materials and providers.

Name, Purity / %, CAS number	Supplier, Location
methanol, ≥ 99.8, 67-56-1	Fisher Scientific, Leicestershire, UK
d-methanol, > 99.8, 811-98-3	Cortecnet, Paris France
chloroform, > 99, 67-66-3	Fisher Scientific, Leicestershire, UK
toluene, ≥ 99.8, 108-88-3	Fisher Scientific, Leicestershire, UK
tetraethylammonium bromide, ≥ 99, 71-91-0	Fisher Scientific, Leicestershire, UK
acetic acid, > 99.8, 64-19-7	Fisher Scientific, Leicestershire, UK

Name, Purity / %	Supplier, Location
0.1 mol dm^{-3} perchloric acid in glacial acetic acid, 98, 7601-90-3	Fisher Scientific, Leicestershire, UK
formamide, > 99.5, 75-12-7	Arcos Organics, Geel Belgium
1,2-propanediol, > 99.5, 57-55-6	Merck, New Jersey, United States
diiodomethane, > 99, 75-11-6	Fisher Scientific, Leicestershire, UK
glycerol, > 99.5, 56-81-5	Fisher Scientific, Leicestershire, UK
ethylene glycol, > 99, 107-21-1	Fisher Scientific, Leicestershire, UK

3.2 Epoxy Resin Sample Preparation

3.2.1 Formulations Studied

All the systems studied consisted of an epoxide component (D.E.N. 431 and RDGE), an amine-based curing agent (PAC-M), and/or accelerators (DMP-30, 1-MI, 2-E-4-MI). The epoxide component, for all systems, consisted of RDGE and D.E.N. 431, which were first separately heated to approximately 50 °C (to reduce viscosity for ease of handling), and mixed at a 3:1 mass ratio. Exact reactant masses of each component can be found in Table 3.3. This epoxide component and PAC-M were then incubated for 1 hour at the corresponding experimental temperature (25 or 35 °C: Table 3.4) before being mixed until visibly homogeneous (*i.e.*, no streaks). These reactants were then mixed at two distinct ratios to produce two stoichiometries: 100% (1:1 of epoxide groups to amine active hydrogens) and 35% (1:0.35 ratio of epoxide groups to amine active hydrogens). Each mix totalled 50 grams (Table 3.3). In addition, 0.96 g of DMP-30, 1.37 g of 1-MI and 0.68 g of 2-E-4-MI was added to each 35% stoichiometry 50 g epoxy/amine mix to promote homopolymerisation of the epoxide components. These stoichiometries allow for the comparison of systems utilising different distributions of reaction mechanisms, namely step-growth amine - epoxy addition (100%) and step-growth amine - epoxy addition in combination with anionic chain-growth polymerisation of epoxide groups (35%). Initially a 0% stoichiometry formulation (no curing agent) was attempted, but the lack of curing agent did not lead to the formation of a solid film under ambient conditions. The 35% stoichiometry formulation contained the lowest concentration of curing agent, while still capable of producing a solid film under ambient conditions. Resins and additives used in this work and the relative ratios were all sourced from Patent submissions and MSDS's.[107,108]

Post mixing, an induction time of <0.5 or 15 minutes was observed before film casting (Table 3.4). In accordance with the analytical technique used, sample thickness was varied throughout this research. Casting techniques are described below.

Table 3.3: Masses of each component used in the systems studied.

Component	Stoichiometry / g	
	100%	35%
D.E.N. 431	8.87	10.94
RDGE	26.62	32.81
PAC-M	14.51	6.12
DMP-30	0	0.96
1-MI	0	1.37
2-E-4-MI	0	0.68

3.2.2 Casting of 150 µm Epoxy Resin Films for Surface Characterisation

A large portion of the work within this thesis was performed using films of layer thickness 150 µm, which is a typical thickness specified in industry. After mixing and the application of a specified induction time, reactants were cast onto glass slides (75 mm x 25 mm) using a cube applicator with gap 300 µm (TQC Sheen, Netherlands). A cube applicator with a gap of 300 µm was used as solvent-free films cast using an applicator typically have a thickness which is half the gap of the applicator. Films were then allowed to cure for 24 hours under controlled conditions. Cure temperature and relative humidity (RH) were controlled using a vacuum oven and saturated salt solutions to produce films under the range of conditions; Table 3.4. Temperature and humidity were monitored using a Fisher Scientific thermo hygro 433 MHz cable-free pro sensor. The selected conditions, including temperatures of 25 or 35 °C, align with the typical ambient temperature range for the application of these coatings in industry. Moreover, RH levels of <5%, 40%, and 80% were chosen strategically: sub-50% RH is crucial for industrial application (carbamation mitigation), and the inclusion of 80% RH allows for a comparison of extremes, providing insight into potential outcomes when RH control measures may falter.

Table 3.4: The conditions under which films were cured.

Induction Time / Mins	Temperature / °C	Relative Humidity / %
<0.5	25	40
15	25	40
<0.5	25	80
15	25	80
15	25	<5
15	35	<5
15	35	40
15	35	80

When investigating variation in ambient temperature (25 - 35 °C), RH was maintained at 40 %. When investigating variation in ambient RH (<5 - 80 %) temperature was maintained at 25 °C.

3.2.3 Casting of 150 µm / layer Epoxy Resin Films for Interface Characterisation

The films of 150 µm thickness per layer used to characterise the interface had a larger surface area than those used to characterise the first coat surface properties. These films were instead cast onto 150 mm x 100 mm glass slides using an 89.1 mm width x 150 µm thickness single bar applicator (BYK, Wesel Germany). Films were again allowed to cure under the conditions shown in Table 3.4 before being overcoated with a second layer of identical composition. Films were cured at either 25 °C or 35 °C for 4 or 3 days respectively before being overcoated at right angles. These overcoating intervals were selected as they are typical of the maximum-advised overcoating intervals used in commercial systems, and longer overcoating intervals have been linked to adhesion failure.[109] Directly after overcoating, a glass jar with the bottom cut off and wrapped in tin foil was placed on the film (Figure 3.1). This acted as a solvent reservoir, which could be easily removed later for further experiments (ion microbeam, Raman); films used for ingress / egress studies did not require tin foil as the jar did not need to be removed. Following this, the 2-layer films were cured under the same controlled conditions for 3 days before a 16-hour post cure at 80 °C.

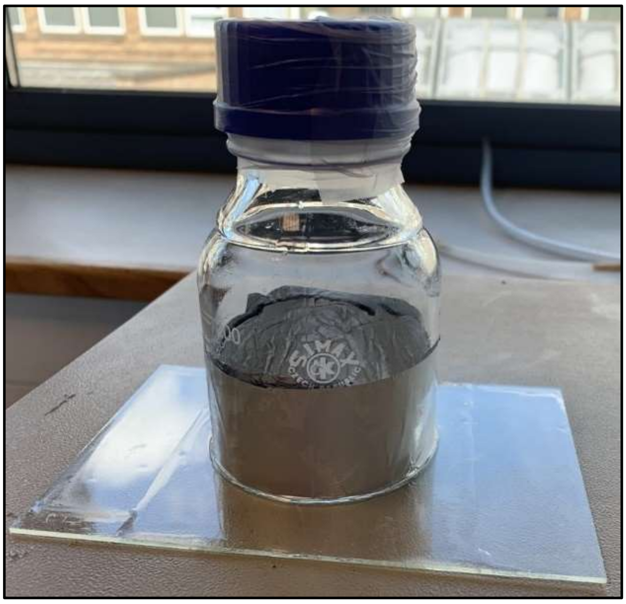

*Figure 3.1: 89.1 mm * 89.1 mm * 300 µm 2-layer film with solvent well attached.*

3.2.4 Spin Cast Epoxy Resin Films (~ 100 nm)

Neutron reflectometry, ellipsometry and other related techniques utilised spin cast films of ~ 100 nm per layer. Films were spin-cast onto silicon wafer or blocks (Miller index = (100)) using a Laurell WS-650MZ-23NPP spin-coater. The silicon-substrate was first heated to 1000 °C, followed by treatment with piranha solution (a combination of concentrated sulfuric acid and hydrogen peroxide). Epoxy spin cast films can be prone to dewetting so thorough cleaning prior to casting is a necessity. In the context of this project, dewetting refers to the tendency of epoxy spin-cast films to form discontinuous patches or beads upon a substrate. This is a result of poor adhesion to the substrate, stemming from strong internal cohesion and breaks or decreases in liquid-to-surface adhesion. Following this the substrate was covered in acetone and accelerated at 1000 rpm/s to 3000 rpm for 15 seconds to remove any dust and surface debris. Each formulation (35% and 100%) was mixed and then incubated at either 25 °C or 35 °C, 40% RH for a 15-minute induction time. Approximately 0.1 grams of epoxy system mix was dissolved in chloroform (100% stoichiometry = 4% epoxy in chloroform concentration; 35% stoichiometry = 5% epoxy in chloroform concentration) using an IKA RCT digital hotplate and magnetic stirrer (1500 rpm, 1 minute). Toluene was originally used as the solvent until it was discovered that chloroform produced more uniform films, especially in systems containing accelerators which were prone to dewetting.

For experimental techniques requiring a silicon wafer substrate, approximately 0.4 ml of the solvent-epoxy solution was placed on a cleaned silicon wafer (~ 1 cm x 1 cm) and spin cast for 12 seconds at 10,000 rpm and 6,000 rpm/s acceleration. Optimal spin casting parameters aimed at decreasing radial streaking, including rapid spin speeds and accelerations, were determined through systematic variation (Table 3.5). Faster spin speeds, generating higher centrifugal forces, contribute to even liquid material distribution on the substrate, while increased accelerations counteract dripping or sagging tendencies during spinning. For experimental techniques requiring a silicon block substrate, approximately 1.5 ml of the solvent-epoxy solution (2% epoxy in chloroform concentration) was placed on a cleaned silicon block and spin cast for 8 seconds at 2,000 rpm and 2,000 rpm/s acceleration. Samples were then placed in an incubator and cured at 25 or 35 °C, 40% RH for varying overcoating intervals (1-7 days). Samples cured at 35 °C were first cured at 25 °C for 3 hours to reduce the potential for dewetting. Samples were removed from the oven and overcoated with the second layer which was identical in composition, preparation and spin coating technique as previously discussed. The two-layer samples were then cured at 25 or 35 °C, 40% RH for 3 days before being post cured at 80 °C for 16 hours.

Table 3.5: Qualitative measure of spin cast film quality relative to casting parameter.

Epoxy in chloroform / %	Rotation Speed / rpm	Acceleration / rpm/s	Duration / s	Image
5	3000	1000	30	
5	3000	5000	30	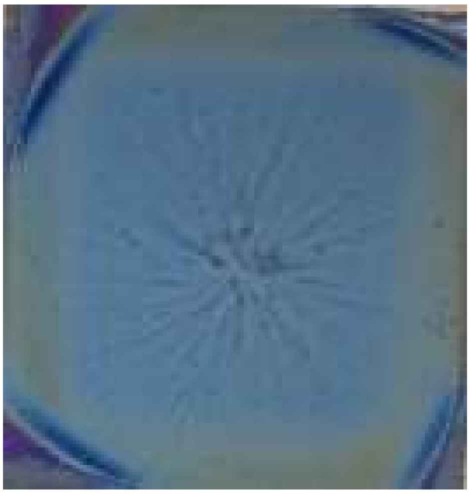
5	6000	5000	30	

Epoxy in chloroform / %	Rotation Speed / rpm	Acceleration / rpm/s	Duration / s	Image
7	6000	5000	30	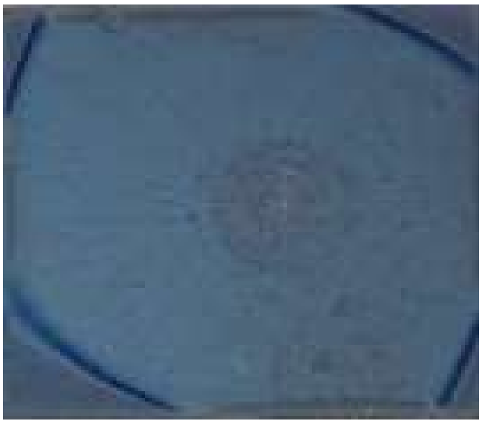
7	10000	5000	12	
7	10000	6000	12	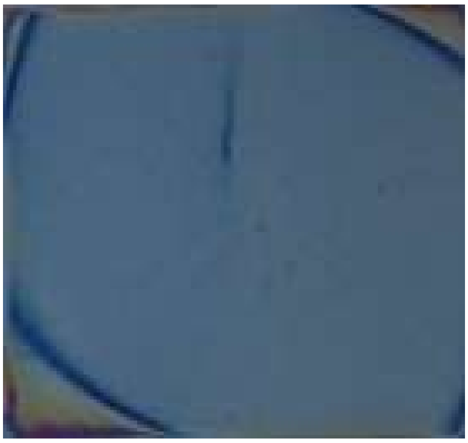

3.2.4.1 Measuring Spin Cast Film Thickness Using Ellipsometry

Ellipsometry is a non-destructive, non-contact measurement technique which can be used to accurately determine sample thickness on the nm scale (precision: ± 0.1 Å). This is achieved by directing a linearly polarised incident light beam at a sample and measuring the resultant elliptical polarisation, post refraction (through sample) and reflection (off silicon substrate). Essentially, linearly polarised light contains electric fields both parallel (p-) and perpendicular (s-) to the plane of incidence, and the enabling principle of ellipsometry is that p- and s- polarised light reflect differently, resulting in a change in polarisation of the light beam. From this the complex reflectance ratio, ρ, of a system can be measured, quantified by the amplitude ratio, Ψ, and the phase difference, Δ using the following equation:

$$\rho = \frac{R_p}{R_s} = tan(\Psi)e^{i\cdot\Delta} \qquad 3.1$$

where R_p is the sample reflectivity for p-polarised light and R_s is the sample reflectivity for s-polarised light.

Within this research, ellipsometry was used to determine spin cast epoxy layer thickness as well as to monitor the extent of swell over time, caused by the ingress of solvents. A Sentech SE500 single wavelength combined ellipsometer/reflectometer, equipped with a 632.8 m, He-Ne laser was used to determine sample thickness (~ 100 nm / layer) and refractive index (epoxies: ~ 1.6) of spin cast epoxy films using the Sentech SE400 software. The operational principle involves rotating polarizers, which measure the phase shift and rotation of polarised incident light, often referred to as the ellipsometric angles, psi (ψ) and delta (Δ). The Sentech SE400 software operates on a model-based approach, where layers are defined by predetermined estimates of thickness and refractive index values. By iteratively adjusting these estimates, the software converges to values that optimally align with the experimental ellipsometric angles, enabling precise determination of the epoxy layer thickness and refractive index.

3.2.5 Casting of Thicker Epoxy Resin Films (> 1 mm) for Bulk Characterisation

Techniques such as dynamic mechanical analysis (DMA) and positron annihilation lifetime spectroscopy (PALS) require sample thickness to be larger than those previously discussed. The latter, for example, requires a thickness large enough (> 1 mm) to absorb most of the positrons being fired into the sample. Sylgard 184 PDMS was used to produce a flexible mould in which samples could be cured and then easily removed. Reactants were incubated to reaction temperature, mixed and then an induction time applied as previously described. Following this each mixture was poured into a PDMS mould and allowed to cure at controlled conditions (Table 3.4) for 24 hours.

3.3 Titration Calculations to Determine EEW

To accurately calculate formulation stoichiometry, epoxide equivalent weight (EEW) should first be determined, as it determines the mass of epoxy compound which contains one mole of epoxy functional groups.[110] Once EEW has been determined for each epoxy component, mixture EEW can be determined based on the weight ratio of each epoxy component using equation 3.2.

$$EEW_{\ Mixture} = \frac{100}{\left(\frac{Wt\%_{\ epoxy\ 1}}{EEW_{\ epoxy\ 1}}\right) + \left(\frac{Wt\%_{\ epoxy\ 2}}{EEW_{\ epoxy\ 2}}\right) + \cdots} \tag{3.2}$$

Active hydrogen equivalent weight (AHEW) is the mass of curing agent which contains one mole of amine active hydrogens and can be calculated using equation 2.2 (Section 2.3.1). Therefore, a mixture of $EEW_{mixture}$ grams of epoxy with AHEW g of amine would produce a 100% stoichiometry formulation, or equal numbers of epoxide and active hydrogen groups.

EEW was determined titrimetrically for RDGE and D.E.N. 431 using ASTM-1652.[111] The principle of the titration is as follows: the addition of perchloric acid to a mixture of epoxy functional compound with tetraethylammonium bromide (TEAB) produces hydrogen bromide which reacts with epoxide. Once all the epoxide is consumed, the production of further HBr causes a colour change in a suitable indicator.

Tetraethylammonium bromide (40 g, 0.19 mol) was dried at 100 °C for 1 hour before being dissolved with heating in glacial acetic acid (450 mL), and then allowed to cool. Following this, eight drops of 0.5% crystal violet solution in glacial acetic acid were added, and the mixture neutralised to an emerald, green colour using 0.1 mol dm^{-3} perchloric acid in glacial acetic acid. Epoxy samples (0.1 g) were then added and dissolved. The mixture was then titrated with 0.1 mol dm^{-3} perchloric acid in glacial acetic acid (~ 5 cm^{3}) and neutralised to an emerald, green colour endpoint. EEW (g mol^{-1}) was then calculated using equation 3.3:

$$EEW = \frac{m}{T \times [PA]} \qquad 3.3$$

where *m* is the sample mass (g), *T* is titre (dm^3), and *[PA]* is the concentration of perchloric acid (mol dm^{-3}).

3.4 Solution State Nuclear Magnetic Resonance Spectroscopy

Nuclear Magnetic Resonance (NMR) spectroscopy is a technique which can be used to determine the molecular structure, purity, or composition of a sample.[112] When a sample is placed inside a strong magnetic field, the spin of the nuclei present align to form a net macroscopic magnetization, if the nuclei possess a magnetic moment (^{1}H, ^{2}H, ^{13}C or ^{15}N are the important ones here). An external radiofrequency (RF) radiation pulse is then delivered to the sample, generating an additional, temporary magnetic field, orthogonal to the primary field. This applies torque to the nuclear spins, moving them out of alignment. The nuclear spins then begin to relax back to their original state of alignment, termed the Free Induction Decay (FID) which is captured as a function of signal intensity against time. This time-domain signal is then converted to frequency-domain using Fourier Transformation to produce an NMR spectrum.

Several variations of solution state NMR were performed on RDGE, D.E.N. 431 and PAC-M separately to confirm molecular structure: ^{1}H NMR, ^{13}C NMR, ^{1}H-^{1}H COSY NMR and ^{13}C-^{1}H HSQC NMR. 0.1 g of each sample was dissolved in 2.0 mL of deuterated chloroform. 750 µL of the solution was transferred to a 5 mm diameter NMR tube. ^{1}H NMR and ^{13}C NMR spectra were recorded using a Bruker Avance III-HD-400 spectrometer. ^{1}H spectra were acquired over 8 transients, at 294.5 – 295.3 K, with an acquisition time of 4.0894 s. Spectrometer operating frequency was 400.06 MHz and spectral width was 8.0128 kH. ^{13}C spectra were acquired over 1024 transients, at 296.2 – 296.6 K, with an acquisition time of 1.3631 s. Spectrometer operating frequency was 100.6 MHz and spectral width was 24.0385 kH.

^{1}H-^{1}H COSY and ^{13}C-^{1}H HSQC spectra were recorded using a Bruker Neo 700 MHz spectrometer. ^{1}H-^{1}H COSY spectra were acquired over a single transient, at 295.0 K, with an acquisition time of 0.3666 - 0.682 s, using the following relaxation delays: 1.8251 s (D.E.N. 431), 1.8148 s (RDGE), and 1.5097 (PAC-

M). Spectrometer operating frequency were 400.06 - 400.06 MHz and spectral width was 1.51 – 1.83 kH. ^{13}C-^{1}H HSQC spectra were acquired over 2 transients, at 25.0 K, with an acquisition time of 0.15 s. Spectrometer operating frequency were 599.36 - 150.72 MHz and spectral width was 5.6 – 30.1 kH.

3.5 Differential Scanning Calorimetry to Measure Epoxy Resin T_g

Differential Scanning Calorimetry (DSC) is a thermal analysis technique, which can be used to identify thermal transitions in materials that show a change in heat capacity during the transition, such as the glass transition temperature (T_g). Two types of DSC are commonly used: heat flux or power compensated. Heat flux DSC measures the difference in heat flow into a sample relative to a reference, as temperature is changed at a constant rate. Whereas power compensated DSC maintains sample and reference temperature, and the electrical power required to maintain sample temperature equal to that of the reference is measured.[113] In this research, only power compensated DSC was utilised.

DSC was performed on RDGE, D.E.N. 431, and PAC-M separately as well as the mixed resin systems to provide a measure of T_g. Measurements were performed using a Perkin Elmer DSC 8000. Approximately 20 mg of sample was weighed into a DSC pan and heated at 10 °C / minute (unless otherwise stated) from -50 °C to 50 °C for single components, and 10 °C to 200 °C for resin systems. DSC measurements were carried out by Douglas Carswell at the thermal analysis service, Department of Chemistry, Durham University.

3.6 Gravimetric Analysis

Gravimetric analysis is a class of techniques that use change in mass to calculate amount or concentration of an analyte, as the term gravimetric refers to weight measurement. Gravimetric analysis was used in this research to quantify surface layer formation as a function of stoichiometry and cure condition.

3.6.1 Surface Layer Formation Quantification

PAC-M carbamate is water soluble and so can be removed with cleaning with H_2O. Therefore, carbamate formation can be determined using gravimetric analysis by determining the change in sample mass pre and post cleaning with H_2O.

Sample and substrate (glass slide) mass was recorded using a Sartorius CPA124S microbalance, precision ± 0.00005 g. The film surface (9 cm^2) was then cleaned using a cotton bud soaked in D_2O to remove any carbamate (water soluble). This solution was retained for NMR analysis. Sample and substrate mass was then re-recorded, and the difference determined. It is important to note that the accuracy of this method may be impacted, as traces of cotton bud fibres could potentially be left on the balance, affecting the weight measurement. Despite this limitation, this approach was deemed the most practical and effective for the given circumstances.

3.6.2 Solvent Ingress and Egress into Epoxy Resins

Solvent studies allow rate and extent of solvent ingress (uptake) and egress (departure) to be determined by monitoring the change in mass of a sample, in or out of contact with a solvent, over time. Given the application of the films studied in this research is as a barrier for the transport of small-molecule solvents, understanding ingress and egress as a function of cure condition and stoichiometry will give insight into viability. However, it is important to recognise that this is only a crude measurement, as during film-solvent interaction, processes other than just solvent ingress or egress can occur and therefore potentially influence the measurement. This may include the possible absorption of moisture (weight gain), the possible loss of any finite reactive material present from film because of incomplete reaction during the film formation process (weight loss), or possible degradation of the coating by the solvent (weight loss). To ensure the rigor and meaningfulness of the measurements, careful consideration was given to validating the observed mass changes. This involved thoughtful evaluation of the potential confounding factors and a detailed interpretation of the data, taking into account the various processes that may contribute to the observed weight changes.

Sample and substrate (Figure 3.1) mass was recorded using a Sartorius B3100p basic balance, precision ± 0.005 g. ~ 20 ml of solvent was then poured into the chemically bound jar (solvent reservoir) and the lid tightly sealed. After a given time, the jar was emptied, and all sample surfaces dried with paper towel. Sample and substrate mass was then re-recorded, and the difference determined (ingress). This process was repeated at regular intervals for 30 days to determine rate and extent of ingress. 30 days was selected as this is a typical duration that coatings would be exposed to solvent during transport. Ultimate ingression is defined as the maximum possible uptake of solvent by a film, indicated by a plateau in mass uptake during solvent exposure. Following this 30-day period of ingress, solvent was removed from the solvent reservoir and for the next 30 days, the sample was left in a fume cupboard to allow the ingressed solvent to evaporate from the system. Sample mass was again recorded at regular intervals to determine rate and extent of egress.

3.7 Fourier-Transform Infrared Spectroscopy

Fourier-Transform Infrared (FTIR) spectroscopy is an analytical technique used for the characterisation of chemical bonds. When infra-red light passes through a material, if the wavelength of the incoming radiation is the same as the frequency of the vibrational mode of the species present, IR light is absorbed. This is graphically depicted as peaks in absorbance at the corresponding wavelength. Therefore, by scanning over a wavelength range, and studying the wavenumber at which a particular absorption occurs, information regarding material chemical structure and quantity of bonds can be determined. Within epoxy resin chemistry, this principle can be utilised to monitor rate and extent of cure by tracking the absorbance of the oxirane ring during curing (Figure 2.8).

Within this research, two FTIR technique variations were carried out: (i) Transmission FTIR to track the cure reaction; and (ii) ATR FTIR to determine the presence, or lack thereof, of carbamate in a variety of samples.

3.7.1 Transmission FTIR Spectroscopy

The Transmission FTIR spectrometer functions by splitting an infrared beam into two: one of fixed pathlength, and one of variable pathlength controlled by a moveable mirror (Figure 3.2). These beams are then reflected off their respective mirrors and reformed into a single beam. By varying the distance between the pathlengths using the moveable mirror, a series of constructive and destructive interferences occur. This in turn induces variation in the intensity of the beam allowing for scanning over a range of wavelengths.

A Perkin Elmer Spectrum 2 FTIR spectrometer was used for scanning and a background reading was taken prior to analysis. Phenyl glycidyl ether and 4-methylcyclohexylamine were mixed thoroughly, pressed between two glass slides, and quickly mounted inside the spectrometer. To measure the oxirane ring (4530 cm^{-1}) concentration over time, scans were recorded at 20-minute intervals between 5000 – 4000 cm^{-1}, with a resolution of 4.00 cm^{-1} and acquisition time of 10 s.

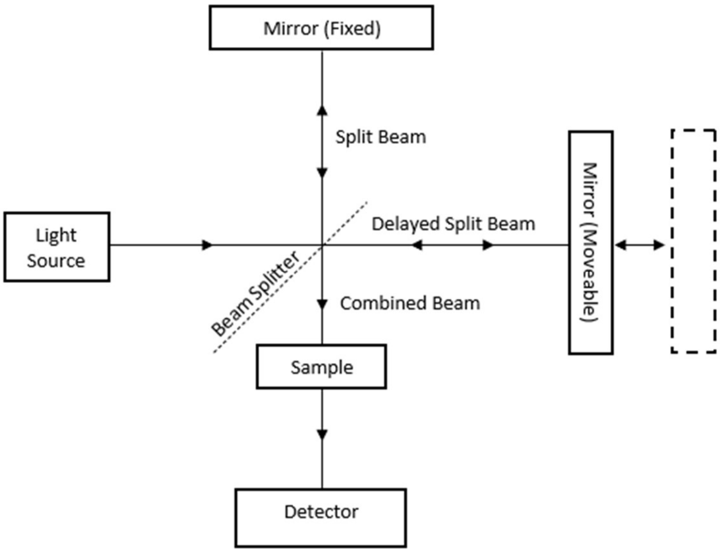

Figure 3.2: A diagram of a FTIR spectrometer.

3.7.2 Attenuated total reflectance (ATR) FTIR Spectroscopy

An ATR accessory functions by measuring the change in an internally reflected IR beam upon contact with a sample, enabling material characterisation with a penetration depth of 1-5 microns. An IR beam is directed onto an optically dense crystal of high refractive index at a critical angle. The beam is internally reflected, generating evanescent waves at the inflection points between the propagating light and sample (Figure 3.3). This wave extends beyond the surface of the crystal into the sample, dictated by wavenumber and the difference in crystal and sample refractive index. At the corresponding wavelength where the sample absorbs energy, the amplitude of the evanescent wave is attenuated. The attenuated beam returns to the crystal where it is directed towards a detector. The detector records the attenuated IR beam as an interferogram signal, which is then converted to an IR spectrum.

A Perkin Elmer Spectrum 2 FTIR spectrometer equipped with ATR accessory was used for scanning. A background reading was taken prior to analysis and following which, IR spectra of PAC-M, PAC-M carbamate, and a cured resin system were recorded between 4000 – 500 cm^{-1}, with a resolution of 4.00 cm^{-1}. Further details are provided in Section 5.2.1.2.

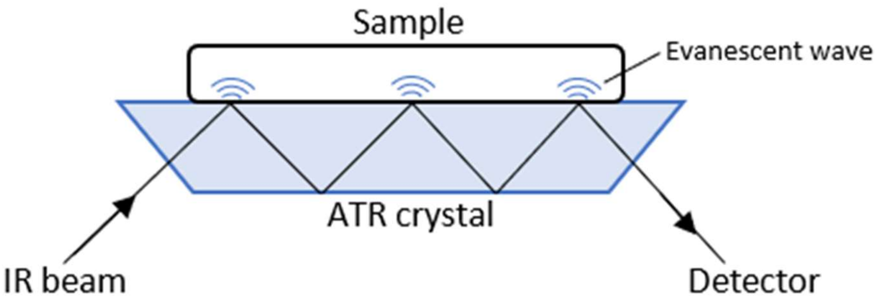

Figure 3.3: A diagram of an ATR-FTIR system.

3.8 Atomic Force Microscopy

Atomic force microscopy (AFM) is a well-established technique for mapping lateral surface variation on the nm to µm scale. AFM uses a sharp (diameter ~10 nm) probe attached to a flexible cantilever to detect small variations in surface height and mechanical properties. The deflection of the cantilever is detected through the deflection of a laser beam, which is reflected from the back of the cantilever to a split photodiode. In imaging, the probe is rastered across the surface to generate a map.

Before delving into mapping, it is helpful to consider the forces that act on an AFM probe as it approaches or retreats from a sample surface. At any point, a force-distance curve is generated detailing the force exerted on the probe. An example is shown in Figure 3.4. As the tip approaches the sample surface, attractive forces (van der Waals) cause the cantilever to bend toward the surface allowing the tip to snap into contact with the sample (a, Figure 3.4). However, as probe-to-surface distance decreases further, increasingly repulsive forces cause the cantilever to bend away from the surface (b). Upon probe withdrawal, the tip remains in contact with the surface until the strength of attractive forces is overcome by the bending force arising from the probe spring constant (c). At this point the cantilever snaps back into its undeflected position (d). [114,115]

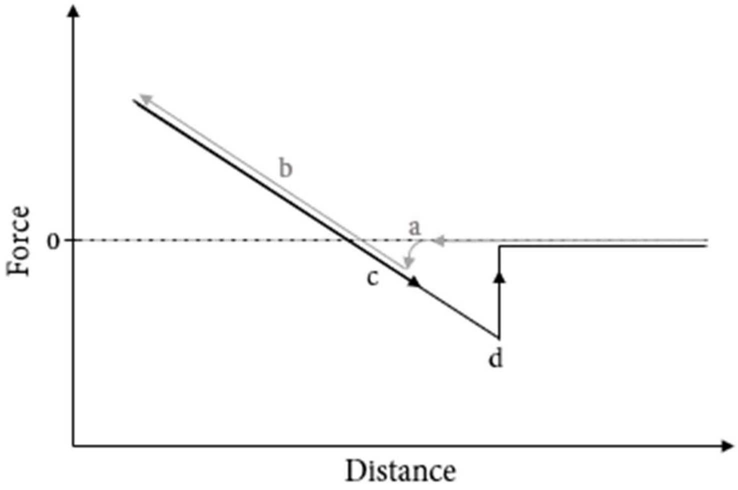

Figure 3.4: Force distance curve showing the adhesion force between the sample and cantilever during approach (grey) and retraction (black).

AFM mapping can be used in a variety of modes which are usually differentiated into continuous contact (“contact”) or intermittent (“tapping”) modes. However, as only one mode, PeakForce quantitative nano-mechanical mapping (QNM), a form of tapping mode, was utilised in this work, only the latter will be discussed in detail. In contact mode, the cantilever scans across the sample surface while maintaining tip-surface contact. Upon contact with surface features, the strong repulsive forces between tip and surface cause the cantilever to bend, mapping the surface. However, the relative simplicity of this mode is offset by the potential for sample damage, tip wearing or probe-surface sticking. PeakForce QNM mode takes this a step further by utilising a high-speed feedback loop to continuously and rapidly modulate the cantilever-sample separation to maintain a constant maximum force between the tip and the surface. This minimises the lateral forces, reducing the potential for sample damage and tip wear.

AFM images were recorded using a Bruker MM8 AFM. The films were studied using PeakForce QNM mode capturing 10 x 10 µm images with 512-line resolution. NuNano Scout 150 probes with an 18 N/m spring constant and 150 kHz resonant frequency were used. Deflection sensitivity, spring constant and tip radius were determined prior to use *via* tip calibration protocol (ramp, thermal tune) using silicone and sapphire calibration standards. Images were processed and analysed using NanoScope Analysis. Within this thesis, two measures of surface roughness will be considered (i) rugosity, defined by the percentage difference in the projected geometric and measured surface area (percentage surface area difference). (ii) root-mean-square surface roughness (R_q), determined using the following equation:

$$R_q = \sqrt{\frac{1}{N}\sum_{i=1}^{N} r_i^2} \qquad 3.4$$

where N is the number of data points and r_i is the deviation in height of a point from the mean.[116] Prior to roughness analysis, a 'Flatten' function was applied to transform the image, removing distortion attributed to image tilt or bow.[117]

3.8.1 Scratch Tests

As mentioned in section 3.2.4.1, ellipsometry was used to measure the thickness of spin cast epoxy systems. The technique measures the phase difference between an incident laser beam and the resultant elliptical polarised light. To determine sample thickness, the data is processed by a fitting software which requires an estimate of layer thickness for accurate fitting. While the colour of spin cast films is indicative of layer thickness, AFM scratch tests offer a more accurate measure and so was used to estimate layer thickness prior to ellipsometry.

Spin cast films were horizontally scratched using a razor blade, with meticulous attention to exclusively scratch the film and not the silicon substrate. Achieving this precision involved initially testing the blade on a clean silicon wafer to determine the minimal pressure required for scratching. Subsequently, a reduced pressure was applied to the silicon-film sample. Images were generated across a scratch using PeakForce QNM mode capturing 15 x 15 µm images. Images were then flattened, and a peak and trough height determined by using the sectioning tool to generate plots such as in Figure 3.5.

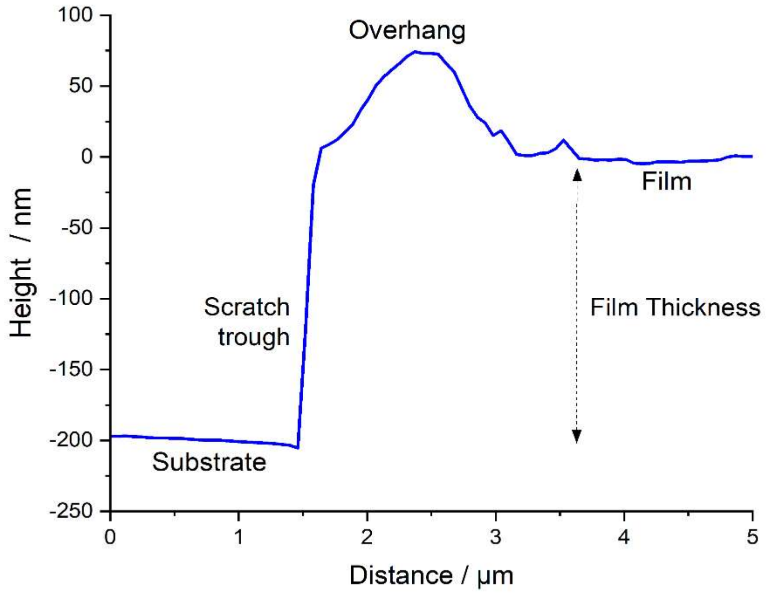

Figure 3.5: Height v distance plot across the scratch.

3.9 Contact Angle Analysis

Contact angle analysis is a technique used to evaluate the solid-liquid interfacial interaction as it offers a quantitative measure of solid surface wetting by a liquid. When a droplet is placed on a surface, its contact angle geometry is determined by the balance of three interfacial energies: the liquid-vapour (γ_{LG}), the solid-vapour(γ_{SG}) and the solid-liquid (γ_{SL}). This energy balance is described using the Young's Equation,[118]

$$\cos(\theta) = \frac{\gamma_{SG} - \gamma_{SL}}{\gamma_{LG}} \qquad 3.5$$

where θ is the contact angle between the droplet and substrate. This relationship is demonstrated in Figure 3.6.

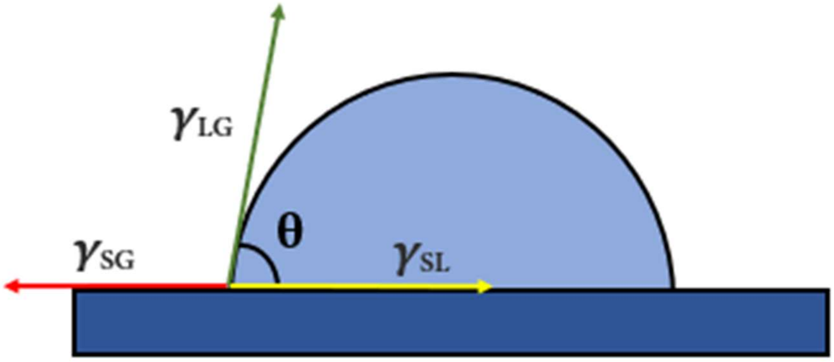

Figure 3.6: The relationship between liquid droplet contact angle on a solid substrate and the interfacial tensions at the three-phase boundary.

Equation 3.5 assumes a smooth sample surface. However, using the Wenzel correction (Equation 3.6), the impact of surface rugosity on equilibrium contact angle can be determined.

$$\cos(\boldsymbol{\theta})_{roug} = r\cos(\boldsymbol{\theta})_{smoot} \qquad 3.6$$

where *r = (1 + rugosity / 100).*[119] This correction has the effect of shifting θ away from 90°, which for the films analysed in this thesis is > 90° i.e., $\theta_{smooth} < 90° \rightarrow \theta_{rough} < \theta_{smooth}$.

Contact angle measurements were collected using the sessile drop technique and recorded using a UI-3370CP-M-GL Rev.2 camera equipped with a telecentric lens to remove the effect of field depth. The sample was placed on a calibrated level platform. 10 μL of probe liquid (UHP water, glycerol, formamide, ethylene glycol, 1,2-propanediol or diiodomethane) was placed on the film surface, focus optimised, and the steady state contact angle (Zisman plot, Owen-Wendt model) or advancing contact angle recorded and measured using the DropSnake plug-in on ImageJ (Fuji), Figure 3.7.[120] For advancing contact angle analysis, videos of 5 minutes duration were recorded. Frames were extracted at following sampling rates: every 0.1 seconds (0 – 1 s), 0.5 seconds (1 – 10 s) and 10 seconds (10 – 300 s).

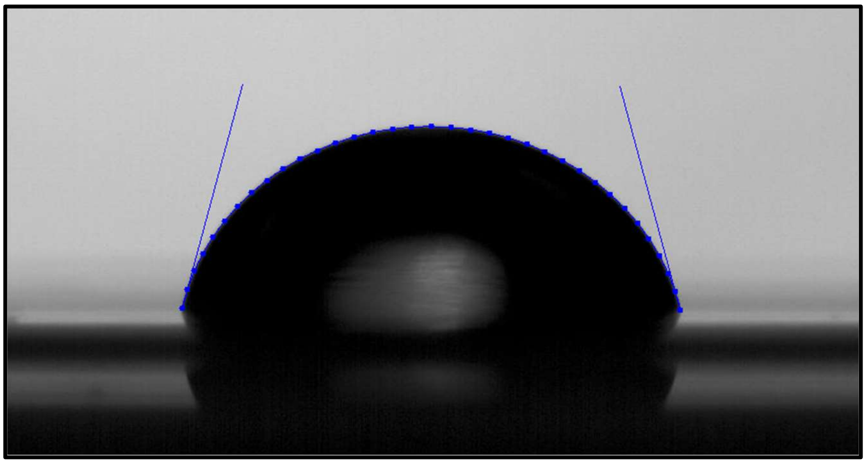

Figure 3.7: Droplet and analysis lines.

3.9.1 Surface Free Energy

Water contact angle analysis offers a convenient measure of surface wettability and hydrophobicity; typically, θ > 90° indicates a hydrophobic surface while θ < 90° indicates hydrophilicity. However, this alone cannot be used to evaluate surface free energy (SFE) and commonly techniques such as Zisman plots, and the Owens-Wendt model are adopted. While some authors regard surface chemistry and the ability to form an interpenetrating network as the most relevant factors in interface formation,[79,80] others have proposed the importance of surface energy.[70,74,75]

3.9.1.1 Zisman plot

Surface energy cannot be measured directly, and so instead, a Zisman plot uses an extrapolation approach by plotting the cosine of contact angle for a series of probe liquids against their respective known surface tensions and applying a regression line. The line of best fit is calculated using the Excel LINEST function, determining slope and intercept coefficients for the linear equation. This equation is then applied to the dataset to create the regression line, which is extrapolated out to the point where cos θ = 1. This is the hypothetical point of complete surface wetting. The surface tension corresponding to the intersection between the extrapolated line and cos θ = 1 is termed the critical surface tension and is equal to the surface free energy (Figure 3.8).

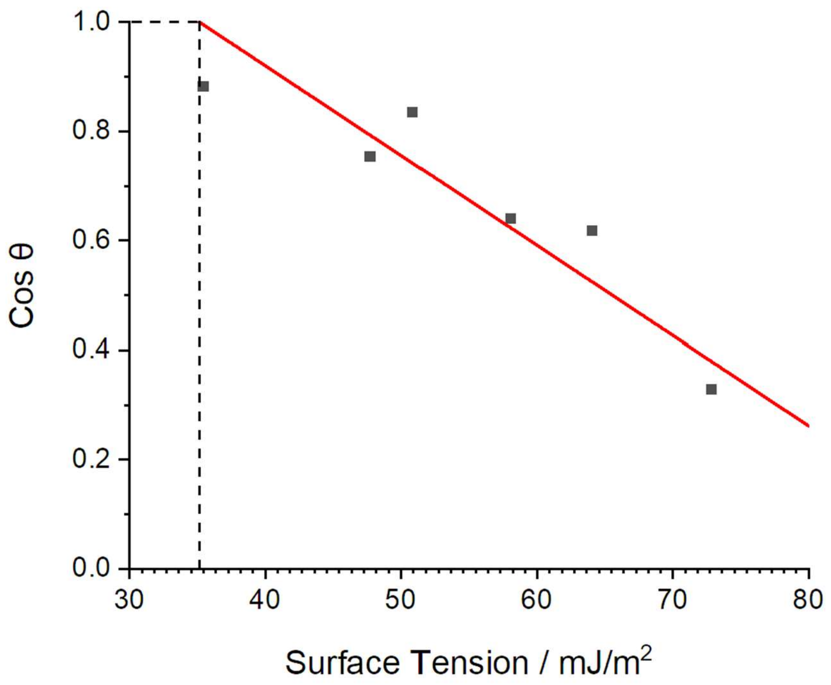

Figure 3.8: An example Zisman plot (sample: 100% stoichiometry, 25 °C, 40% RH).

3.9.1.2 Owens-Wendt Model

The Owens-Wendt model estimates SFE by determining the polar and dispersive components of SFE using the Bethelot hypothesis, which states that interactions between surface layer molecules of two substances are equal to the geometric mean of intermolecular interactions within each substance. Both components can be combined with the Young's equation to determine SFE.[121]

$$\gamma_{SL} = \gamma_{SG} + \gamma_{LG} - 2\left(\sqrt{\gamma_S^D \gamma_L^D} + \sqrt{\gamma_S^P \gamma_L^P}\right) \qquad 3.7$$

where γ^D is the geometric mean of the dispersive part, and γ^P is the geometric mean of the polar part. Dispersive energy contributions consist of weak, non-hydrogen bond van der Waals interactions while the polar energy contributions are associated with strong, interactions arising from permanent dipoles.

The steady state contact angle of glycerol, formamide and diiodomethane was measured using contact angle analysis. Values of surface tension and SFE dispersion components were taken from literature. These three solvents were selected due to their varying polar and dispersive SFE contributions (glycerol $\gamma_L^P = 30$, $\gamma_L^D = 34$ mJm^{-2}; formamide $\gamma_L^P = 27$, $\gamma_L^D = 31.4$ mJm^{-2}; diiodomethane $\gamma_L^P = 0$, $\gamma_L^D = 50.8$ mJm^{-2}) providing for more complete analysis. The complex combined standard uncertainty for total SFE ($\upsilon_c(\gamma_s)$) was calculated using equation 3.8,[85]

$$\upsilon_c(\gamma_s) = \sqrt{\left(\frac{\delta\gamma_s}{\delta\theta_w}\,\upsilon_w\,(\bar{\theta}_w)\right)^2 + \left(\frac{\delta\gamma_s}{\delta\theta_f}\,\upsilon_f\,(\bar{\theta}_f)\right)^2 + \left(\frac{\delta\gamma_s}{\delta\theta_d}\,\upsilon_d\,(\bar{\theta}_d)\right)^2 + \upsilon_s^2(\gamma_s)}\,, \qquad 3.8$$

where $\delta\gamma_s$ is the change in SFE, $\delta\theta_x$ is the change in solvent contact angle, υ_x is the standard uncertainty in solvent contact angle, $\bar{\theta}_x$ is the average solvent contact angle, and $\upsilon_s^2(\gamma_s)$ is the difference in SFE according to variation in literature values assuming uniform distribution (0.88 mJ/m^2).[85]

3.10 Dynamic Mechanical Analysis

Dynamic mechanical analysis (DMA) is a technique used to determine viscoelastic material properties and phase transitions as a function of temperature, time, frequency, or stress. For this research, multi-frequency strain mode was employed in which a sinusoidal strain is applied to the material over a temperature range, and the resulting stress and phase angle are measured (Figure 3.9). From this the complex modulus can be determined, consisting of the storage modulus (E′, Equation 3.9) and loss modulus (E″, Equation 3.10) which represent the elastic and viscous behaviours of the material, respectively.

$$E' = \frac{\sigma_0}{\gamma_0}\cos\delta \qquad 3.9$$

$$E'' = \frac{\sigma_0}{\gamma_0}\sin\delta \qquad 3.10$$

where γ_0 is the strain amplitude, σ_0 is the stress amplitude and δ is the phase angle. The storage and loss moduli can then be used to determine tan δ (Equation 3.11).

$$\tan\delta = \frac{E''}{E'} \qquad 3.11$$

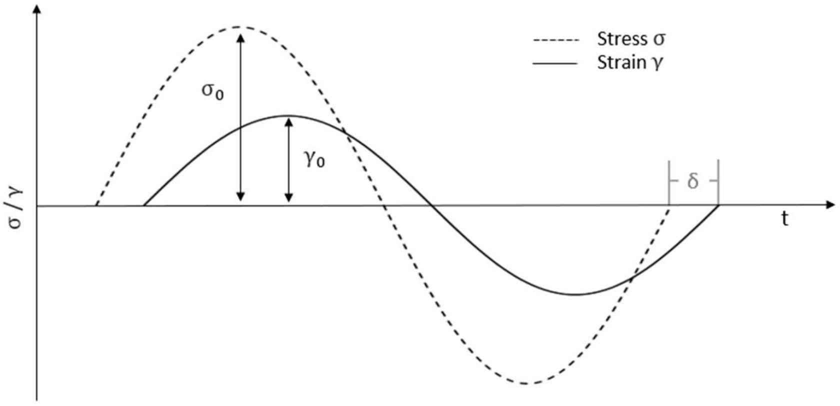

Figure 3.9: The applied sinusoidal strain and measured stress over time, during DMA.

Samples of different stoichiometries were mixed and cast as described in section 3.2.5. These samples were then cured under varying ambient conditions (Table 3.4) before being scanned using a heat ramp at 10 °C / minute from 30 °C to 160 °C. A TA Instruments Q800 DMA was used to perform dynamic mechanical tests on samples with dimensions 4 mm x ~ 13 mm x ~ 3 mm (cantilever length x width x thickness). Samples were oscillated at a frequency of 1 Hz and amplitude of 15 µm in a 4 mm single cantilever.

Within this research, T_g is a phase transition of particular interest, as within epoxy resin chemistry, T_g can give an indication of the conversion achieved, in same stoichiometry systems where the number of competing reactions is consistent.[50] Here, the T_g of ambient-cured samples (3.2.5) was inferred as the onset of decay in storage modulus, as is commonly used with epoxy DMA (Typical data are shown in Figure 3.10). However, as these samples had not reached maximum conversion upon analysis, the heating involved in the DMA experiment inevitably increased epoxy conversion. This is evidenced in Figure 3.10 (black circles) by the slight levelling off seen in the E', E'' and tan δ at ~ 65 °C. Therefore, this measure of 'T_g' is more a comparative value of conversion achieved rather than a direct measure. For an inert system, a heating rate of 3 °C / minute would typically be used to ensure thermal equilibrium. Here, however, a higher heating rate of 10 °C / minute was used to minimise the extent of curing during the measurement. This procedure therefore incurred a systematic error due to the temperature lag between apparatus and sample. Although it is clear that T_g changes over the time scale of DMA experiments and results are offset by changing heating rate, both of these effects are systematic in nature, and a separate experiment using a polystyrene standard (Table 3.6) showed that consistent T_g measurements are possible if heating rate is consistent (± 0.8 °C). A polystyrene standard was heated at either 3 °C or 10 °C / minute from 50 °C to 150 °C to determine T_g. This was repeated 3 times for each heating rate (Table 3.6).

Table 3.6: T_g of a polystyrene standard (M_W = 95,000) at different heating rates.

	T_g / °C				
Heating Rate / °C	1	2	3	x̄	σ
3	126.2	126.2	125.6	126.0	0.3
10	141.8	143.0	143.2	143.7	0.8

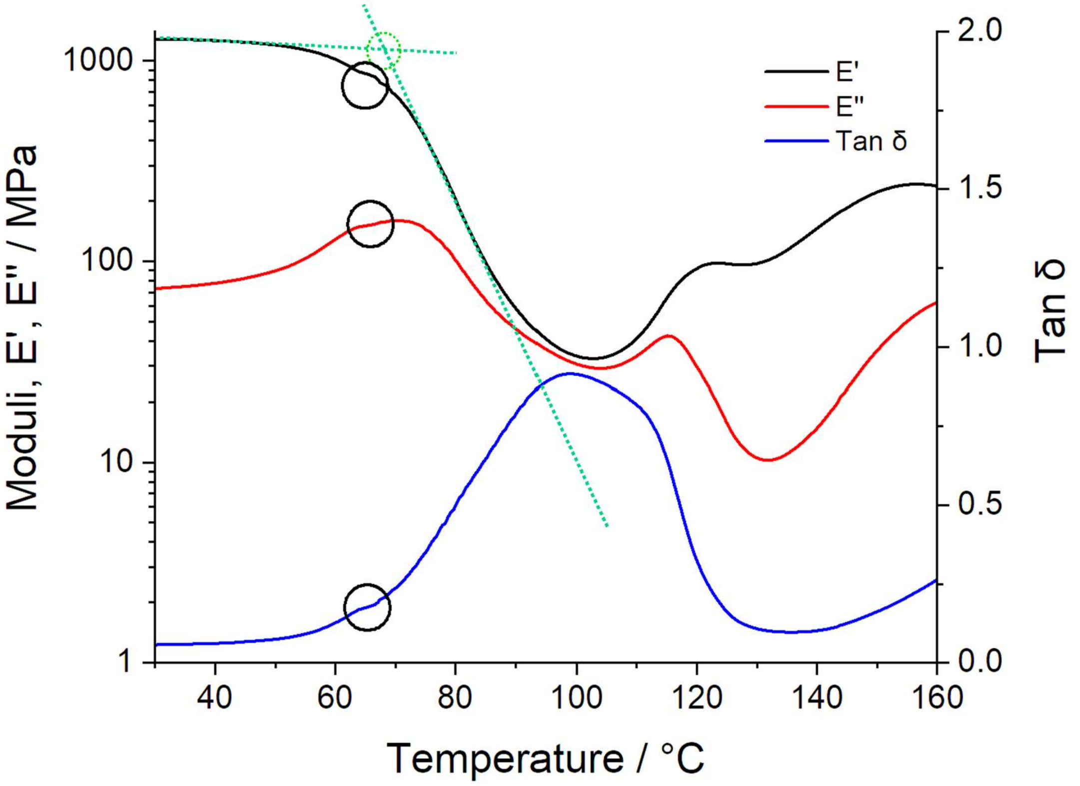

Figure 3.10: Storage modulus, loss modulus and Tan δ against temperature of a 35% stoichiometry system detailing onset ambient cured T_g (green intercept) and evidence of in situ curing (black circles).

3.11 Oscillatory Rheometry

Rheometry is an analytical technique used to characterise the fluid or rheological behaviour of a sample during deformation. Rheological studies of epoxy systems during curing can reveal information about the change in mechanical properties of the films such as the storage (G') and loss moduli (G''). In particular, it could be utilised to characterise the change in system viscosity as a function of cure condition and stoichiometry over the 15-minute induction time.

Samples were analysed using oscillatory rheometry and involved the deformation of a sample between oscillating parallel plate geometry (Figure 3.11). Two parallel plates of surface, *a*, are separated by a distance, *h* (shear gap dimension). The bottom plate remains stationary (deflection = 0), while the upper plate is rotated back and forth by an applied torque. The sample is placed between the two plates and the motion of the upper plate causes shearing of the sample, showing angular displacement $\pm\gamma$. Polymers, such as curing epoxy resins, demonstrate viscoelastic behaviour and so the applied strain, γ, and resultant stress, τ, are defined using the following equations:

$$\tau = \tau_0 \, sin(\omega t) \qquad 3.12$$

$$\gamma = \gamma_0 \, sin(\omega t + \delta) \qquad 3.13$$

where ω is the frequency of strain oscillation, t is time and δ is the phase angle, where $0° < \delta < 90°$. For ideally elastic behaviour $\delta = 0°$, and for ideally viscous behaviour $\delta = 90°$. The storage modulus (elastic response) and loss modulus (viscous response) can be expressed as:

$$G' = \frac{\tau_0}{\gamma_0} \cos \delta \qquad 3.14$$

$$G'' = \frac{\tau_0}{\gamma_0} \sin \delta. \qquad 3.15$$

Tests were conducted on a TA Instruments AR2000 rheometer with a 25 mm parallel plate geometry, chosen to provide a sufficiently large surface area for the sample. This configuration ensures a more pronounced response to applied shear stress during rheological analysis. The epoxy reactants were incubated at either 25 or 35 °C, before being mixed at either 100% or 35% stoichiometry and cast onto the bottom plate. A furnace then enclosed the plates where temperature was maintained at either 25 or 35 °C. A time-sweep with 5% strain amplitude was carried out for 10 hours. Frequency was kept constant at 1.5 Hz as is advised for epoxy rheology studies.[122]

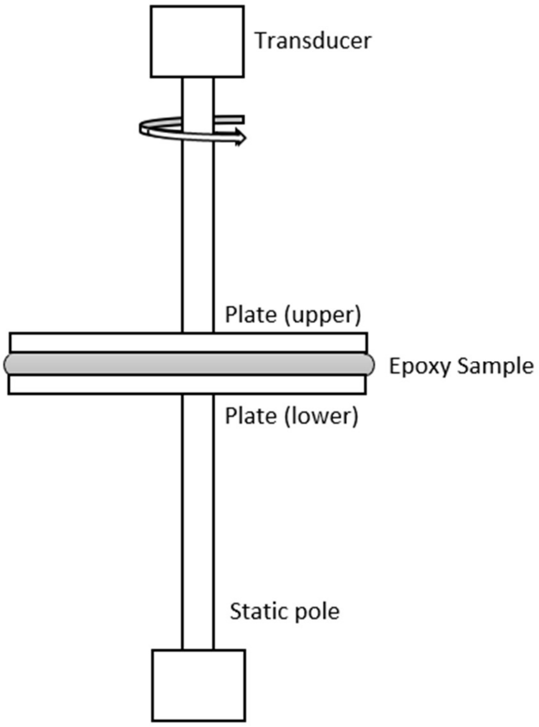

Figure 3.11: Rheometer with parallel plate geometry.

3.12 Positron Annihilation Lifetime Spectroscopy

Positron annihilation lifetime spectroscopy (PALS) is one of the few techniques which enables the free volume properties of polymers to be probed. Positrons are antiparticles of electrons, and in normal matter have very short lifetimes, annihilating with electrons to form gamma rays. There are three modes of positron decay distinguishable by their variation in lifetime. Free annihilation between positrons and electrons, results from direct impact and has a characteristic lifetime of 0.3 – 0.5 ns (lifetime denoted T_2). The fastest and longest decay modes involve the formation of a bound state between the positron and electron, called a positronium. This exists in either a singlet, short lived (vacuum lifetime: ~ 0.125 ns) para-positronium state, p-Ps, (lifetime denoted T_1), or a triplet, long lived (> 0.5 ns) ortho-positronium state, o-Ps, (lifetime denoted T_3), depending on the spin configuration of the constituent particles (p-Ps: anti-parallel positron and electron spins; o-Ps: parallel positron and electron spins). In matter, p-Ps lifetime is relatively unchanged due to self-annihilation. However, o-Ps do not experience self-annihilation and instead annihilate through collisions with the local environment, termed pick-off annihilation. As a result, the lifetime of o-Ps is directly related to void size and thus forms the basis of PALS.

Experimentally, ^{22}Na was used as a positron source, which decays to ^{22}Ne, emitting a 1.27 MeV gamma ray, and a positron. Upon positronium annihilation, gamma rays of 0.511 MeV are generated. Therefore, two gamma ray detectors were utilised to detect both energies. Upon detection of a "birth" 1.27 MeV gamma ray, a clock cable of resolving nanoseconds events is started and stops upon detection of a "annihilation" 0.511 MeV gamma ray. By measuring the time between emission and annihilation photons, the positron lifetime can be determined.

PALS experiments were carried out in the Department of Mechanical Engineering at the University of Sheffield, UK, using a fast-fast coincidence circuit (50 ns).[31] Two identical sample films (Section 3.2.5) sandwiched a ^{22}Na positron source and were placed between a pair of fast plastic scintillators and photomultiplier tubes (gamma detectors) to acquire lifetime spectra. Each spectrum was collected to a minimum of 1 million counts from annihilation events and the time resolution was monitored to 470 ± 18 ps (Figure 3.12).

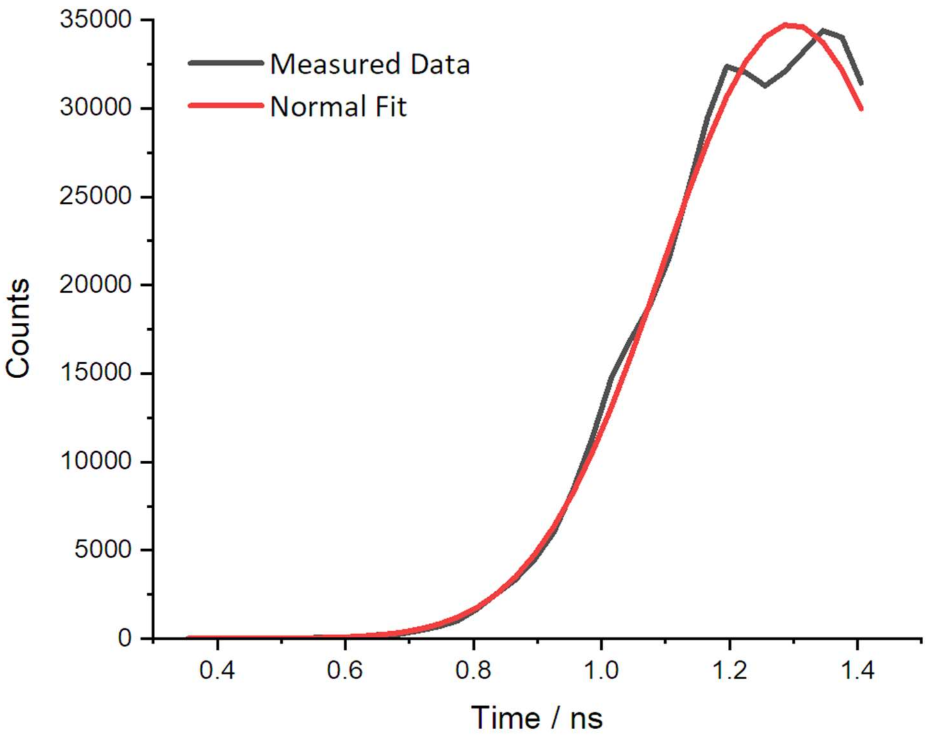

Figure 3.12: Counts against time for example epoxy sample, resolution determined using FWHM of the normal fit.

The positron decay spectra consisted of a series of lifetimes due to the different positron annihilation mechanisms. The Lifetime data was resolved into three finite components, T_1, T_2 and T_3. Using the Tao-Eldrup model, which assumes voids are infinitely deep spherically symmetric potential wells, T_3 was correlated to the mean void size by first determining the medium free volume cavity radius using the empirical Equation 3.16:

$$\frac{1}{T_3} = 2\left[1 - \frac{R}{R_0} + \frac{1}{2\pi} sin\left(\frac{2\pi R}{R_0}\right)\right] \tag{3.16}$$

where R is void radius and $R_0 = R + \Delta R$ where ΔR is 1.656 Å.[123,124] Free volume cavity radius can then be used to calculate average void volume (Equation 3.17) and fractional free volume (Equation 3.18):

$$AVV = \frac{4}{3}\pi R^3 \tag{3.17}$$

$$\mathrm{FFV} = \mathrm{I_3} \times \mathrm{AVV} \tag{3.18}$$

where *AVV* is average void volume, *FFV* is fractional free volume and I_3 is the relative intensity of the o-PS annihilation lifetime (the percentage of positrons annihilating by the pickoff mechanism).[31,125]

3.13 Raman Spectral Mapping

Raman spectral mapping allows for the generation of detailed false colour chemical images based on material composition and structure. This is achieved by recording a complete Raman spectrum at each pixel within a scan area or image. Laser light of specified wavelength, is directed at a sample, scattering all photons upon interaction with molecules. Photons can scatter in one of three ways:

Elastically (Rayleigh scattering): no net energy transfer between photon and molecule.

Inelastic (Stokes scattering): the photon is scattered with lower energy than the incoming energy.

Inelastic (anti-Stokes scattering): the photon is scattered with higher energy than the incoming energy.

Post scattering, the wavelength, and hence energy, of most light remains unchanged (Rayleigh scattering). However, approximately 1 in 100 million scattered photons loses energy via molecular excitation, causing a decrease in photon energy (and an increase in wavelength), termed the Raman shift. This energy change, and resultant bond vibration and change in polarizability, is dependent on bond strength and atomic mass, and therefore is unique to each bond, acting as a molecular fingerprint. The photons then enter an optical filter which differentiates between Raman and Rayleigh scattered light, reflecting the latter. The Raman scattered light then passes through a spectrograph where it is directed toward a charged coupled device at varying angles based on wavelength. Here Raman scattering intensity is given as a function of wavelength. This is changed to a function of wavenumber (cm^{-1}) by defining the laser wavenumber as 0 cm^{-1}, as the relative wavenumber of Raman scattering is directly proportional to the energy between vibrational states.

Two separate Raman spectral mapping experiments were carried out using a Horiba Jobin Yvon LabRAM HR confocal Raman microscope, equipped with a Peltier-cooled CCD. A 632.8 nm wavelength He-Ne laser of beam of spot size 1-2 µm was focused on the sample using a 50× LWD Leica objective, and spectra recorded every 10 µm.

For experiment 1, samples were prepared as described in section 3.2.3 (producing reservoir attached, 100% stoichiometry, 2-layer films (~ 150 µm / layer) which were cured at 25 °C or 35 °C prior to post curing at 80 °C). Approximately 10 ml of d-methanol was placed in the reservoir (Figure 3.1) and allowed to ingress into the samples for 30 days prior to analysis. Directly prior to analysis, the d-methanol and solvent traps were removed, and samples were fractured along the centre *via* scoring with a scalpel blade and snapping along this fracture to expose a clean cross-sectional surface for analysis with minimal variation in R_q (Figure 3.13). Raman spectral mapping was carried out vertically across the exposed cross section to generate a vertical composition profile. Spectra were collected from 200 – 3500 cm^{-1}, over a 2 s acquisition time using 2 accumulations.

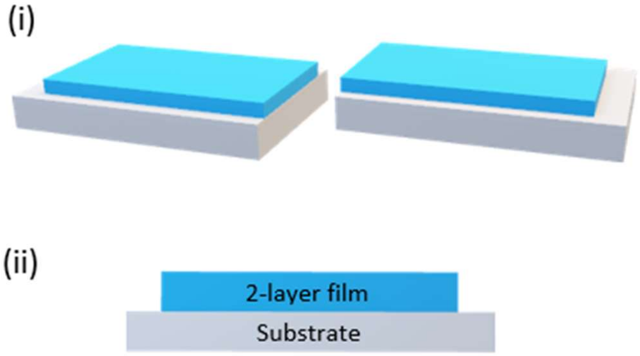

Figure 3.13: (i) Sectioned film (ii) Schematic of exposed interface which is analysed during microbeam scanning.

For experiment 2, samples were prepared as described in section 3.2.3 (producing ~ 150 µm, 100% stoichiometry, 1-layer films cured at 25 °C or 35 °C). Samples were then overcoated with 4-chlorophenyl glycidyl ether (4-ClPGE) as it has a similar structure (Table 3.7), volume (Table 3.7), and Hansen solubility parameter (Figure 3.14) to that of second coat components, but also contained a unique functional group which could be identified using Raman spectroscopy. After 3 or 4 days, excess probe compound remaining on the sample surface was removed. Samples were then fractured and analysed as described for experiment 1.

Table 3.7: HSPiP determined dispersive, polar and hydrogen bonding energy, and molecular volume of RDGE (grey) and 4-ClPGE (white).

Compound	**δ / MPa$^{1/2}$**			**MVol / Å^3**	**Structure**
	D	**P**	**H**		
RDGE	19.0	8.8	7.0	178.6	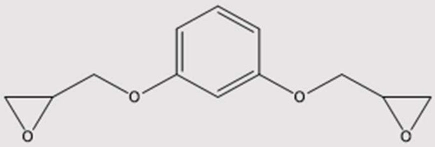
4-chlorophenyl glycidyl ether	19.3	7.7	6.4	146.3	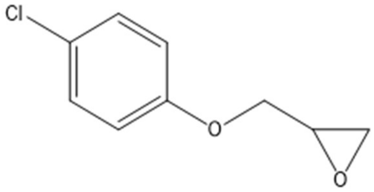

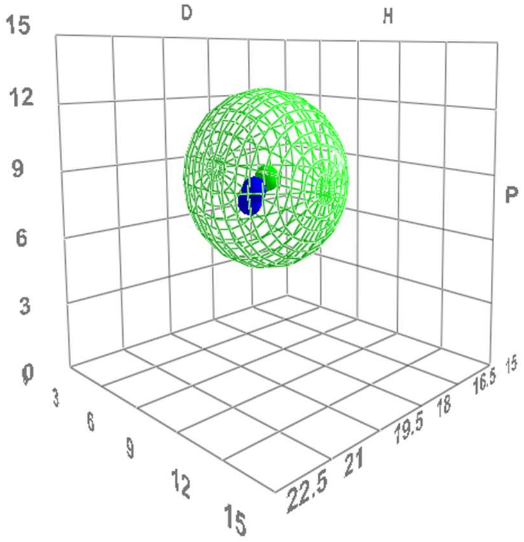

Figure 3.14: HSPiP generated Hansen solubility parameter plot displaying RDGE (green circle), and possible probe compounds, including 4-chlorophenyl glycidyl ether (blue circle) and the measure of similarity (green wireframe circle).

3.14 Particle Induced X-ray Emission

Ion beam analysis (IBA) encompasses a range of techniques that utilise the acceleration of a beam of ions towards a sample, and the detection of subsequent ion scattering or emittance. This can be used to quantify depth distributions and therefore produce vertical composition profiles of films. Particle induced X-ray emission (PIXE) is a branch technique of IBA used for elemental analysis of a sample. As an incident proton travels through a sample, it loses energy primarily by exciting electrons in nearby atoms. If provided with sufficient energy, this can cause inner shell electrons to eject, resulting in an unstable electron atomic configuration. Consequently, electrons from higher shells drop down to fill vacancies which releases excess energy in the form of X-rays (Figure 3.15).[126] The energies of these X-rays are characteristic of the element and so can be used to identify elemental sample composition. Additionally, by measuring the relative intensities of characteristic X-ray lines, the elemental concentration in a sample can also be determined (± 1 ppm). As PIXE uses an incident beam angle perpendicular to the sample surface, the technique can be used in a scanning capacity. Therefore, if PIXE is carried out over a sample cross section, a 2-dimensional vertical composition map can be generated. PIXE can be advantageous over other IBA techniques, such as nuclear reaction analysis (NRA), for a variety of reasons. PIXE X-ray yield is much higher than the particle yield for scattering reactions, and thus data collection is quicker, leading to minimal beam damage to the sample. In addition, regarding the generation of vertical composition maps, PIXE allows for depth profiling over a larger range than IBA techniques, enabling the analysis of larger samples. This is because during NRA, upon penetration of the sample by $^{3}He^{+}$ ions, the rate of energy loss by said ions increases with sample penetration depth, limiting the maximum depth at which the ion beam is effective (~ 10 µm). Ultimately, the maximum depth capable for analysis is limited by the effective threshold energy below which reaction cannot occur, and reaction products are of insufficient energy to reach the detector.[127]

PIXE measurements were carried out by Dr Catia Costa at the EPSRC Ion Beam facility at the University of Surrey (Surrey, U.K.). Samples were prepared as described in section 3.2.3 (producing reservoir attached, 100% stoichiometry, 2-layer films (~ 150 µm / layer) which were cured at 25 °C or 35 °C for 4 or 3 days, then post cured at 80 °C). Approximately 20 ml of 2-bromoethanol was placed in the reservoir (Figure 3.1) and allowed to ingress into the sample for 30 days prior to analysis. Directly prior to analysis, the 2-bromoethanol and solvent trap were removed. The sample was then fractured along the centre, exposing a clean surface for analysis (Figure 3.13).

A 2.5-MeV collimated proton beam of 2 µm diameter was directed at normal incidence to the sample. X-ray reaction emissions were detected using a lithium-drift silicon detector equipped with a 130 µm beryllium foil to stop backscattered particles reaching the detector. For each sample, a ~ 300 µm vertical composition profile of 2-bromoethanol saturation was generated (3 repeats) by determining elemental composition at regular 2 µm intervals. The X-ray responses were calibrated using a BCR-126A glass standard.[128] OMDAQ 3 (Oxford Microbeams Ltd., U.K.) software was used to collect and process the spectral data.

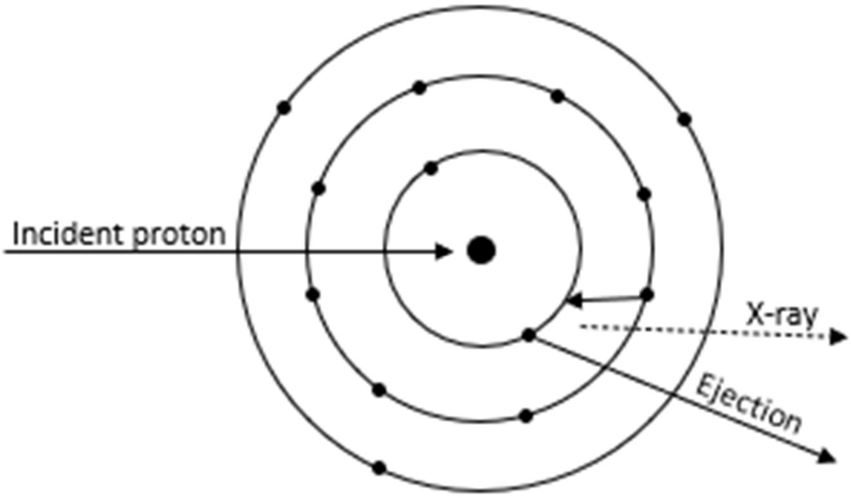

Figure 3.15: The Coulomb interaction between an incident proton and nucleus resulting in inner shell electron ejection, the resultant filling of said electron vacancy by outer shell electron migration, and the emission of excess energy via X-rays.

3.15 Neutron Scattering

Neutrons are neutral (uncharged), subatomic particles exhibiting wave-particle duality, with its wavelength, λ, defined by the de Broglie relationship,

$$\lambda = \frac{h}{mv}, \qquad 3.19$$

where *h* is Planck's constant and *m* and *v* are the mass and velocity of the neutron respectively. Their neutral electrostatic charge means free neutrons can penetrate further into materials than charged particles of similar kinetic energy. In addition, through interactions with either atomic nuclei or unpaired electrons in the surrounding orbitals, free neutrons can scatter.[129,130] This unique combination of properties (high penetration depth and the ability to scatter) makes neutrons a valuable resource for probing bulk properties and buried interfaces within materials. Within this work, only scattering from the nucleus was studied.

Scattering can either be elastic or inelastic. Inelastic scattering involves energy transfer to or from the neutron during collision and has application in molecular rotation and vibration. Therefore, inelastic scattering has potential to be used to monitor epoxy cure reactions.[131] Elastic scattering involves no energy change of the neutron during collision and has application in structure characterisation.[132] Within this work, only elastic scattering techniques were used and so scatting will be considered under elastic regime. In elastic scattering the modulus of the incident and reflected wavevector are equal, given as

$$|\overrightarrow{k_\iota}| = |\overrightarrow{k_f}| = \frac{2\pi}{\lambda} \tag{3.20}$$

where $\overrightarrow{k_\iota}$ and $\overrightarrow{k_f}$ are the momentum vectors of the incident and final wave respectively.[132] The momentum transfer vector, Q, is defined as the difference in the momentum of $\overrightarrow{k_\iota}$ and $\overrightarrow{k_f}$, described by Equation 3.21, and illustrated in Figure 3.16.

$$Q = |\overrightarrow{k_\iota} - \overrightarrow{k_f}| = \frac{4\pi}{\lambda} sin\theta \tag{3.21}$$

The strength of interaction between neutron and nucleus is determined by the scattering length of the nucleus, b. From the scattering length, the probability of a neutron being scattered can be obtained, termed the scattering cross-section, σ,[132]

$$\sigma = 4\pi|b|^2. \tag{3.22}$$

Therefore, σ is a measure of the scattering power of a material. This measure is isotope dependent; the difference in scattering lengths of different isotopes is the origin of contrast in this technique. In particular, hydrogen and deuterium have a large difference in scattering lengths (Table 3.8) and consequently many neutron-experiments function by substituting deuterium for hydrogen atoms in probe solvents or samples, to produce contrast.

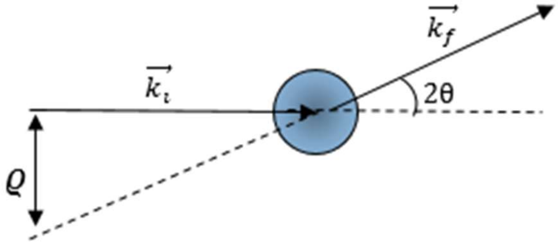

Figure 3.16: Schematic of elastic neutron scattering and associated wavevectors.

Table 3.8: Coherent scattering lengths of elements of interest.

Element	b_i / 10^{-15} m
H	-3.746
D	6.671
C	6.646
N	9.360
O	5.803
Si	4.149

The total scattering cross section, σ_s, is the sum of the coherent and incoherent cross sections,

$$\sigma_s = 4\pi\langle b\rangle^2 + 4\pi(\Delta b)^2 = \sigma_{coh} + \sigma_{incoh}. \qquad 3.23$$

The coherent cross section describes the correlation between the position of different nuclei and is used to uncover sample structural information. The incoherent cross section describes the correlation between the position of the same nucleus at different times, contributing only to noise.[130]

The above theory describes the probability of a neutron scattering from a single nucleus, whereas within this research the length scale is much larger than atomic dimensions. Therefore, a scattering length density (SLD), ρ , is defined, expressed as[130]

$$\rho = \frac{\sum_i^n b_i}{\overline{V}} \tag{3.24}$$

where b_i is the scattering length of the relevant atom and $\overline{V}$ is the volume containing the n atoms. Using ρ, the scattering behaviour of domains in a sample can be characterised.

3.15.1 Neutron Reflectivity

Neutron reflectivity (NR) is a surface-sensitive depth profiling technique capable of producing vertical composition profiles with < 1 nm resolution. NR measures the fraction of incident neutrons that are reflected from a surface as a function of the scattering wavevector, $\boldsymbol{Q}$. This fraction is termed the reflectivity, *R*($\boldsymbol{Q}$), and by definition lies between 0 and 1.

The refractive index, *n*, of a boundary is defined as

$$n = \frac{k_1}{k_0} \tag{3.25}$$

where k_1 and k_0 are the wavevectors inside and outside a given medium, respectively. In most materials, *n* can also be approximated to[133]

$$n = 1 - \frac{\lambda^2 \rho}{2\pi}. \tag{3.26}$$

Under vacuum, $n = 1$ and R($\boldsymbol{Q}$) = 0, but typically, $n < 1$ and consequently total external reflection (TER) is observed at low contact angles, less than the critical angle, θ_c. The critical angle can be obtained using Snell's law,

$$cos\theta_c = \frac{n_1}{n_0}. \tag{3.27}$$

The relationship between critical angle, neutron wavelength and scattering length density of a material is given as

$$\theta_c = \lambda\sqrt{\frac{\rho}{\pi}}. \tag{3.28}$$

The critical value for the wave transfer vector, Q_c, is given in equation 3.29 and 3.30 when the external medium is air or other interfaces, respectively.

$$Q_c = \sqrt{16\pi\rho} \tag{3.29}$$

$$Q_c = \sqrt{16\pi\Delta\rho} \tag{3.30}$$

where $\Delta\rho$ is the difference in SLD between the two media. Neutron radiation is partly transmitted and reflected at each interface. Using Fresnel's law, the reflection, R, of neutrons at a single interface between two materials can be described, where $\theta \geq \theta_c$,[130]

$$R = \left|\frac{n_0\, sin\theta_0 - n_1\, sin\theta_1}{n_0\, sin\theta_0 + n_1\, sin\theta_1}\right|^2. \tag{3.31}$$

The Born approximation assumes that each neutron only scatters once while passing through a sample, meaning reflectivity can be expressed as[134]

$$R(Q) = \frac{16\pi^2\Delta\rho^2}{Q^4} \tag{3.32}$$

for a single sharp interface. This can be extended to multiple interfaces using

$$R = \left|\frac{r_{01} + r_{12}\, exp(2i\beta_1)}{1 + r_{01}r_{12}\, exp(2i\beta_1)}\right|^2, \tag{3.33}$$

where β_j is the optical path length and r_{ij} is the Fresnel coefficient for a film of thickness d_j.[133,134]

$$r_{ij} = \frac{(p_i - p_j)}{(p_i + p_j)} \qquad 3.34$$

$$\beta_i = \frac{2\pi}{\lambda} n_i d_i \, sin\theta_i \, . \qquad 3.35$$

where $p_i = n_i \, sin\theta$ and θ_i is defined according to Figure 3.17.

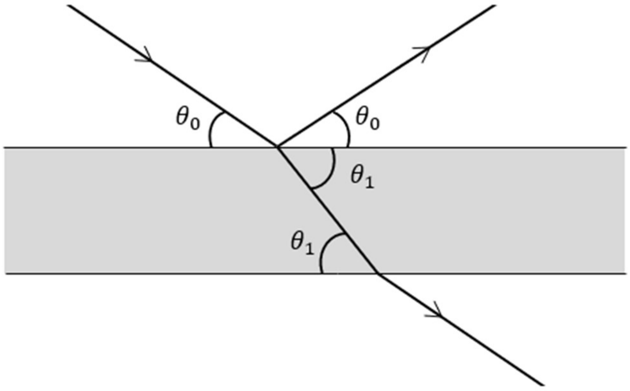

Figure 3.17: Refraction and reflection of neutrons displaying angles related to Equation 3.33. Typically, n is close to 1 and the extent of beam refraction is small.

To calculate reflectivity from a system with many interfaces, a systematic approach is essential. Using the Born and Wolf approach, which assumes that neutron wave function and gradient are continuous across each interfacial boundary, a characteristic matrix, M_i, for each layer is derived,

$$\mathrm{M}_i = \begin{bmatrix} \cos\beta_i & -\frac{i}{k_i}\sin\beta_i \\ -ik_i \, \sin\beta_i & \cos\beta_i \end{bmatrix}, \qquad 3.36$$

where $k_i = n_i \, sin \, \theta_i$. By performing the operation $\mathrm{M} = [\mathrm{M}_1][\mathrm{M}_2] \ldots [\mathrm{M}_n]$, the resultant reflectivity can be calculated using

$$R = \left|\frac{(\mathrm{M}_{11} + \mathrm{M}_{12}P_s)P_a - (\mathrm{M}_{21} + \mathrm{M}_{22})P_s}{(\mathrm{M}_{11} + \mathrm{M}_{12}P_s)P_a + (\mathrm{M}_{21} + \mathrm{M}_{22})P_s}\right|, \quad 3.37$$

where P_a and P_s are parameters that represent the amplitude of the incident and scattered neutron waves, respectively. These calculations are only strictly valid for smooth interfaces, whereas real samples are likely to contain interfacial roughness and diffuse surfaces. This roughness offsets specular reflectivity by a Nevot-Croce factor,

$$R = R_0\, exp(-q_0 q_1 \sigma^2)\,, \quad 3.38$$

where σ is the root mean square roughness and $q_i = 2k\, sin\theta$ $(k = \frac{2\pi}{\lambda})$. Therefore, to account for surface roughness in multiple layers, an alternative formation is required. This can be achieved using the Abeles matrix formulation, which applies a Gaussian roughness to the Fresnel coefficients of each interface (Equation 3.39) to define the characteristic matrix of each layer (Equation 3.40).

$$r_{ij} = \left(\frac{p_i - p_j}{p_i + p_j}\right) exp\left[-0.5\left(q_i q_j \sigma^2\right)\right] \quad 3.39$$

$$\mathrm{C}_M = \begin{bmatrix} e^{i\beta_{m-1}} & r_m e^{i\beta_{m-1}} \\ r_m e^{-i\beta_{m-1}} & e^{-i\beta_{m-1}} \end{bmatrix}. \quad 3.40$$

From the resultant matrix, the reflectivity can be obtained,

$$R = \frac{M_{21}M_{21}^{*}}{M_{11}M_{11}^{*}}\,. \quad 3.41$$

Therefore, it is possible to obtain a vertical composition profile from NR data through generating a reflectivity curve for a multi-layer sample with rough interfaces.

3.15.2 Experimental Procedure

Specular neutron reflectometry was conducted using the OFFSPEC reflectometer at the ISIS Pulsed Neutron Source (STFC Rutherford Appleton Laboratory, Didcot, U.K.). Data was collected with the assistance of Dr. Stephen Hall, ISIS UK.

Single layer, ambient-cured samples were produced at 100% and 35% stoichiometry, at 25 and 35 °C, and some retained for NR analysis. The rest were then overcoated at varying intervals, and post cured as described in section 3.2.4. The two-layer samples were then immersed in deuterated methanol for 7 days.

Vertical sample composition profiles were generated under three possible conditions:

i. Single layer ambient-cured film exposed to an air interface (Geometry 1, Figure 3.18)
ii. Single layer ambient-cured film exposed to a deuterated methanol interface (Geometry 2, Figure 3.18)
iii. Two-layer post-cured film, following ingress of deuterated methanol (Geometry 2, Figure 3.18)

Figure 3.18 shows the two geometries used to achieve these experimental conditions. The first ensures the film is exposed to air while the second allows for an interface with deuterated methanol. The second geometry involved inverting the block and film onto a layer CD_3OD and D_2O; this acted as a solvent reservoir to reduce solvent evaporation from the sample during the measurement. A mixture of CD_3OD and D_2O was utilised rather than just CD_3OD to further reduce rate of evaporation. As CD_3OD/D_2O (1:1) has a comparatively high SLD compared to the silicon substrate ($\sim 6e^{-6}$ to $2e^{--6}$ $Å^{-2}$), the geometry must be inverted to ensure TER and the formation of a sharp critical edge. Additionally, in the case of condition (iii), the layer of d-methanol also ensured that ingressed d-methanol could not egress prior to or during analysis.

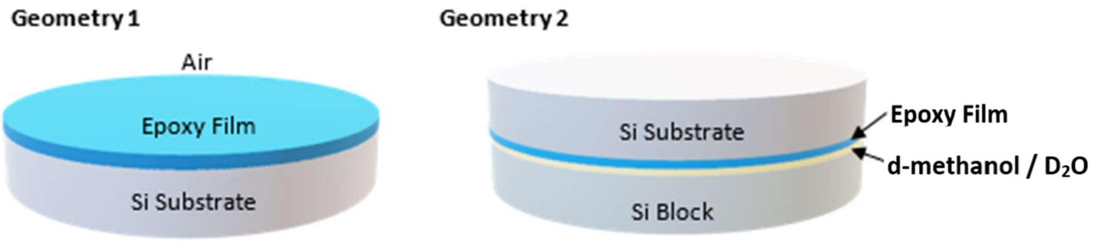

Figure 3.18: Geometries used in NR experiments: (1) film surface exposed to air (2) silicon substrate & film inverted in d-methanol on silicon block. The upper surface of the Si block is rough and does not contribute to reflection of neutrons.

Deuterium labelling of the probe solvent (methanol) was used to ensure contrast via differences in SLD. Reflectivity profiles were collected from critical edge to background using 3 incident angles (0.5°, 1.2°, 2.3°) to obtain a momentum transfer range of approximately $0.008 < Q$ / Å^{-1} < 0.5. Acquisition time ranged from 2-3 h per sample.

3.15.3 Neutron Reflectivity Data Fitting

RasCAL software accessed through ISIS's 'Data Analysis as a service' (IDaaS) dashboard was used to fit the reflectivity data to scattering length density profiles using the Nelder-Mead Simplex fitting approach. The scattering length density profiles were optimised by defining unique layer parameters including thickness, SLD, roughness, and saturation, to minimise the Chi squared goodness of fit (χ^2) value between the measured and calculated reflectivity. Reflectivity data, fits and SLD profiles were exported and plotted in Origin. An example data set, fit and SLD profile is shown in Figure 3.19.

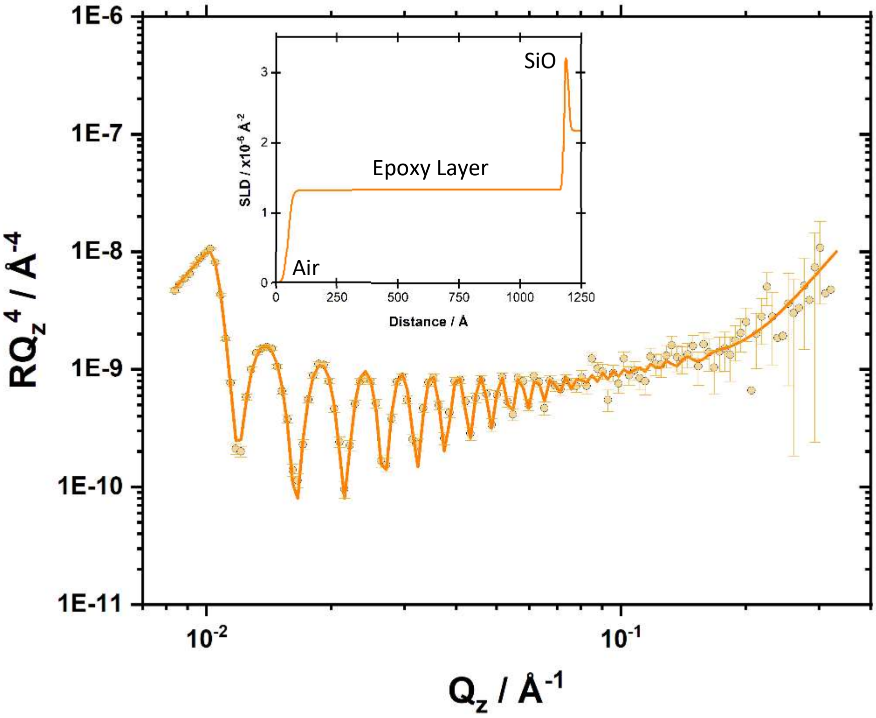

Figure 3.19: An example neutron reflectivity profile, fitting line, and SLD model (system: single layer, 100% stoichiometry system cured at 25 °C).

Chapter 4

Material Characterisation

4.1 Chapter Introduction

This chapter focuses on the characterisation of the raw materials used within this research. Prior to sample casting and subsequent analysis, it is first important to determine raw material properties such as purity, equivalent weights, and confirmation of structure. This allows for more accurate control over epoxy : amine stoichiometry as well as to better understand the chemistry of the subsequent experiments on full resin systems.

4.2 Results & Discussion

4.2.1 Structural Confirmation of D.E.N. 431, RDGE and PAC-M

^{13}C, ^{1}H and ^{1}H-^{1}H COSY NMR spectra were acquired for D.E.N. 431, RDGE and PAC-M to confirm molecular structure through peak assignment and comparison with literature. Figure 4.1 and Figure 4.2 display the ^{1}H-^{1}H COSY spectra of D.E.N. 431 and RDGE respectively. ^{1}H-^{1}H COSY (correlated spectroscopy) is a useful tool as it can be used to determine which signals arise from neighbouring protons. Therefore, using this principle, molecules can be systematically mapped to determine structure. Using Figure 4.1 and Figure 4.2, as well as literature, it was possible to assign all the major ^{1}H peaks to components expected in the structure of D.E.N. 431 (Figure 4.3) and RDGE (Figure 4.4), thus confirming structure.

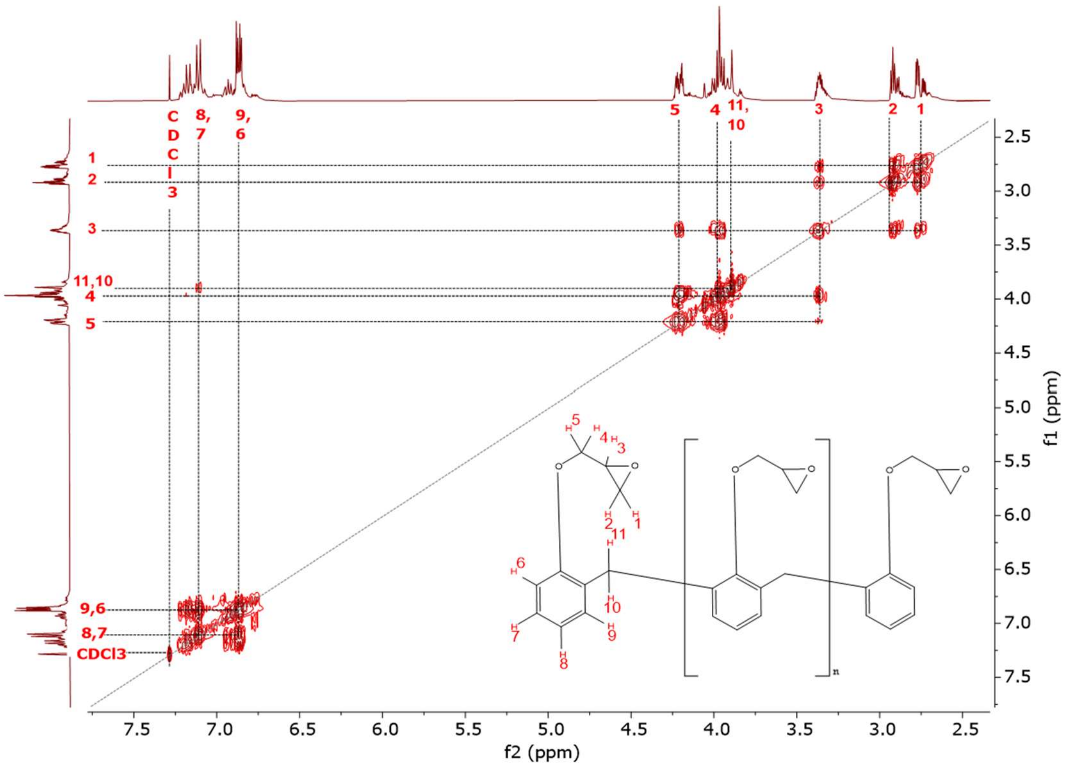

Figure 4.1: ^1H-^1H COSY spectrum of D.E.N. 431. (Solvent: $CDCl_3$. Spectrometer frequency: 400.06 MHz).

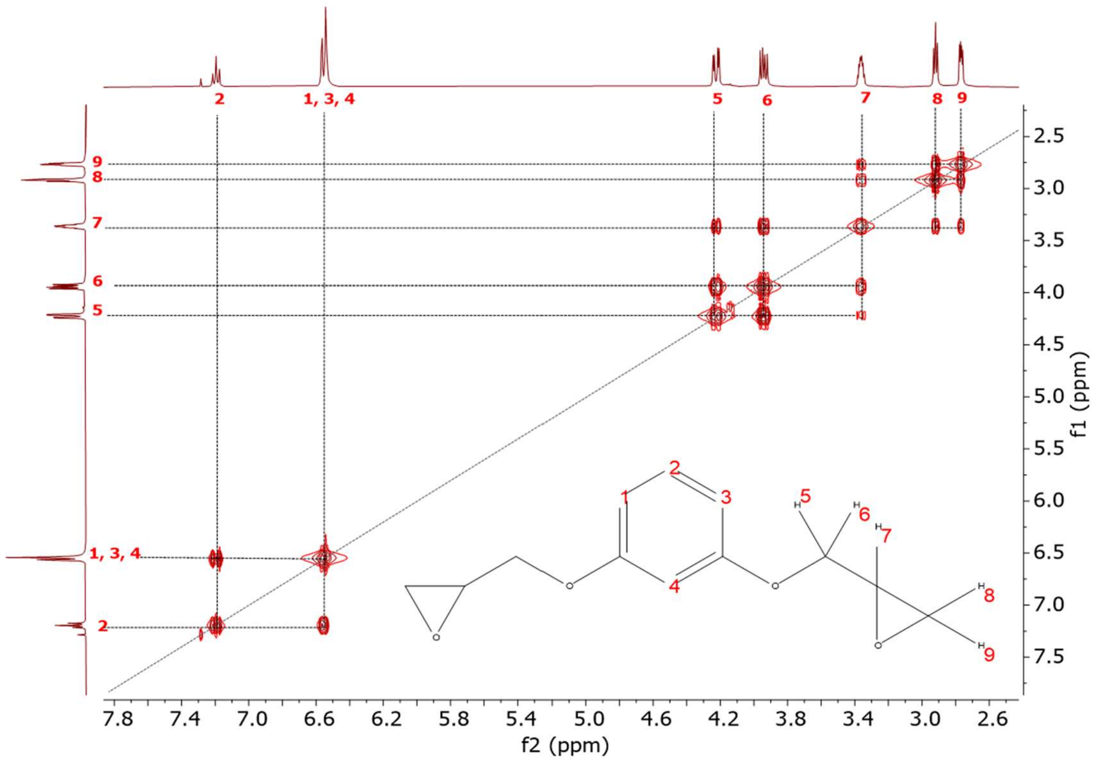

Figure 4.2: ^1H-^1H COSY spectrum of RDGE. (Solvent: $CDCl_3$. Spectrometer frequency: 400.06 MHz).

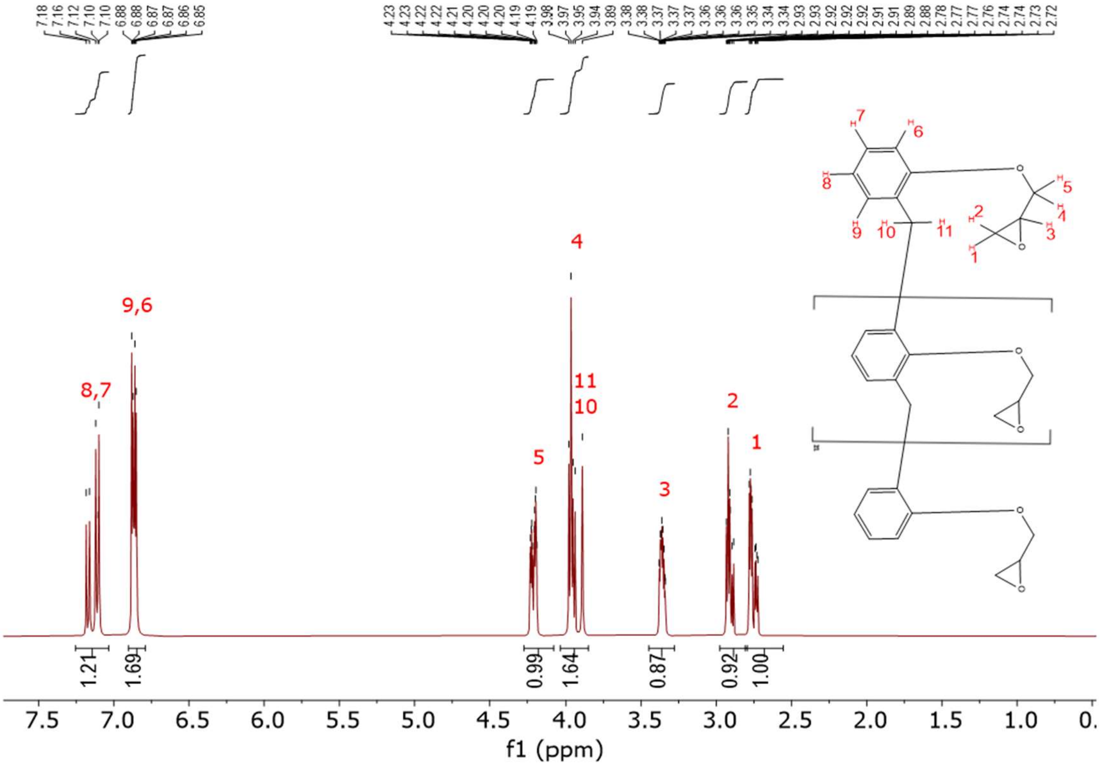

Figure 4.3: ^1H spectrum of D.E.N. 431. (Solvent: $CDCl_3$. Spectrometer frequency: 400.06 MHz).

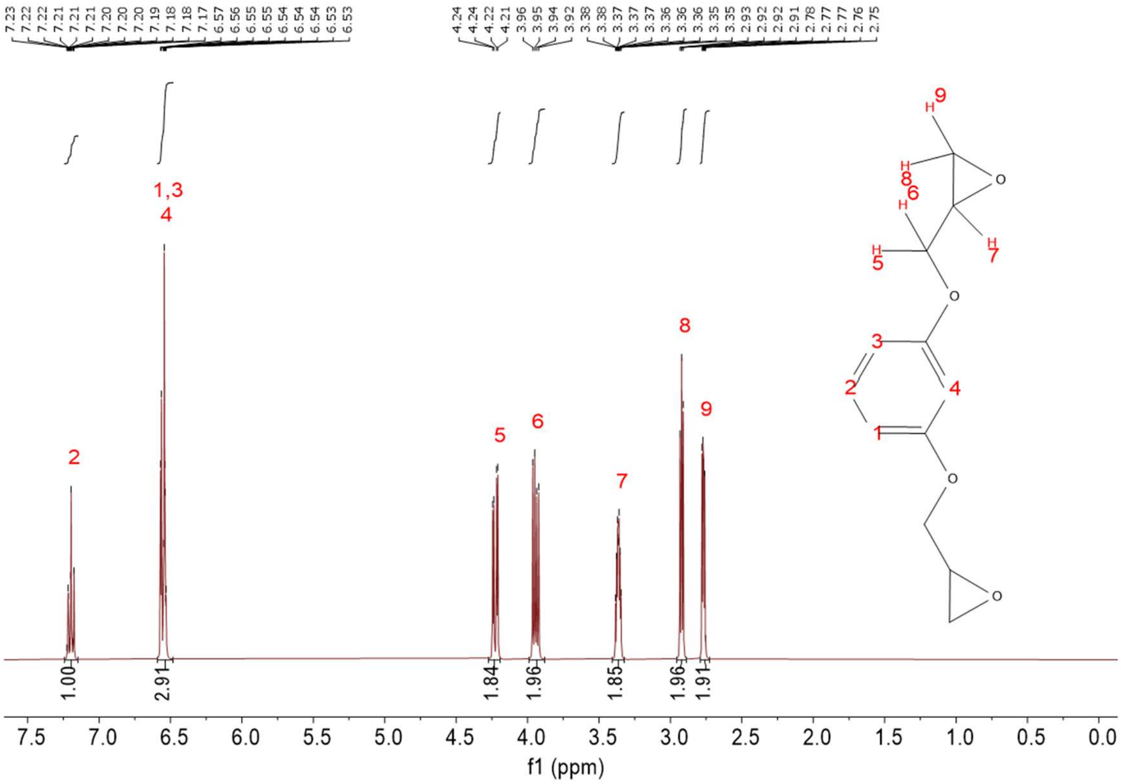

Figure 4.4: ^1H spectrum of RDGE. (Solvent: $CDCl_3$. Spectrometer frequency: 400.06 MHz).

Compared to D.E.N. 431 and RDGE, ^{1}H NMR spectrum peak assignment of PAC-M, and resultant confirmation of structure proved more challenging due to the presence of *cis* and *trans* geometric isomers. Therefore, multiple NMR techniques were used to confirm structure. ^{13}C NMR spectroscopy was primarily used to confirm the presence of isomers in the spectrum, Figure 4.5. Large intensity peaks could be observed as well as several smaller intensity peaks, indicative of isomers. Relative proton position was determined using ^{1}H-^{1}H COSY (Figure 4.6), allowing for peak assignment. HSQC was then used to confirm the proposed peak assignment as HSQC reveals proton-carbon single bond correlations (Figure 4.7). Figure 4.8 displays the ^{1}H NMR spectrum of PAC-M showing that all major peaks can be assigned to components expected in the structure of PAC-M.

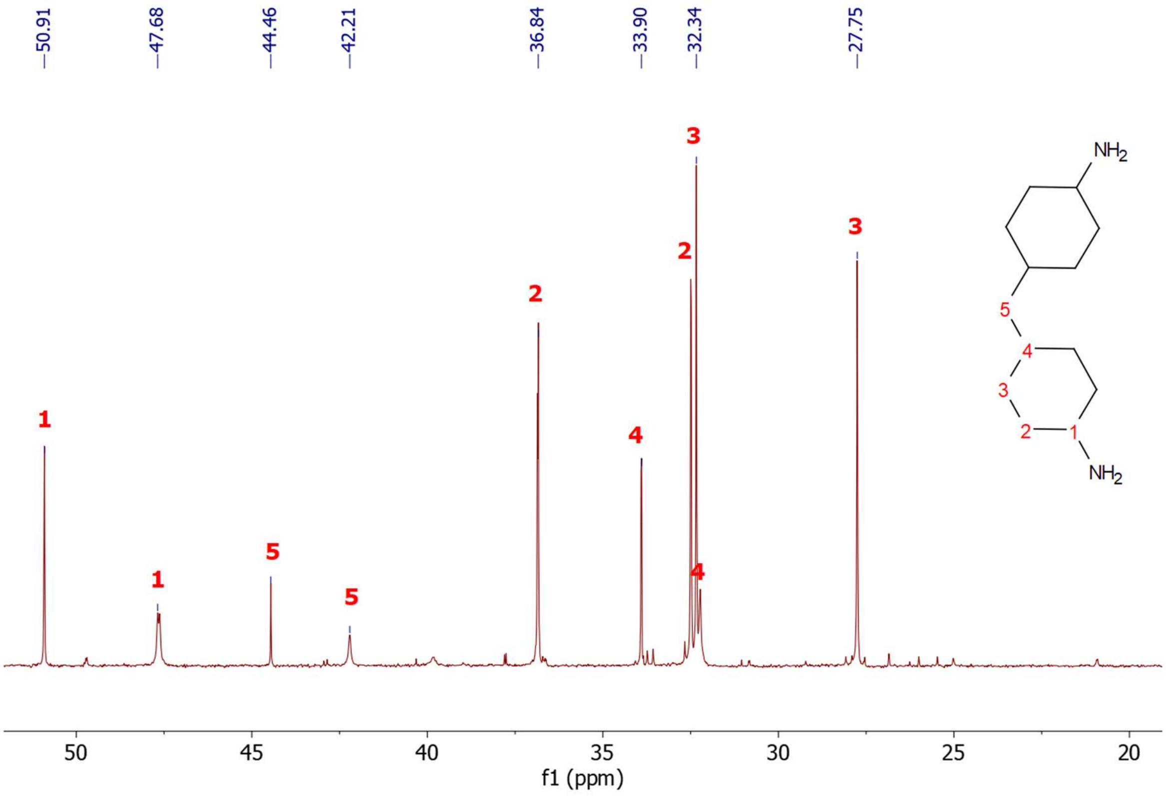

Figure 4.5: ^{13}C spectrum of PAC-M. (Solvent: $CDCl_3$. Spectrometer frequency: 100.6 MHz).

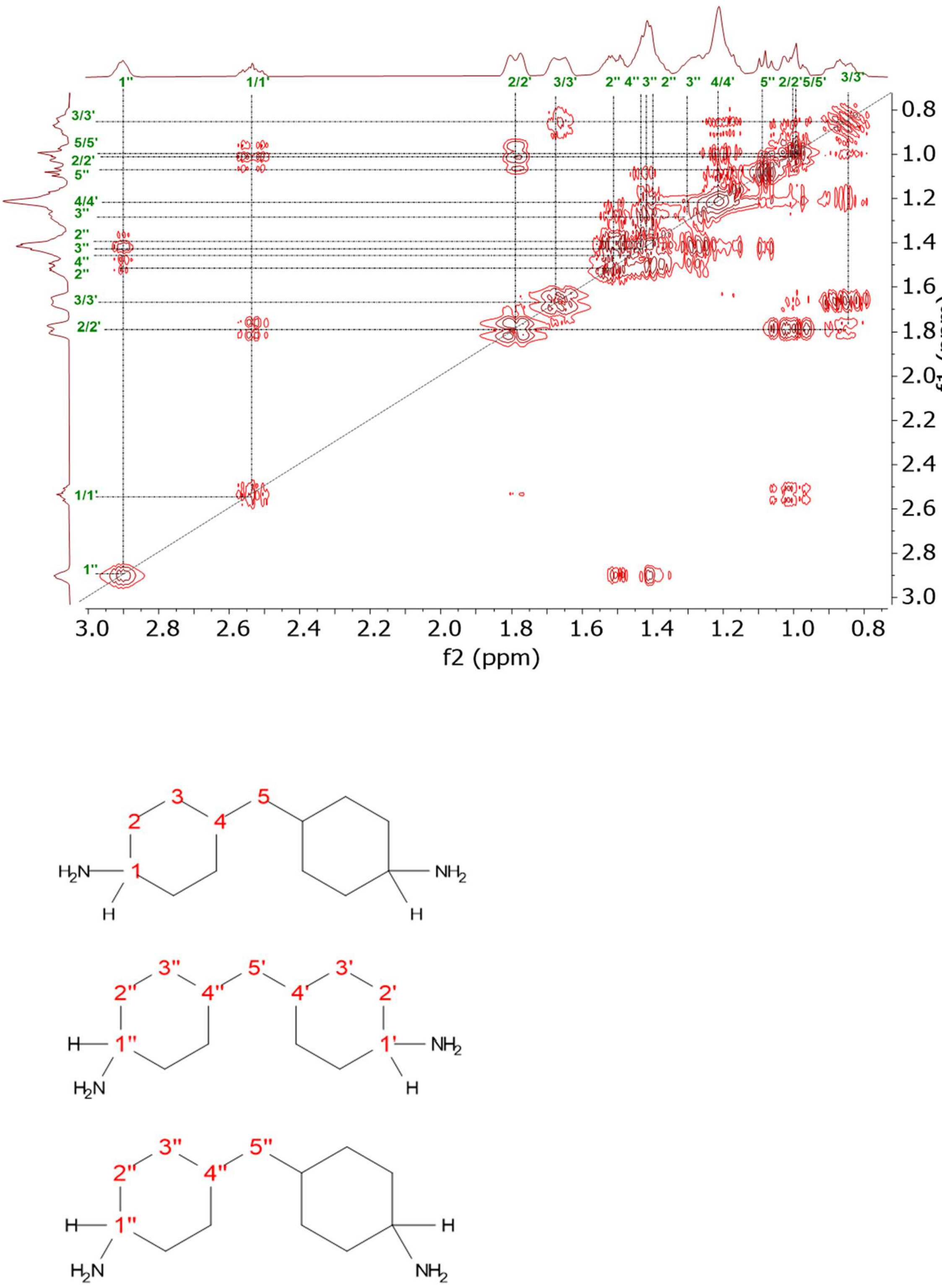

Figure 4.6: ^1H-^1H COSY spectrum of PAC-M and isomers. (Solvent: $CDCl_3$. Spectrometer frequency: 400.06 MHz).

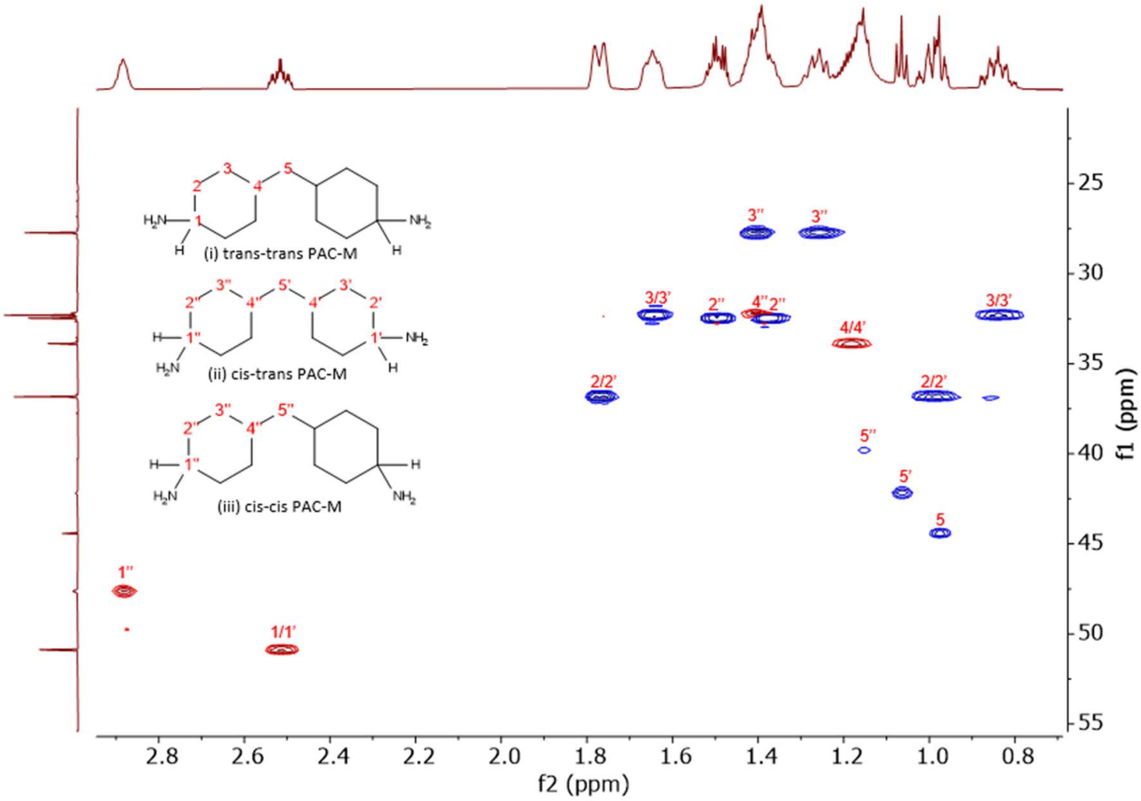

Figure 4.7: HSQC spectrum of PAC-M and isomers. (Solvent: $CDCl_3$. Spectrometer frequency: 599.36, 150.72 MHz).

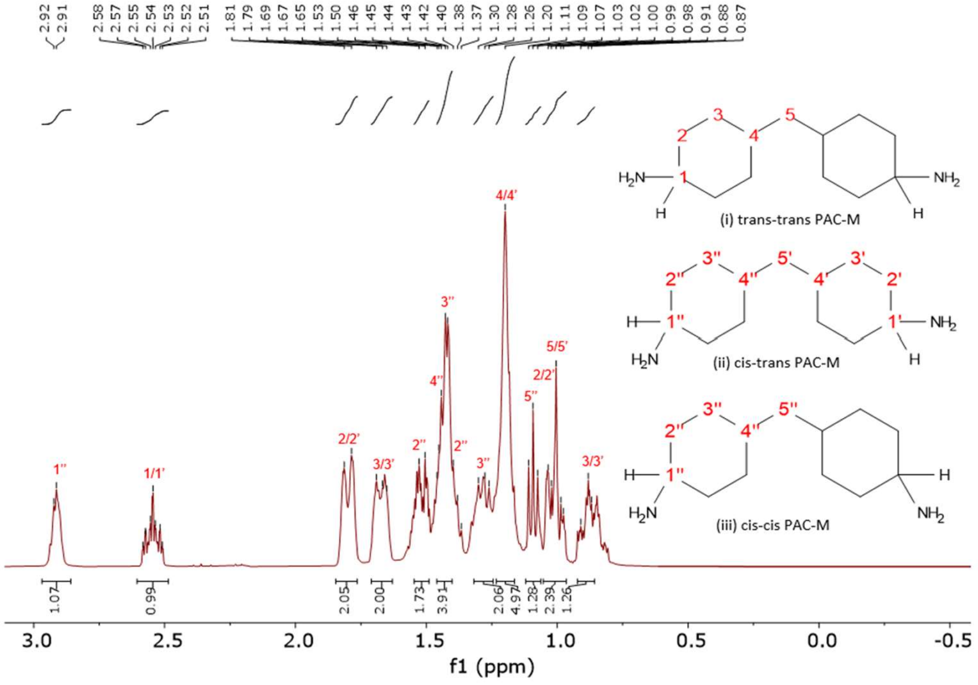

Figure 4.8: ¹H spectrum of PAC-M and isomers. (Solvent: $CDCl_3$. Spectrometer frequency: 400.06 MHz).

The NMR spectra obtained in this work, which were used to confirm molecular structure, were mostly consistent with that reported in literature for D.E.N. 431,[135,136] RDGE[137] and PAC-M.[10,138] Some inconsistencies were observed between the spectra reported in this work and those in literature, however inconsistencies were also noticeable between the differing reports within literature.[135,136] These inconsistencies were likely related to impurities in the components, as typically epoxy manufacturers provide an expected EEW range, which is above nominal EEW.[139] The preference for utilising less pure materials in industrial applications is driven by reduced cost and increased availability. Alternatively, in the case of PAC-M, variation in spectra can be attributed to relative isomer concentration. For example, Didsbury compared the NMR spectra of solid wax PAC-M from Sigma Aldrich to a liquid sample from Air Products and reported variation in peak intensity and position.[10]

4.2.2 Epoxide Equivalent Weight and Stoichiometry Calculations

System stoichiometry was an independent variable of particular interest throughout this research and so accurate calculation of stoichiometry was essential. To determine the stoichiometry of the mixed epoxy amine systems, first the EEW of the reactant epoxies should be measured as this determines the relative number of curing agent active hydrogens (and therefore mass of curing agent) required to produce a given stoichiometry. As explained in Section 2.3.1, equivalent weight is simply the mass of material required to give 1 equivalent of functional groups, and theoretically, the nominal epoxy prepolymer equivalent weight can be determined using equation 2.1. Therefore, using RDGE as an example (M_w = 222.24 g mol^{-1}; functionality = 2) nominal EEW is 111.12 g mol^{-1} (222.24 / 2). However, as mentioned above, the measured EEW range provided by manufacturers is characteristically higher than nominal EEW, as there are typically impurities that affect EEW; OLIN quotes the EEW range of RDGE between 115 – 122 g/mol^{-1}. Therefore, a slightly greater mass of RDGE than would be expected from the nominal formulation is likely to be required to provide the necessary number of epoxy groups. While raw material manufacturers often provide an expected EEW range, and within industry the midpoint of the quoted range is often taken as the EEW, through inhouse titrimetric analysis, a more accurate measure of EEW can be determined.

Table 4.1 shows the mass of D.E.N. 431 and RDGE used, the titre required, and their respective EEWs determined using equation 2.1. It can be noted that there are two batches of RDGE as an insufficient mass of RDGE was originally obtained and more was required to carry out all proposed experiments. While both batches were obtained from the same supplier, it was important to determine the EEW of each batch independently to identify any variations between the two, and thus recalculate stoichiometry, enabling consistency between experiments.

Table 4.1: EEW of D.E.N. 431 and RDGE determined titrimetrically.

Epoxy	Repeat	Epoxy Mass / g	Titre / cm^3	EEW / g mol^{-1}	x̄ / g mol^{-1}
D.E.N. 431	1	0.0992	5.54	179.1	
	2	0.0984	5.47	179.9	
	3	0.106	5.93	178.8	179.2 ± 0.5
RDGE – "Batch 1"	1	0.1038	8.94	116.1	
	2	0.1025	8.78	116.7	
	3	0.105	8.99	116.8	116.5 ± 0.3
RDGE – "Batch 2"	1	0.1058	9.04	117.0	
	2	0.0954	8.1	117.8	
	3	0.0992	8.4	118.1	117.6 ± 0.5

D.E.N. 431 had a measured EEW of 179.2 ± 0.5 g mol^{-1}, falling close to the upper bound of the manufacturer's expected range (172 – 179 g mol^{-1}). RDGE 'batch 1' had an EEW of 116.5 ± 0.3 g mol^{-1}, falling within the manufacturer's expected range (115 – 122 g mol^{-1}). RDGE 'batch 2' had an EEW of 117.6 ± 0.5 g mol^{-1}, falling within the manufacturer's expected range (115 – 122 g mol^{-1}). There was a very slight, but statistically significant difference in the EEW of RDGE between the two batches, highlighting the importance of measuring EEW for accurate determination of stoichiometry. Given both D.E.N. 431 and RDGE displayed measured EEW higher than theoretical nominal EEW, this indicates the presence of high molecular weight impurities or incomplete functionalisation. This is in agreement with Section 4.2.1, which also suggested the presence of impurities in the epoxies.

Using the measured individual EEWs (Table 4.1), 1:3 D.E.N. 431:RDGE mixture EEW ($EEW_{mixture}$) was calculated as follows:

$$EEW_{mixture} = \frac{100}{\left(\frac{wt\ RDGE}{EEW\ RDGE}\right) + \left(\frac{wt\ D.E.N.431}{EEW\ D.E.N.431}\right)} \ . \qquad 4.1$$

PAC-M of purity >99% was utilised, but assumed to be pure and so AHEW was calculated as 52.59 g mol^{-1}, determined using equation 2.2. Using this and the EEW$_{\text{mixture}}$, the relative mass required to formulate the two stoichiometries (Equation 2.3) used in this research (35% and 100%) was determined (Table 4.2). The relative masses displayed in Table 4.2 were calculated using the EEW of RDGE "batch 2". As the majority of systems produced throughout this research were synthesised from this batch, only these masses have been presented.

Table 4.2: Mass of each component at 35% or 100% stoichiometry in a 50 g mix.

Stoichiometry / %	Component Mass / g					
	D.E.N. 431	RDGE ("Batch 2")	PAC-M	Accelerators		
				DMP-30	1-MI	2-E-4-MI
35	10.94	32.81	6.26	0.96	1.37	0.68
100	8.87	26.62	14.51	-	-	-

4.2.3 T_g of D.E.N. 431, RDGE and PAC-M

For epoxy resins and curing agents to mix and subsequently react, reaction temperature must exceed component T_g (and T_m). Therefore, DSC was carried out on D.E.N. 431, RDGE and PAC-M independently to determine component T_g (Table 4.3) and establish the practical lower temperature limits required to induce curing.

Table 4.3: T_g of D.E.N. 431, RDGE and PAC-M.

Component	T_g / °C
D.E.N. 431	-8.5
RDGE	-40.0
PAC-M	-10.3

Throughout this research, systems were cured at 25 °C (ambient lower), 35 °C (ambient higher) or 80 °C (post cure). As all reaction temperatures exceed all component T_g's (D.E.N. 431 = -8.5 °C, RDGE =

-40.0 °C, PAC-M = -10.3 °C), the temperature range applied to samples in this research was therefore sufficient to allow curing to begin.

4.3 Chapter Conclusions

This short chapter focused on the characterisation of the individual system components, determining EEW, T_g, and confirming molecular structure. Such information underpins all further work reported in this thesis.

The structure of reagents utilised in this work (D.E.N. 431, RDGE, and PAC-M) were confirmed through solution-state NMR. The NMR spectra aligned with published literature, and the determined structures matched the industrial specifications. D.E.N. 431 and RDGE EEW were determined titrametrically to be 179.2 ± 0.5 g/mol^{-1} and 116.5 ± 0.3 (batch 1) to 117.6 ± 0.5 g/mol^{-1} (batch 2), respectively, falling within the manufacturer expected range. This importantly allowed for the accurate determination of system stoichiometries (100% or 35%). The lower temperature reaction limit applied in this work (25 °C cure) was shown to exceed component T_g's, indicating the applied temperature range was sufficient to induce curing.

Chapter 5

The Influence of Cure Conditions and Stoichiometry on the Surface and Bulk Properties of Epoxy Resin Coatings

Some of the work comprising this chapter has been published as: C. Bannister, A. Guy, R. Mihaylova, J. Orgill, S. Burg, A. Parnell, R. Thompson. *RSC Advances,* 2022, **12**, 28746-28754.

5.1 Chapter Introduction

While thermoplastic interface chemistries have been extensively studied[71,140,141] and previous work has investigated epoxy-substrate interfaces,[54,55,142–144] epoxy-epoxy interfacial chemistry remains less documented and consequently the causes of these intercoat adhesion failures in two coat systems are not fully understood. Epoxy-epoxy interface adhesion is hypothesised to be influenced by first coat surface properties. During practical application, cure conditions (induction time, ambient temperature and ambient relative humidity, RH) are often variable, and the impact on surface properties not fully characterised. Some authors suggest that roughness and surface energy are important for adhesion.[74–77] However, while these properties may contribute towards adhesion, others regard these as quite weak adhesive effects and instead propose that surface chemistry and the ability to form an interpenetrating network are more relevant.[79,80] Consequently, if the latter is shown to be true, for strong adhesion between layers of epoxy, it is thought that some interdiffusion between the first and second layers must occur, so that the cross-linked structure propagates across the interface. [65–67] Roche and Bentadjine showed how epoxy-diamine prepolymers can form an interphase with a metallic substrate *via* metallic ion interdiffusion to form organometallic complexes, and that the resulting interphase properties varied dependent on substrate nature, diamine nature and cure cycle.[54] This demonstrates that diffusion into uncured epoxy is possible, but it remains less clear whether uncured epoxy can diffuse into ambient-cured epoxy resin first coat.

This chapter explores the impact of stoichiometry, cure conditions and the interplay of cure conditions (induction time, RH, temperature) on first layer epoxy systems prior to overcoating and post curing, by systematically changing these variables. By doing this, the effects of these variables on surface or bulk properties can be determined and the potential implications on epoxy-epoxy intercoat adhesion identified. Subsequent chapters will then go on to directly characterise interphase width and properties as a function of these same variables thus allowing any correlations between cure conditions, stoichiometry, and interphase formation to be identified.

5.2 Results & Discussion

5.2.1 The Impact of Induction Time on the Extent of Carbamate Formation in Epoxy Resins

5.2.1.1 Quantification of Surface Layer Formation

In the systems used, amine carbamate forms when PAC-M reacts with carbon dioxide at the film-air interface. Carbamate uses up amine active hydrogen functional groups and is non-reactive to epoxy groups, and therefore is often associated with interlayer adhesion failure in industrial systems. By introducing an induction time, carbamate formation is expected to reduce as it improves amine-epoxy compatibility[145] and increases bulk viscosity, therefore decreasing the potential for random surface migration of PAC-M.[43] In addition, as H_2O is a catalyst for amine carbamation (Section 2.3.2), decreasing RH is expected to reduce carbamate formation, and consequently in industrial application attempts are made to maintain RH at < 50%.

Carbamate surface formation was quantified as a function of stoichiometry, induction time, and RH using gravimetric analysis to determine the influence of these variables on extent of carbamation in the systems studied. Gravimetric analysis was chosen for its simplicity, ease, and expeditious data generation, making it a practical and efficient method for the measurement of carbamate formation. Films of 100% and 35% stoichiometry were produced with a < 0.5- or 15-minute induction time at 40 or 80% RH. As carbamate is water soluble, the mass loss following surface wiping with D_2O provided a simple measure of the extent of surface layer formation (Table 5.1). D_2O was used rather than H_2O so that removed surface residue could be analysed using NMR spectroscopy.

Wiping samples to remove carbamate revealed no detectable change in mass (> 5 x 10^{-5} g) for 100% stoichiometry coatings that were allowed to cure at 25 °C, 40% RH (Table 5.1). It is important to note that of the total sample mass (~5 g), approximately 80% was attributed to the substrate. In addition, considering that the change in mass being recorded originates solely from a surface reaction of the sample, the expected change in mass would be inherently small. However, at 80% RH there was a detectable mass loss, and the inclusion of an induction time to the film (100% stoichiometry system, 80% RH) significantly reduced this mass loss. This highlights the prosed impact of induction time: the pre-reaction of amine and epoxy prior to casting to increase mixture viscosity and therefore decrease the potential of amine bulk-to-surface migration, and thus amine-carbamate formation. While 80% RH exceeds what is specified in industrial environments (typically < 50%), by using a slightly larger experimental range a more detailed characterisation was obtained and potential problems resulting from loss of climate control can be identified. These results are consistent with the works of Didas and Flaig who also reported that carbamation of amines tends to increase with increasing RH.[146,147] At 35% stoichiometry, no detectable carbamate was evident as mass loss from any system. The 35% stoichiometry systems had a much lower concentration of the carbamation suspectable compound, PAC-M, thus decreasing the potential for carbamate formation.

Table 5.1: Change in mass of the epoxy resin systems pre- and post-cleaning with D_2O.

Stoichiometry / %	**Induction Time / Mins**	**RH / %**	**Change in Mass / mg mm^{-2}**
100	<0.5	40	0.0 ± 0.0
100	15	40	0.0 ± 0.0
100	<0.5	80	1.3 ± 0.2
100	15	80	0.7 ± 0.2
35	<0.5	40	0.0 ± 0.0
35	15	40	0.0 ± 0.0
35	<0.5	80	0.0 ± 0.0
35	15	80	0.0 ± 0.0

5.2.1.2 Detection of Carbamate

While both qualitative visual inspection (Figure 5.1), and the quantitative gravimetric analysis (Table 5.1) were indicative of carbamate formation in high humidity, low induction time films, spectrochemical analysis techniques were also utilised to determine the presence of carbamate on the systems used. Two techniques were attempted: NMR and Transmission FT-IR.

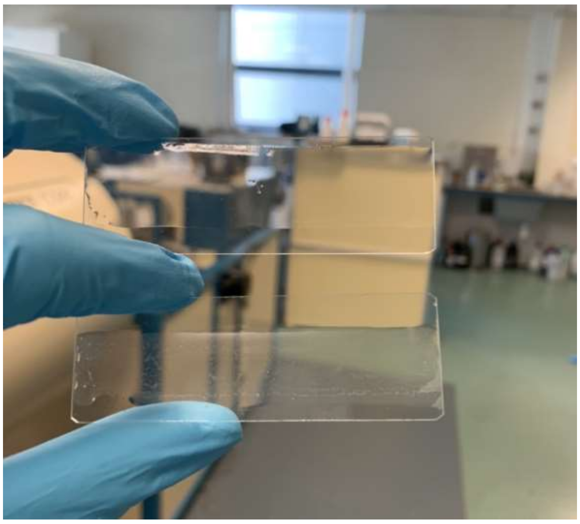

Figure 5.1: Image of films cast at <5% RH (top) and 80% RH (bottom).

Carbamate Detection using Solution State NMR

The D_2O system surface residue solution from Section 5.2.1.1 was retained for ^1H and ^{13}C NMR analysis. To determine the presence of carbamate (Figure 5.2) in this solution, the NMR spectra of the surface residue solution were compared to that of spectra of raw PAC-M and PAC-M carbamate (Figure 5.3 and Figure 5.4). The latter was obtained by exposing a sample of pure PAC-M to air for 24 hours and removing the subsequent carbamate formation *via* cleaning with D_2O.

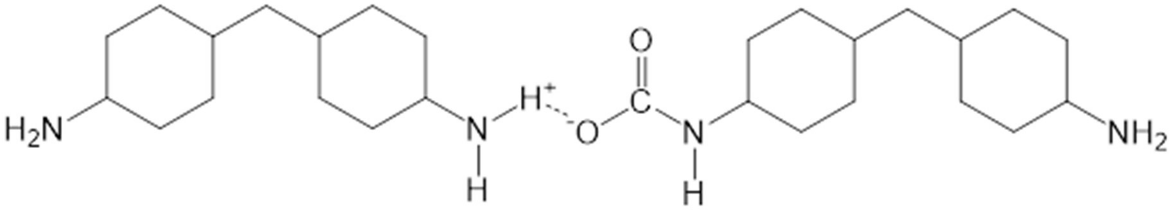

Figure 5.2: Structure of PAC-M carbamate salt.

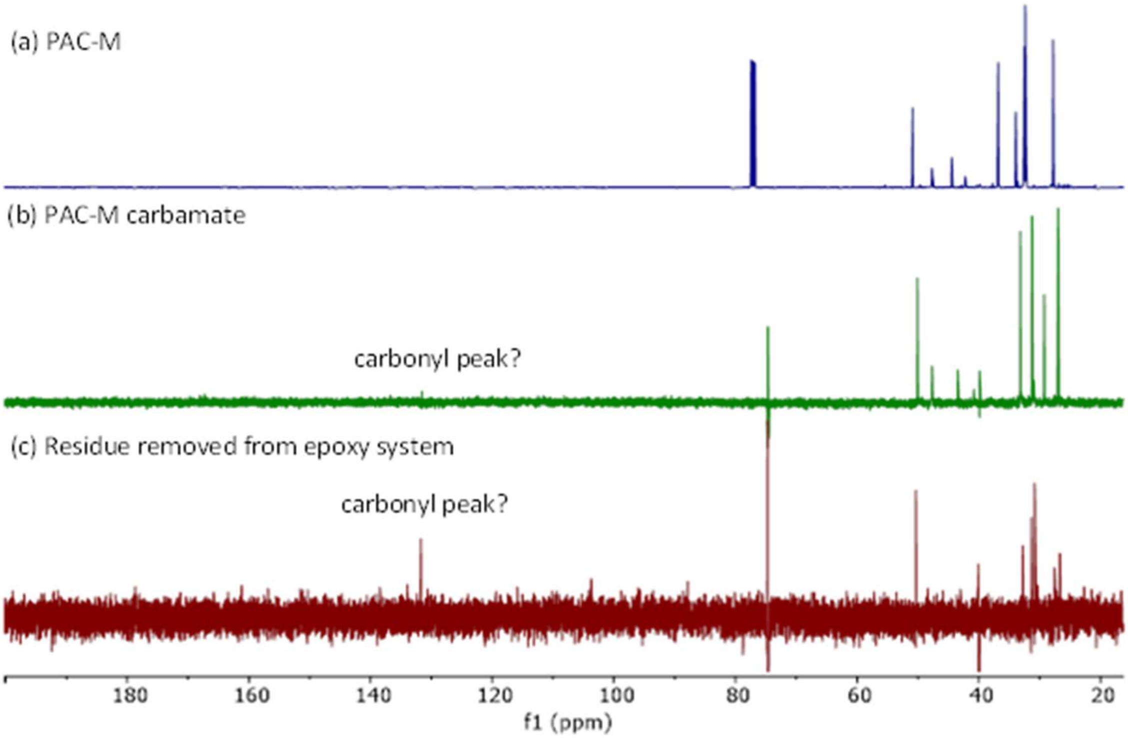

Figure 5.3: Stacked ^{13}C NMR spectra of (a) PAC-M (b) PAC-M carbamate (c) residue removed from epoxy system via cleaning with D_2O. (Solvent: $CDCl_3$ (PAC-M), D_2O (carbamate, residue). Spectrometer frequency: 100.6 MHz (PAC-M), 150.7 MHz (carbamate, residue)).

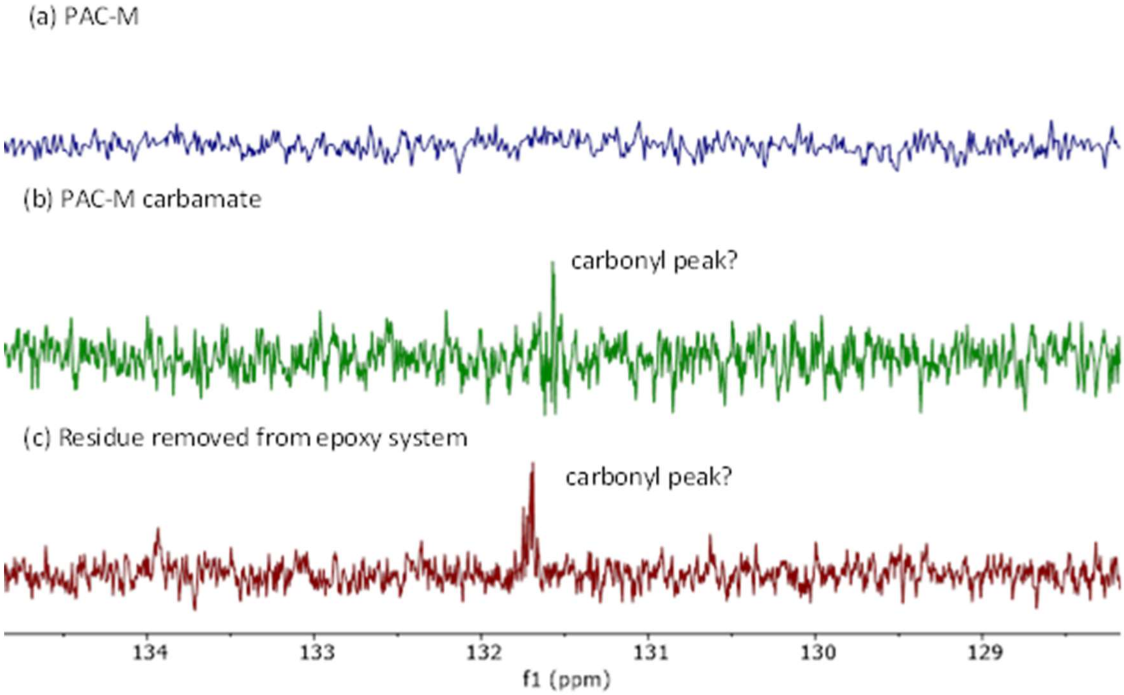

Figure 5.4: Stacked ^{13}C NMR spectra of (a) PAC-M (b) PAC-M carbamate (c) residue removed from epoxy system via cleaning with D_2O, focused on the peak associated with the carbonyl group. (Solvent: $CDCl_3$ (PAC-M), D_2O (carbamate, residue). Spectrometer frequency: 100.6 MHz (PAC-M), 150.7 MHz (carbamate, residue)).

Figure 5.3 displays the ^{13}C NMR spectra of PAC-M, PAC-M carbamate and the residue removed from the 100% stoichiometry, 80% RH, <0.5-minute induction time film. The latter was selected as it produced the greatest change in mass during gravimetric analysis (Table 5.1), and so was most likely to produce higher intensity carbamate-associated signals. In Figure 5.3, it is observed that in the PAC-M spectra, the peaks corresponding to the aliphatic ring (Figure 5.5; 27 - 37 ppm) exhibit a slight upfield shift in comparison to the PAC-M carbamate and residue spectra. This suggests the occurrence of chemical reaction. However, it's important to note that variations in solvent composition (D_2O or $CHCl_3$) can also contribute to shifts in peak locations. A small peak at ~132 ppm is seen in the ^{13}C NMR spectra of both the PAC-M carbamate and the system surface residue but not in the PAC-M NMR spectrum (Figure 5.3). This peak could be indicative of the carbonyl group present in carbamate given it is unique to the structure of carbamate (Figure 5.2) and is not present in the PAC-M spectrum. However, peak intensity is quite low (Figure 5.4), as typically carbonyl signals are quite difficult to detect using ^{13}C NMR spectroscopy, and literature tends to assign carbonyl peaks higher at ~ 160 ppm.[148] Therefore, it is difficult to definitively conclude the presence of PAC-M carbamate using this technique. PAC-M carbamate could not be detected using the corresponding ^{1}H NMR spectra shown in Figure 5.6, instead suggesting little difference between the samples.

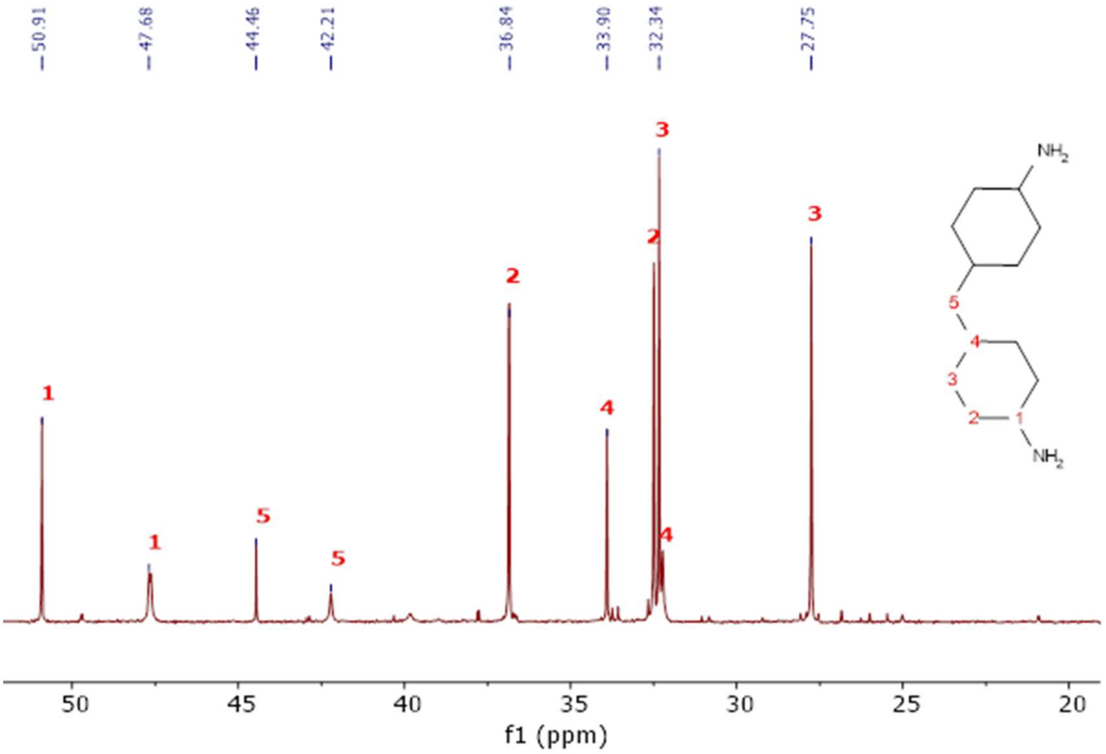

Figure 5.5: ^{13}C NMR spectrum of PAC-M. (Solvent: $CDCl_3$. Spectrometer frequency: 100.6 MHz).

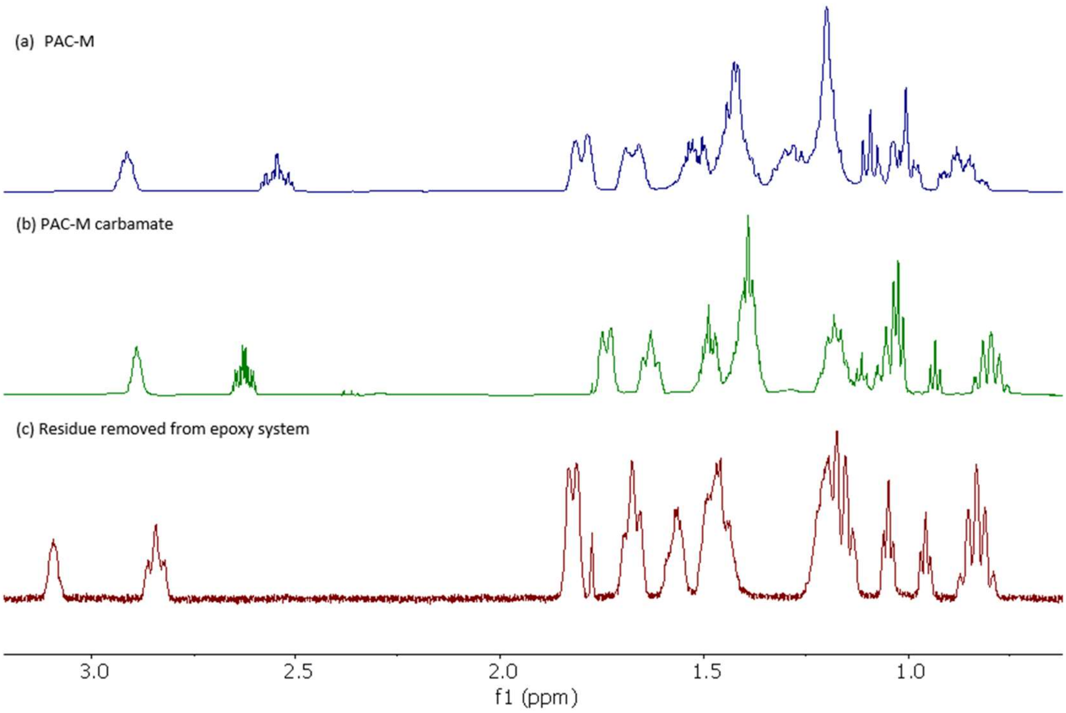

Figure 5.6: ^{1}H NMR spectra of (a) PAC-M (b) PAC-M carbamate (c) residue removed from epoxy system via cleaning with D_2O. (Solvent: $CDCl_3$ (PAC-M), D_2O (carbamate, residue). Spectrometer frequency: 400.06 MHz (PAC-M), 599.26 MHz (carbamate, residue)).

Carbamate Detection using ATR FT-IR

IR spectra of PAC-M and PAC-M carbamate were obtained using ATR FT-IR analysis (Figure 5.7). The spectra were then compared to allow for the identification of peaks unique to the PAC-M carbamate spectrum relative to the PAC-M spectrum. These peaks could then be used as a PAC-M carbamate 'fingerprint', allowing for the detection of PAC-M carbamate in the investigated epoxy systems.

The spectrum of the PAC-M carbamate revealed a distinctive peak at approximately 1479 cm^{-1}, absent in the PAC-M spectrum. Previous studies have assigned the COO^- bond of amine carbamate to this region and so this peak could be evidence of carbamation.[149,150] Therefore, the surrounding region was magnified (arrow, Figure 5.7) and following a similar protocol as with the NMR characterisation, the expansion compared to the spectrum of a film cured at high RH (Figure 5.8), "System A". Peaks were normalised to relative intensities using the C-N stretch at ~1444 cm^{-1}. While the peak associated with the C-N stretch in System A may have undergone alterations due to the epoxy-amine reaction, it remains the most viable option for normalization within the scope of the study.

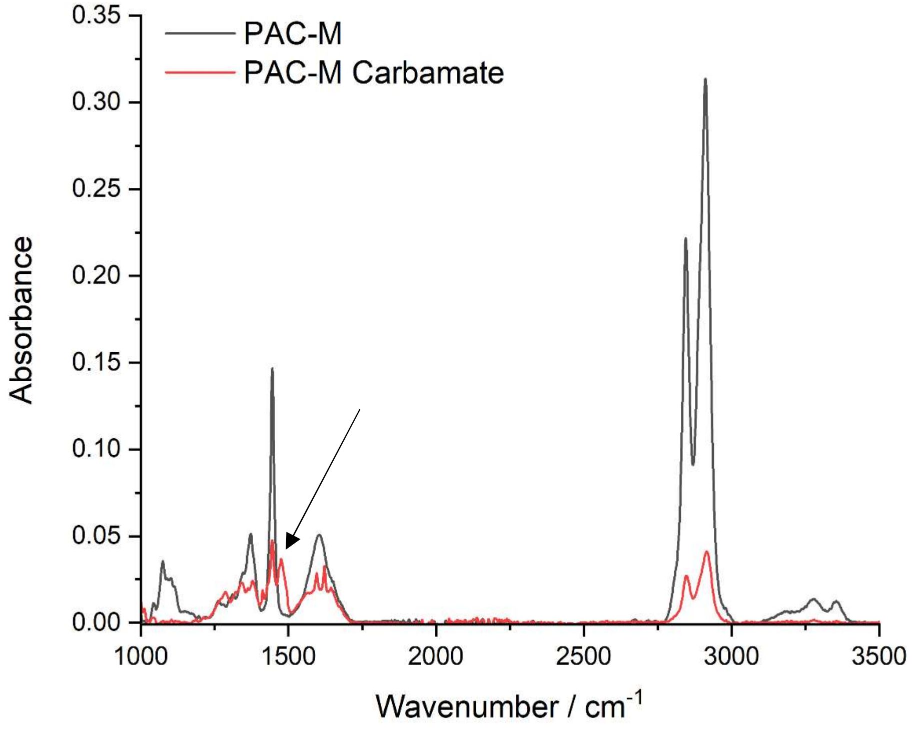

Figure 5.7: FT-IR spectra of PAC-M and PAC-M carbamate.

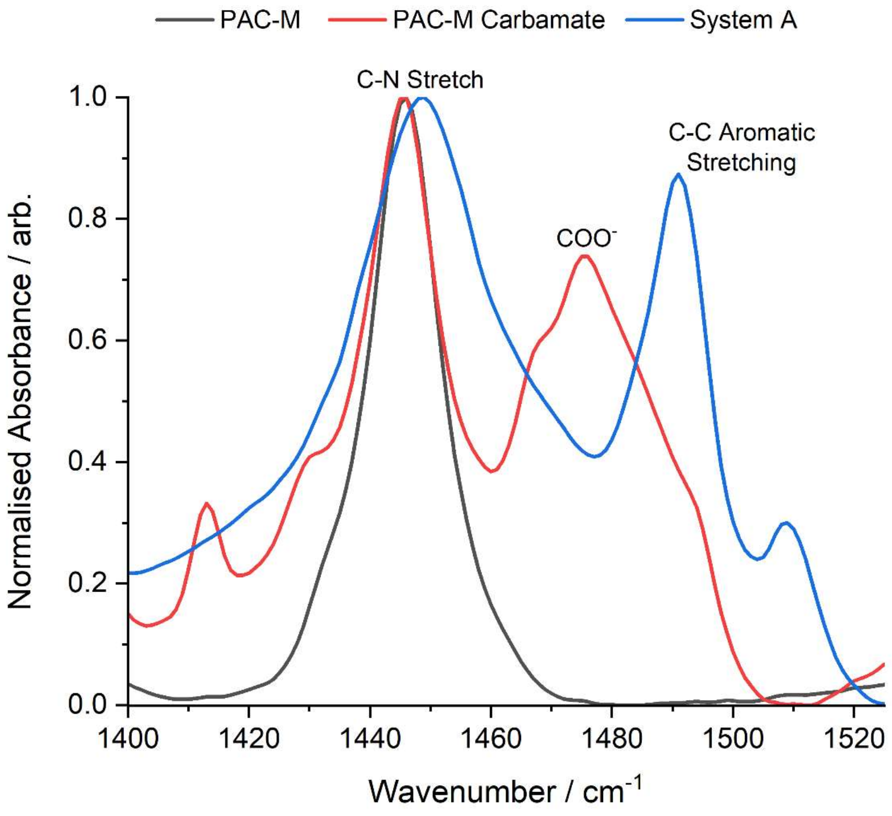

Figure 5.8: Normalised FT-IR spectra of PAC-M, PAC-M carbamate, and System A.

A carbamate peak (~1479 cm^{-1}) in the spectrum of the surface residue removed from the system cured at high RH would be expected to be of smaller intensity than that seen in the PAC-M carbamate. However, it is not at all visible in 'system A' as it is covered by a peak at ~1491 cm^{-1} associated with C-C aromatic stretching of the epoxy components (Figure 5.8). Therefore, for the systems investigated, FT-IR did not provide direct evidence of carbamation.

For completeness, 'System A' (100% stoichiometry film, 80% RH, <0.5-minute induction time) was compared to that of a system of identical composition but cured under a nitrogen atmosphere, for which the formation of carbamate is highly unlikely (Figure 5.9). However, as is shown in Figure 5.9, the IR spectra are near identical indicating that the amount of carbamate formed on 'System A' was very low, in agreement with the NMR spectra. As FTIR is not very surface specific and will measure the average composition over a few microns, results suggest that any carbamate layer (probed by FTIR) is thin on the micron scale.

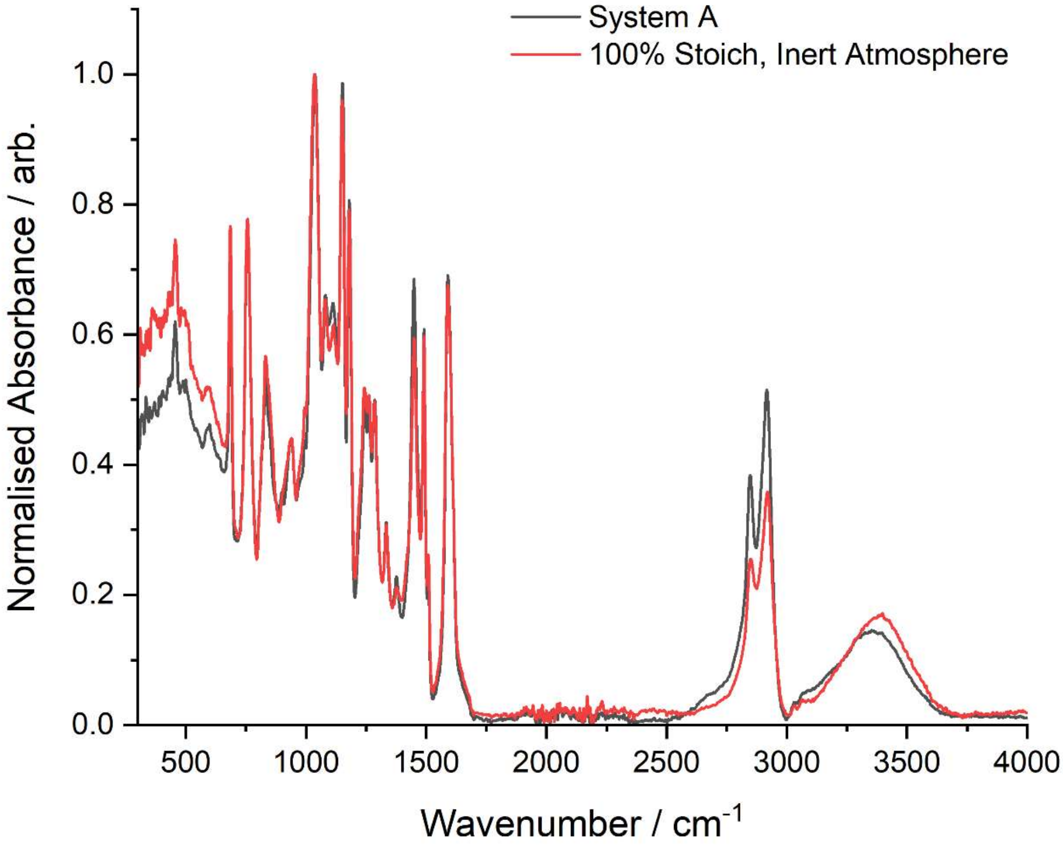

Figure 5.9: Normalised FT-IR spectra of System A and a 100% stoichiometry system cured in an inert atmosphere.

5.2.1.3 The Impact of Induction Time, Stoichiometry, and Cure Temperature on System Viscosity

Induction time was hypothesised to increase mixture viscosity, and consequently decrease the potential for amine surface migration by allowing both the pre-reaction of amine and epoxy, and also thixotropic recovery;[151] the return to a more viscous state as sample dynamics change from agitated (stirring) to static (stirring stops). Using rheometry, the complex viscosity, η^*, of a material, defined as the measure of the total resistance to flow as a function of time at a single frequency, can be determined. By measuring epoxy system η^* over time, the change in viscosity over the first 15-minutes can be measured and thus the impact of induction time on system viscosity quantified. Figure 5.10 displays the complex viscosity of 100% and 35% stoichiometry systems cured at 25 or 35 °C, over time.

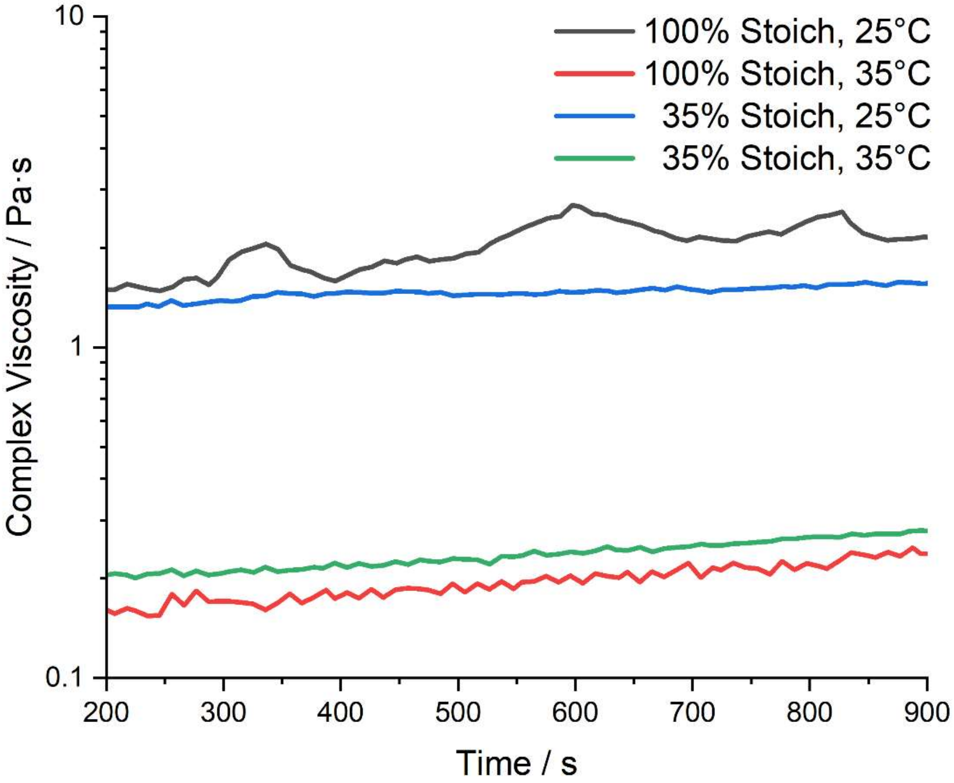

Figure 5.10: Complex viscosity of epoxy systems over time.

Figure 5.10 shows that as time advanced, viscosity increased slightly for all 4 systems, and is almost an order of magnitude lower at the higher cure temperature. By applying the Stokes-Einstein equation

(5.1) to this data set over a longer time scale, the influence of viscosity on diffusion coefficient, *D,* for systems with or without an induction time can be estimated.

$$D = \frac{k_B T}{6\pi\eta r} \tag{5.1}$$

where k_B is the Boltzmann's Constant, *T* is the absolute temperature and *r* is the radius of a spherical particle. For a Brownian particle, *D* can be used to determine the mean square displacement (MSD) and thus provide an estimate of the depth at which it is possible for amine to migrate to the surface over time. By deducting the MSD within the first 15-minute interval, it is possible to compare the depth at which amine can migrate to the surface as a function of induction time (Figure 5.11). Here it is assumed that the amine behaves as a particle of 1 nm radius.

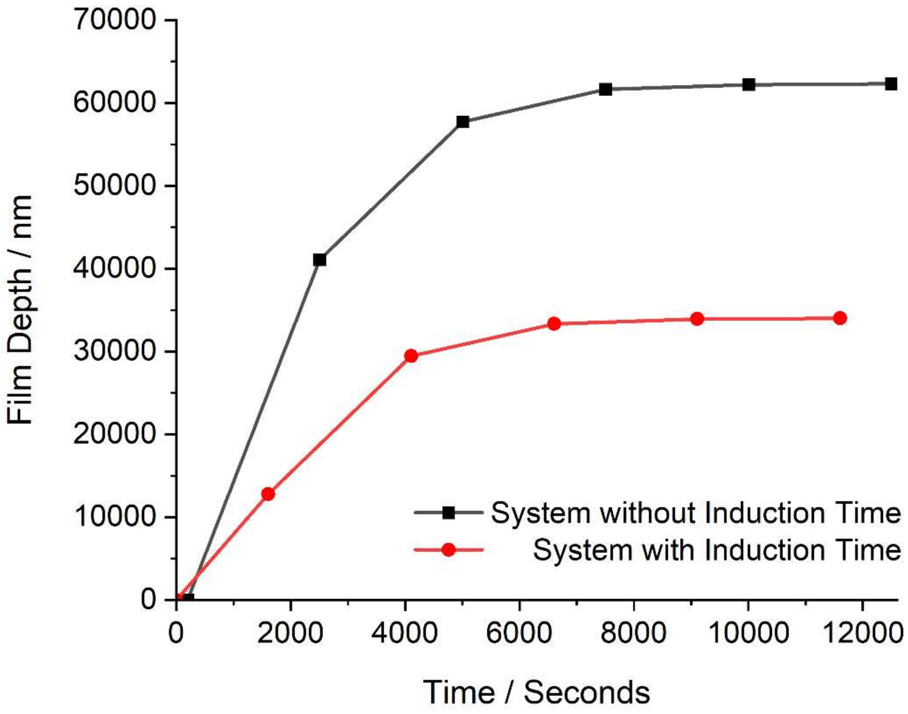

Figure 5.11: Estimation of the depth within the film from which amine can migrate to the surface over time, as a function of Induction time (system: 100% Stoichiometry, 35 °C, 40% RH).

Figure 5.11 predicts that the application of an induction time, and thus a reduction in the total amount of time over which the sample has low viscosity while in the film state, significantly reduced the total distance (MSD) capable of being travelled by an amine molecule within the film. Therefore, when an induction time is applied, a smaller proportion of amine can reach the surface *via* random migration, thus decreasing the amount of material capable of forming carbamate at the surface.

5.2.2 Film Surface Topography

5.2.2.1 Surface Rugosity and R_q

Interdiffusion, entanglement and crosslinking are proposed to be factors that influence epoxy-epoxy intercoat adhesion.[65–67] Surface wettability limits interdiffusion and entanglement as it concerns the ability of a liquid to spread and permeate cracks within a substrate. Therefore, as surface roughness influences wettability (Wenzel equation), it is important to characterise first coat surface roughness, as a function of cure chemistry and stoichiometry, to determine the effect on wettability and mechanism (Wenzel or Cassie-Baxter).[119,152]

Single layer, ambient cure films were produced according to section 3.2.2 and AFM QNM mode was used to probe surface properties and generate 10 x 10 µm images (Figure 5.12), 6 repeats per sample. Two measures of surface roughness, defined in Chapter 3, were used for analysis: R_q and rugosity.

As shown in Figure 5.13, the 35% stoichiometry systems had a significantly lower R_q and rugosity than the 100% stoichiometry systems. In addition, while increasing the cure temperature from 25 °C to 35 °C led to a decrease in R_q and rugosity at both stoichiometries, this effect was less pronounced in the 35% stoichiometry systems, particularly concerning R_q. According to Kendall, decreasing surface roughness should increase adhesion capability as it allows greater 'molecular contact'.[79] However, while the data points were significant within the precision of the AFM measurement, the rugosity never exceeded 1%, and films were relatively smooth with an $R_q < 12$ nm and no distinct features were observed on the µm scale (Figure 5.12). Therefore, while we cannot be certain, it is unlikely that a decrease in surface roughness of this magnitude would significantly impact second coat adhesion.

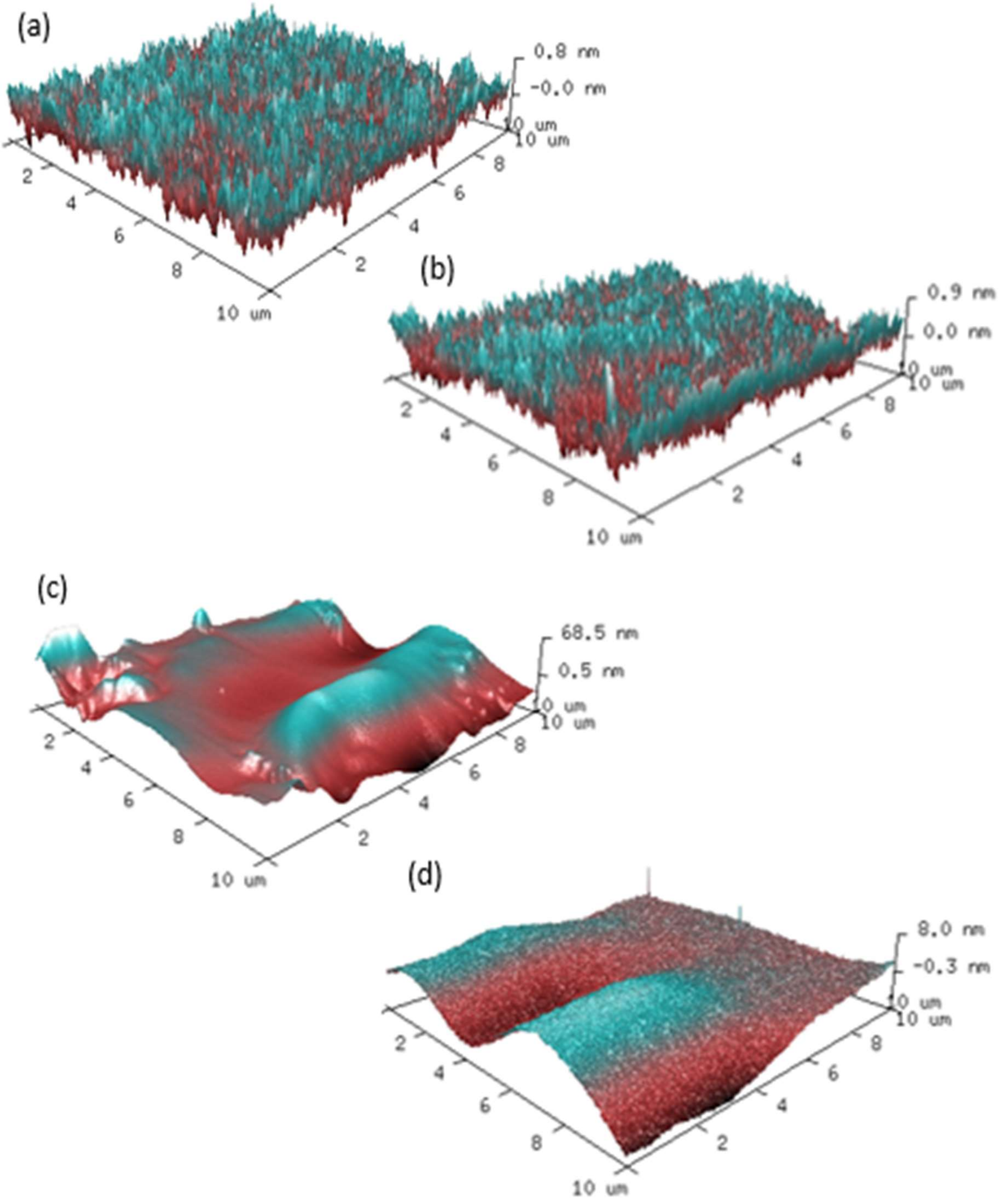

Figure 5.12: AFM images of films cured at (a) 35% stoichiometry, 25 °C (b) 35% stoichiometry, 35 °C (c) 100% stoichiometry, 25 °C (d) 100% stoichiometry, 35 °C. In each case, vertical scales have been optimised to highlight any surface features.

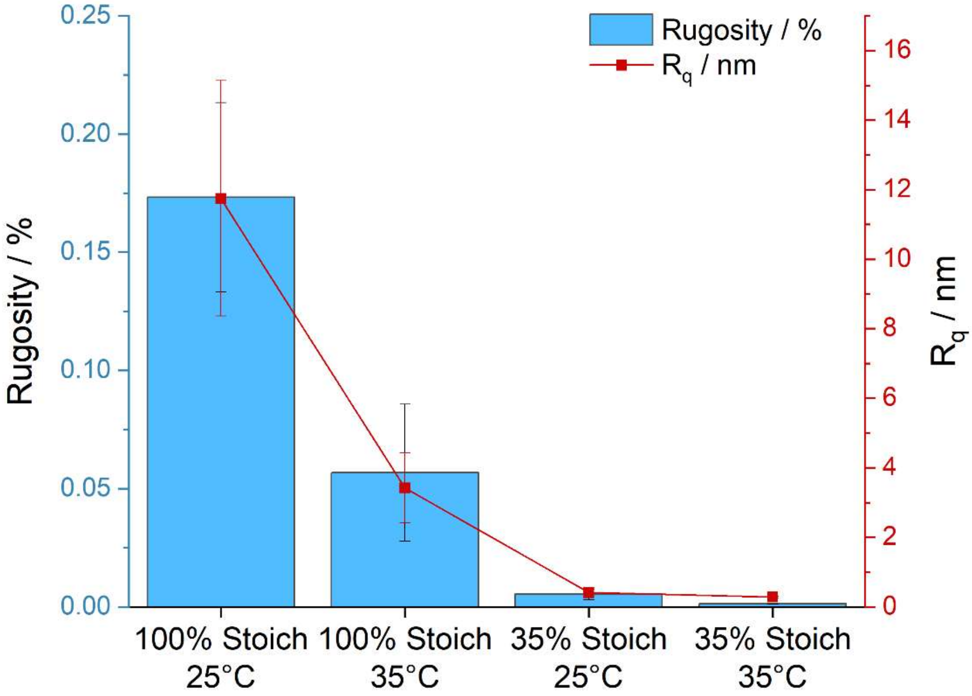

Figure 5.13: The surface roughness (R_q / nm) and rugosity of 100% and 35% stoichiometry systems cured at 25 and 35 °C, 40% RH.

Increasing RH and decreasing induction time significantly increased surface roughness (Figure 5.14; Figure 5.15) and maximum peak height (Figure 5.16). This is interesting as one may expect the mixture with the lower viscosity (due to a shorter induction time) to form a flatter surface under gravity. However, this increase was likely due to carbamate formation. The effect of induction time remained far more apparent at 80% RH compared to at 40%, consistent with the gravimetric analysis. In addition, the impact of increasing RH on roughness was more apparent in the 100% stoichiometry formulation than the formulation at 35% stoichiometry. The 100% system contains a greater proportion of primary amine groups that are susceptible to carbamation.

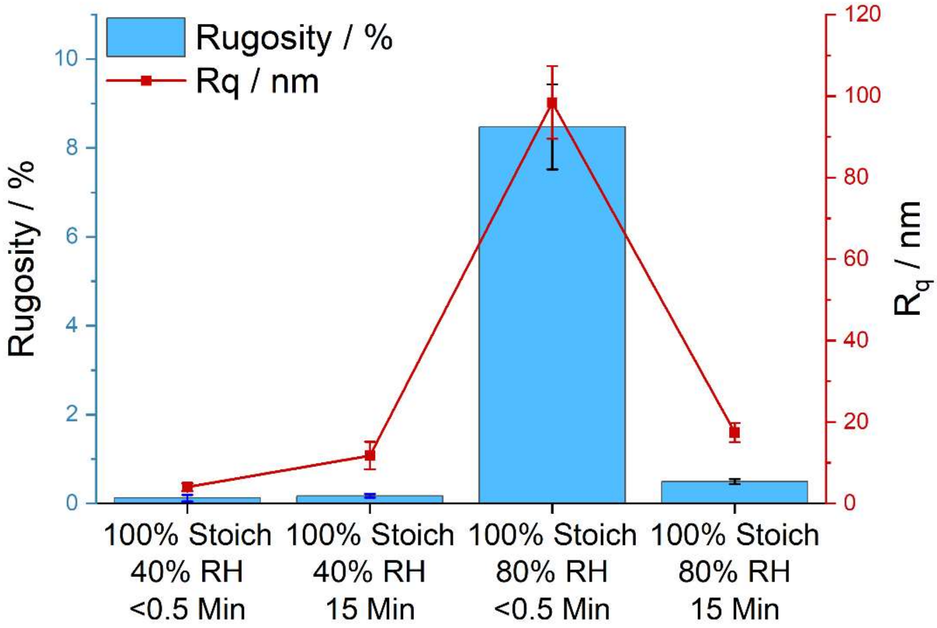

Figure 5.14: The surface roughness (R_q / nm) and rugosity of 100% stoichiometry systems cured at 40% and 80% RH, 25 °C, with a <0.5- or 15-minute induction time.

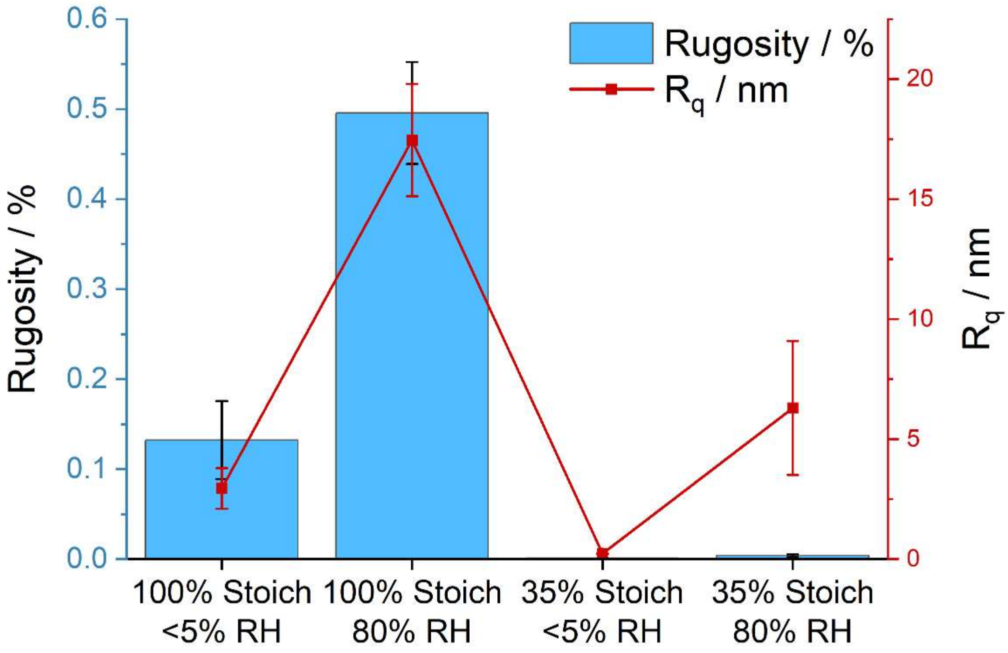

Figure 5.15: The surface roughness (R_q / nm) and rugosity of 100% and 35% stoichiometry systems cured at <5% and 80% RH, 25 °C.

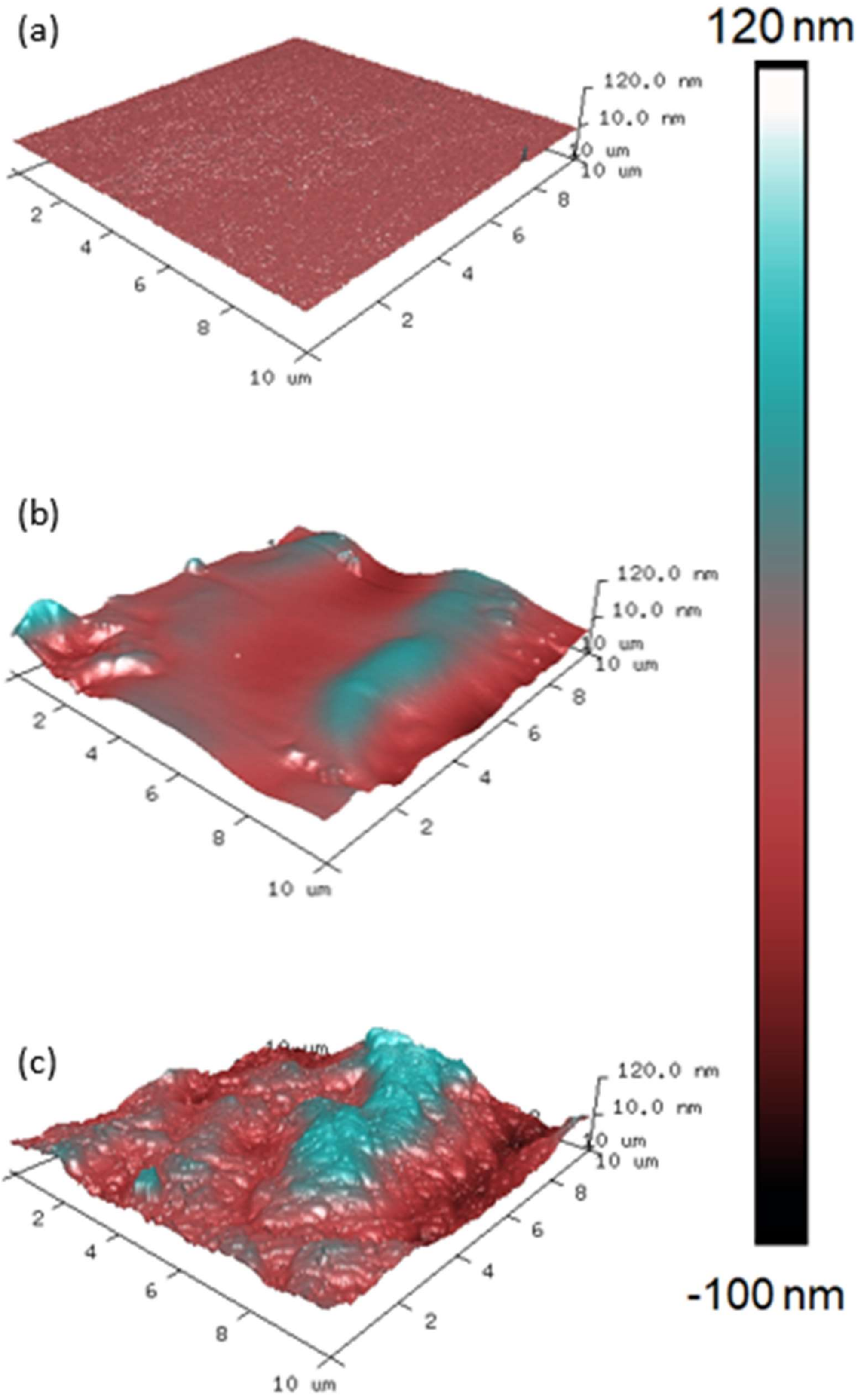

Figure 5.16: AFM Images of 100% stoichiometry films cured at (a) < 5% RH (b) 40% RH (c) 80% RH, temperature maintained at 25 °C. In each case, consistent vertical scales have been used to compare the variation in surface height.

The above AFM analysis indicates that it may be possible to detect early stages of carbamation using AFM; surface roughness increased when cure conditions were more favourable for carbamate formation. To confirm this, a 100% stoichiometry film was cured in an inert, nitrogen rich atmosphere (CO_2 free), where carbamation should be theoretically impossible, and its surface roughness compared to a same composition film cured in an ambient environment (CO_2 present). Figure 5.17 shows that system R_q and rugosity was lower in the film cured in an inert atmosphere were carbamation should be impossible, agreeing with the idea that carbamation increases surface roughness and is detectable using AFM.

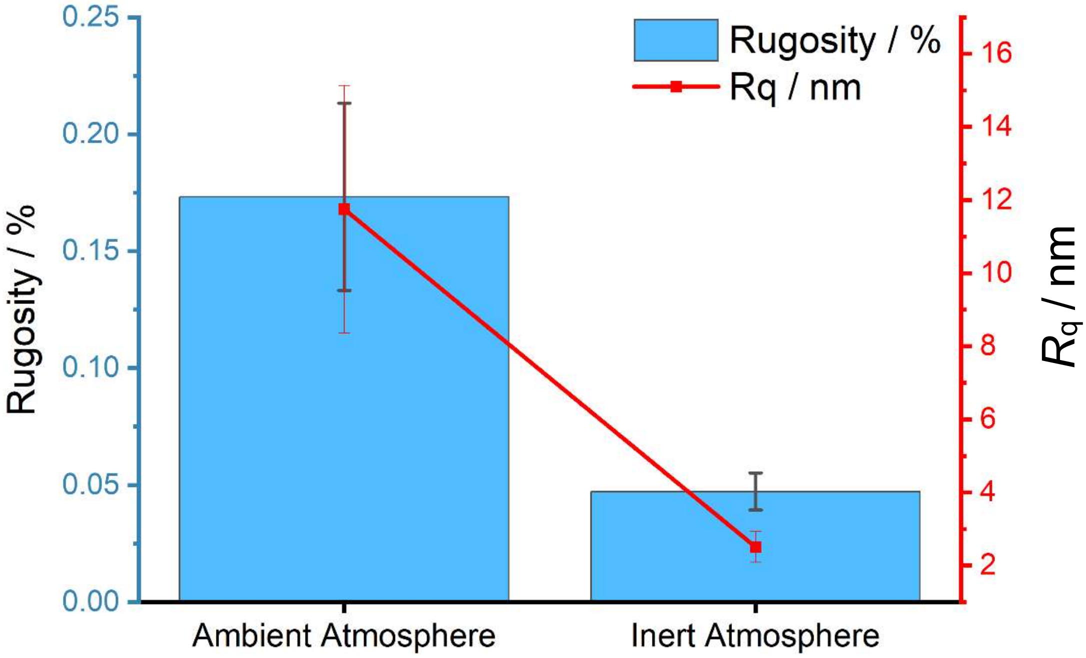

Figure 5.17: The surface roughness (R_q / nm) and rugosity of 100% stoichiometry systems cured in either ambient or inert nitrogen, rich atmospheres.

5.2.3 Film Surface Wettability

Surface wettability is a physicochemical parameter that is usually characterised by the contact angle of a fluid on a surface. In epoxy-epoxy interface formation, wettability translates to the ability of the second coat of epoxy (liquid) to spread upon the first coat (solid) during application and permeate any cracks that may be present in the first coat. An increase in surface wettability would increase the surface area for interdiffusion and thus interface formation. Therefore, contact angle analysis (CA) was used to characterise surface wettability as a function of stoichiometry and cure condition. Water contact analysis (WCA) is commonly used as a convenient measure of wettability, and therefore, water was generally selected as the probe liquid in this work, rather than the liquid second coat mixture. This allowed comparisons to be made with literature of studies on related materials. Figure 5.18 shows a comparison of the wetting behaviour of water and epoxy on 100% and 35% stoichiometry films.

Figure 5.18 shows that while there is a difference in the contact angle of the water and liquid epoxy droplet, both attain θ < 90°, and behave similarly. Therefore, water is an acceptable model for second coat surface wettability.

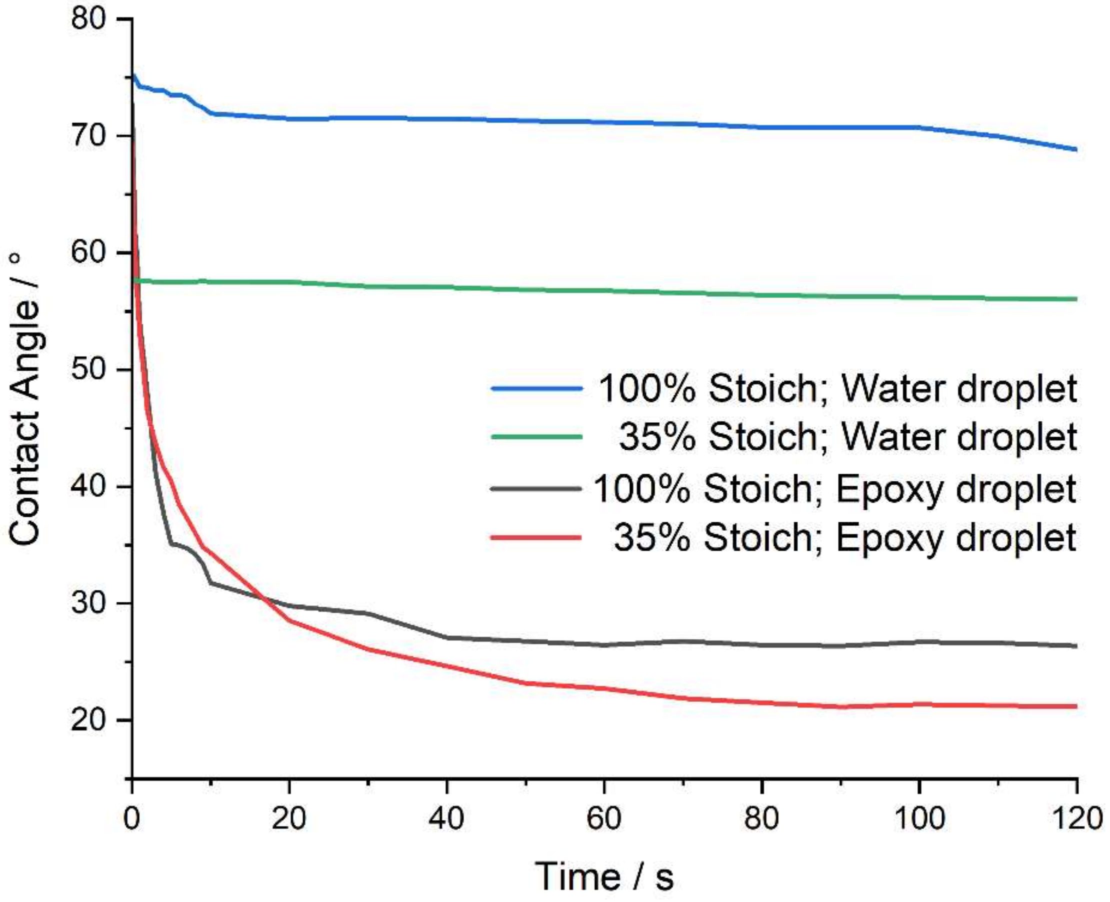

Figure 5.18: Advancing contact angle of water and liquid epoxy (same composition as the wetted surface) on the 100% and 35% stoichiometry systems. Cure processes were 25 °C and 40% RH.

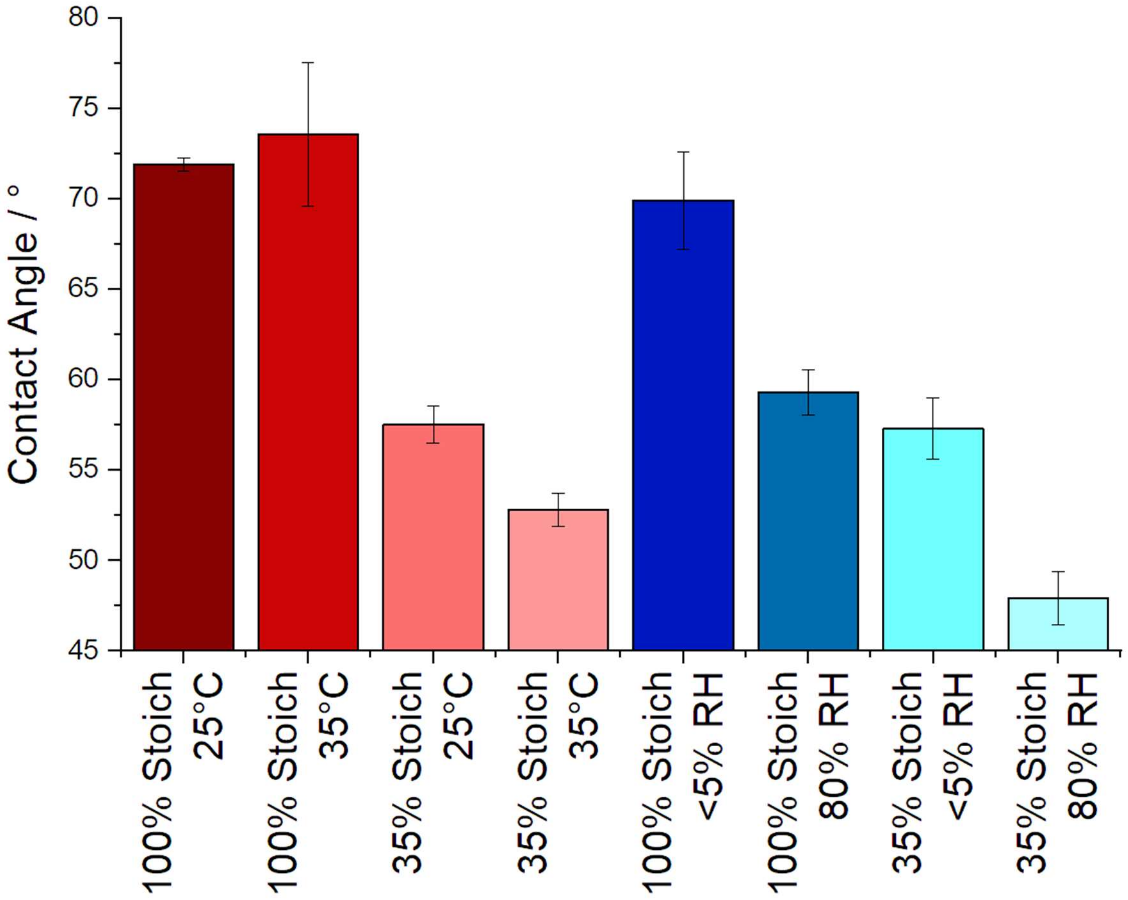

Figure 5.19: The average water contact angle over 120 seconds of each epoxy system and uncertainty. Cure processes were 25 °C and/or 40% RH unless otherwise stated.

Figure 5.19 shows the water contact angle of systems cured at varying stoichiometries and cure conditions. The most significant difference in surface wettability was that between the two stoichiometries, with the 35% systems being more hydrophilic than the 100% systems. This is interesting as the 35% stoichiometry system might be expected to be the more hydrophobic of the two stoichiometries given the 100% stoichiometry system would likely have a greater number of polar hydroxyl groups within its network. It is not clear why the 35% stoichiometry system displayed more hydrophilic behaviour. The two contributing factors toward surface hydrophobicity are surface chemistry and topography. Since all systems attained low roughness (Figure 5.13), it appears unlikely that this difference can be attributed to surface topography, instead suggesting surface chemistry as culpable. Perhaps anionic polymerisation leaves ammonium salts, providing the observed hydrophilicity. This would also explain why no mass loss was observed attributed to cleaning with D_2O (Table 5.1), as ammonium salts would likely be bound into some covalent structure, and so be insoluble in water. It is unclear how salt of this composition would affect interface formation. While it is known that carbamate salts inhibit the formation of strong epoxy-epoxy interfaces,[3,44–47] other salt compositions, including ammonium chloride, have been hypothesised to disrupt the noncovalent polar interactions within amine-cured epoxy matrices, facilitating plasticisation.[153] If this was to occur at the film surface, and should epoxy-epoxy interface forms *via* interdiffusion, plasticisation may enhance ease of second coat ingress. However, even if ammonium salt formation was detected on the samples in this work, discerning whether a change in plasticisation was solely attributed to salt formation or instead stems from an inherently different network structure, or perhaps a combination of both factors, poses a considerable challenge. Consequently, determining such nuances may be considered unrealistic using available analytical methods.

The cure temperature only significantly affected the water contact angles of the 35% stoichiometry films with an increase in cure temperature increasing hydrophilicity. However, when samples were cured under high RH, at both stoichiometries, the resulting film surfaces were more hydrophilic than those cured at lower RH. This increase in wettability may be due to the presence of water-soluble carbamate on the surface, as humidity promotes carbamation.[146,147] Alternatively, it may simply be that the absorption of water from the higher humidity atmosphere into the systems creates a more hydrophilic surface.

5.2.3.1 The Impact of Rugosity on Film Surface Wettability

As explained in section 5.2.2.1, surface rugosity impacts contact angle. Therefore, rugosity, measured using AFM, was used to estimate the impact of roughness on equilibrium contact angles using the Wenzel correction:

$$\boldsymbol{\cos\theta_{rough} = r\cos\theta_{smooth}} \tag{5.2}$$

where θ_{roug} is the contact angle measured on the real surface including roughness, and θ_{smoot} is what the contact angle would be for the same surface chemistry on a perfectly smooth film, and *r = (1 + rugosity / 100).*[119] For these films where contact angles are < 90°, contact angles decrease with increasing *r*. Figure 5.20 displays the water contact angle and Wenzel corrected contact angle on 100% stoichiometry systems cured at 0% and 80% RH. These systems were selected as they had the highest (80% RH: ~ 0.50%) and lowest (< 5% RH: ~ 0.13%) rugosity values. Application of the Wenzel correction showed that the change in WCA was typically < 0.1°, indicating that the difference in surface wettability was likely to be due to chemical differences rather than physical roughness.

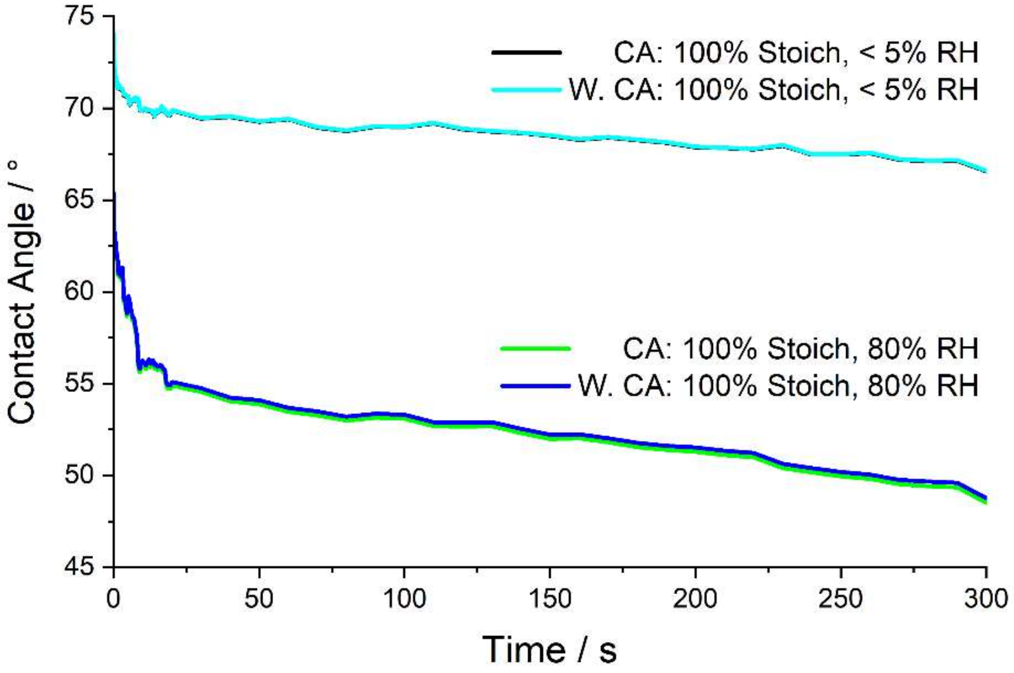

Figure 5.20: The Advancing contact angle (CA) and Wenzel corrected contact angle (W. CA) of water on 100% stoichiometry systems cured at 0 and 80% RH.

5.2.4 Film Surface Free Energy

Surface Free Energy (SFE) is a characteristic, thermodynamic property describing the state of equilibrium of atoms at a materials surface.[85] While some authors suggest the impact of SFE on intercoat adhesion as minimal,[79] others have shown it to have a significant impact.[76] Therefore, for the systems studied, SFE was estimated as a function of stoichiometry and cure condition using Zisman plots.

5.2.4.1 Zisman Plot Derived SFE of Ambient-Cured Epoxies

Zisman plots provide an estimation of SFE through the assumption that when the surface tension of the probe liquid is equal to or less than the surface energy of the solid, the contact angle will be zero (complete wetting). By plotting the cosine of a series of solvents' contact angles against their known surface tensions and extrapolating the plot out to the point where $\cos \theta = 1$ (i.e., theta = 0), the surface energy can be estimated. Surface tension values were obtained from literature. The contact angle of a range of solvents (water, glycerol, formamide, diiodomethane, ethylene glycol and 1,2-propanediol) were measured on a variety of films. Contact angle was taken at the point of steady state before the effect of evaporation, also known as the static contact angle. This was interpreted as at 10 seconds for all solvents except for glycerol (Figure 5.21), which has a higher viscosity and much lower volatility than the other liquids. In Figure 5.21, the contact angle of glycerol undergoes an initial rapid decrease over the first 5 seconds, attributed to the initial droplet-to-surface impact and gravity. Following this, the decrease in contact angle slows, eventually reaching a steady state at approximately 90 seconds. The use of initial or steady state contact angle for surface energy measurements is debated. Figure 5.21 suggests the plateauing contact angle would be more suitable for Zisman plot analysis as at this point, solvent contact angle has a linear correlation with respective surface tension. Zisman plots were generated for each system (Figure 5.22), and the surface energy and associated error calculated (Figure 5.23).

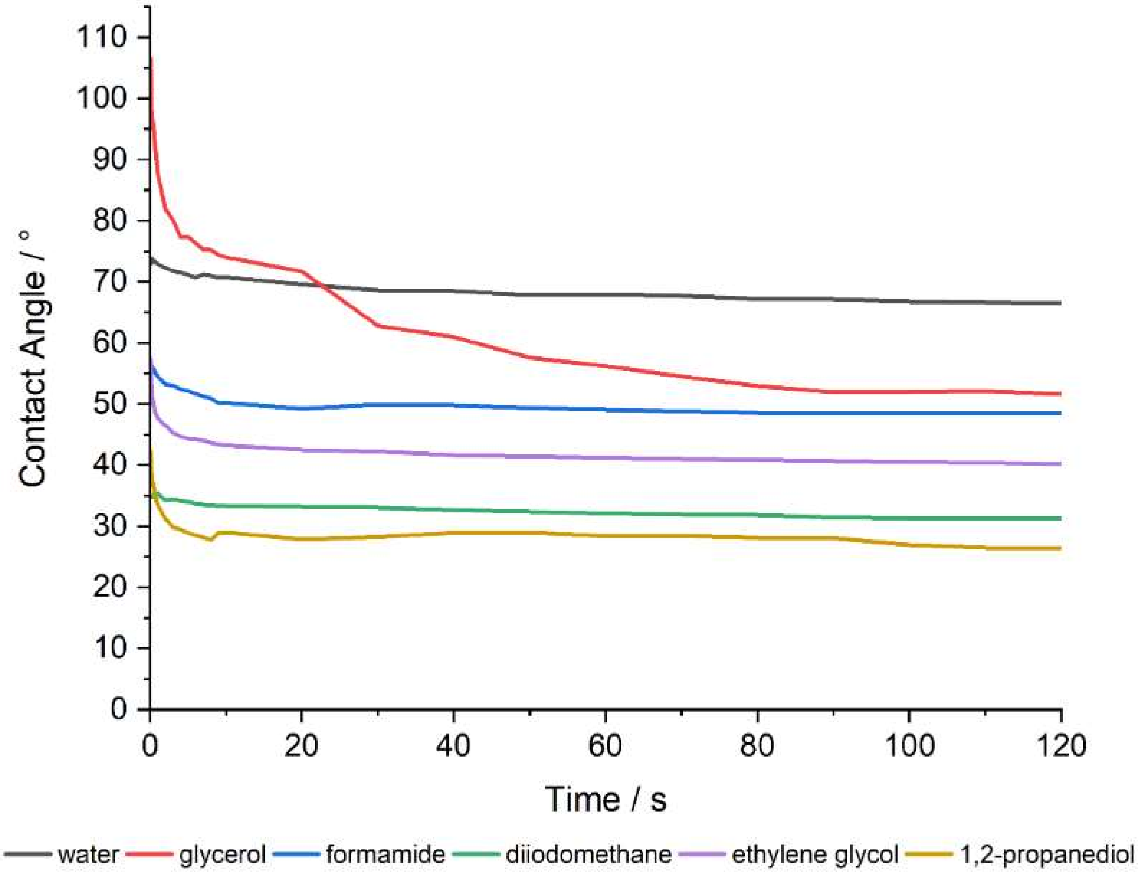

Figure 5.21: Advancing contact angle of a series of solvents over 120 seconds (system: 100% Stoichiometry, 25 °C, 40% RH).

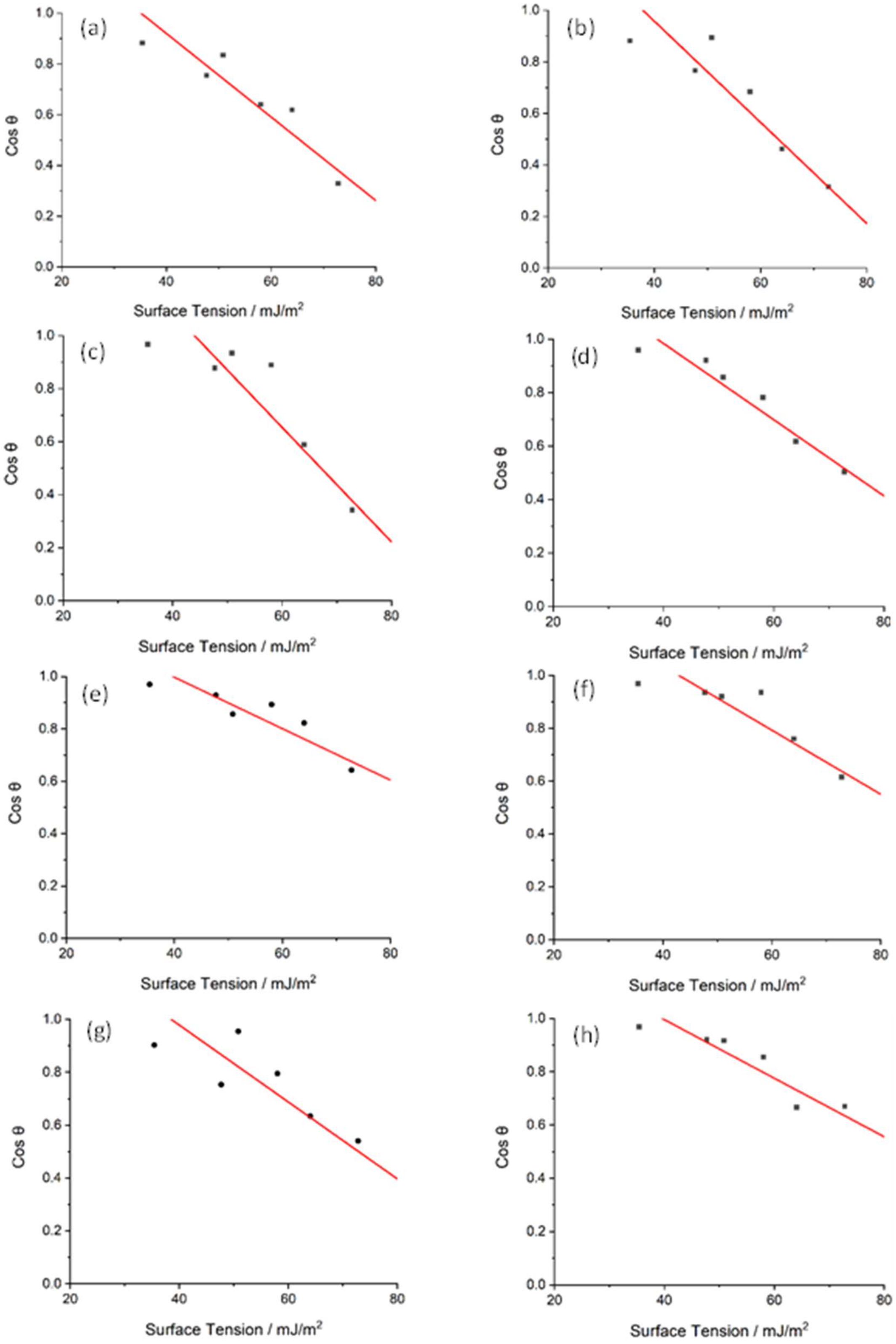

Figure 5.22: Zisman plots of the following systems (a) 100% Stoich, 25 °C, 40% RH (b) 100% Stoich, 35 °C, 40% RH (c) 100% Stoich, 25 °C, <5% RH (d) 100% Stoich, 25 °C, 80% RH (e) 35% Stoich, 25 °C, 40% RH (f) 35% Stoich, 35 °C, 40% RH (g) 35% Stoich, 25 °C, <5% RH (h) 35% Stoich, 25 °C, 80% RH.

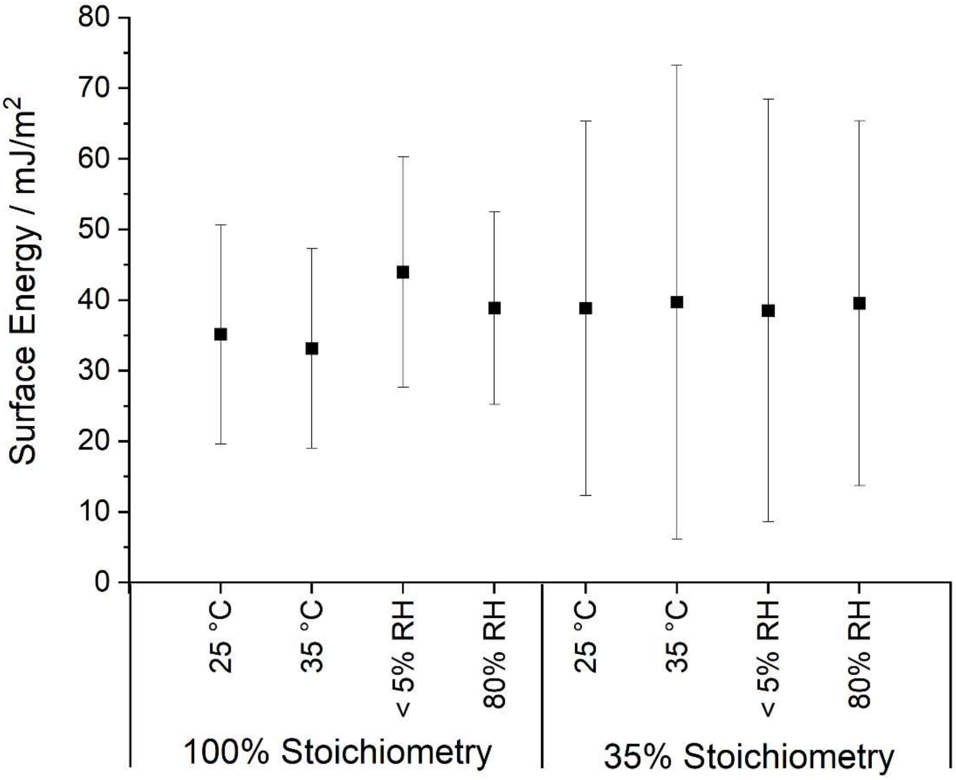

Figure 5.23: Surface energy of each system and associated error calculated using Zisman plots.

Figure 5.23 shows the SFE estimated from the Zisman plots of each system and respective propagated error. The propagated error of each SFE estimation was large compared to the relatively small differences in apparent SFE. Large, propagated error, attributed to poor fitting line correlation coefficient is typical of Zisman plots,[154,155] and consequently not often reported in literature. This is because Zisman plots estimate SFE based on a linear dependence of cos θ on surface tension, but the two are not always necessarily linear.[155] Therefore, the propagated error in the regression line can be quite high. Some authors also highlight the importance of uncertainty when evaluating SFE due to the extensive sources of possible error within the technique such as variation in droplet size, surface impurities, focal depth consistency, humidity, fitting consistency.[85] However, efforts were made to control these variables in these experiments.

Figure 5.23 suggests that variation in stoichiometry and cure conditions does not dramatically impact SFE and that the previously observed large variation in WCA (Figure 5.19) was likely due to water changing the surface rather than changes in SFE. This is highlighted in Figure 5.24 as the film cured at higher RH, and so more prone to water-soluble carbamate formation, caused a much greater decrease in the contact angle of water compared to all other solvents analysed. While water is commonly used as a fluid for contact angle measurements, there is some concern in amine-cured resins that water is unsuitable for SFE calculations as it may dissolve the carbamate. For the validity of surface energy calculation by contact angle analysis, it is essential that the probe liquid does not cause any change to the properties of the surface. Therefore, a second method of SFE estimation, using the Owens-Wendt model, was carried out and WCA data excluded.

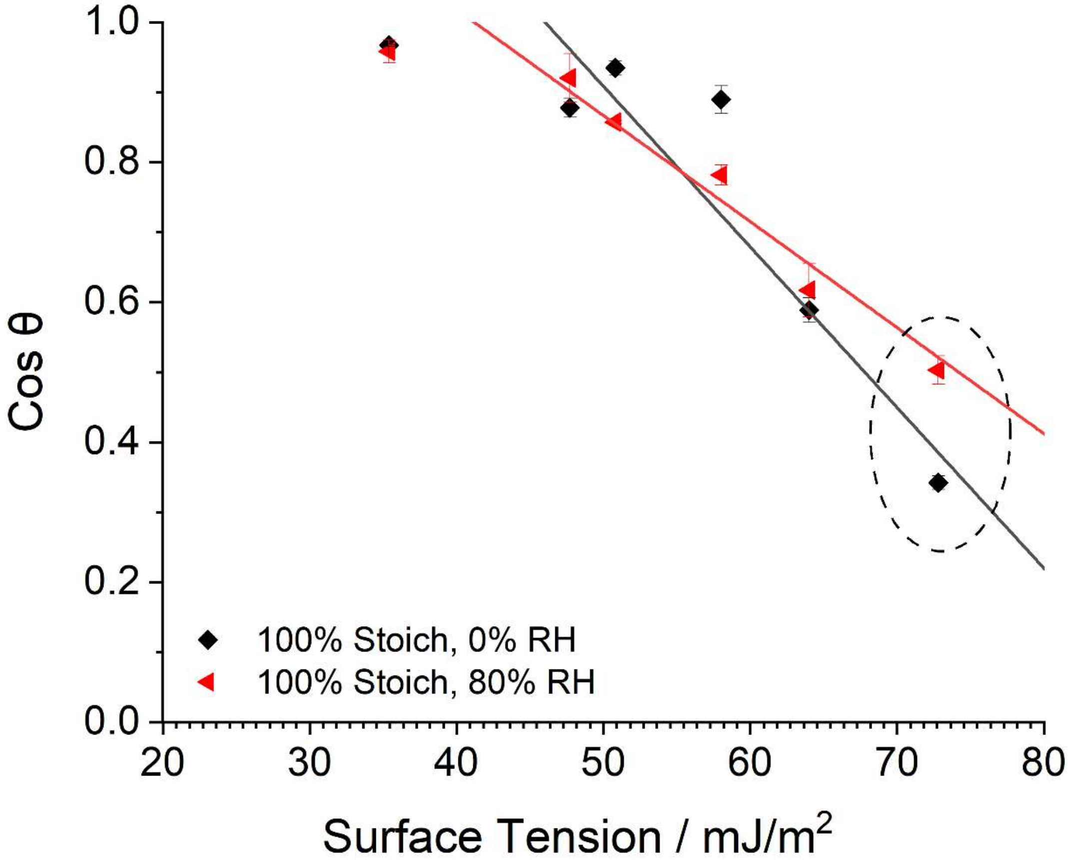

Figure 5.24: Zisman plot of the 100% stoichiometry system cured at <5% or 80% RH, 25 °C. The points associated with WCA have been circled.

5.2.4.2 Owens-Wendt Model Derived SFE of Ambient-Cured Epoxies

The Owens-Wendt model estimates SFE through determining and combining the polar and dispersive components of SFE based on the Berthelot hypothesis.[121] This was achieved by measuring the static contact angle of glycerol, formamide and diiodomethane using contact angle analysis and applying equation 3.7. Error propagation was determined according to the method of Rudawska *et al*.[85]

Figure 5.25 shows that variation in cure conditions had no significant impact on SFE. This agreed with the Zisman plot SFE analysis conclusions, indicating that the observed large variation in WCA was due to water changing the surface rather than changes in SFE. There is arguably a significant difference between the behaviour measured for all 35% samples and that for all 100% samples. However, it is not statistically significant within the level of precision measured for any one sample. The estimated values of SFE significantly varied depending on the characterisation method used (Zisman or Owens-Wendt), but this is consistent with literature; Schuster, *et al.* showed that SFE estimation varied by ~20% depending on the method used.[156]

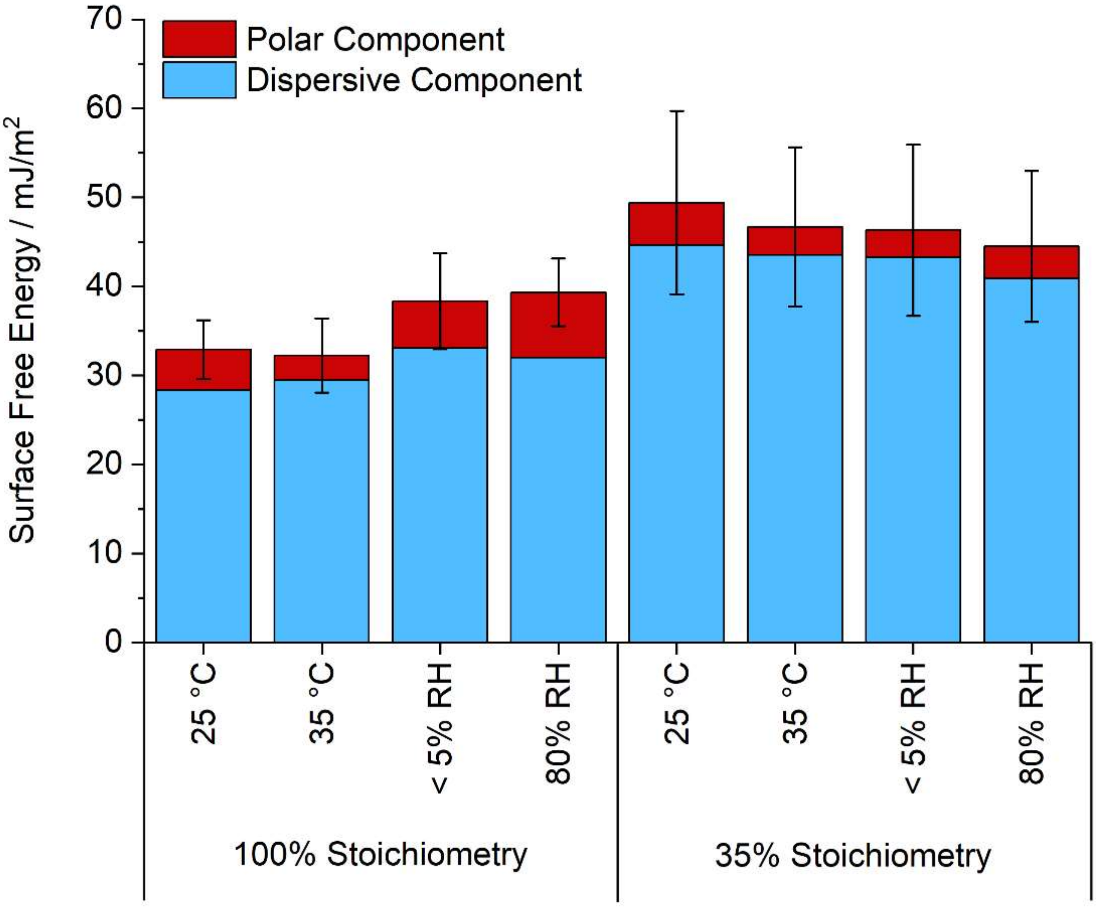

Figure 5.25: Owens-Wendt derived surface energy and standard error of each epoxy system.

5.2.5 Ambient-Cured First Coat Bulk Properties

5.2.5.1 Gelation Time

Rheology can be used to measure the gelation time of curing epoxy resins, characterised (in this work) by the point where the storage and loss modulus intercept, Figure 5.26.[157] Alternatively, gel point can be characterised by the point at which tan delta becomes independent of frequency.[157] Gelation time is unambiguously defined as the point at which a polymer moves from a liquid to solid like state. To comprehensively investigate interface formation as a function of overcoating interval, it was first important to determine the minimum overcoating interval as the first coat cannot be successfully overcoated while still in the liquid phase. While the minimum overcoating interval is usually considerably past the gelation point, knowledge of the gel point will at least give a base understanding of the lower limits of this process.

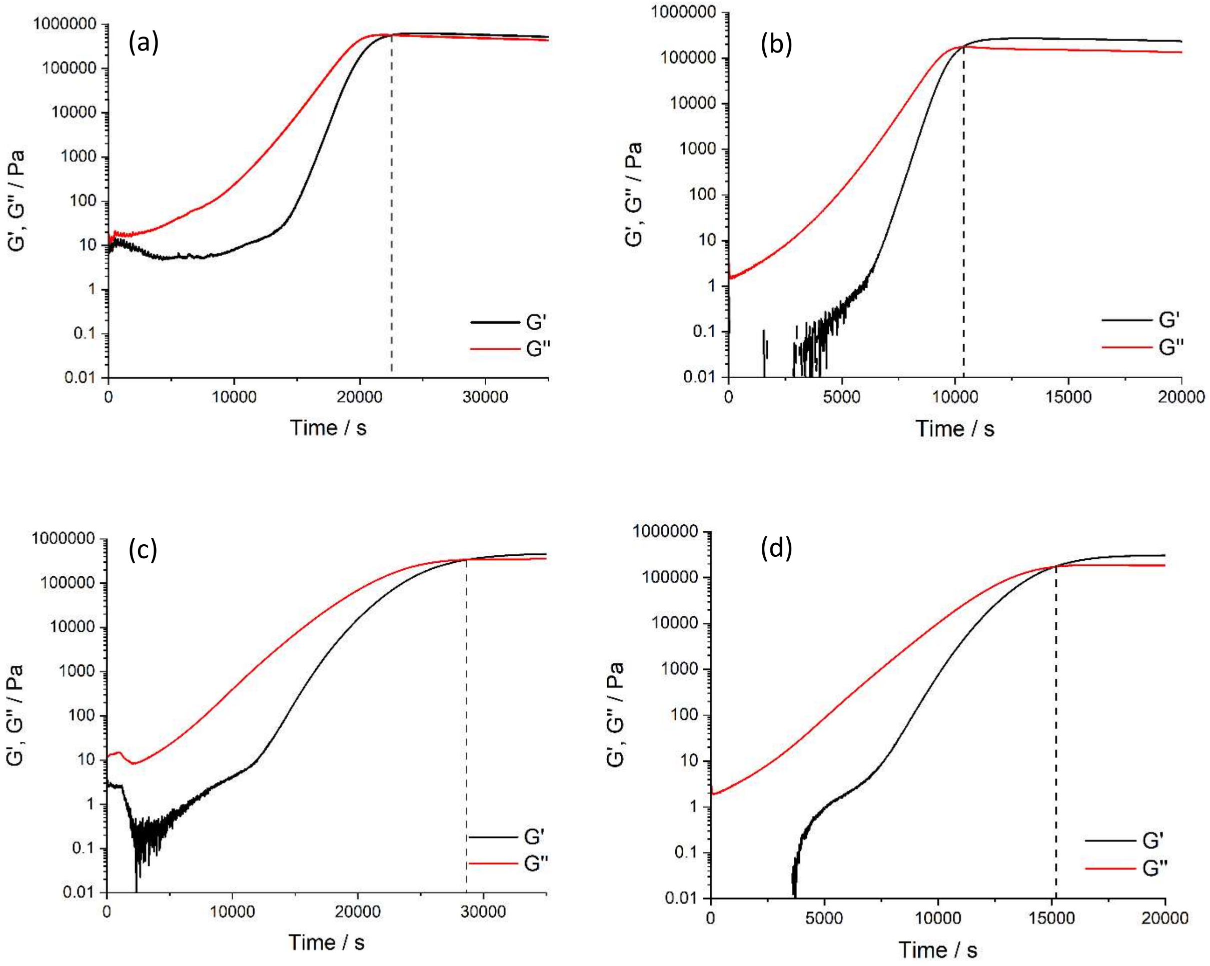

Figure 5.26: Storage and loss modulus of a curing epoxy film and gel point annotated (a) 100% stoich, 25 °C, 40% RH (b) 100% stoich, 35 °C, 40% RH (c) 35% stoich, 25 °C, 40% RH (d) 35% stoich, 35 °C, 40% RH.

Epoxy reactants were incubated at either 25 or 35 °C, before being mixed at either 100% or 35% stoichiometry and cast onto the bottom plate. A combination of single-use plates and careful application was utilised to prevent epoxy coming into contact with the rheometer where subsequent removal would be challenging. A furnace then enclosed the plates where temperature was maintained at either 25 °C or 35 °C. A time-sweep with 5% strain amplitude was carried out for 10 hours using parallel plate geometry. The gel time of each epoxy system has been listed in Figure 5.27.

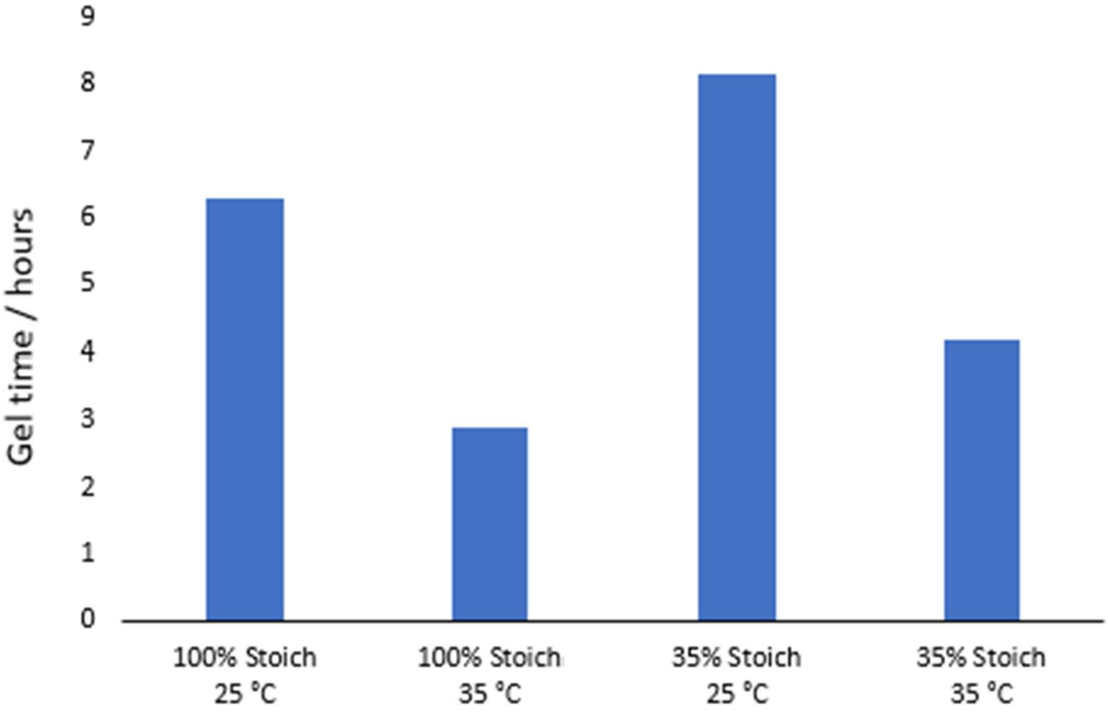

Figure 5.27: Gel time of each epoxy system.

As shown in Figure 5.27 the gel time was approximately halved at 35 °C compared to 25 °C. This is unsurprising as the increase in cure temperature would increase rate of reaction. The gel time was also quicker at 100% stoichiometry compared to 35% stoichiometry formulations. The maximum gel time observed was for the 35% stoichiometry, 25 °C cure temperature system at ~ 8.17 hours indicating that when investigating the influence of overcoating interval interface formation, this is the minimum possible interval that must be applied.

5.2.5.2 Determining Ambient-Cured First Coat Epoxy Conversion *via* DMA

The extent of cure (or conversion achieved) of an epoxy system, rarely complete in practical coating applications, is thought to be important for barrier properties, flexibility, and surface properties. Within epoxy resin chemistry, system T_g can give an indication of the conversion achieved, in same stoichiometry systems where the number of competing reactions is consistent.[50] Therefore ambient-cure system T_g was characterised as a function of cure chemistry prior to interface characterisation.

Samples were systematically cured at varying stoichiometries, temperatures and RHs for 24 hours. DMA was then carried out on these samples from 30 to 160 °C to determine the storage modulus, loss modulus and tan delta over time. The onset temperature of the decay in storage modulus was utilised as a measure of epoxy conversion achieved.

Table 5.2 shows the onset temperature of the decay in the storage modulus which was used as a comparative measure of conversion achieved, in same stoichiometry systems, as a function of cure condition. Accurate comparisons of T_g cannot be made between the two different stoichiometries as the systems have a number of different competing polymerisation reactions. Unlike the 100% stoichiometry systems, the 35% stoichiometry systems are in epoxide excess and contain accelerators which promote anionic chain-growth polymerisation of epoxide groups (epoxy homopolymerisation). While epoxy homopolymerisation can increase crosslink density, and therefore T_g, through intramolecular etherification,[158–160] the activation energies of the competing reactions may differ, and thus a higher T_g in an epoxide excess system with two competing reactions could represent a lower conversion of epoxide groups. It is notable that the final storage modulus is consistently higher in the 100% stoichiometry samples than the 35% stoichiometry samples, Table 5.2, which may indicate the differing structures.

Table 5.2: DMA of each epoxy system detailing the onset temperature of the decay in storage modulus (onset ambient T_g) and storage modulus.

Stoichiometry / %	Cure Temperature / °C	Cure RH / %	Onset Temperature of Decay in Storage Modulus / °C	Storage Modulus / MPa
100	25	40	67.6 ± 1.9	1150 ± 120
100	35	40	78.3 ± 2.1	1070 ± 210
100	25	< 5	66.1 ± 3.5	1150 ± 200
100	25	80	66.8 ± 5.7	1520 ± 720
35	25	40	80.5 ± 2.0	930 ± 210
35	35	40	95.4 ± 2.7	730 ± 310
35	25	< 5	72.3 ± 4.8	960 ± 290
35	25	80	84.1 ± 3.6	920 ± 340

Variation in RH did not significantly affect the temperature of decay in storage modulus for the 100% stoichiometry system. RH was hypothesised not to significantly affect the bulk properties of the samples. Unlike with cure temperature, RH influences the film by direct contact, *i.e.*, H_2O facilitates the reaction of CO_2 and amine at the sample surface to from carbamate. While this can lead to a disproportionate fraction of amine consumed at the sample surface, this effect does not propagate throughout the whole sample and the affected area at the surface (< 1 µm) is insignificant when compared to the sample thickness (2 mm), and therefore bulk properties should be unaffected. This is consistent with the FTIR analysis presented in Section 5.2.1.2. Unexpectedly, a difference was seen in the 35% stoichiometry system as a function of RH. No significant difference in storage modulus attributed to variation in cure condition was observed.

At both stoichiometries, an increase in ambient cure temperature significantly increased the temperature at which the onset decay in the storage modulus was observed. This agrees with work carried out by Michel and Ferrier who reported that T_g increased by ~ 15 °C in epoxy samples when cure temperature was increased from 20 to 40 °C.[161] Within polymers, once significant conversion has been achieved, a crosslinked network may be formed, depending on the system. Given 2-layer epoxy interfaces are thought to form through interdiffusion and a percolating network of bonds,[65–67] elevated crosslink density in the first coat would be expected to decrease second coat diffusion potential thus decreasing interfacial width forming a smaller boundary layer. Therefore, this suggests that systems cured at higher ambient temperatures may have an elevated crosslink density and so would be less favourable for second coat interdiffusion, forming a smaller boundary layer.

Epoxy system T_g can be estimated using either the peak in tan delta, the peak in loss modulus, or the onset decay in storage modulus.[162] As shown by Figure 5.28, the different approaches can lead to different values of measured T_g.

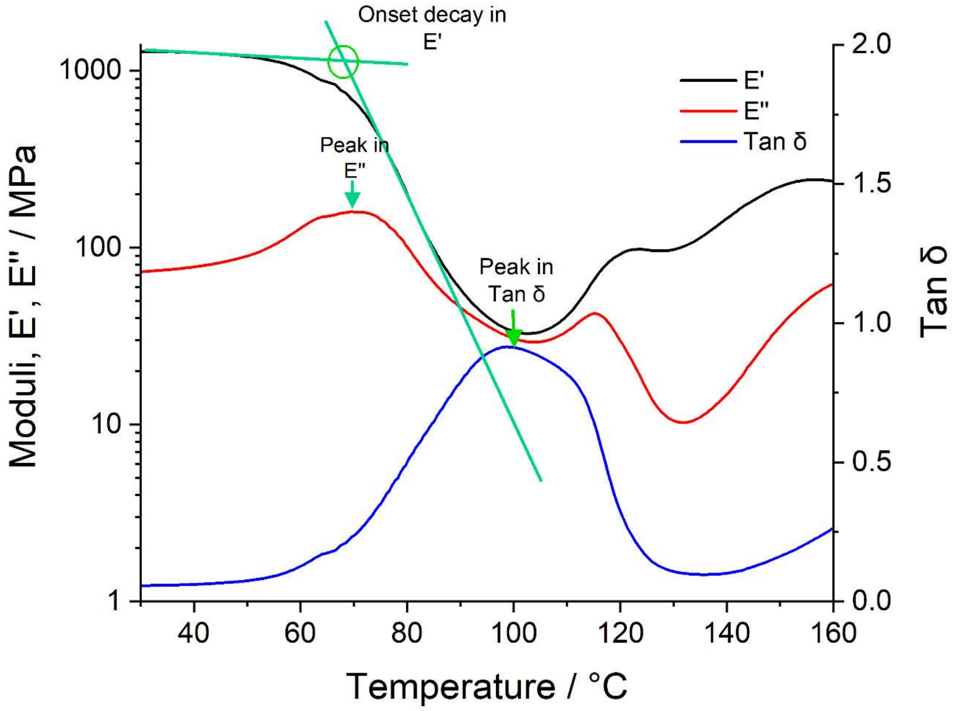

Figure 5.28: DMA trace detailing possible measures of T_g (system: 35% stoichiometry, 25 °C).

Within the work of this thesis, the onset decay in storage modulus was utilised as the values were more in line with literature reported T_g's of similar systems (measured using thermomechanical analysis).[161] In addition, in some repeats, there were obvious signs of *in situ* curing visible in the peak in tan delta, decreasing the reliability of this approach as a measure of T_g. Figure 5.29 shows an irregular point-shaped tan delta peak of an epoxy sample obtained *via* DMA, caused by in situ curing.

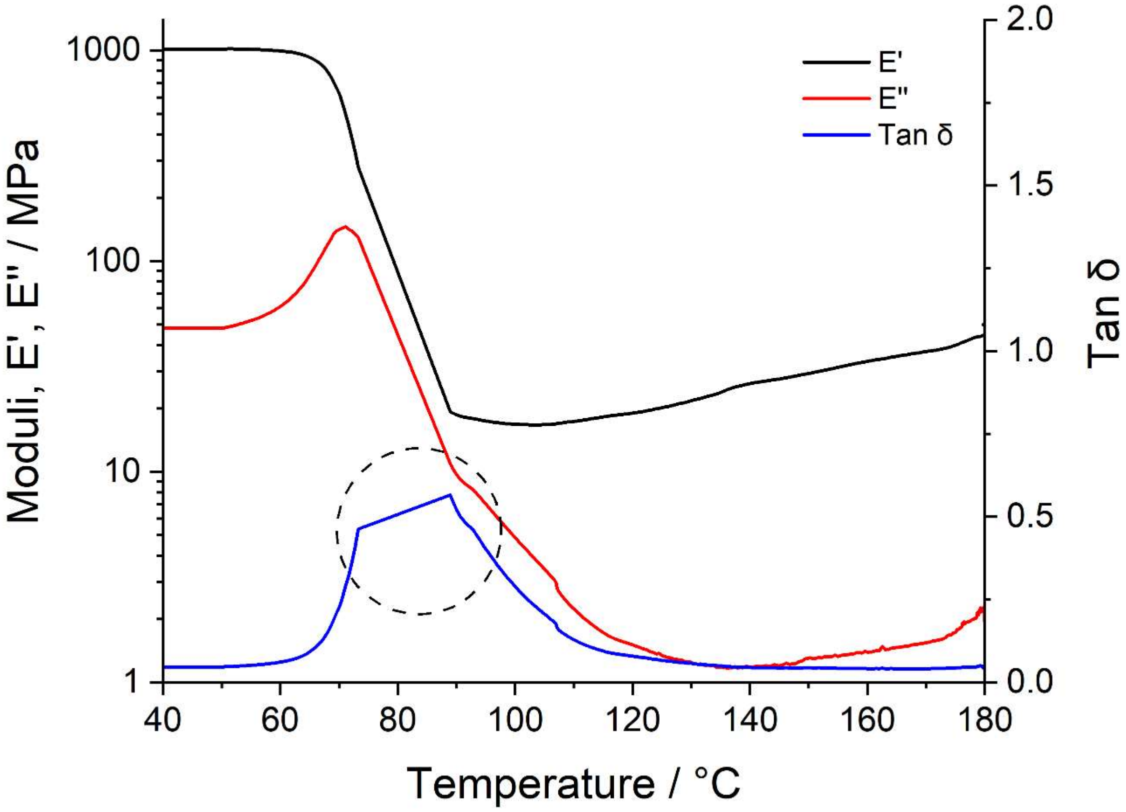

Figure 5.29: DMA trace with evidence of in situ curing in the Tan delta peak (circled) (system: 100% stoichiometry, 25 °C).

5.2.5.3 Determining Ambient-Cured First Coat Epoxy Conversion *via* DSC

DMA indicated that increasing the cure temperature from 25°C to 35°C increased the extent of epoxy conversion (Table 5.2). To confirm this observation a second method of T_g determination, DSC, was attempted. Figure 5.30-33 show the DSC thermograms of each system studied. Samples were heated at 10 °C/min.

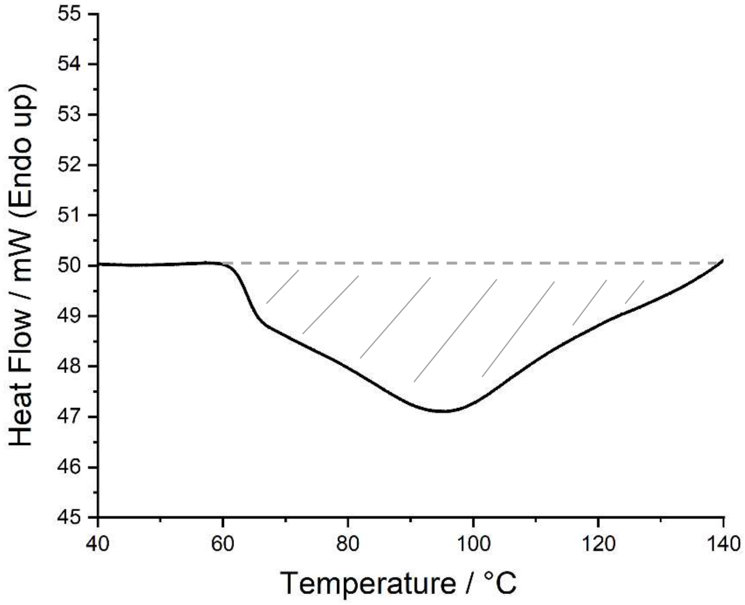

Figure 5.30: DSC thermogram of the 35% stoichiometry cured at 25 °C sample.

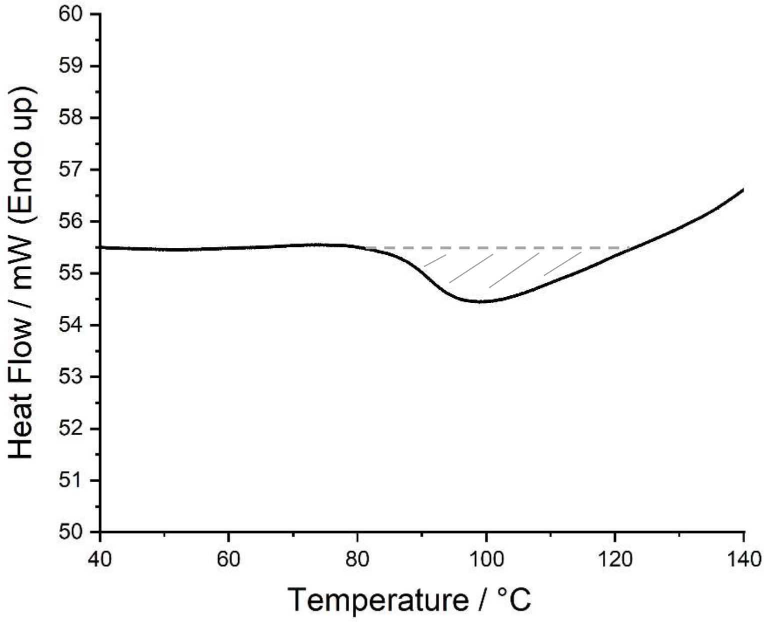

Figure 5.31: DSC thermogram of the 35% stoichiometry cured at 35 °C sample.

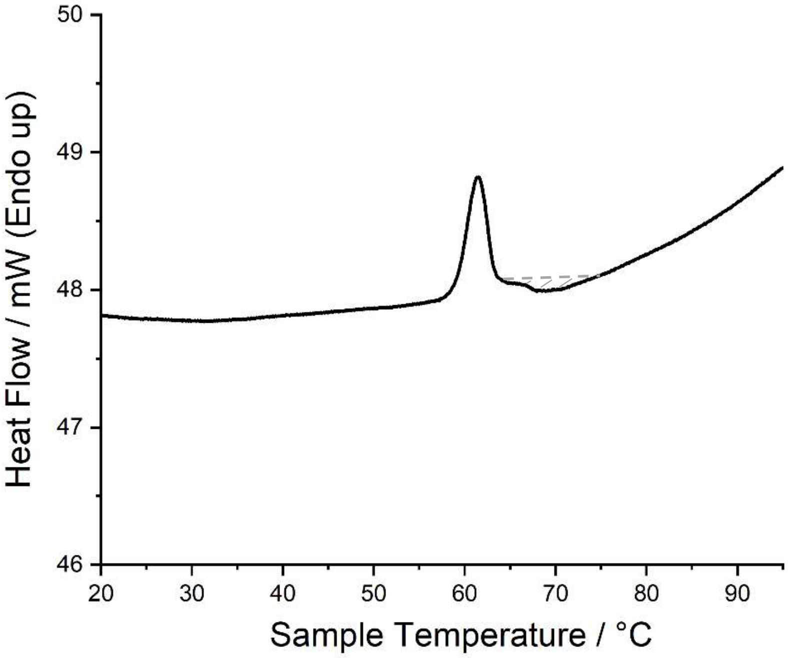

Figure 5.32: DSC thermogram of the 100% stoichiometry cured at 25 °C sample.

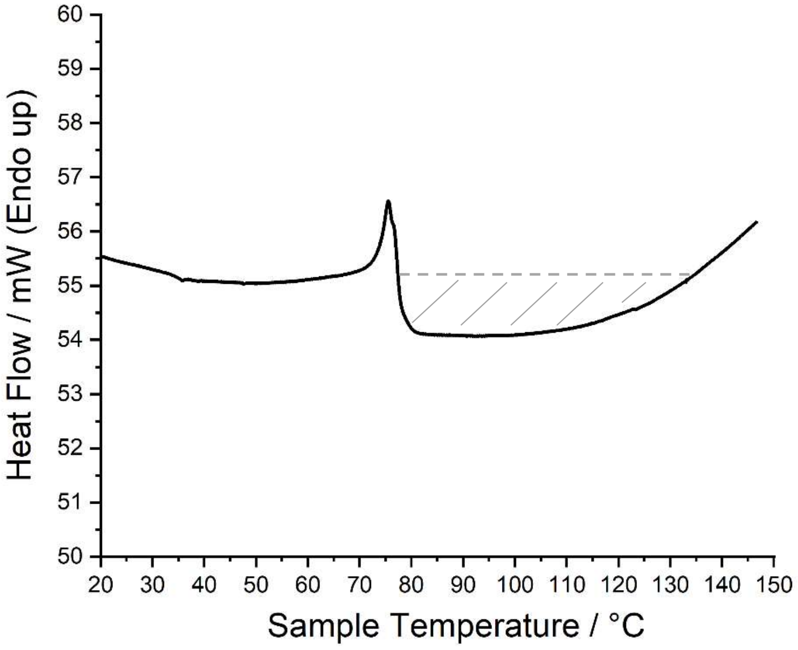

Figure 5.33: DSC thermogram of the 100% stoichiometry cured at 35 °C sample.

At both stoichiometries (35% and 100%) and cure temperatures (25 °C and 35 °C), there is no obvious T_g visible in the DSC thermograms, and so T_g cannot be determined for these systems using this protocol. (It is possible that a much faster heating rate may have resolved the T_g). The thermograms of the 35% stoichiometry samples are dominated by a large exotherm (shaded areas), indicative of additional curing, which starts at approximately 60 °C for the 25 °C-cured sample (Figure 5.30) and 80 °C for the 35 °C cured-sample (Figure 5.31). The exotherm is larger for the sample cured at the lower temperature and indicates a greater amount of unreacted epoxy in this sample. The higher onset temperature for the exotherm in the 35 °C cured sample could be consistent with this sample having a higher T_g, and the reaction being unable to continue until the sample is heated to above this temperature. The 100% stoichiometry DSC thermograms (Figure 5.32 and Figure 5.33) have an endothermic transition within the range expected for the melting point of PAC-M carbamate.[163] The breakdown of PAC-M carbamate and resultant dissociation of PAC-M may then allow for further reaction with residual epoxy leading to the broad endotherm, which is indicative of further curing. Alternatively, this may be the melting of a crystalline, oligomeric component of either RDGE or D.E.N. 431 and PAC-M which has formed during the ambient cure phase. Further structural analysis, using perhaps XRD, would be required to determine the cause of this thermal transition. Regardless, the temperature at which this proceeds is ~ 15 °C higher in the sample cured at 35 °C showing that the increase in cure temperature has shifted the temperature at which thermal transitions occur.[164]

Figure 5.34 shows the DSC thermogram of the same 100% stoichiometry sample but instead post-cured at 80 °C. The sample was heated from 60 to 200 °C at 10 °C / minute, cooled and then heated again under the same conditions. Interestingly, an endothermic transition observed in the samples cured at 25 °C and 35 °C was still present in the post cured sample (80 °C), instead occurring at a higher temperature (black line). The transition is not observed in the second heating cycle (red line) whereby the sample has been exposed to temperature of >200 °C. The fact that increasing the cure temperature increased the temperature at which this transition occurs may instead indicate that this transition is caused by the loss of volatiles from the system, rather than the melting of PAC-M carbamate or crystalline, oligomeric components. The increase in cure temperature, may increase system T_g, thus increasing the energy required to enable chain mobility and therefore enable the loss of volatiles. Further analysis would be required to determine this, perhaps using Simultaneous Thermal Analysis (STA) to see if the peak relates to volatilisation.

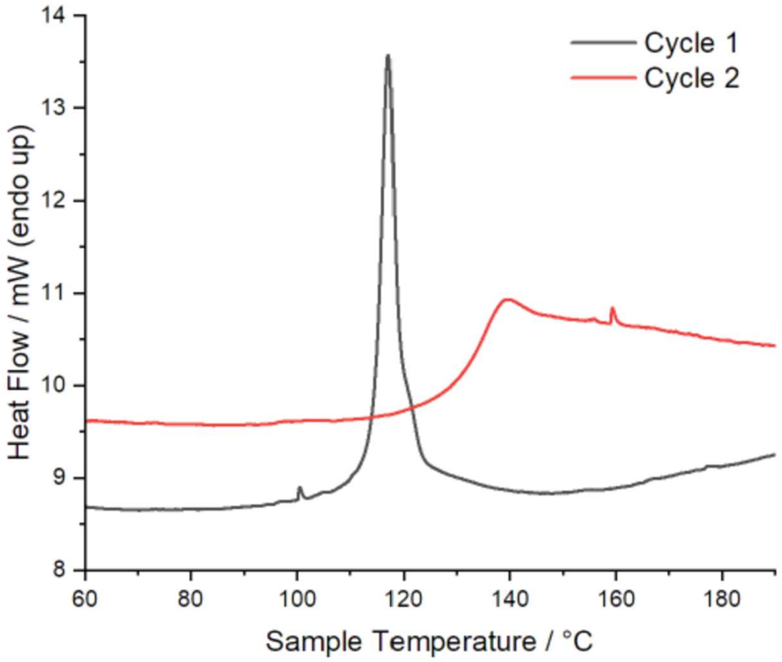

Figure 5.34: DSC thermogram of a 100% stoichiometry, post cured (80 °C) sample heated from 60 °C to 180 °C (black), heating rate 10 °C / min, followed by cooling and heating again (red).

5.2.5.4 Average Void Volume and Fractional Free Volume

Positron annihilation lifetime spectroscopy (PALS) allows for accurate estimations of polymer average void volume, AVV (mean free volume void size) and fractional free volume, FFV (total amount of free volume within a sample / free volume fraction) by measuring electron induced positron annihilation lifetime inside a free volume void and using this measurement to determine free volume void size (Equation 3.17 & 3.18).[123,124] Previous studies have shown a correlation between increased AVV / FFV and increased rate and extent of solvent ingress.[31] However, nothing has been documented regarding the impact of AVV and FFV on the extent of second coat interdiffusion. We can consider the unreacted monomers of a second coat material as being like solvent molecules, but they are quite large compared to many organic solvents. In particular, penetrant molecular volume associated with second coat interdiffusion (D.E.N. 431: ~584 Å^3 / RDGE: ~305 Å^3 / PAC-M: ~368 Å^3) would be much larger than previously characterised probe solvents (methanol: ~67 Å^3) and the rate of ingress has been shown to significantly decrease in fully cured resins when penetrant volume exceeds AVV.[31,96]

Samples were systematically cured at varying stoichiometries, temperatures and RHs for 24 hours. PALS was then carried out on these samples to determine the average void volume and fractional free volume (Figure 5.35).

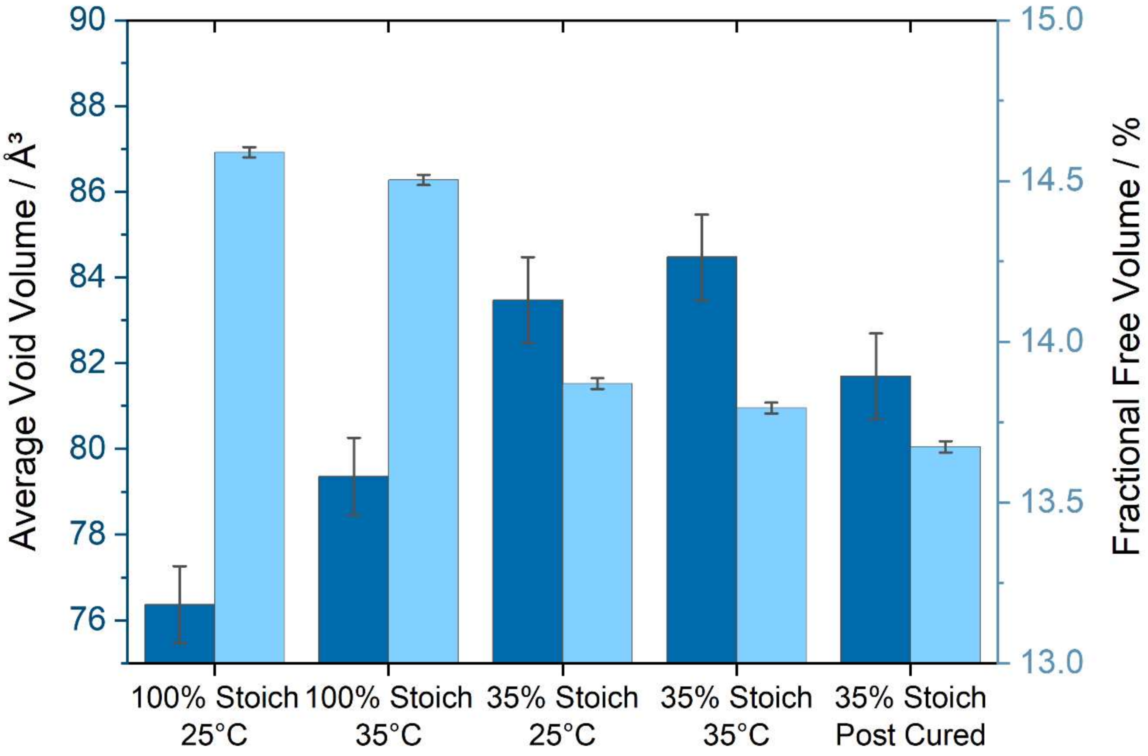

Figure 5.35: Average void volume (dark) and fractional free volume (light) of each epoxy system.

Increasing the cure temperature from 25 to 35 °C significantly decreased FFV in the 35% system, Figure 5.35. However, it both increased AVV and decreased FFV in the 100% system. A similar pattern was seen as a function of stoichiometry, as the 35% system recorded a higher AVV, but lower FFV compared to the 100% system. Since the AVV and FFV are not proportional to one another, this indicates that the number of voids detected by PALS is very sensitive to the cure conditions applied. This result could be interpreted as the increase in cure temperature or use of a 35% stoichiometry led to a smaller number of larger voids (increasing AVV), while the overall fraction of free volume was lower (decreasing FFV). Frank, *et al.* reported a similar inverse correlation between AVV and FFV in glassy networks derived from multifunctional epoxies.[106] Currently it is not fully understood which property, AVV or FFV, is more influential in promoting intercoat diffusion; previous studies have detailed the importance of both properties in extent of penetrant ingress.[31,96,106] Jackson, *et al.* reported that solvent ingress into amine cured glassy epoxy networks decreased as AVV decreased.[37] Shackleton showed that the rate and extent of organic solvent ingress into epoxy networks increased when AVV and FFV was increased by exposure to xylene.[36]

Sample (100% and 35% stoichiometry films) AVV ranged from ~76 - 85 Å^3, which is significantly smaller than the calculated molecular volume of the second coat penetrants. Jackson, *et al.* stated that solvent ingress was undetectable (0.1 mg / 300 mg sample) when penetrant volume vastly exceeded substrate AVV.[37] Therefore, it is expected that the rate of and ultimate extent of interdiffusion upon overcoating will be relatively low forming a narrow interface. Alternatively, the results may imply that the first coat may require some kind of surface plasticisation (*e.g.,* by the second coat) to increase AVV in order to allow second coat penetration, or perhaps that the bulk AVV, which is measured using PALS, is not consistent with surface AVV.

5.3 Chapter Conclusions

Factors affecting amine-cured resin surfaces, such as carbamation, are known to influence their performance as substrates for adhesion, but can be challenging to characterise with bulk chemistry techniques such as NMR, or with IR. We have found that for a variety of controlled conditions, and their combinations, detection of the early stages of carbamation using AFM and contact angle analysis is possible, providing promising avenues for future research on carbamate-related experiments. The most important single parameter appears to be RH, and its impact is most noticeable in formulations with high amine content.

WCA results indicated that the low amine content resin systems were most hydrophilic. Since these resins all have T_g values well above room temperature, and low roughness, it appears unlikely that this difference can be attributed to either reorientation of surface molecules or to surface topography; therefore, surface chemistry is most likely responsible for the greater wettability.

Increasing the cure RH significantly increased surface roughness, surface layer formation, and wettability, but increasing the cure temperature had less of an effect on the surface properties. Noticeably, although hydrophobicity could be sensitive to curing conditions, the apparent surface free energy is little affected. This indicates that WCA alone is a flawed measure of surface properties in these systems but may provide a convenient indication of carbamation.

Cure temperature more significantly affected the bulk properties compared to RH, with increasing cure temperature increasing extent of cure and FFV while decreasing AVV.

The material properties (R_q, rugosity, wettability, T_g, AVV, FFV) characterised in this study are hypothesised to be influential in intercoat adhesion and show statistically significant variation when ambient cure conditions and stoichiometry are varied. This indicates that in order to optimise interdiffusion and achieve strong second coat binding, the cure conditions and chemistry utilised should be considered, but physical topography has limited influence. The next chapter will quantify interphase width as a function of the cure conditions and stoichiometries used in this chapter. Therefore, relationships can be drawn between interface formation and the physical properties exhibited in resins prior to overcoating due to variation in cure conditions and stoichiometry.

Chapter 6

Bilayer Epoxy Interface Characterisation

6.1 Chapter Introduction

Bilayer epoxy interface adhesion failure is a fatigue-associated issue seen in epoxy coatings used to line steel tanker cargo holds, which house small molecule chemicals during marine transport. While the financial cost of adhesion failure can be substantial, ultimately little is known about the interfaces of these materials where adhesion failure occurs. This is because the interface is difficult to detect as the formulations that compose each layer are often chemically identical and so very little contrast is expected between the successive layers or at their interface, other than the carbamation discussed in the previous chapter. In addition, adhesion failure manifests more quickly in some instances than others with no obvious causation, leading coating manufactures to question the root cause of these issues.

In the previous chapter, a variety of first coat surface and bulk properties were characterised as a function of ambient cure condition and stoichiometry as it was hypothesised that variation in these parameters would affect the first coat properties and in turn the resultant 2-layer interphase strength after overcoating. This chapter will explore how these parameters directly impact interface formation, drawing relationships between first coat surface properties and the physicochemical properties of the interface. Through doing this, potential weaknesses whereby adhesion failure may initiate and propagate can be identified. This was achieved by first determining the diffusion processes behind interface formation, using Raman mapping, before then going onto characterise the physicochemical properties of the interface as a function of cure condition and stoichiometry. Neutron reflectometry, Raman mapping and ion beam analysis were used as the primary tools to determine vertical depth composition profiles, and thus map bilayer epoxy interfaces in films of varying cure conditions and stoichiometries.

6.2 Results & Discussion

6.2.1 Epoxy-Epoxy Interface Formation Mechanism

While the interface formation mechanism of epoxy-substrates[51–56] and epoxy-thermoplastics[57–63] has been previously documented, bilayer epoxy interface chemistry remains less studied and this is the first attempt of which the author is aware to characterise the interface formation mechanism of same-stoichiometry, 2 (+) layer epoxy resin systems. Understanding the mechanism of interface formation may be crucial toward uncovering the cause of intercoat adhesion failure in bilayer epoxy systems and so should be determined.

It is hypothesised that to form a strong interface, the topcoat needs to diffuse into the first layer to form an interphase, reinforced by covalent bonding between the two coats in the interphase region. This is challenging to measure because of the lack of chemical contrast between the layers, and because it is possible that there is a simultaneous process in which the sol phase of the ambient-cured (25/35 °C) first layer is extracted by contact with the uncured second coat. The possibility of sol removal was tested by measuring the thickness of spin-cast, ambient-cured epoxy films, before and after rapid exposure to a volatile solvent (chloroform, spin-cast), which evaporates within a few seconds of contacting the first layer. Results show significant depletion (Figure 6.1; ~ 18% decrease in film thickness) so it would not be possible to isolate the ingress of one or other epoxy component from the egress of the sol in such an experiment. Therefore, to determine if the second coat can diffuse into the first coat, the use of labelled molecules to distinguish between the two layers is essential.

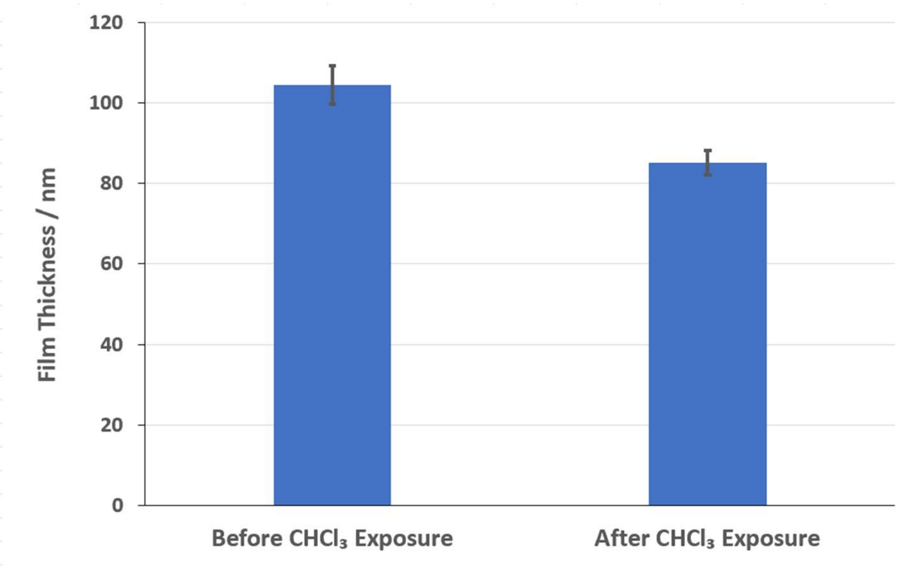

Figure 6.1: Spin coated epoxy film thickness pre and post exposure to chloroform.

6.2.1.1 Diffusion Mapping using Raman Spectroscopy

Raman spectroscopy is used to determine the identity and relative concentration of chemical bonds within a sample and has been widely used to study polymer blends.[165] By recording spectra at set intervals across a sample surface, the surface can be 'mapped', quantifying chemical composition. Technique resolution is typically ~ 1 µm,[166,167] determined by laser spot size, but can rise to up to 10 µm due to sample properties (homogeneity, topography, etc).[168] Using this method, the extent or distance of ingress of a chemically unique or labelled compound into a sample can be determined by sectioning the sample after ingress and mapping the exposed cross-section. In this section, 100% and 35% stoichiometry films were cured at 25 °C or 35 °C, and overcoated after 1-, 3-, 4- or 7-days with a compound of similar structure to that of the second coat components but was spectroscopically distinguishable. By quantifying ingress into these samples, the impact of stoichiometry, cure temperature and overcoating interval on interphase dimensions can be understood.

For the diffusing compound to be distinguishable from the bulk using Raman spectroscopy, it must contain a unique functional group. Within this research, epoxy layers 1 and 2 are compositionally identical (D.E.N. 431, RDGE and PAC-M), and so unsuitable. Therefore, instead of using a second coat component as the diffusant, a compound with an elementally unique functional group but similar overall structure (Figure 6.2) and volume, to the second coat components was used, 4-chlorophenyl glycidyl ether (4-ClPGE). 4-ClPGE was selected as theoretically this compound should behave and diffuse in a similar manner to that of RDGE (second coat component) but be spectroscopically distinguishable from the other components. Figure 6.3 and Figure 6.4 show the Raman spectra of RDGE and 4-ClPGE, highlighting the peak at 624 cm^{-1} associated with the Cl-C bond which is unique to 4-ClPGE, as well as the aromatic CH bonds at ~ 3000 cm^{-1} present in both compounds which were used for spectra normalisation. Figure 6.5 also shows that the 624 cm^{-1} Cl-C peak observed in the raw spectrum of 4-ClPGE (Figure 6.3) can also be observed in an epoxy resin and 4-ClPGE system. Therefore, this peak was used to track 4-ClPGE ingress depth into the first layer.

Figure 6.2: RDGE (left) and 4-ClPGE (right).

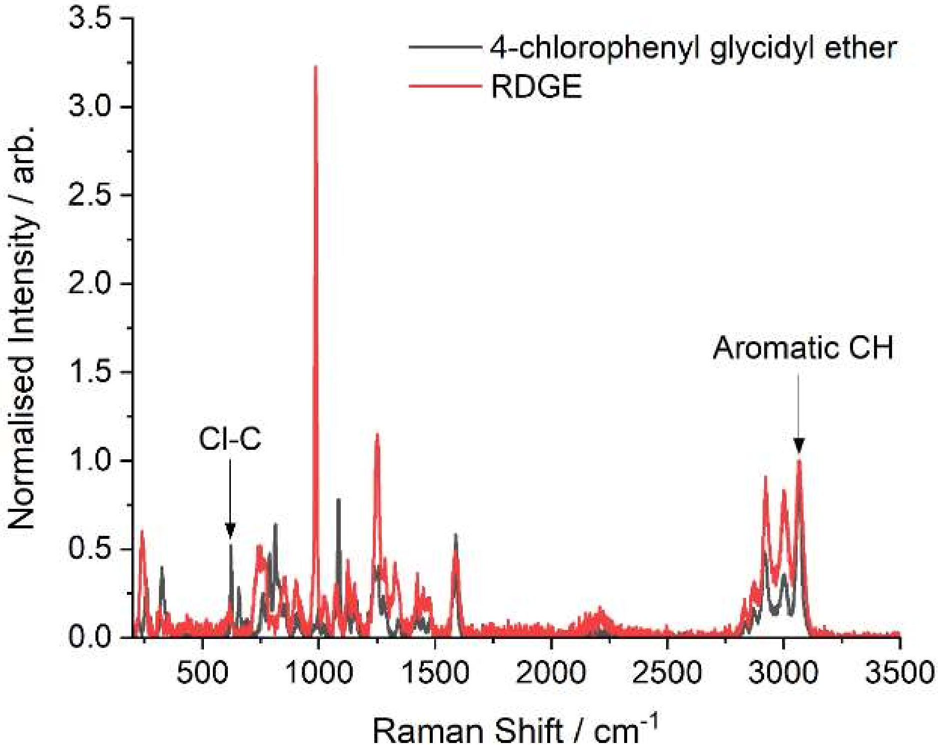

Figure 6.3: Raman shifts of 4-ClPGE and RDGE, 200 – 3500 cm^{-1}.

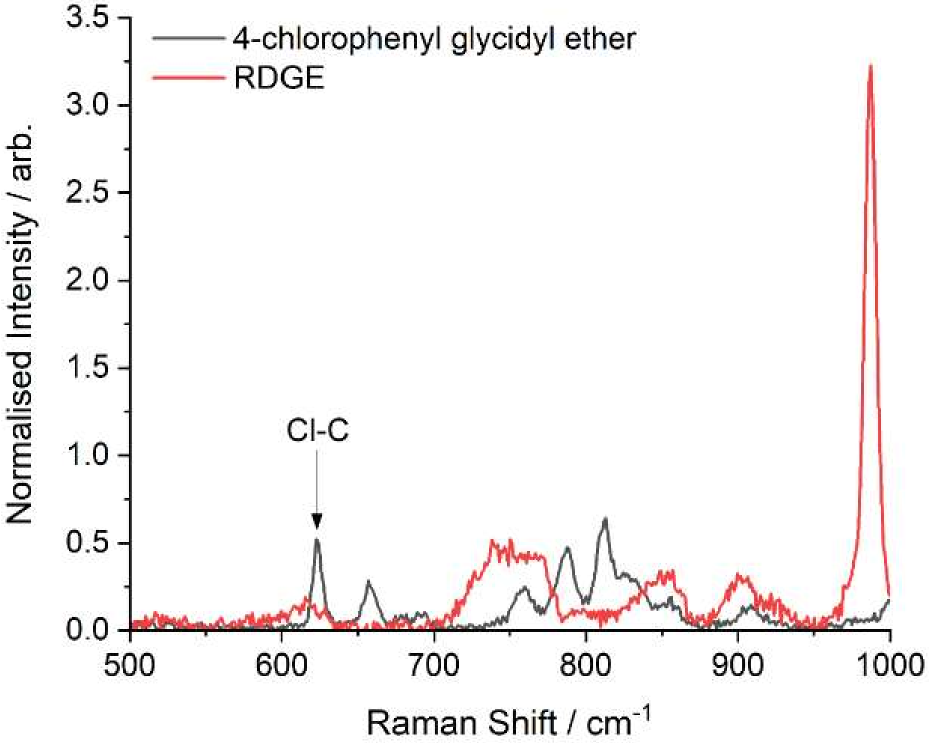

Figure 6.4: Raman shifts of 4-ClPGE and RDGE, 500 – 1000 cm^{-1}.

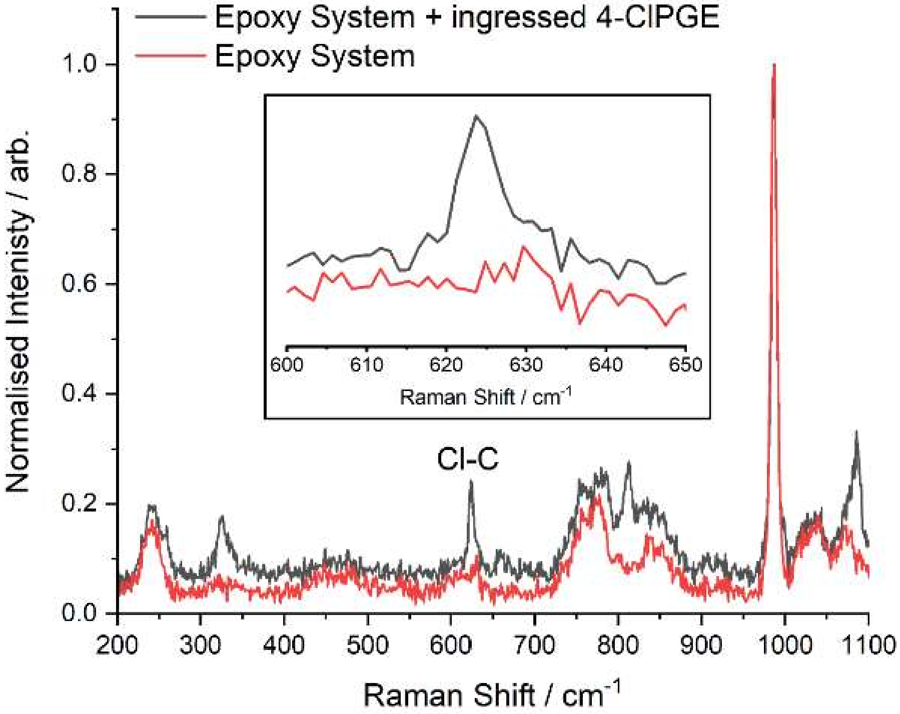

Figure 6.5: Raman shifts of an epoxy system and an epoxy system ingressed with 4-ClPGE, 200 – 1100 cm^{-1}.

A 1-layer ambient-cured film (35 °C, 40% RH, 100% stoichiometry) was overcoated with 4-ClPGE for 3 days. Upon completion of the 3-day ingress interval, excess surface 4-ClPGE, which had not diffused into the sample was removed *via* wiping with fibreless tissue while still in the liquid phase. Following wiping, samples were then sectioned by first scoring horizontally across the sample surface using a sharp razor blade and then snapping along the score to produce a clean break. Alternatively, a microtome could have been used to expose the interface. Raman mapping was then carried out on the newly exposed cross-section at advancing 10 µm intervals from the original sample surface. Focus was recalibrated at each interval to account for any variation in surface roughness which may have arisen during sample preparation. This produced a vertical chemical bond composition profile of the sample, thus allowing the presence of 4-ClPGE to be determined at a series of sample depths (Figure 6.6).

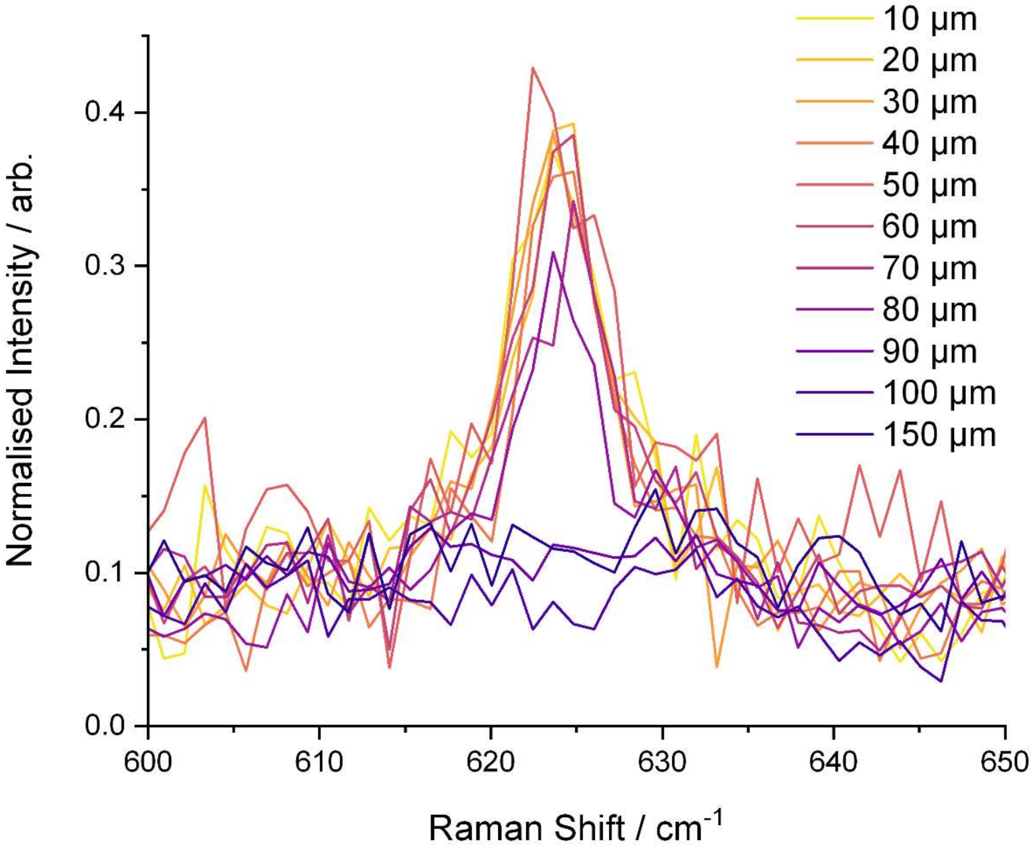

Figure 6.6: Raman shifts of the Cl-C bond in 4-ClPGE at increasing depths into an epoxy resin system post ingress.

Figure 6.6 displays the Raman shift of a sectioned epoxy resin film post overcoating with 4-ClPGE. Each spectrum was recorded at increasing distance from the original film surface thus quantifying chemical composition at increasing film depth. Spectra have been presented in the 600 – 650 cm^{-1} range as the 4-ClPGE Cl-C peak of interest was observed in this region. The Cl-C peak of 4-ClPGE is visible in the Raman spectra up to 80 µm into the epoxy resin film. Figure 6.7 displays the peak intensity of the 4-ClPGE Cl-C peak (~ 624 cm^{-1}) as the distance from the film surface increases. The dotted line (red) highlights how peak intensity remains high until a sample depth of ~ 60 µm (region 1), at which point intensity begins to decrease (region 2). While at depths exceeding 90 µm (region 3), the signal is consistently around 0.1 - 0.15 in region 3, we can be confident that there is no 4-ClPGE here as this is simply background plus noise related to imperfections of the normalisation software (Origin). The total film thickness was 180 microns; therefore, significantly exceeds the measured range of 4-ClPGE penetration.

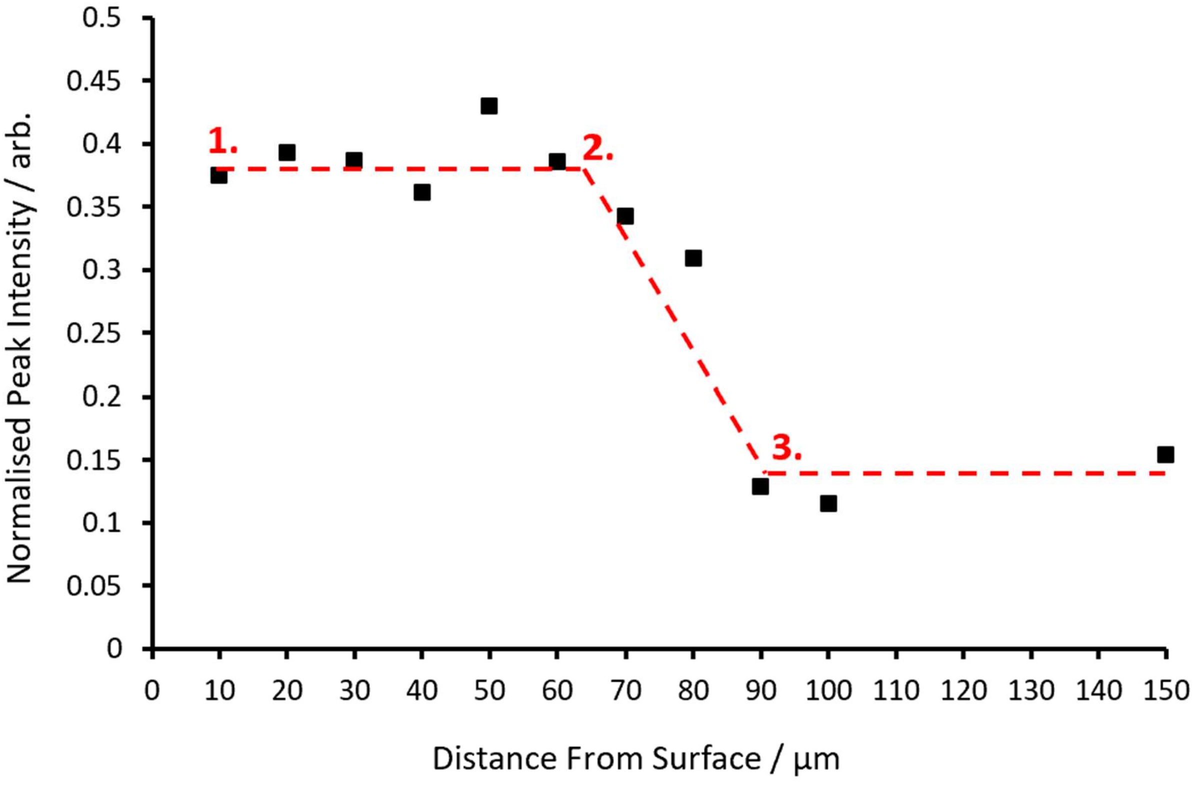

Figure 6.7: The normalised peak intensity of the 4-ClPGE Cl-C bond as a function of film depth (black) and fitted line (red): (1) 4-ClPGE at highest concentrations within the film (2) The peak intensity decreases as the concentration of 4-ClPGE decreases as film depth increases (3) 4-ClPGE is undetectable. For ease of visualisation, only 1 repeat has been presented; all repeats are reported in Figure 6.12.

Figure 6.6 and Figure 6.7 show that molecules with similar dimensions and properties to the second coat components are capable of diffusing tens of microns into the first coat during the ambient cure phase, thus indicating that epoxy-epoxy interphases form *via* interdiffusion. It should be noted that the range of diffusion may be less in bilayer materials utilising reactants with a functionality of ≥ 2 due to diffusant polymerisation. However, as diffusion is shown here to occur over quite a broad range, this could allow for two contributions to bonding across the interface: (i) reaction of the infusing species with the first layer network and propagation back to the second layer to form a continuous network; (ii) dangling ends of the first layer reaching into and reacting with the second layer. Perhaps removal of the first layer sol into the second layer helps to expose the reactive dangling ends of the first layer to the uncured resin components of the second layer or, perhaps as the diffusion front of the second coat penetrates deep into the first coat, it may leave behind a region of decreased first coat T_g. This may increase the reaction rate in the region and stimulate the diffusion of elastically inactive, dangling polymer chains, bound to the first coat surface into the second coat. Subsequently, only a few nanometres of first coat diffusion may be required to provide the necessary interfacial strength if the chains are able to interconnect covalently. However, investigation of this theory cannot be determined using this method and would likely be very challenging to achieve using any current analytical technique.

As sol fraction was not measured experimentally by conventional means for the ambient cured films, 18% was crudely estimated as the sol fraction remaining after the ambient cure stage (as suggested by Figure 6.1), and applied to the Miller Macosko theory,[42] to estimate epoxy conversion at this stage. By doing so, we can better understand if the above, latter hypothesis is realistic. In this calculation it was assumed that D.E.N. 431 comprises four components (for ease of computation) as shown in Table 6.1.

Table 6.1: Molar mass and fraction of D.E.N. 431 at increasing functionality used in the computation of network parameters by Miller Macosko Theory (see Figure 6.8).

Component, n	**Molar Mass**	**No. Epoxy groups**	**Mole Fraction**
1	312	2	0.45
2	474	3	0.35
3	636	4	0.15
4	798	5	0.05

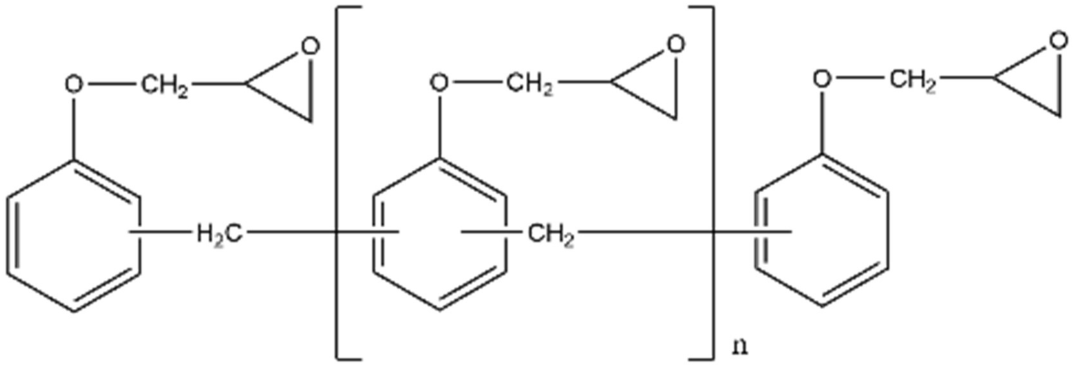

Figure 6.8: Representation of D.E.N. 431.

Figure 6.9 shows the calculated evolution of weight fraction of sol, weight fraction pendant chains and the weight fraction of elastically active chains as a function of conversion for a mixture of 75% w/w RDGE and 25% w/w D.E.N. 431 cured with PAC-M at 100% stoichiometry. This was calculated using Miller Macosko theory: a polymer and network modelling approach based on random step-growth processes and uses a recursive probability methodology to compute the parameters of interest.[42] In the post-gel stage, such parameters include the weight fraction of sol, the weight fraction of pendant chains and the weight fraction of elastically active chains, as well as others such as crosslink density. The properties of the system in the post-gel stage depends on a calculated parameter appropriately termed the “probability of a finite chain”. By way of example, the sol fraction depends on all the chains on a molecule being finite, while pendant chains on the network require a path through the network to an unreacted functional group. The method adopts Flory and Stockmeyer’s simplifying assumptions in step-growth polymerisation processes, namely: [169,170]

1. Functional groups of the same chemical type have equal reactivity and react independently of one another.
2. The reactivity of a functional group is independent of the size of the chain to which it is attached.
3. No intramolecular reaction occurs in finite species *i.e*., before the gel-point.

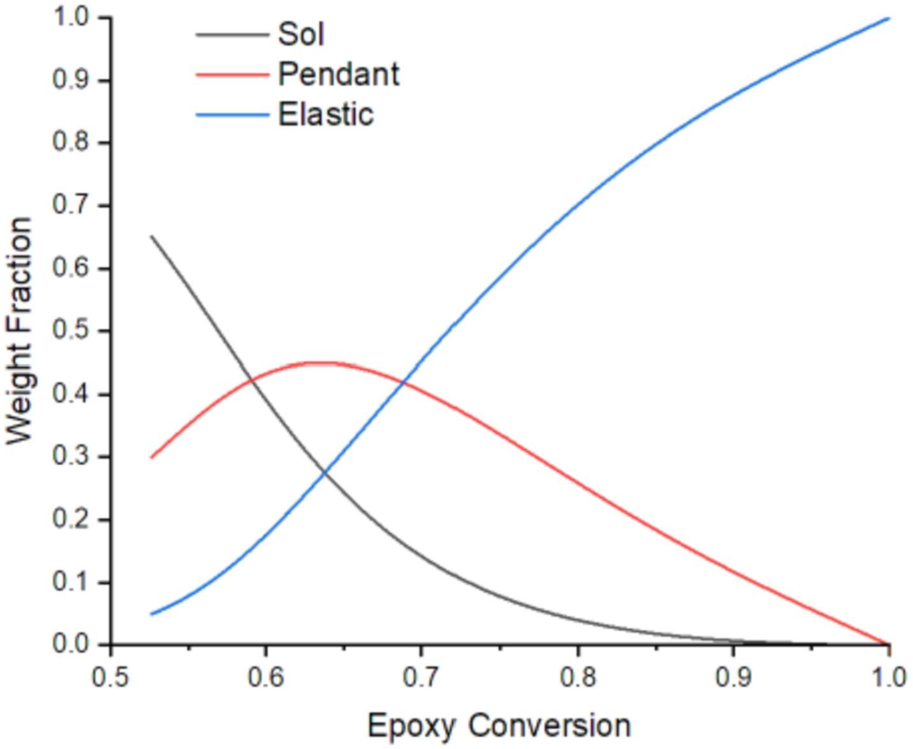

Figure 6.9: Weight fraction of sol, pendant chains, and elastically active chains as a function of epoxy conversion, in a 100% stoichiometry formulation (75% w/w RDGE and 25% w/w D.E.N. 431, cured with PAC-M).

An epoxy conversion of approximately 67% would be required for the sol fraction to drop to around 18%. At this conversion just over 40% of the mass of the chains are pendant, with a similar fraction elastically active. If this represents the point at which the basecoat film is overcoated, there is a significant possibility of pendant chain penetration into the topcoat, especially if it is plasticised by topcoat monomer diffusion into the basecoat. Such penetration, if it is accompanied by reaction of the unused functionality at the end of (or in the middle of) the pendant chains, then the two films will be covalently bonded across the interface. A higher epoxy conversion at the point of overcoating would lead to fewer pendant chains and a higher T_g, leading to less facile diffusion between coats and a weaker interface. A lower epoxy conversion would lead to the converse. Thus, conversion in the basecoat would appear to be an important parameter in determining the interfacial adhesive and cohesive strength.

This distribution of species in D.E.N. 431 gives a number average functionality for of 2.8 and an EEW of 158. The Olin Epoxy website quotes the D.E.N. 431 epoxy novolac product as having an average functionality of 2.8 and an EEW of 172 – 179.[139] Whilst the EEW for the assumed four component mixture is a little lower than the published range, this is due to neglect of the imperfections in the actual structure, causing the deviation from the theoretical structures given here. Since D.E.N. 431 only comprises 25% of the total mass of epoxy in the coating, it is reasonable to suppose that as a first approximation, the four-component model is adequate for the purposes of this demonstration of the impact of incomplete conversion in the first coat on the properties of the resulting network. RDGE is assumed to be a pure species of molar mass 222 and epoxy functionality of two, and PAC-M was assumed to be a pure species of molar mass 210 and active hydrogen equivalent weight 52.5.

Miller Macosko theory in its original formulation only applies to step-growth processes, proceeding by a single chemical reaction, and can therefore only realistically be applied to the stoichiometric coatings described in this thesis. Other modelling approaches, such as kinetic methods or Monte Carlo methods, may be better for application to the mixed mechanism systems in this thesis, but is beyond the scope of this work.

As explained in Chapter 5, the polymeric average void volume (AVV) of this ambient-cured first coat was measured to be less than 80 $Å^3$ but the molecular volume of 4-ClPGE is significantly larger at ~ 146 $Å^3$ (as calculated using HSPiP software). This is particularly interesting as previous studies have reported that ingress into epoxy resin systems was gravimetrically undetectable (± 0.05 mg) when diffusant molecular volume exceeds epoxy average void volume.[96] However, these studies were performed on glassy, post-cured systems where the extent of conversion was substantially closer to completion, while ambient-cured systems contain a relatively large proportion of unreacted material, as suggested by Figure 6.1 and Figure 6.9. This means that post-cured systems are typically more rigid, attributed to a significantly lower concentration of mobile molecules present, amongst other reasons. The diffusion observed here indicates that first coat free volume is perhaps less important to the extent of penetrant diffusion into ambient cured systems and instead indicates that extent of conversion is more influential. Therefore, we hypothesise that ingress is possible in the ambient cured systems, but not in the post cured systems, as the ambient cured systems contain a larger proportion of unreacted, mobile material which allows for molecular migration within the film, even if one end of the molecule is bound to the basecoat network. To test this hypothesis a control experiment was carried out using a post-cured epoxy film as the first layer (Figure 6.10).

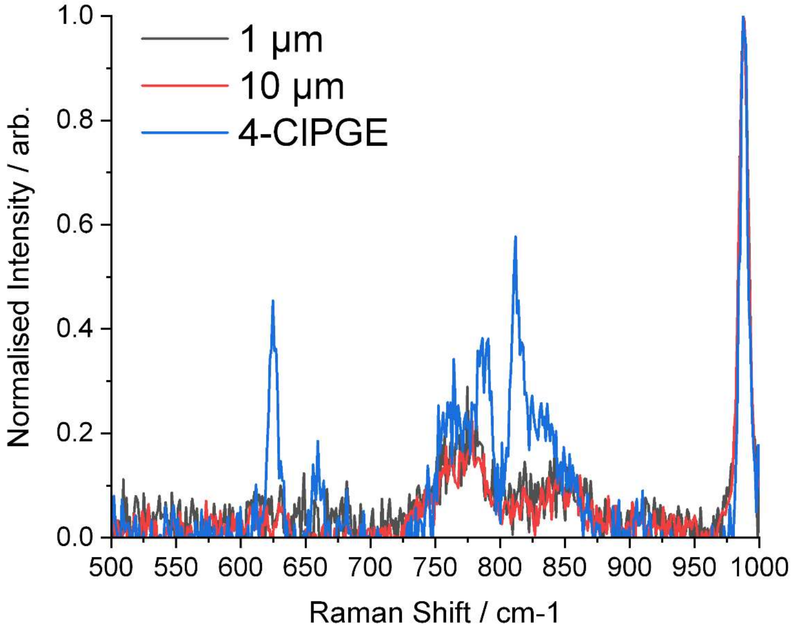

Figure 6.10: Raman shifts of a sectioned, post-cured epoxy film at increasing depths from the surface (black and red lines), post ingress of 4-ClPGE (Cure conditions: 35 °C, 40% RH, 3-day OC interval, post-cured). A reference line (blue) has also been plotted to show where the Cl-C peak would be if present in the other spectra. (Normalisation peak: ~ 980 cm^{-1}).

The spectra shown in Figure 6.10 were normalised using the peak associated with the epoxy resin at ~ 980 cm^{-1}.[171] The presence of 4-ClPGE was undetectable in the post cured film indicating that ingress into the post cured film did not occur. This agrees with the conclusions of Jackson *et al.* who stated that ingress into post cured epoxy networks was undetectable when diffusant molecular volume exceeded void volume.[96] Given that in chapter 5 it was shown that the application of a post cure step only slightly decreased the system average void volume, yet ingress of 4-ClPGE was significantly limited in the post cured system, this strongly suggests that free volume is less important to the extent of penetrant diffusion into ambient cured systems. Instead, this supports the hypothesis previously proposed above which suggested that ingress was possible in the ambient cured film but not the post cured film due to the reduced T_g and network rigidity in the ambient cured film.

The mechanism of ambient cured bilayer epoxy interface formation observed here may have some features in common with that of epoxy-thermoplastic interfaces. However, it is not identical due to the varying thermodynamic response of thermoplastics and thermosets to temperature; thermoplastics are solid resins, which experience increased molecular mobility upon heating, therefore greater interface widths are usually expected when processed at higher temperatures. However, for epoxy-epoxy systems, increasing temperature progresses the cure; therefore, the extent of interdiffusion is ultimately limited by network formation. Epoxy-thermoplastic adhesion theory suggests that adhesion is developed through interdiffusion, especially while both polymers are at temperature above their respective T_{g}.[59] This can be achieved by heating above thermoplastic T_{g} and applying the epoxy resin during the liquid cure phase. Vandi *et al.* state that interface formation is initially dictated by polymer compatibility and wettability, followed by interdiffusion which can ultimately lead to the formation of an interphase.

The initial experiments showed that the Raman technique was able to monitor ingress of a model compound (4-CIPGE) into ambient-cured epoxy film. Unfortunately, it could not be used with 35% stoichiometry systems because of the high fluorescence levels in this formulation, but the influence of process parameters on ingress into 100% stoichiometry film could be studied. In the following sections, the dependence of ingress on cure temperature, overcoating interval and cure humidity are presented thus providing new results in an unexplored area.

6.2.1.1.1 Short Overcoating Interval (1-day)

In the previous section, it was shown that interdiffusion is possible in partially cured epoxy amine systems and is likely to be important in the formation of interfaces that bond layers. It was hypothesised that this mechanism was possible in the ambient cured systems but not the post cured systems due to lower conversion achieved (and T_{g}) in the ambient cured systems. Therefore, ingress depth of 4-ClPGE into the ambient cured first layer was characterised as a function of cure temperature and overcoating interval, as these cure conditions are expected to influence extent of conversion. Overcoating interval is the duration of time allocated to the ambient cure phase before overcoating with the second coat.

100% stoichiometry films were cured at 25 or 35 °C and overcoated after 1-day with 4-ClPGE. Following the same method explained in Section 6.2.1.1, sectioned samples were produced, and spectra collected at increasing sample depth. In all cases the variation in Raman signal followed a similar pattern to that shown in Figure 6.7. For clarity, only the data for the depth ranges over which the signal changes significantly, corresponding to the extent of 4-ClPGE penetration into each film, are shown. Figure 6.11 and Figure 6.12 display the Raman shift intensity of 4-ClPGE at increasing depth into epoxy films cured at 25 °C (Figure 6.11) and 35 °C (Figure 6.12).

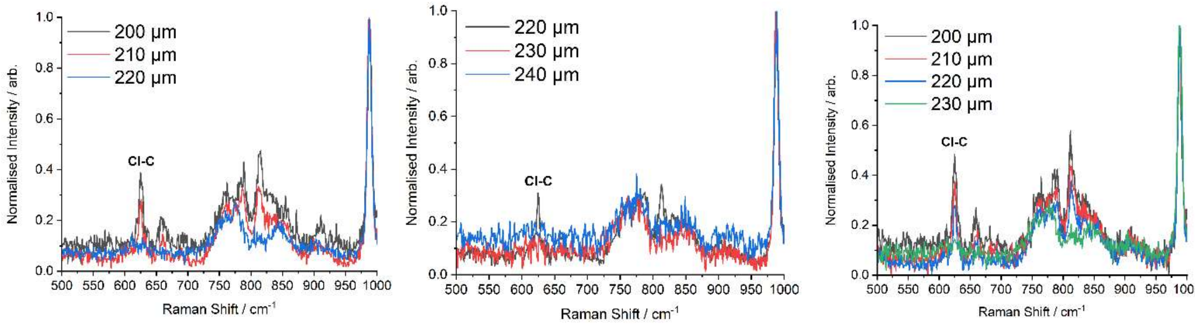

Figure 6.11: Raman shifts of a sectioned epoxy film (3 repeats) at increasing depths from the surface, post ingress of 4-ClPGE. (Cure conditions: 25 °C, 40% RH, 1-day OC interval; Normalisation peak: ~ 980 cm^{-1}).

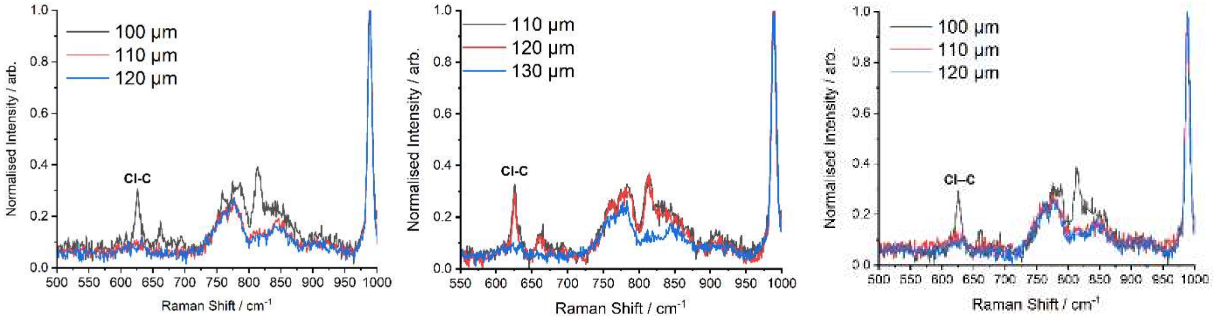

Figure 6.12: Raman shifts of a sectioned epoxy film (3 repeats) at increasing depths from the surface, post ingress of 4-ClPGE. (Cure conditions: 35 °C, 40% RH, 1-day OC interval).

Data was collected over a 100 – 3500 cm^{-1} range, but has only been presented between 550 – 1000 cm^{-1} as this was the range over which signals related to 4-ClPGE were visible. The sample depth at which the 4-ClPGE associated signal disappeared was taken as the limit of penetration of 4-ClPGE into the sample. 4-ClPGE was able to penetrate 210 - 220 µm into the film cured at 25 °C (Figure 6.11). Film thickness was originally ~ 180 µm but swelled to 250 µm post ingress of 4-ClPGE. This represents an 84 - 88% penetration depth into the film (penetration depth (%) = (total distance ingressed/final film thickness)*100). Extent of ingress on this scale is comparable to that of interdiffused epoxy-thermoplastic interphases as interphase width has been shown to range from a few microns up to 300 µm.[57,58,63] 4-ClPGE was able to penetrate 100 - 120 µm into the film cured at 35 °C (Figure 6.12). No difference in film thickness (swell) was observed in this film so film penetration depth was 56 – 66%. As swelling was only observed in one of the samples, this may suggest either a softer matrix which is more readily swollen, an element of experimental error, or perhaps that there is a critical threshold of free volume, which must be first occupied to enable swelling; further repeats would be required to determine this hypothesis. The 35 °C cured system saw decreased ingress depth compared to the 25 °C cured system. As shown in Chapter 5, the 35 °C cured system has a higher extent of conversion than the 25 °C cured system (DMA determined T_g: 25 °C cure = 68 °C; 35 °C cure = 78 °C). Therefore, the 35 °C cured system likely achieves greater network rigidity, which decreases the ease of penetrant mobility during ingress, and therefore decreases diffusion depth. This may explain the decrease in extent of 4-ClPGE diffusion seen in the 35 °C system and agrees with the hypothesis proposed in Section 6.2.1.1. In both samples, sample thickness exceeded diffusion distance of the 4-ClPGE indicating that there are at least two regions present in the sample: a region unaffected by diffusion of 4-ClPGE and a region containing interdiffused material (interphase).

6.2.1.1.2 Maximum Advised Overcoating Interval (3- or 4-day)

Samples were produced using the same method described in Section 6.2.1.1.1 but instead allowed to cure for a longer overcoating interval (25 °C cure = 4 days; 35 °C cure = 3 days).[172] Data was collected as described in Section 6.2.1.1.1 and displayed in Figure 6.13 (25 °C cure) and Figure 6.14 (35 °C cure).

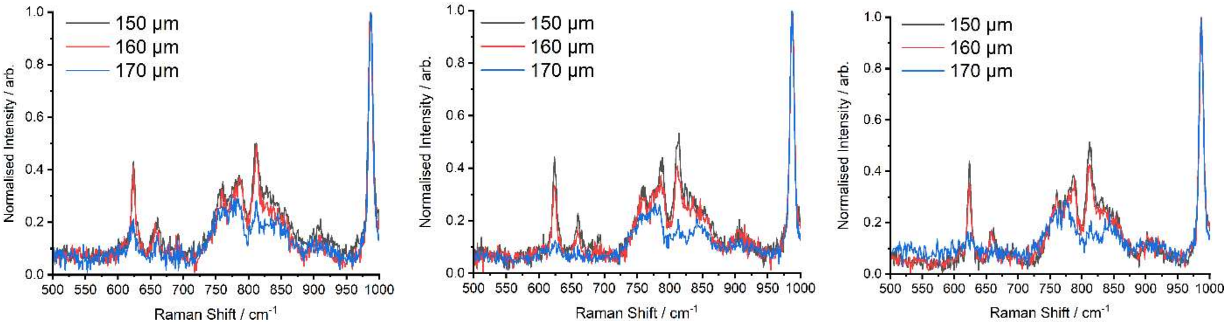

Figure 6.13: Raman shifts of a sectioned epoxy film (3 repeats) at increasing depths from the surface, post ingress of 4-ClPGE. (Cure conditions: 25 °C, 40% RH, 4-day OC interval).

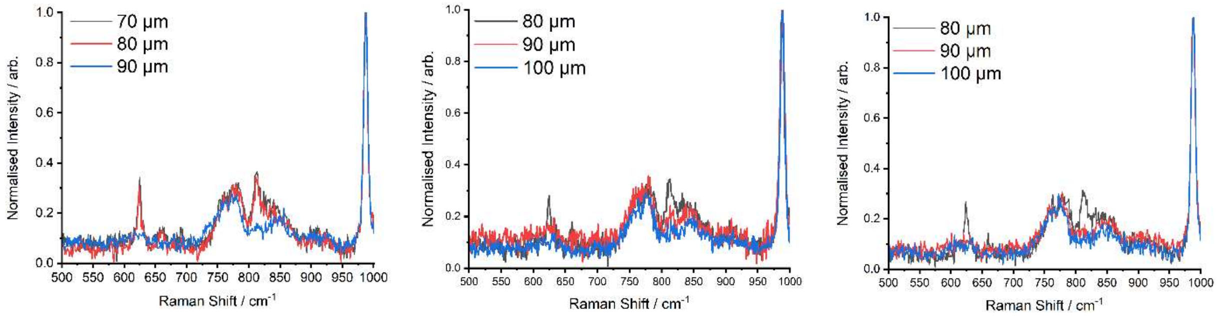

Figure 6.14: Raman shifts of a sectioned epoxy film (3 repeats) at increasing depths from the surface, post ingress of 4-ClPGE. (Cure conditions: 35 °C, 40% RH, 3-day OC interval).

4-CIPGE was able to penetrate significantly further (160 um) into films cured at 25 °C than into the equivalent films cured at 35 °C. This suggests that despite the slightly longer cure time at the lower temperature, the extent of cure at 35 °C is greater and the resulting coating is less readily penetrated by the probe molecules. This trend was consistent with the data reported for the 1-day overcoating interval which also showed that ingress depth decreased with increasing cure temperature. However, in the 1-day OC interval films, at both cure temperatures, the extent of ingress was higher compared to that observed in the films with a longer 3-/4-day OC interval. This was likely as due to decreased conversion achieved (and therefore lower T_g) in the 1-day OC interval systems, making internal molecular migration more favourable.

6.2.1.1.3 Long Overcoating Interval (7-day)

Samples were produced using the same method previously described, but instead with a longer overcoating interval of 7 days. Data was collected as before and is displayed in Figure 6.15 (25 °C cure) and Figure 6.16 (35 °C cure).

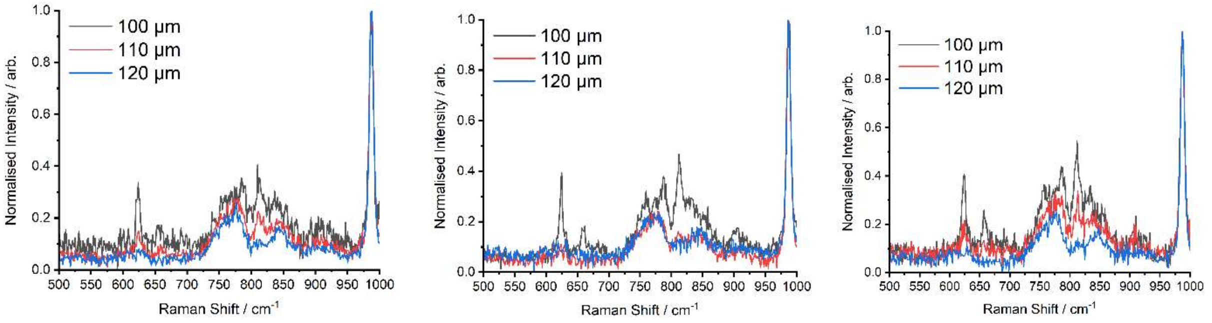

Figure 6.15: Raman shifts of a sectioned epoxy film (3 repeats) at increasing depths from the surface, post ingress of 4-ClPGE. (Cure conditions: 25 °C, 40% RH, 7-day OC interval).

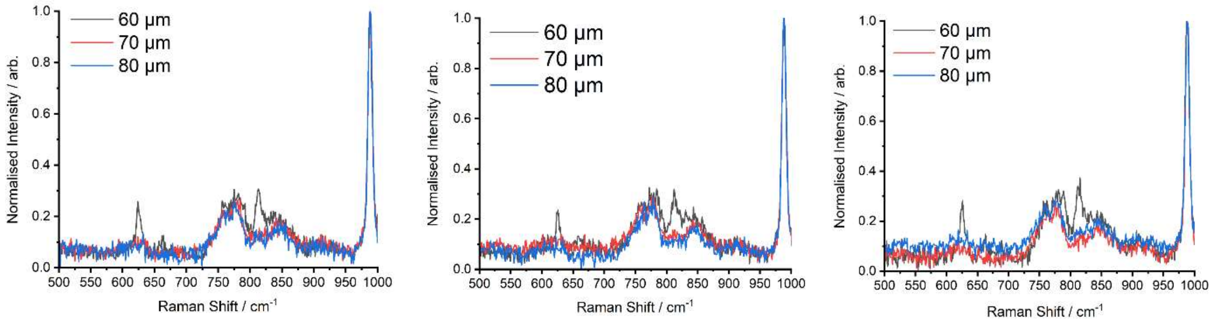

Figure 6.16: Raman shifts of a sectioned epoxy film (3 repeats) at increasing depths from the surface, post ingress of 4-ClPGE. (Cure conditions: 35 °C, 40% RH, 7-day OC interval).

As shown in Figure 6.15 and Figure 6.16, curing at 25 °C lead to a 4-ClPGE ingress depth of 100 – 110 µm, which decreased to 60 µm in the 35 °C cure films. This was consistent with the trends observed in the 1-day and 3/4-day OC interval films. For both stoichiometries, the further increase in overcoat interval slightly reduces the range of 4-ClPGE penetration. This supports the previous hypothesis, that increasing the OC interval increased the conversion achieved in the first coat and thus decreased internal molecular migration and interlayer diffusion potential.

6.2.1.1.4 Ingress into highly carbamated film

In Chapter 5 we showed how extent of carbamation can be controlled through considering the cure conditions and stoichiometry used, but the exact reason to why carbamation causes a weaker boundary layer is less clear. To investigate the impact of carbamate formation on the interphase width of interdiffused epoxies, a similar 4-ClPGE ingress study was carried out. Samples were produced as described in Section 6.2.1.1.1, but instead RH was increased to 80% during the first layer ambient cure stage, thus increasing the likelihood of carbamate formation, as shown in Section 5.2.1.1. Figure 6.17 displays the Raman shift intensity of 4-ClPGE at increasing depth into the epoxy films cured at 80% RH.

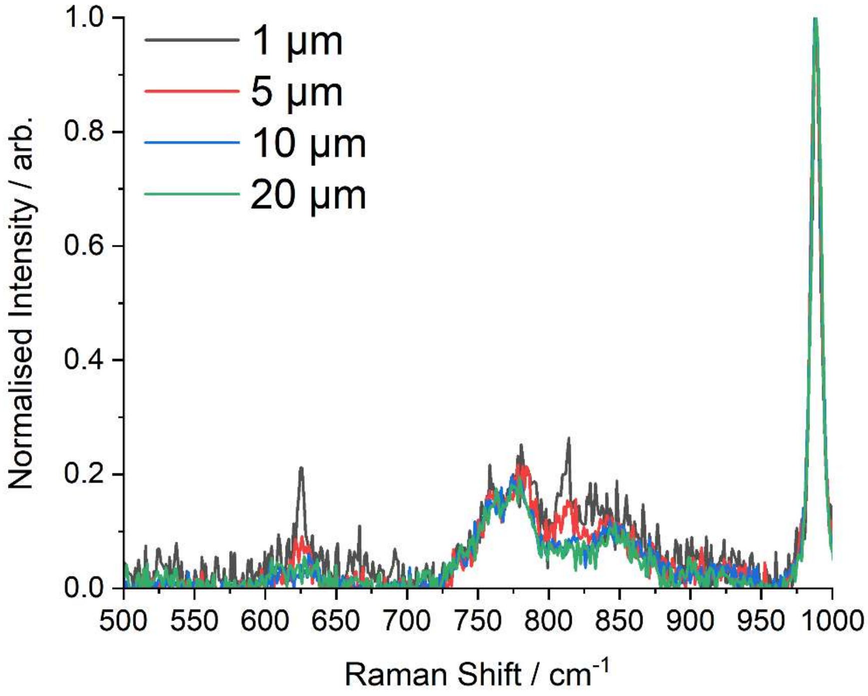

Figure 6.17: Raman shifts of a sectioned, 80% RH cured epoxy film at increasing depths from the surface, post ingress of 4-ClPGE. (Cure conditions: 25 °C, 80% RH).

4-ClPGE was only significantly detectable at a depth of around 1 µm into the first layer, significantly lower than all other ambient cured systems studied. There is a slight signal at 5 µm, but this could be due to the beam partially illuminating the surface layer.[168] If 4-ClPGE had penetrated the surface layer, based on the proven mobility of 4-ClPGE within these samples, it would be expected that 4-ClPGE would diffuse further than 5 µm after penetration. Therefore, it is probable that the carbamate is a complete barrier and contributes towards intercoat adhesion failure by suppressing interdiffusion of sequential layers. In the future, it would be interesting to explore whether the barrier properties of carbamate extend to other probe molecules with differing size or hydrophobicity.

While previous interface characterisation studies of similar epoxy systems (such as that between epoxy resins and thermoplastic substrates) have shown that significant interdiffusion between epoxy systems and a probe molecule that is similar in size to 4-ClPGE is possible;[60,62] no academic literature could be found, which characterised bilayer epoxy interface formation, and this is a promising new approach to investigate surfaces and interfaces of epoxy resins that are otherwise quite intractable. Based on the Raman studies with 4-CIPGE ingress into epoxy coatings, the following can be concluded.

- Ambient cured bilayer epoxy interphases are likely to form *via* interdiffusion.
- Interdiffusion was observed in the ambient cured films but not in the post cured films indicating that ingress is more favourable when the conversion achieved in the first coat prior to overcoating is lower, likely related to decreased first coat T_g and network mobility.
- Increasing the cure temperature from 25 °C to 35 °C reduced the average ingress depth range by up to tens of microns, depending on the overcoating interval.
- OC interval duration correlated with extent of ingress, as increasing the OC from 1 day to 7 days decreased extent of ingress by tens of microns.
- Increasing the RH most significantly reduced extent of diffusion, with the presence of carbamate almost completely suppressing it.

A summary of all results is given in Table 6.2.

Table 6.2: The extent of ingress of 4-ClPGE into different epoxy systems.

Cure Conditions	Ingress depth of 4-ClPGE / µm	Coating Thickness post Ingress / µm	Average Ingress depth of 4-ClPGE / %
25 °C, 1-day OC interval	215 ± 5	250	87
35 °C, 1-day OC interval	110 ± 10	180	59
25 °C, 4-day OC interval	160 ± 5	220	73
35 °C, 3-day OC interval	80 ± 5	180	44
25 °C, 7-day OC interval	105 ± 5	180	57
35 °C, 7-day OC interval	60 ± 5	150	40
35 °C, 80% RH	5 ± 5	180	3
Post Cured Control	0 ± 5	200	0

6.2.2 Epoxy-Epoxy Interface Mapping with CD_3OD using Raman Spectroscopy

As shown in section 6.2.1, interdiffusion into part-cured epoxy systems is possible and is likely to be important in the formation of interfaces that bond layers. Although not explicitly studied, it is worth noting that perhaps the diffusion of first coat sol (remembering these molecules still possess reactive functional groups) and elastically inactive (dangling) chains (again possessing unreacted functionality) into the second coat may equally occur, and reactions of these species with the second coat molecules, may lead to broadening of the interfacial region. While very few studies, with the exception of the work of Weeks *et al.*,[173] have investigated the cohesive strength of partially cured epoxies, it has been hypothesised that this interfacial region may sometimes have areas of decreased crosslink density, where adhesion failure may initiate and propagate.[63] For example, as well as chain intermingling from the first coat into the second coat, the stoichiometry throughout the interphase may also be determined by the first coat stoichiometry upon overcoating and the differing solubilities of the individual second coat components through the first coat, and their diffusion rates. As shown in Figure 6.18, the Hansen solubility parameters, which can be used as part of a prediction of diffusion, significantly vary between the different second coat components, and so differing diffusion rates could be expected. Ultimately, this could lead to areas of insufficient curing agent, thus reducing crosslink density whereby solvent can accumulate after saturation. Even here, there is some doubt as the post-cure conditions may help promote crosslinking side-reactions. For example, within the distribution of epoxy bearing molecules, the larger, multifunctional species, which are the most able to form networks would be expected to diffuse more slowly than the smaller bis-epoxy molecules.

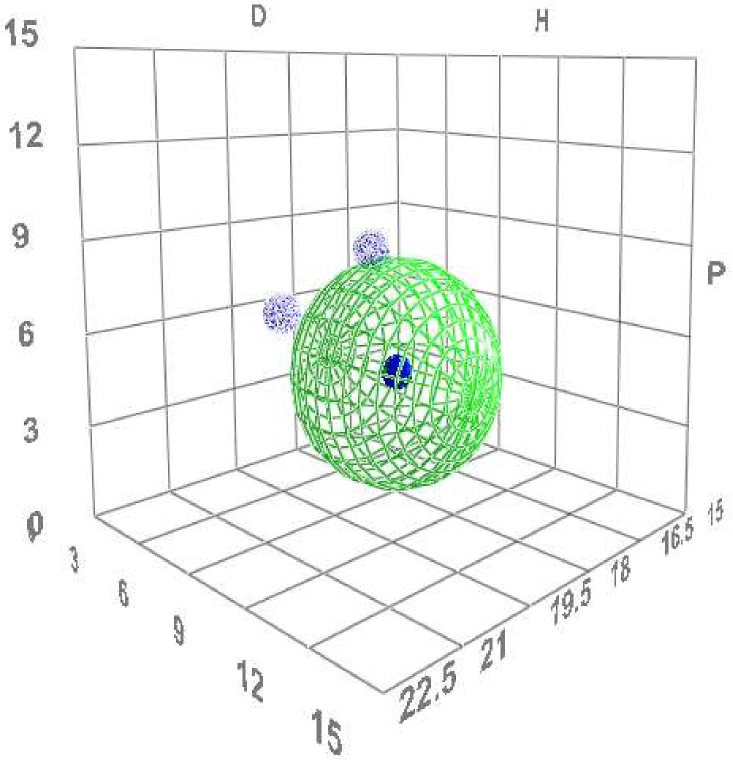

Figure 6.18: HSPiP generated Hansen solubility parameter plot displaying PAC-M (blue full circle), RDGE (blue mesh circle right), D.E.N. 431 (blue mesh circle left) and the measure of similarity (green wireframe circle).

The direct characterisation of crosslink density is difficult using current analytical methods and so instead is often measured indirectly; swelling analysis is commonly carried out as a means of measuring crosslink density in bulk materials.[174] Here, the idea is to apply this method locally with spatially resolved measurements of swelling to quantify solvent accumulation within the 2-layer samples using vertical mapping techniques, after solvent ingress. 100% stoichiometry, 2-layer samples were cured at 25 °C or 35 °C followed by post curing at 80 °C, as described in Section 3.2.3. CD_3OD was then allowed to ingress until saturation. Following ingress, the 2-layer films were sectioned using a scalpel blade and Raman mapping carried out at 10-micron intervals across the newly exposed cross section.

Prior to the mapping experiment, the Raman spectrum of a clean epoxy system was first compared to the Raman spectrum of the same epoxy system post saturation with CD_3OD (Figure 6.19). These spectra were normalised using the peak associated with the saturated CH bond at ~ 2924 cm^{-1}. This allowed for the identification of peaks unique to the CD_3OD, which were therefore used to identify CD_3OD within the epoxy during Raman mapping.

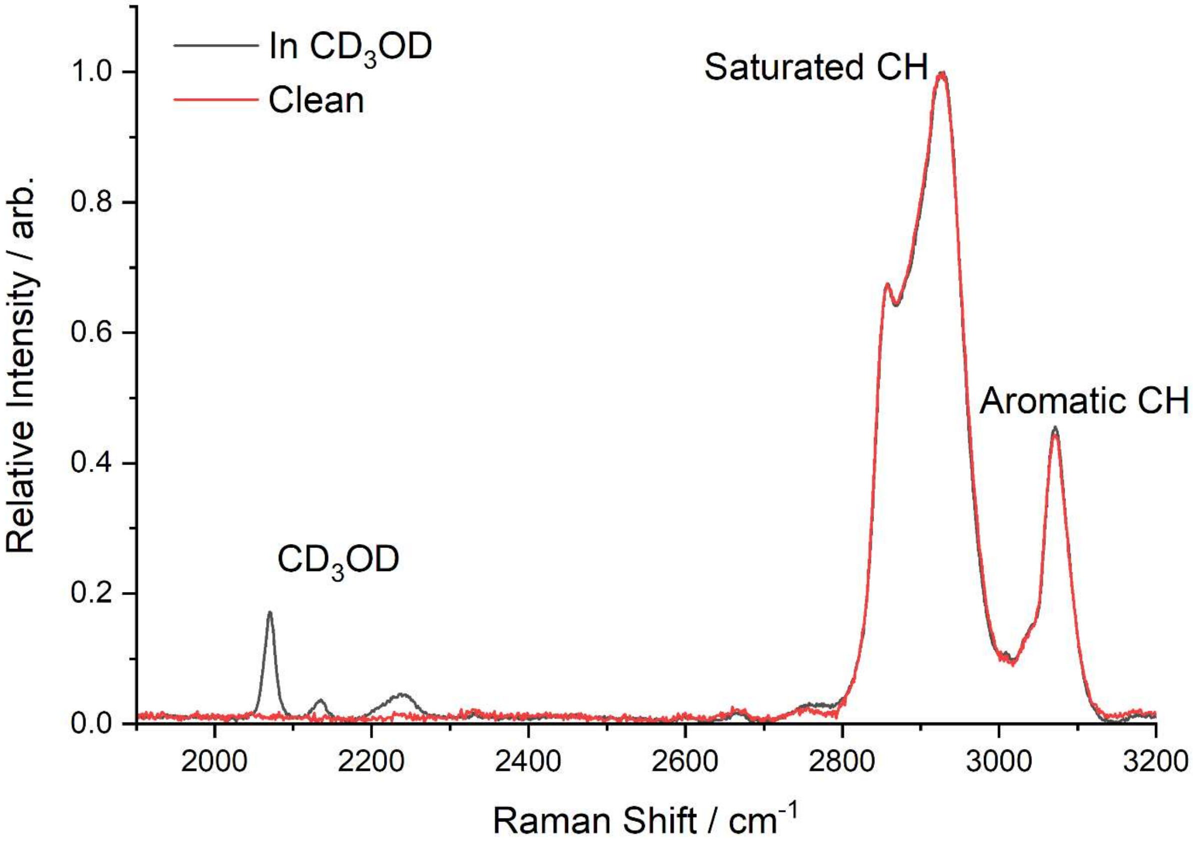

Figure 6.19: Raman shifts of a 100% stoichiometry epoxy resin film (red) and the same film post immersion in CD_3OD, 1900 – 3200 cm^{-1}.

As shown in Figure 6.19, there are peaks visible between 2000 - 2300 cm^{-1} in the CD_3OD saturated system, but not in the clean system indicating that these peaks correspond to bonds present in the CD_3OD. The peak at ~ 2071 cm^{-1} had the greatest intensity and so was used to track CD_3OD presence within the epoxy film, during Raman mapping. As peak intensity correlates directly with bond concentration, the comparative intensity of the 2071 cm^{-1} CD_3OD peak recorded at each 10 µm interval along the cross section provided a relative measure of the CD_3OD concentration over this interval. This is shown in Figure 6.20 as the relative CD_3OD concentration is plotted as a function of increasing film depth, throughout 100% stoichiometry films, which were cured at 25 °C for 4 days or 35 °C for 3 days, prior to post curing at 80 °C for 16 hours, as described in Section 3.14.

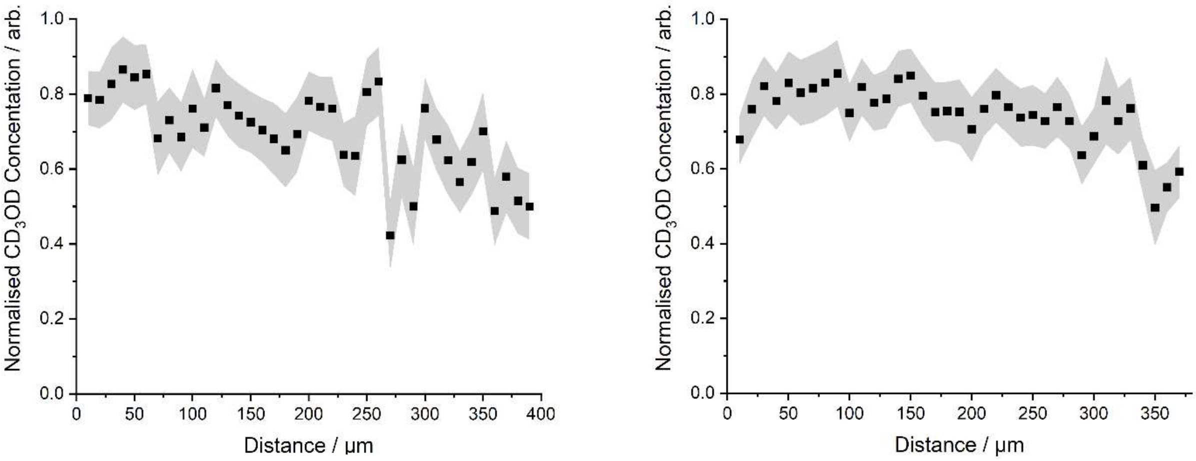

Figure 6.20: Normalised CD_3OD concentration as a function of film depth in the 100% stoichiometry, 25 °C (left) and 35 °C (right) films (note both films were post-cured at 80 °C).

Should variation in ambient cure temperature influence the crosslink density across the interface, this could be identified using Figure 6.20, as solvent will accumulate at areas of lower crosslink density thus causing a spike in CD_3OD concentration. Overall, it appeared as though the system cured at 35 °C achieved a more homogeneous crosslink density as CD_3OD concentration fluctuated less throughout the film. However, this may be related to variation in signal noise and so cannot be definitively concluded; the grey regions correspond to uncertainty calculated at two standard deviations (95% confidence interval). It can be noted that there is a slight downward trend in both datasets, which may be caused by solvent loss due to evaporation during the experiment. In both samples, there are no obvious signs of large decreases in crosslink density, such as a prominent concentration spike, around the film centre compared to the rest of the film. This indicates that at this resolution (10 µm), there is no significant variation in crosslink density between the interphase and sample bulk. Therefore, a technique with greater resolution (1 µm), that of particle induced X-ray emission spectroscopy, or PIXE, was also utilised to indirectly map network crosslink density.

6.2.3 Epoxy-Epoxy Interface Mapping with C_2H_5BrO using PIXE Spectroscopy

Particle induced X-ray emission (PIXE) spectroscopy is a form of ion beam analysis (IBA) used for elemental analysis of a sample. By scanning across a sectioned epoxy sample, following ingress of a solvent with a unique elemental component, this element and its concentration can be mapped throughout the sample. The concept is like that of the Raman mapping used in Section 6.2.2, but is advantageous for the systems used in this research as PIXE can analyse any stoichiometry because fluorescence has no impact on the X-ray spectrum that is measured. In addition, PIXE could be carried out at 1 micron-intervals, thus more accurately resolving the data.

Data were obtained by Dr Catia Costa at the University of Surrey Ion Beam Centre. Measurements were carried out on the following systems and overcoating intervals:

- 2-layer, 100% stoichiometry, 25 °C cure temperature, 4-day OC interval, 80 °C post cure
- 2-layer, 100% stoichiometry, 35 °C cure temperature, 3-day OC interval, 80 °C post cure
- 2-layer, 35% stoichiometry, 25 °C cure temperature, 4-day OC interval, 80 °C post cure *
- 2-layer, 35% stoichiometry, 35 °C cure temperature, 3-day OC interval, 80 °C post cure *

Samples marked with an asterisk will not be discussed but can be found in the appendix. Due to limited access to the facility and problems with the facility setup, a limited set of data was obtained and further measurements on marked samples would be required to determine the impact of variation in stoichiometry on crosslink density. To produce the samples listed above, 35% and 100% stoichiometry, 2-layer samples were cured at 25 °C or 35 °C followed by post curing, as described in Section 3.2.3. 2-bromoethanol was then allowed to ingress until saturation, defined by the system achieving constant mass during gravimetric analysis (~ 6% mass increase). 2-Bromoethanol was capable of diffusing into the post-cured systems as polymeric void volume (~ 80 Å^3, Figure 5.35) exceeded the molecular volume of 2-bromoethanol (72.9 Å^3; determined using HSPiP).[96] In Section 6.2.2, CD_3OD was used as the probe solvent, however as ion beams cause heat transfer to the sample during measurement, and CD_3OD is highly volatile, a more involatile compound, capable of yielding detectable X-rays, was instead needed to enable the experiment; 2-bromoethanol was used. The bromine atom is unique in the materials being analysed and so could be used to identify the depth-dependence of solvent ingress. Following saturation, the 2-layer films were sectioned using a scalpel blade and PIXE spectra collected at 1-micron intervals across the newly exposed cross section. PIXE spectra contain peaks which are characteristic of the elements present in the sample. Figure 6.21 shows an example of three of these X-ray spectra taken at different points across a single sample; 010 (black), 011 (blue), and 012 (red), whereby the respective spectra collection locations are labelled on the corresponding PIXE map.

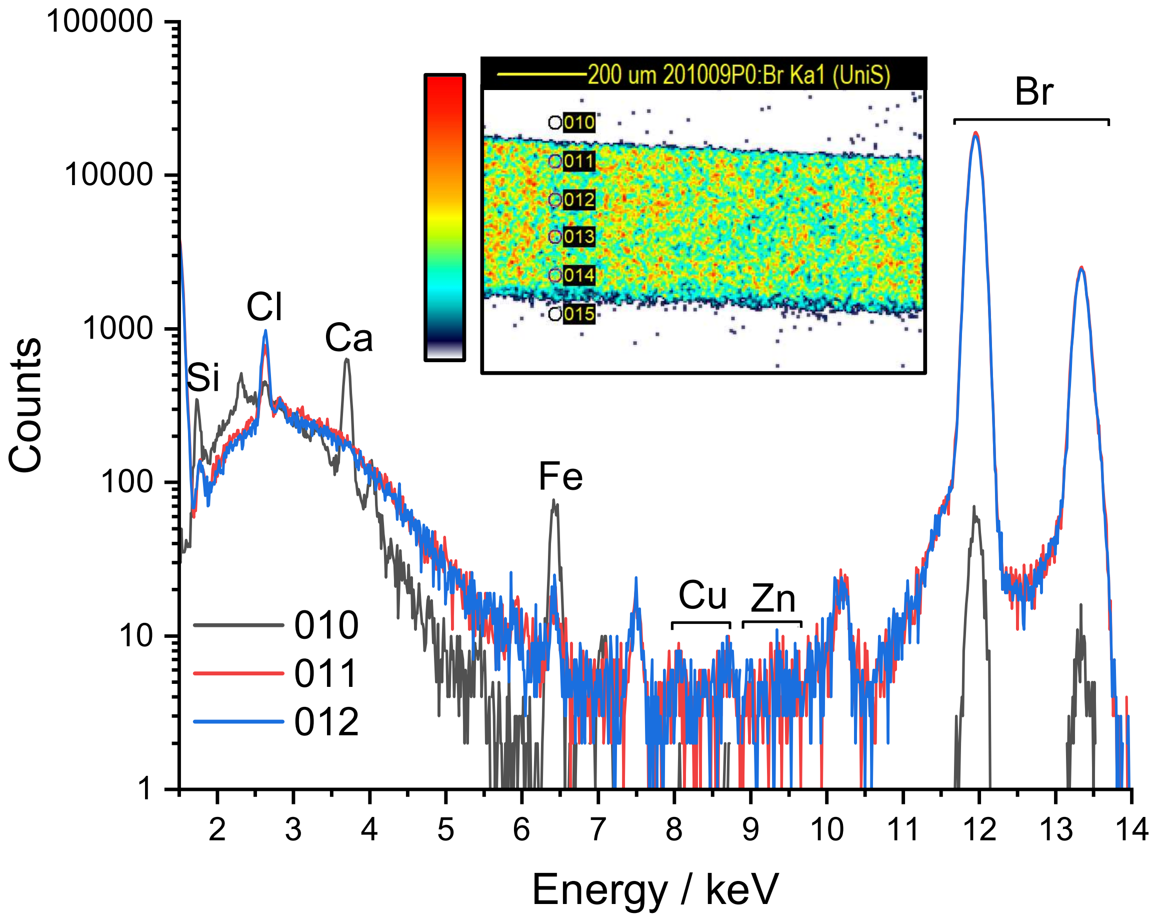

Figure 6.21: X-ray spectra of a 2-bromoethanol saturated epoxy film and the surrounding area. Location of measurement is detailed in the accompanying Br Kα emission PIXE map of the film; colour indicates relative number of counts (high = red; low = white).

As shown in Figure 6.21, elements larger than silicon give rise to unique peak patterns in the X-ray spectra, thus allowing for elemental identification within a sample. Peak identity, as labelled in Figure 6.21, was confirmed using a BCR 126A standard.[175,176] As the epoxy-amine systems studied are organic (C, H, O, N) and so their elemental basis is low-Z, they are not visible in the presented energy range (1 – 14 keV), as this range only correlates to elements of relatively larger atomic mass. The energy of photons emitted from elements smaller than sodium are not normally detectable with PIXE. The bromine peaks displayed the highest intensity as they correlate to the 2-bromoethanol saturated within the film. However, it should be noted that there are many different elements detected in the spectra compared to the elemental composition of the system studied. Metallic elements, such as iron and copper are visible as metal plates were used to hold the sample in place, and copper is a common material found in vacuum chambers, such as for gasket seals, and it is possible that stray beams encountered these areas. (Note that the intensity scale is logarithmic and so sensitively highlights small signals from these species.) This also explains the presence of chlorine, which could arise from several sources but has no bearing on the measurement of brominated solvent concentration in these coatings.

By correlating relative X-ray spectrum peak intensity to elemental concentration, the concentration of the different elements can be mapped at each micron interval producing the PIXE maps shown in Figure 6.22.

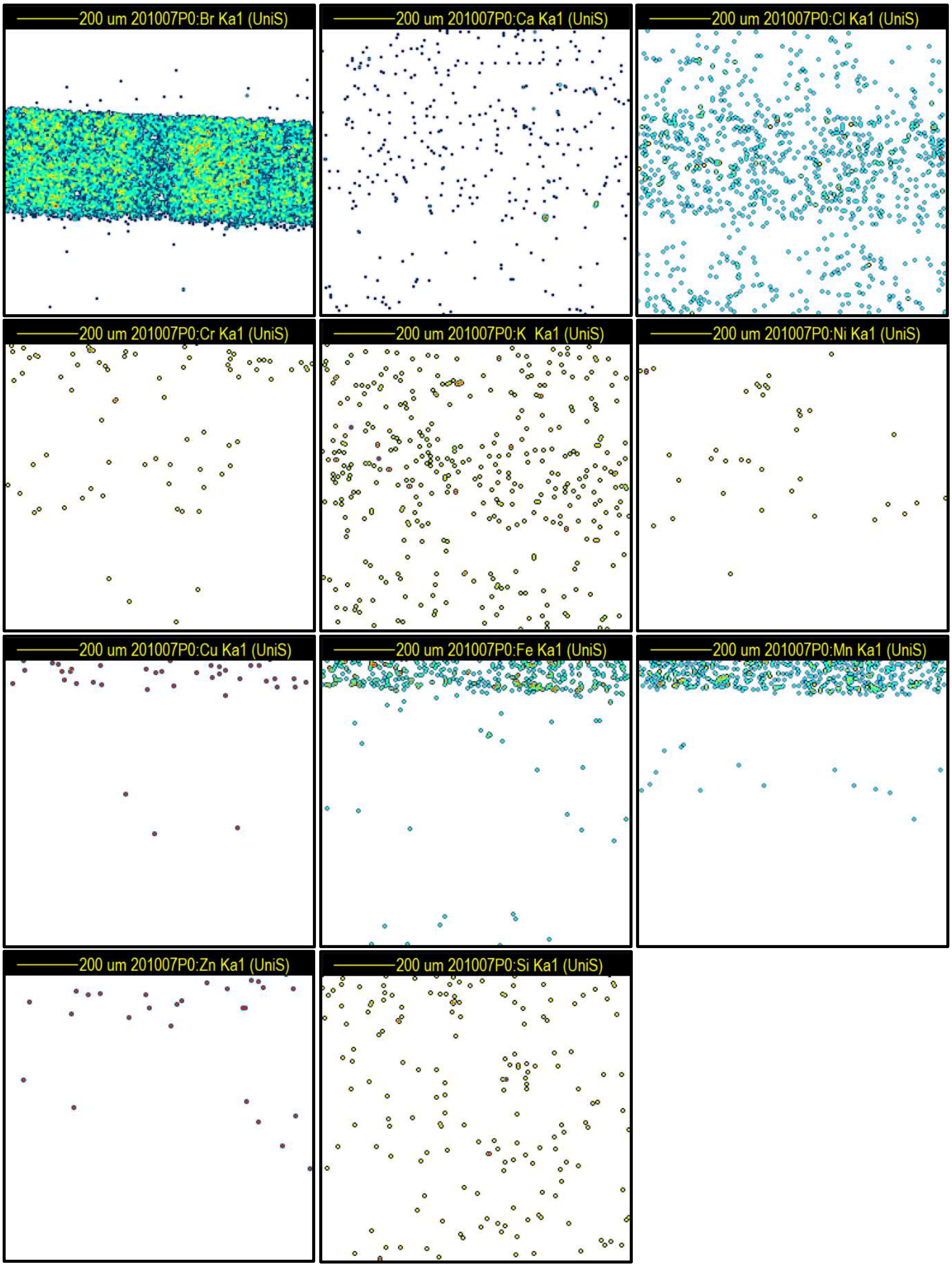

Figure 6.22: PIXE maps of each of the high-Z elements.

As is displayed in Figure 6.22, the PIXE map associated with bromine shows how 2-bromoethanol has diffused to all areas of the films producing a 'sketch' of the film. Excluding bromine, chlorine concentration was relatively high compared to all other elements and tends to be co-located with the bromine in the coating rather than the surroundings, thus highlighting the sensitivity of PIXE to chlorine. Iron and manganese showed a high concentration only at the edge of the frame as these elements were associated with the metal sample holders. All other PIXE maps displayed insignificant elemental concentration.

The bromine peak intensity of the X-ray spectra collected at 1-micron intervals across the 100% stoichiometry, 25 °C cure temperature film is displayed in Figure 6.23 – 25. Each figure corresponds to a repeat of the same sample whereby data has been collected at a separate interval.

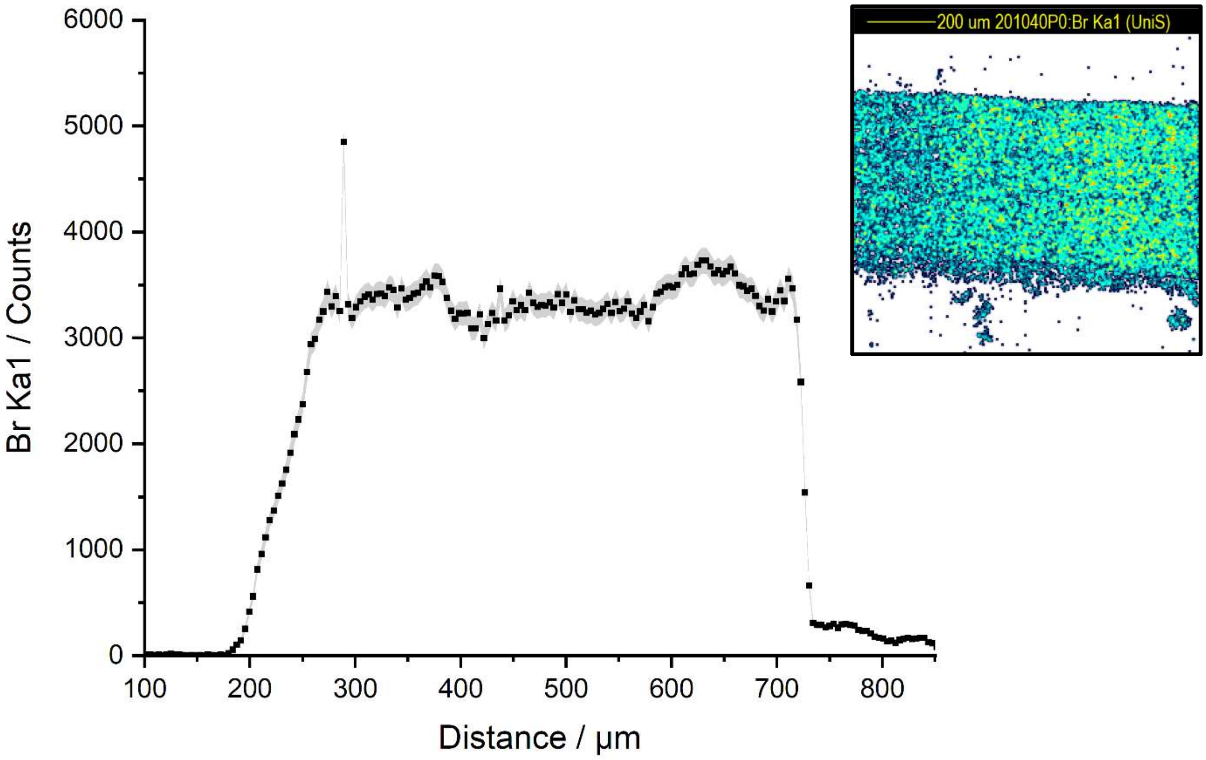

Figure 6.23: Br signal intensity as a function of film depth and accompanying PIXE map (system: 100% stoichiometry, 25 °C cure temperature – repeat 1).

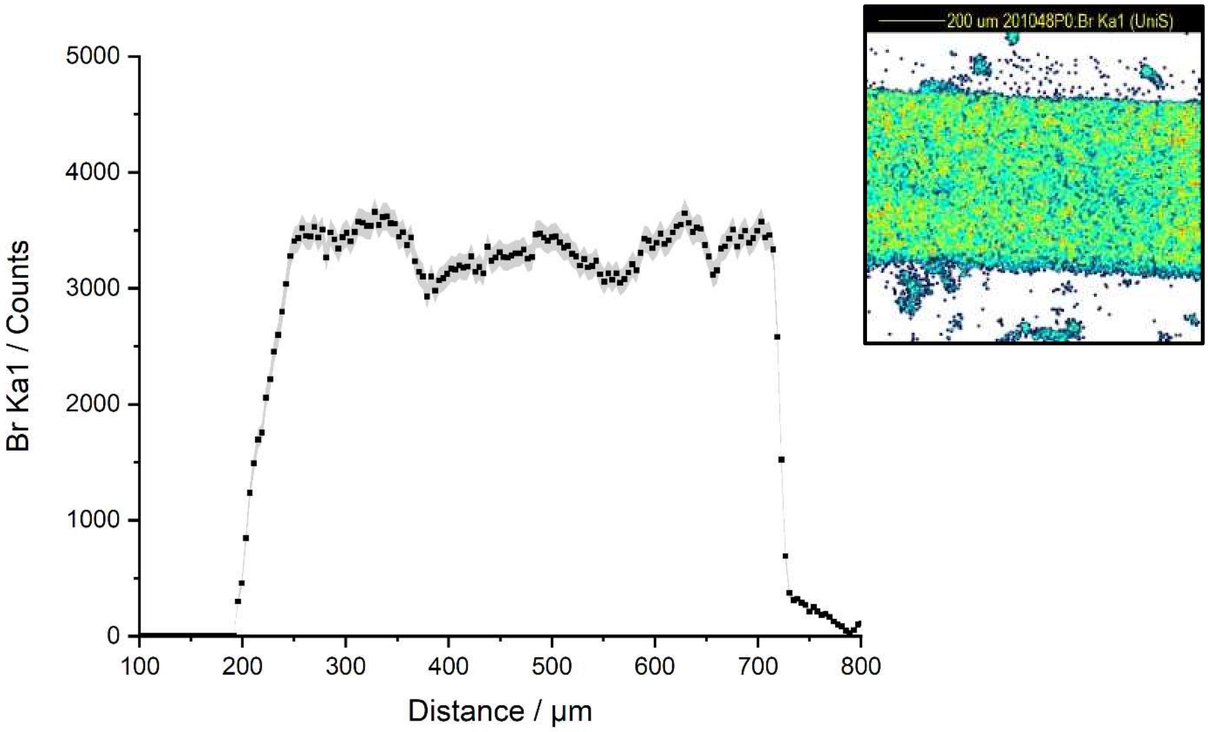

Figure 6.24: Br signal intensity as a function of film depth and accompanying PIXE map (system: 100% stoichiometry, 25 °C cure temperature – repeat 2).

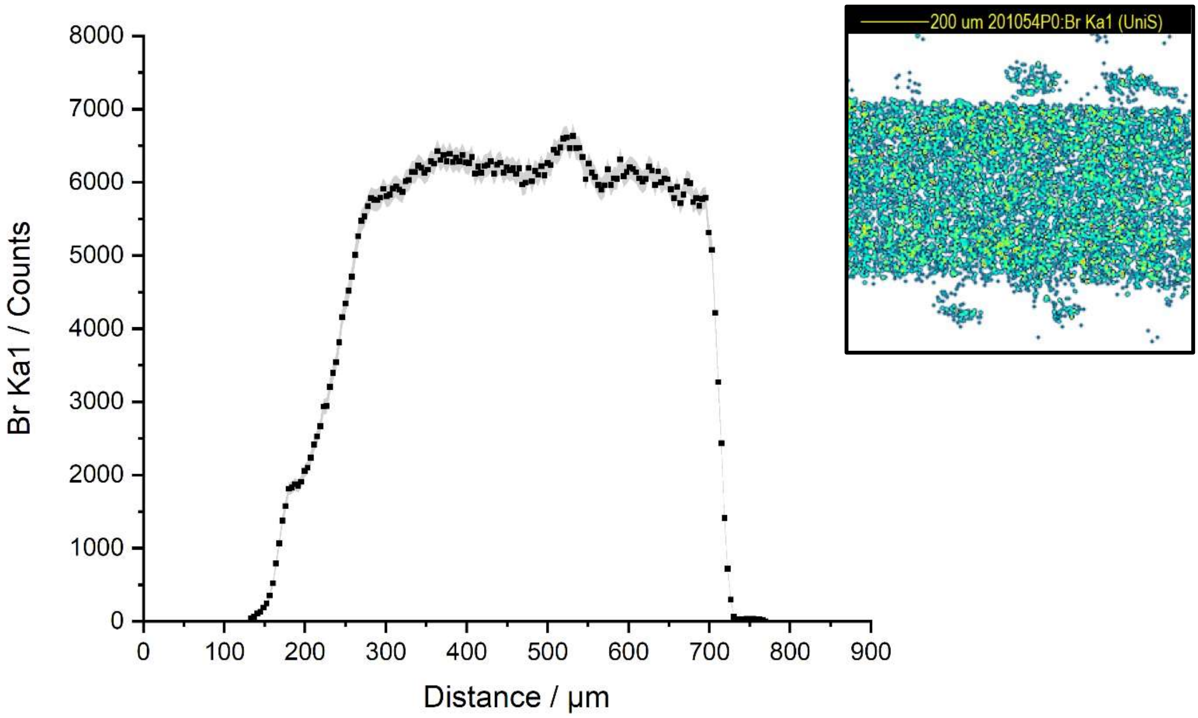

Figure 6.25: Br signal intensity as a function of film depth and accompanying PIXE map (system: 100% stoichiometry, 25 °C cure temperature – repeat 3).

Repeat 1 (Figure 6.23) showed that there is some statistically significant variation in solvent accumulation throughout the film, but showed little correlation with film depth. The uncertainty of each point (grey) was defined by 2 standard deviations providing 95% confidence. There is a single point near the film edge where signal intensity is particularly high, but this was likely an anomalous result corresponding to perhaps an error in the charge counting meaning more beam was delivered to this point than the others, or X-rays generated by sparking discharge in the endstation. The most significant finding from this plot is that there is no obvious region of decreased crosslink density within the interphase (film centre), which would be evident as a spike in bromine intensity and a band (horizontal stripe) in the inset PIXE-map. This therefore indicates that on the micron scale, crosslink density between interphase and bulk is homogenous. Repeat 2 (Figure 6.24) showed the greatest fluctuation in bromine concentration, but as was the case with repeat 1 showed little correlation with film depth. Repeat 3 (Figure 6.25) showed that the bromine concentration was consistent throughout the film, except for a ~ 100 µm region in the centre of the film where intensity peaks. Section 6.2.1.1.2 indicates that this would be within the interphase area and thus may be evidence of a decreased crosslink density region allowing for solvent accumulation. This decrease in system crosslink density homogeneity could suggest potential areas of weakness whereby future repetitive loading and unloading of solvent could further suppress crosslink density in this area. Over time this may then propagate further until adhesion failure occurs. However, the absence of any visible horizontal stripe in the PIXE-map shows that while there is some variation in the intensity displayed by the Br counts-distance curves, there is no correlation to indicate varying solvent concentration at the interphase. Therefore, while the Br counts-distance curves are useful because they give data on a quantitative scale, they may not always be representative of the composition profile. In addition, the observed trend is not seen in any of the other repeats, indicating two possibilities; either the result of repeat 3 is anomalous and so should be rejected, or that the result is real and the trends regarding interphase crosslink density are not consistent throughout the entire film, thus explaining the variability seen over the 3 repeats. Therefore, further repeats are required to thoroughly characterize crosslink density of this film.

It can be noted that the overall bromine signal intensity varied across the three repeats. This was likely due to evaporation of the bromine solvent which occurred prior to or during data collection. In a future experiment, this could be quantitatively confirmed by carrying out a Rutherford backscattering (RBS) IBA experiment to determine the ratio of bromine to carbon in each sample.

The same PIXE experiment was carried out using 100 % stoichiometry films cured at 35 °C. Figure 6.26 – 28 display the corresponding figures whereby each figure is a repeat of the same sample in which data was collected at a separate sample location.

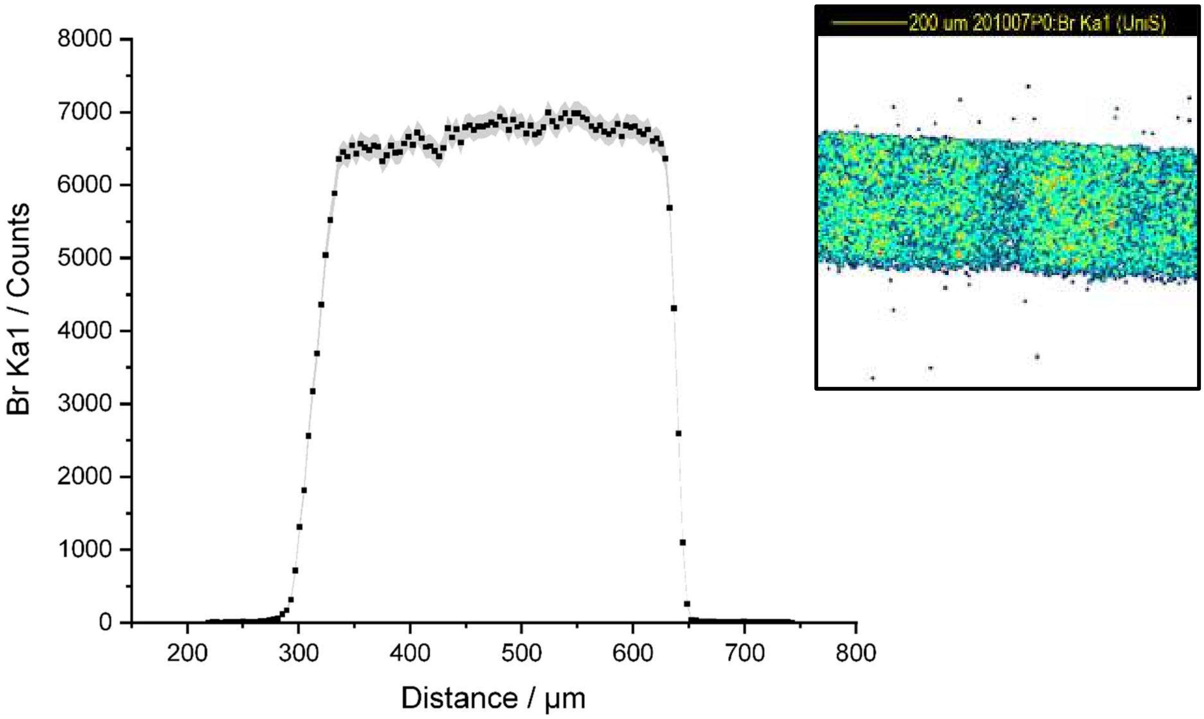

Figure 6.26: Br signal intensity as a function of film depth and accompanying PIXE map (system: 100% stoichiometry, 35 °C cure temperature – repeat 1).

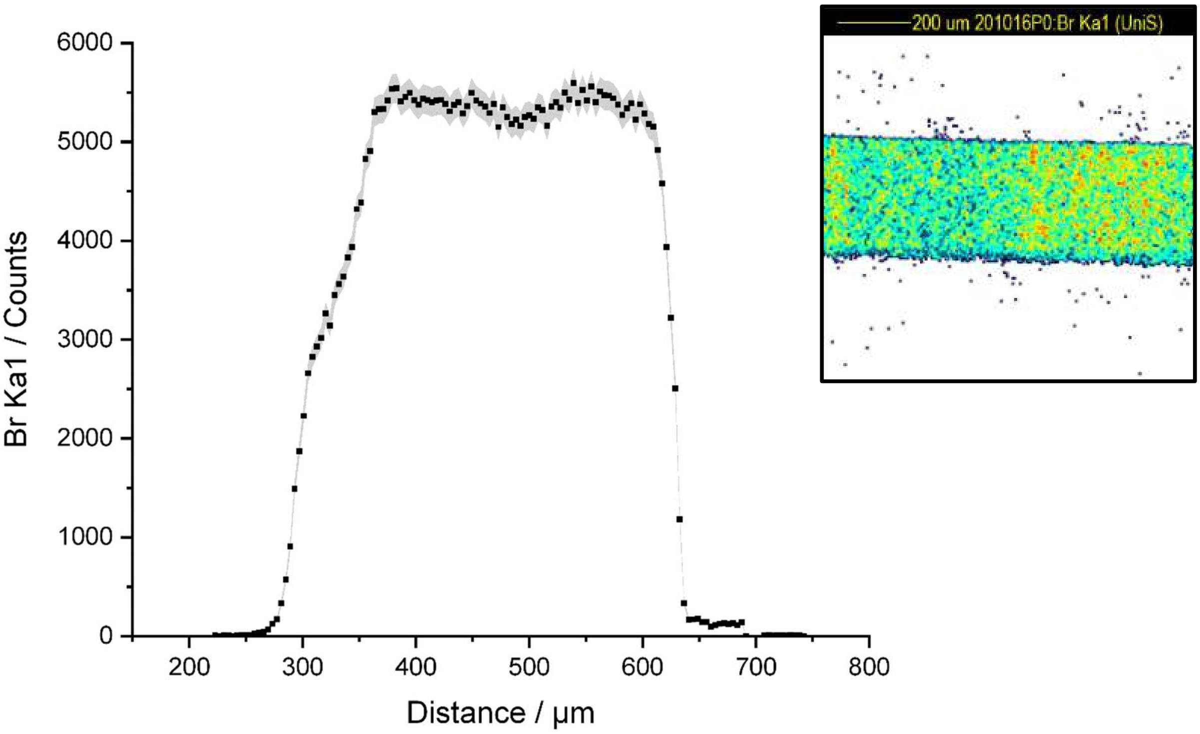

Figure 6.27: Br signal intensity as a function of film depth and accompanying PIXE map (system: 100% stoichiometry, 35 °C cure temperature – repeat 2).

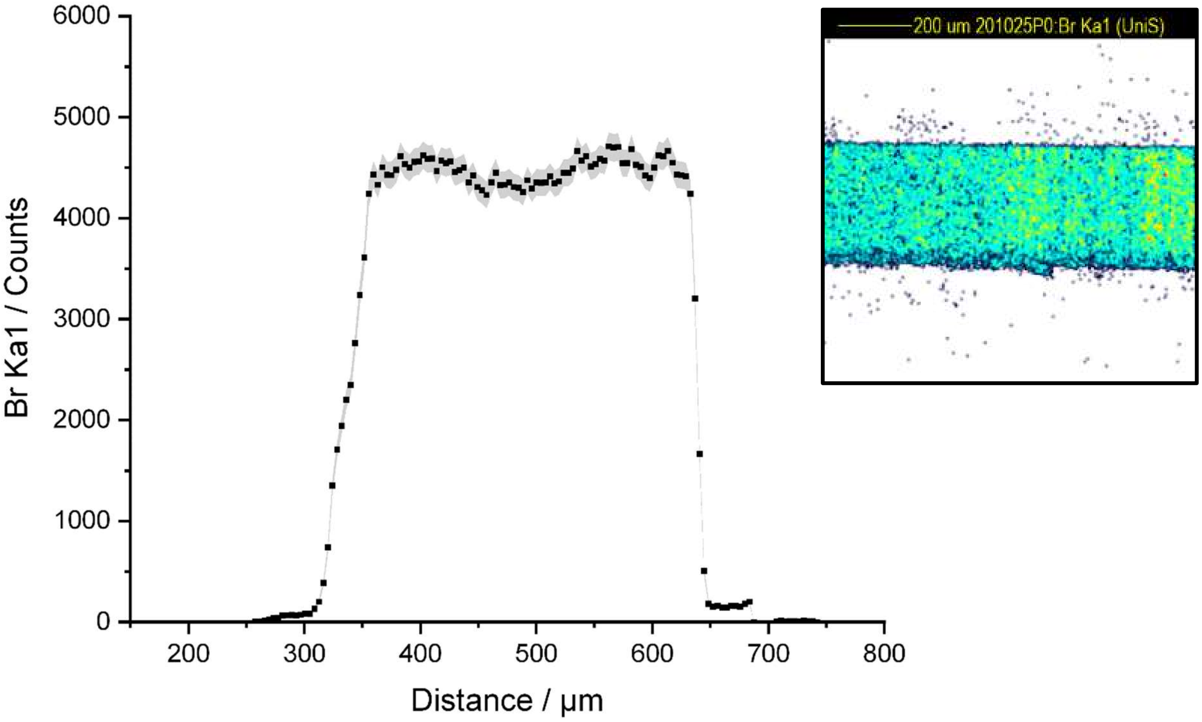

Figure 6.28: Br signal intensity as a function of film depth and accompanying PIXE map (system: 100% stoichiometry, 35 °C cure temperature – repeat 3).

The bromine concentration throughout the 100% stoichiometry, 35 °C cured film was generally consistent throughout all three repeats. This indicates that on the micron scale, crosslink density was homogeneous throughout the film regardless of position, be it at the interphase or the bulk. When comparing the crosslinking density of the 25 °C systems to that of the 35 °C systems, the 35 °C systems generally attained more homogeneous crosslink densities which is consistent with the Raman experiments on deuterated methanol, Section 6.2.2.

6.2.4 Nanometre-scale Surface and Interface Mapping with CD_3OD using Neutron reflectometry

Neutron reflectometry (NR) is a depth profiling technique capable of producing vertical composition profiles of a sample. NR can be advantageous over other vertical profiling techniques as it allows for better resolution (sub-nanometre) than most real-space techniques, and the effective identification of sharp interfaces that may be present in a material.[130,133] It can also be used at atmospheric pressure. Subsequently, NR remains a popular technique for investigating polymer-polymer interfaces.[92,177,178]

While Raman mapping suggested the possibility of a very broad interphase region (tens of microns), but PIXE did not indicate a significant variation in crosslink density, it remains possible that there is still a sharp interface between layers of epoxy coating that is too narrow to detect with either real-space technique. Ideally NR could be used with selectively deuterium-labelled epoxy components to reveal the interface between layers directly, but these materials were not available, and would have required custom synthesis. Consequently, an alternative approach was required.

In a similar way to how PIXE was used in Section 6.2.3, variation in crosslink density can also be indirectly measured using neutron reflectometry, but with greater resolution (sub-nanometre). Again, this is achieved by fully saturating a sample with a solvent and producing vertical composition profiles detailing the accumulation of this solvent, as positional accumulation should depend on localised crosslink density. This approach was previously utilised by Yim *et al.* to characterise single layer epoxy resin crosslink density as a function of curing agent concentration.[179]

Neutron reflectometry requires a maximum sample thickness on the scale of a few hundred nanometres, which is less than the possible interphase width found in Section 6.2.1. It is expected that the second coat will have the potential to ingress the entirety of the first coat thickness if the first coat is ~ 100 nm thick. Therefore, the entirety of the 2-layer samples used could be viewed as a model of the interphase, thus allowing interphase crosslink density to be compared to upper layer crosslink density on the nanometre scale. In the following section, films of varying stoichiometries and cure conditions were analysed using neutron reflectometry to determine the impact of these variables on interface crosslink density. Data were obtained on the Offspec reflectometer in collaboration with Dr Stephen Hall at the ISIS Neutron and Muon Source, Rutherford Appleton Laboratory, Oxford. The systems studied have been listed in Table 6.3.

Table 6.3: The systems attempted using neutron reflectometry, grouped according to experimental procedure.

No. of Layers	Stoichiometry / %	Cure Temperature / °C	Cure Stage	Overcoating Interval / Days	Treatment	Experimental Environment
1	100	25	Ambient	N/A	None	Air
1	100	35	Ambient	N/A	None	Air
1	35	25	Ambient	N/A	None	Air
1	35	35	Ambient	N/A	None	Air
1	100	25	Ambient	N/A	Saturated with CD_3OD	CD_3OD / D_2O
1	100	35	Ambient	N/A	Saturated with CD_3OD	CD_3OD / D_2O
1	35	25	Ambient	N/A	Saturated with CD_3OD	CD_3OD / D_2O
1	35	35	Ambient	N/A	Saturated with CD_3OD	CD_3OD / D_2O
1	100	25	Ambient	N/A	Dried	Air
1	100	35	Ambient	N/A	Dried	Air
1	35	25	Ambient	N/A	Dried	Air
1	35	35	Ambient	N/A	Dried	Air
2	100	25	Post Cured	4	Saturated with CD_3OD	CD_3OD / D_2O
2	100	35	Post Cured	3	Saturated with CD_3OD	CD_3OD / D_2O
2	35	25	Post Cured	4	Saturated with CD_3OD	CD_3OD / D_2O
2	35	35	Post Cured	3	Saturated with CD_3OD	CD_3OD / D_2O
2	100	25	Post Cured	7	Saturated with CD_3OD	CD_3OD / D_2O
2	100	35	Post Cured	7	Saturated with CD_3OD	CD_3OD / D_2O
2	35	25	Post Cured	7	Saturated with CD_3OD	CD_3OD / D_2O
2	35	35	Post Cured	7	Saturated with CD_3OD	CD_3OD / D_2O

The samples described in Table 6.3, have been grouped using line dividers according to the following experiments. Initially, single-layer, ambient cured samples were studied in air, then in a CD_3OD / D_2O (1:1 molar ratio) mixture after saturating the sample with CD_3OD, then in air again after solvent evaporation and drying. By first analysing the less complex, single-layer systems, a base understanding of the fitting parameters can be acquired, making the fitting of the more complex systems manageable. Following this, the bilayer, post cured samples were then saturated with CD_3OD and measured in a CD_3OD / D_2O mixture. To increase the chance of total internal reflection, samples studied in the presence of the CD_3OD / D_2O mixture used inverted sample geometry so that the beam would instead first interact with the comparatively lower SLD Si / SiO and therefore provide a sharp critical edge (the point at which reflection rapidly decreases). In some cases, it was not possible to fit the data with a single physically feasible model. This can be the result of lateral inhomogeneity in the sample arising from dewetting or incomplete contact with solvent. Samples marked in grey (Table 6.3) yielded such intractable data, and will not be discussed, but examples are presented in the appendix. Due to limited access to the facility and problems regarding beamline status, a limited set of data was available. While not every permutation could be examined, it was possible to explore the impact of key parameters from a representative range of samples.

6.2.4.1 Preliminary Work to Determine the Viability of Neutron Reflectometry on the Studied Systems

Prior to data collection, preliminary investigations were carried out to ensure the viability of the planned neutron experiment. For a successful experiment, aspects such as component scattering length densities (SLD's), sample roughness, sample thickness and sample saturation must be established prior to analysis as knowledge of these physicochemical properties is essential for meaningful data and accurate fitting.

Component SLD is vital to neutron reflectometry experiments as a sufficient contrast between components (typically ~ 3×10^{-6} Å^{-2} or more) is necessary for the vertical distribution of the components to have a clear influence on the NR signal. For this experiment CD_3OD was the component of interest. As can be seen from Table 6.4, the SLD of CD_3OD and D_2O were significantly higher than all other components present meaning solvent ingress could be identified in the SLD plots.

Table 6.4: SLDs of compounds used in this chapter.

Component	SLD / 10^{-6} Å^{-2}
Epoxy Film (35%)	1.47
Epoxy Film (100%)	1.19
CD_3OD	5.81
D_2O	6.37
CD_3OD and D_2O mixture	6.09
Silicon dioxide	3.60

It was decided that for a 2-layer system, layers of ~ 1000 Å would be used. To produce films on this scale, spin casting must be used, whereby solution concentration (epoxy system dissolved in chloroform, Section 3.2.4) and spin casting parameters dictate film thickness. The colour of the resultant spin cast film is indicative of film thickness. A light blue colour is typically indicative of ~1000 Å. Figure 6.29 shows how spin cast sample colour changes as thickness increases caused by an increase in the concentration of epoxy system in the casting solution. Once the correct indicator colour was achieved, film thickness was confirmed using ellipsometry.

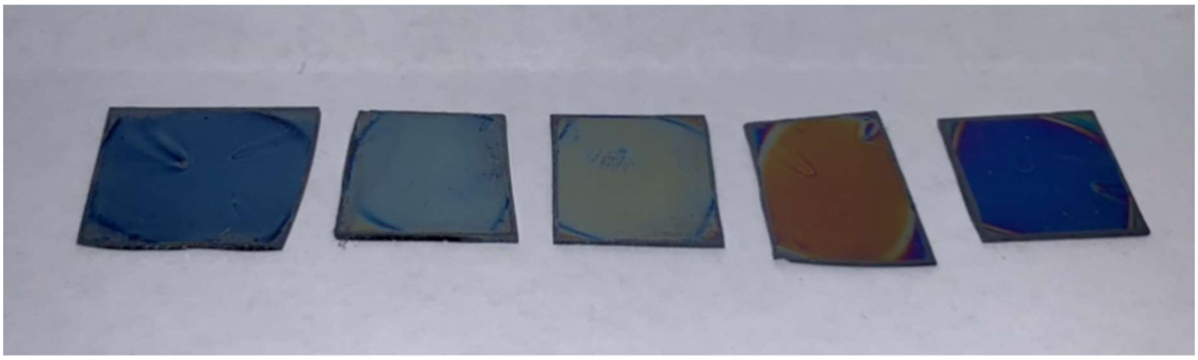

Figure 6.29: Spin cast films produced from epoxy system-solvent solutions with increasing epoxy system concentration. 3%, 4%, 5%, 6% and 7% (left to right).

Sample surface roughness was characterised in Chapter 5, however the samples used were cast using a cube applicator to produce thicker films of ~ 150 microns. To test whether spin casting significantly impacted surface roughness, the surface roughness of cube applicator and spin cast films were compared, Figure 6.30. Although the spin-cast film roughness appears very slightly lower, the difference is very small when it is considered that the total film thickness differs by a factor of approximately 1000. When the experimental uncertainty was considered, it was clear that roughness was not significantly impacted by applicator method.

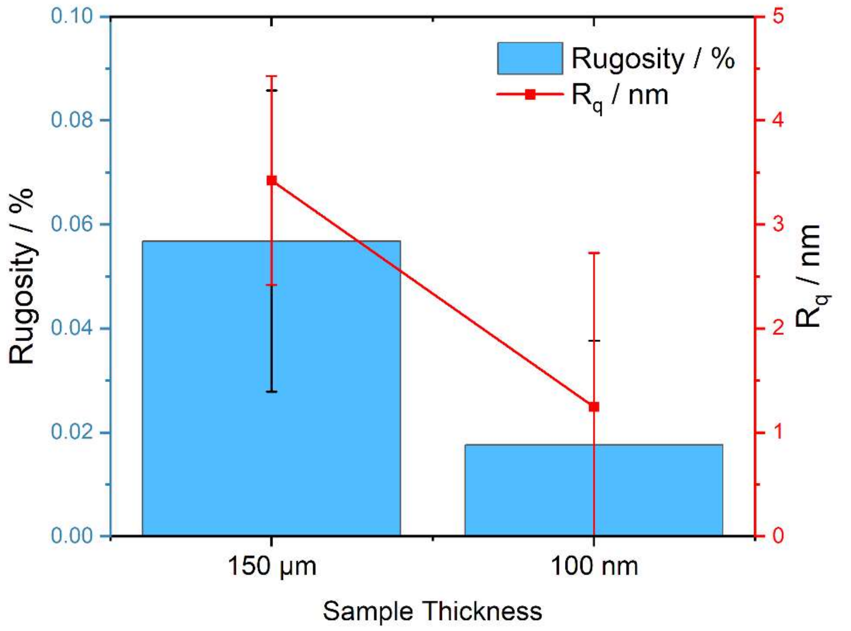

Figure 6.30: The surface roughness (Rq / nm) and rugosity of 100% stoichiometry system cast using either cube application (150 µm) or spin casting (100 nm).

6.2.4.2 Neutron Reflectometry of Single Layer Films

Initial experiments on simple 1-layer films were carried out. Single layer films, ~ 1000 Å thick, of 35% or 100% stoichiometry were spin cast and cured at 25 °C or 35 °C. SLD versus depth profiles were obtained by fitting the measured reflectivity data (Figure 6.31 - 34).

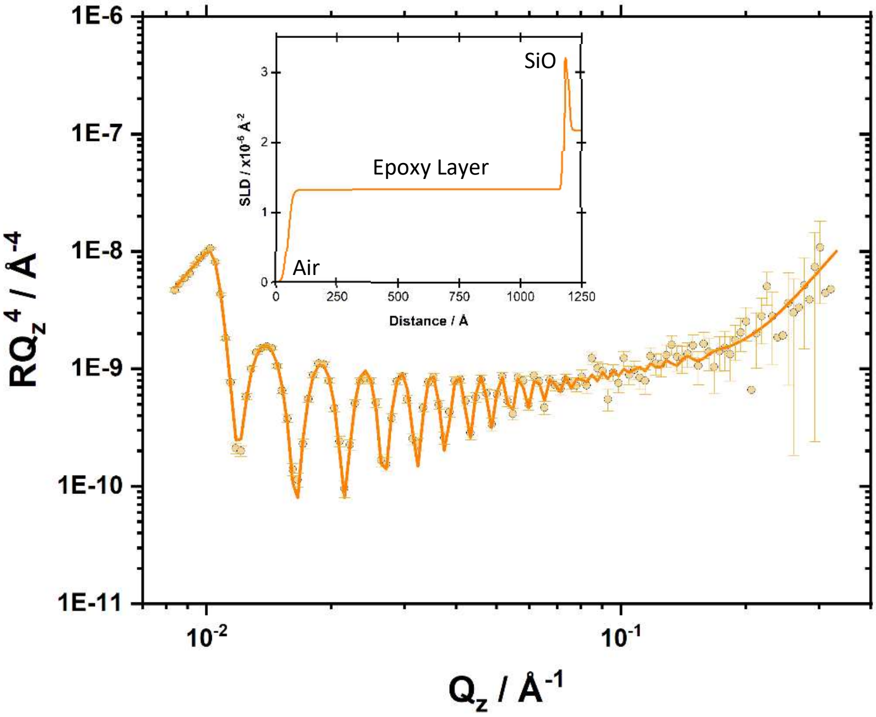

Figure 6.31: Neutron reflectivity profile, fitting line, and SLD model of a single layer 100% stoichiometry system cured at 25 °C.

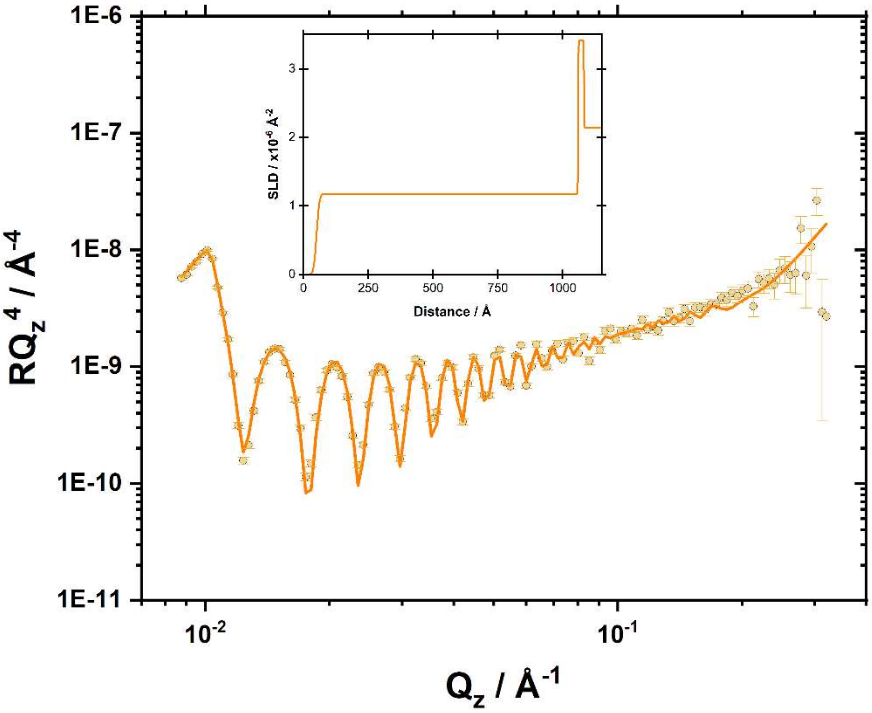

Figure 6.32: Neutron reflectivity profile, fitting line, and SLD model of a single layer 100% stoichiometry system cured at 35 °C.

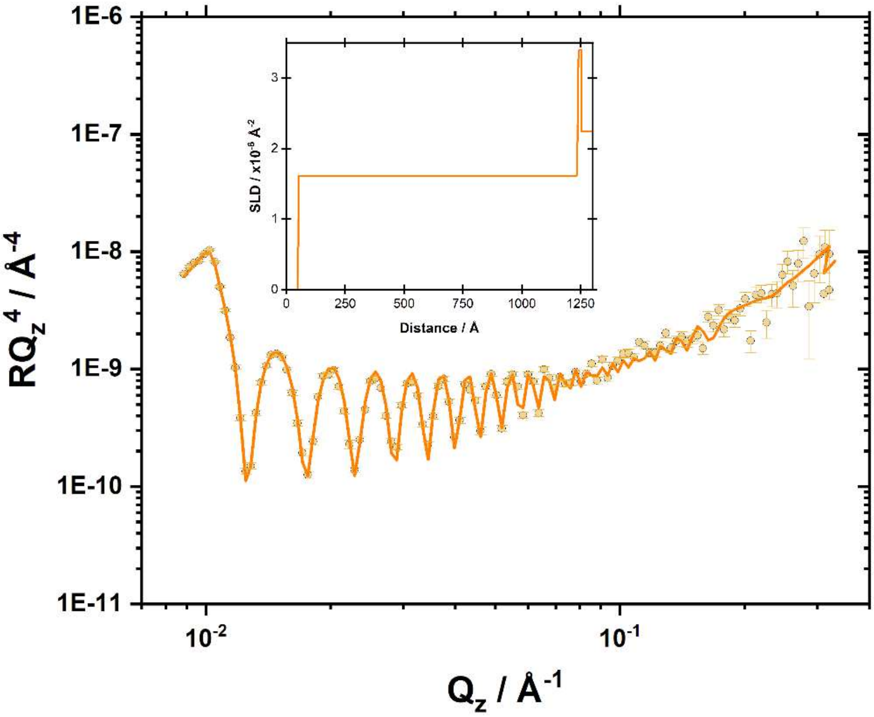

Figure 6.33: Neutron reflectivity profile, fitting line, and SLD model of a single layer 35% stoichiometry system cured at 25 °C.

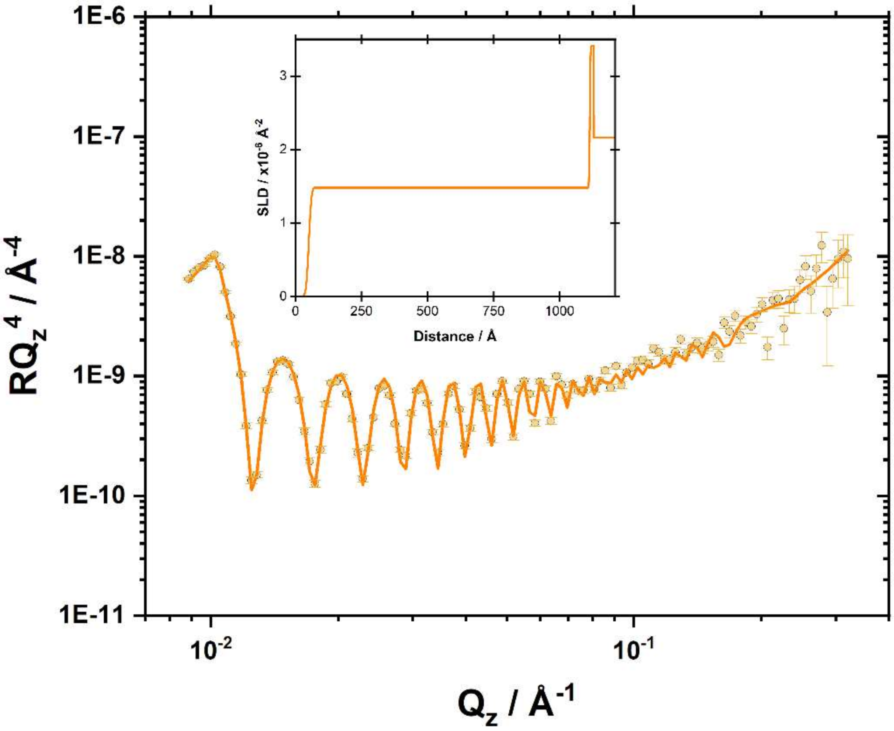

Figure 6.34: Neutron reflectivity profile, fitting line, and SLD model of a single layer 35% stoichiometry system cured at 35 °C.

Figure 6.31 - 34 show the NR profiles and fitting lines of 35 % and 100 % stoichiometry films cured at 25 °C or 35 °C. Reflectivity, R can be plotted against Q_z, and generally, reflectivity decreases with a Q^{-4} dependence. The scattering vector Q is defined as $Q = (4\pi/\lambda \sin \theta)$, where λ is the neutron wavelength, θ is the specular angle of reflection.[180] Here RQ_z^4 has been plotted against Q_z, which removed the Q^{-4} dependence of the data and allows errors in fit accuracy to be more easily identified.

As there are two interfaces present in this system (air-film and film-silicon oxide), Kiessig fringes are visible due to the constructive and destructive interference of the waves reflected from the two interfaces. The frequency of these fringes increases with increasing thickness in a homogeneous film. The data could be adequately fit using the simplest model consisting of a silicon oxide layer and a single homogenous epoxy layer, which agreed with the work of Yim, *et al.*[179] Therefore, it was concluded that when fitting the two-layer system, each layer should be initially considered homogeneous. Moreover, the fitted parameters used to produce these plots were reasonable, as fitted SLD coincided with the predicted values, and fitted roughness was similar to the R_q obtained *via* AFM measurement.

Following these measurements, the samples were then inverted in contact with D_2O/CD_3OD, and measurements retaken. This highlights how saturation in CD_3OD changes the reflectivity plot. Figure 6.35 - 38 display the reflectivity data and fitting lines of systems before and during immersion in CD_3OD.

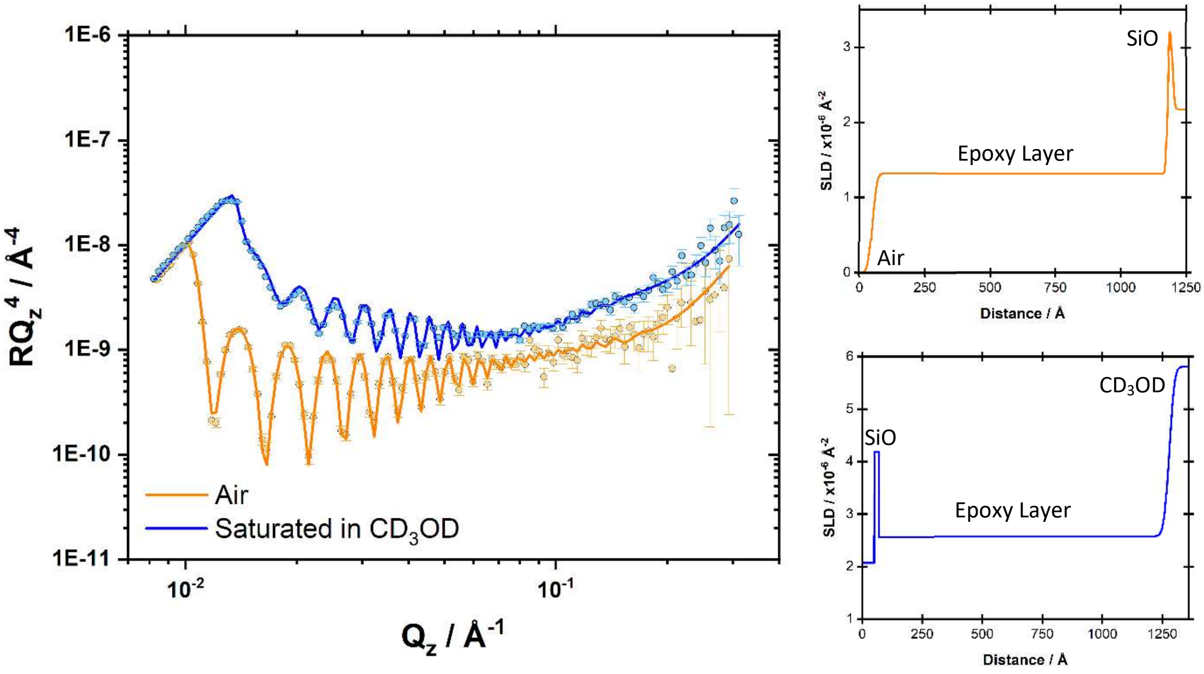

Figure 6.35: Neutron reflectivity profile and fitting line of a single layer 100% stoichiometry system cured at 25 °C pre (orange) and post (blue) saturation with CD_3OD with corresponding SLD profiles.

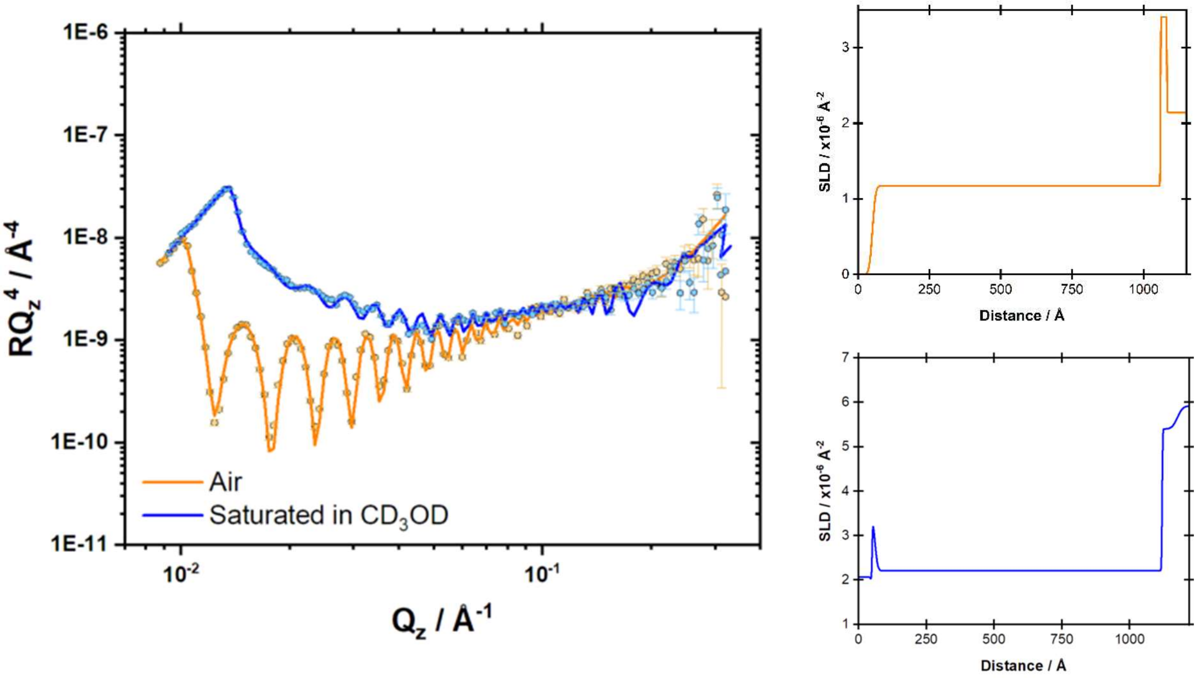

Figure 6.36: Neutron reflectivity profile and fitting line of a single layer 100% stoichiometry system cured at 35 °C pre (orange) and post (blue) saturation with CD_3OD with corresponding SLD profiles.

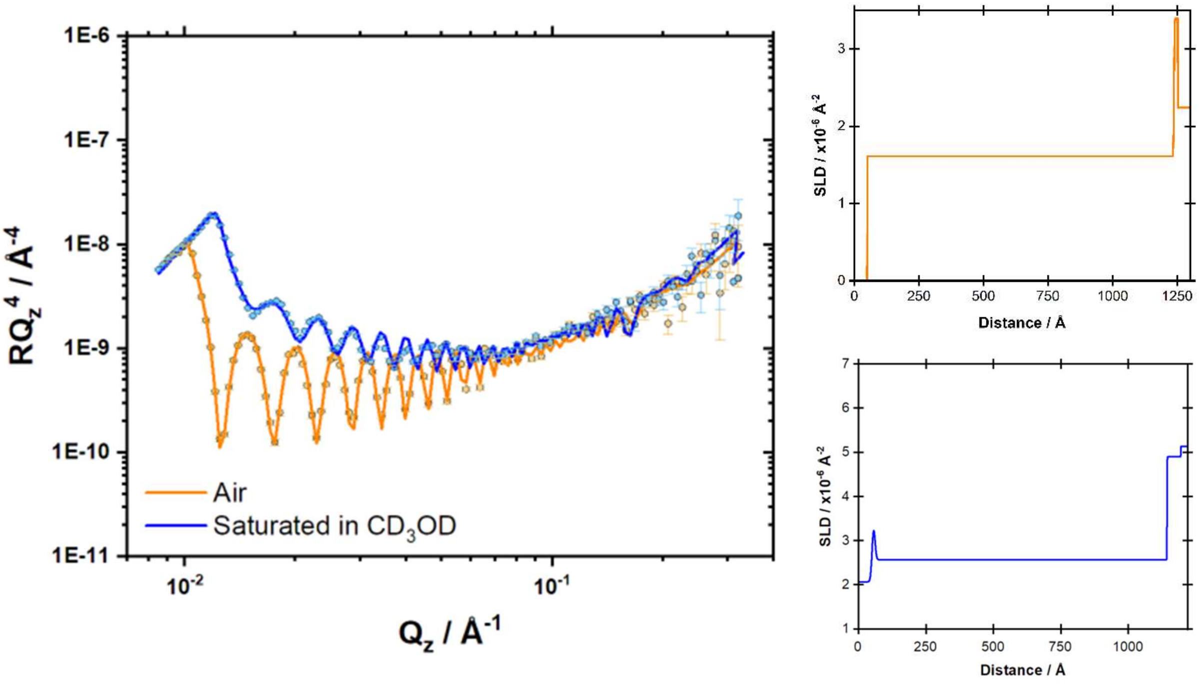

Figure 6.37: Neutron reflectivity profile and fitting line of a single layer 35% stoichiometry system cured at 35 °C pre (orange) and post (blue) saturation with CD_3OD with corresponding SLD profiles.

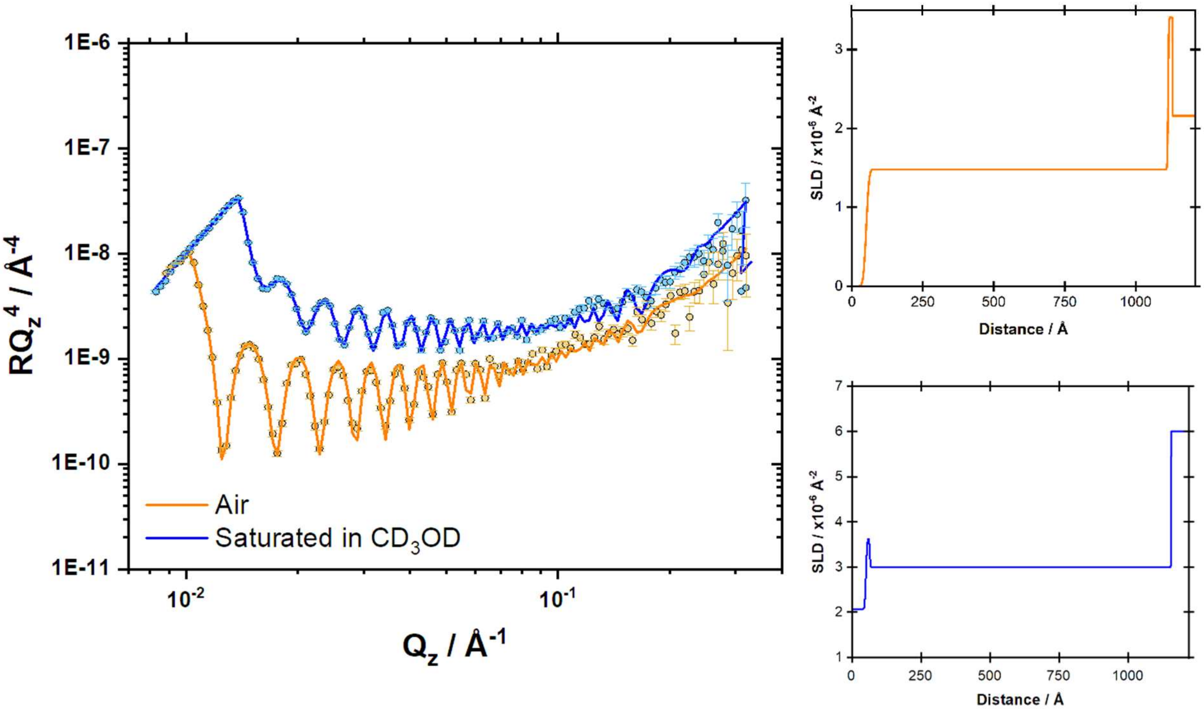

Figure 6.38: Neutron reflectivity profile and fitting line of a single layer 35% stoichiometry system cured at 25 °C pre (orange) and post (blue) saturation with CD_3OD.

In all the above systems (Figure 6.35 - 38), the initial increase in RQ_z^4 is greater in the systems associated with CD_3OD saturation, which is indicative of higher SLD interactions. In addition, the profiles associated with CD_3OD saturation also displayed a higher SLD than those of just the epoxy. This was due to the SLD of the CD_3OD being higher than the epoxy systems at ~ 5.8×10^{-6} Å^{-2} compared to 1.2×10^{-6} Å^{-2} (100 %) and 1.5×10^{-6} Å^{-2} (35 %). This indicates that there is significant uptake of CD_3OD into the epoxy films.

Following these measurements, the samples were then removed from CD_3OD and allowed to dry out. By comparing the reflectivity curves of the film before and after immersion, the impact of solvent exposure on ambient cured epoxy films can be determined. Figure 6.39 - 41 show the neutron reflectivity profiles and respective fits, before and (~ 3 days) after exposure to CD_3OD.

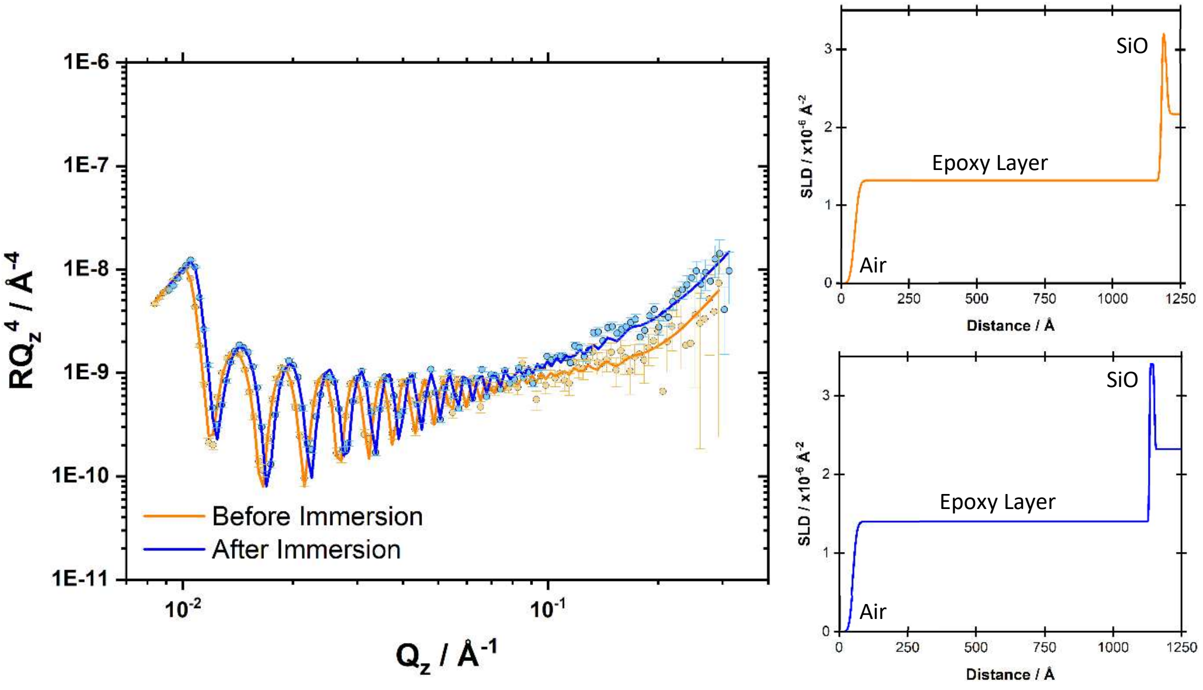

Figure 6.39: Neutron reflectivity profile and fitting line of a single layer 100% stoichiometry system cured at 25 °C pre saturation with CD_3OD (orange) and post saturation and egress (blue).

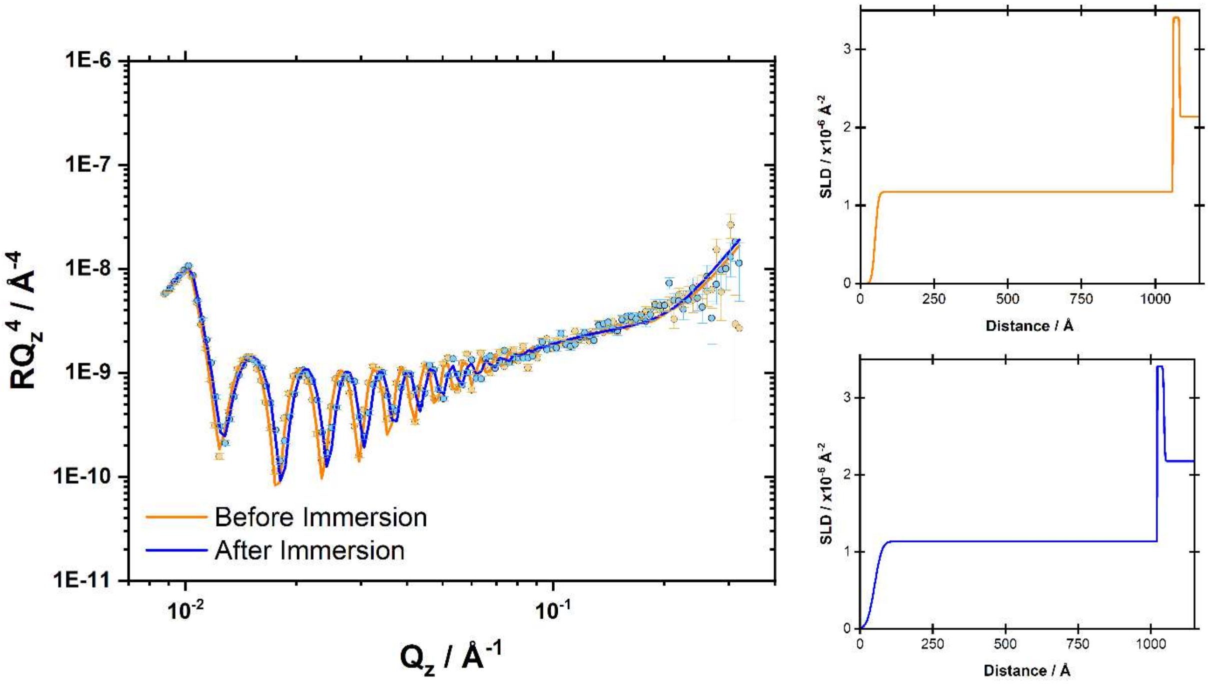

Figure 6.40: Neutron reflectivity profile and fitting line of a single layer 100% stoichiometry system cured at 35 °C pre saturation with CD_3OD (orange) and post saturation and egress (blue).

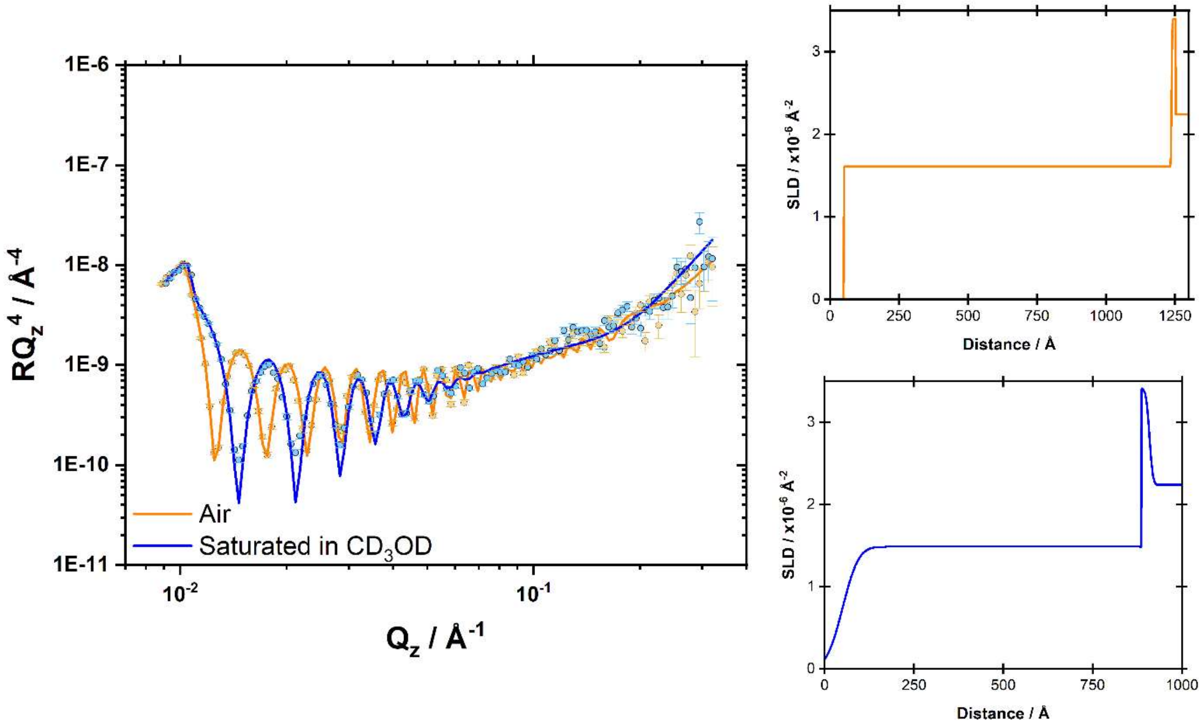

Figure 6.41: Neutron reflectivity profile and fitting line of a single layer 35% stoichiometry system cured at 25 °C pre saturation with CD_3OD (orange) and post saturation and egress (blue).

As shown in Figure 6.39 - 41, in all systems, exposure to CD_3OD caused the fringes to be less tightly bunched, indicating a change in film thickness. As Kiessig fringe frequency is indicative of film thickness, and the fringes of all films are very well defined, accurate resolution of film thickness can be achieved and the difference in film thickness attributed to CD_3OD exposure in ambient curved films quantified. The spacing of Kiessig fringes is given by equation 6.1,

$$\Delta Q = \frac{2\pi}{d} \tag{6.1}$$

where Q is the scattering vector and d is length scale. A very precise measurement of film thickness was obtained by fitting all the Kiessig fringes in the profile. Table 6.5 shows the percentage decrease in film thickness before and after exposure to CD_3OD.

Table 6.5: The percentage decrease in film thickness of each ambient cured system after exposure to solvent.

System (stoichiometry, cure temperature)	Decrease in Film Thickness / %
100%, 25 °C	4.2
100%, 35 °C	3.9
35%, 25 °C	29.6

Given the systems had not been post-cured, there would have been a relatively large concentration of unreacted, extractable material present in the samples. Therefore, it is likely that the exposure to, and subsequent removal of CD_3OD caused some unreacted material to be extracted from the system, thus reducing film thickness. The trend shown here is consistent with that shown in Figure 6.1 (Section 6.2.1), whereby rapid solvent exposure to ambient-cured, spin-cast films decreased film thickness attributed to low-molecular weight extraction from the film. In addition, the 35% stoichiometry film displayed a greater decrease in film thickness attributed to solvent exposure than the 100% stoichiometry films. This is evident by the more significant variation in curve oscillations before and after solvent exposure visible in Figure 6.41 (35% stoichiometry) compared to Figure 6.39 and Figure 6.40 (100% stoichiometry). This therefore indicates that the 35% stoichiometry systems contain a greater amount of extractable material than the 100% stoichiometry systems prior to post curing.

6.2.4.3 Neutron Reflectometry of Two-Layer Films

The impact of overcoating interval, stoichiometry, and cure condition (Table 6.3) on interphase crosslink density was characterised using neutron reflectometry. Approximately 2000 Å thick, 2-layer films of 35% and 100% stoichiometry were produced by spin casting, curing at 25 °C or 35 °C, overcoating after 3, 4 or 7 days, and then post curing, as described in Section 3.2.4. Films were then immersed in CD_3OD until saturation, placed onto a CD_3OD + D_2O reservoir, and SLD versus depth profiles obtained by carrying out neutron reflectometry and fitting the measured reflectivity data, which could be simply converted into a CD_3OD depth profile.

6.2.4.3.1 Justification of Neutron Reflectometry Fits to the Bilayer Epoxy Systems

When attempting to fit neutron reflectometry data, it makes sense to apply Occam's razor by first starting with the simplest model to describe a system, and then increase the complexity to achieve a more accurate fit. Therefore, for a 2-layer epoxy system that has been cast onto a silicon block and ingressed with CD_3OD, the simplest model would describe the silicon block, a silicon oxide layer, and a single homogenous, saturated epoxy network where the two layers are indistinguishable by neutron reflectometry, termed a ‘1-region model’. As such the SLD, roughness, solvent saturation, and thickness of the entire epoxy network would be described by singular parameters (Figure 6.42 - a). A more complex model instead describes the epoxy network as two separate layers with slightly different SLDs, roughnesses, and thicknesses, termed a ‘2-region model’ (Figure 6.42 - b). While experiments on thicker films (Section 6.2.1) indicated that the second layer has the potential to ingress the entirety of a sub-micron first layer, a two-region model may still provide a more accurate fit than a 1-region model as the two layers would have different physical forms, physicochemical properties, and proportions of unreacted material at the point of overcoating, and thus the proportionality of directional interdiffusion between the two layers would be affected. Ultimately, this process may result in regions of varying crosslink density and is described by the most complex model whereby a third region of differing crosslink density is included, hypothesised to be the area where adhesion failure may initiate and subsequently propagate (Figure 6.42 - c). This was termed a ‘3-region model’. In the following section, the chi-square goodness of fit test (χ^2) was used to quantify fit accuracy and determine if the application of different models increased fit accuracy. Optimal fits achieved the lowest χ^2 values and were calculated using Rascal’s simplex fitting algorithm.[181] In this work, it was generally accepted that a fit with a χ^2 of less than 10 was adequate.

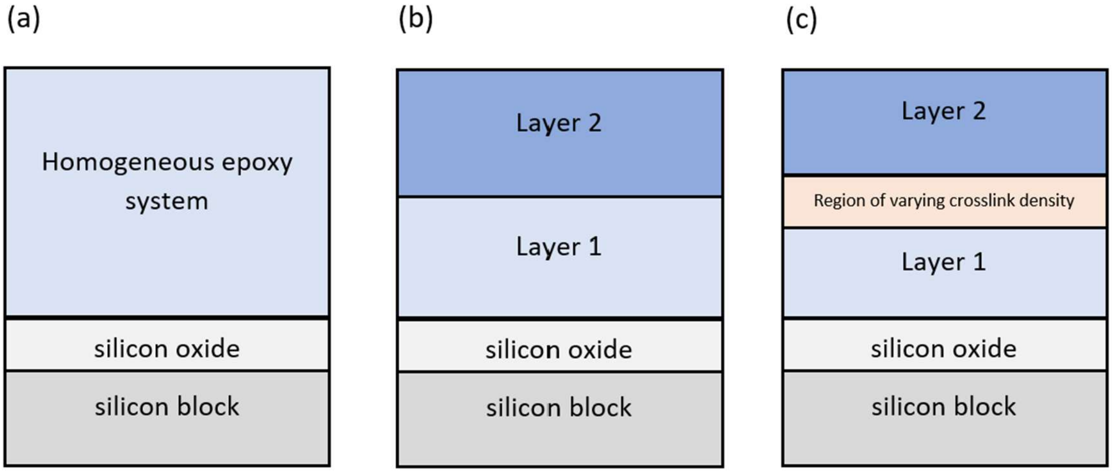

Figure 6.42: Schematics of fitting models (not to scale).

6.2.4.3.2 Bilayer Epoxy System SLD Profiles and Choice of Fitting Model

In this section, vertical composition profiles of CD_3OD saturated films of varying cure temperature, stoichiometry and overcoating interval will be presented to provide an indirect measure of crosslink density. By comparing these profiles, the impact of these variables on relative crosslink density can be determined at the nanometre level. For every system investigated, the 2-region model (Figure 6.42 - b) produced a more accurate fit than the 1-region model (Figure 6.42 - a). Therefore, the 1-region model will only be presented in the first system studied and not discussed for all systems. In occurrences where a 3-region model (Figure 6.42 - c) was concluded to produce a more accurate fit than the 2-region model, statistical analysis of both the 2-region and 3-region fits were presented for comparison. A recap of the systems studied can be found in Table 6.3.

Initially, the films overcoated after 3 or 4 days will be discussed, followed then by those overcoated after 7 days. Figure 6.43 shows the neutron reflectivity plot of a 100% stoichiometry system cured at 25 °C with a 4-day overcoating interval, as well as a 1-region and 2-region based data fit and corresponding SLD models. We can be confident that the features observed in the reflectivity plot will likely be due to CD_3OD positional variation, rather than scattering associated with the film directly as previously it was shown that profiles associated with CD_3OD saturation displayed a higher SLD than those of just the epoxy (Figure 6.38).

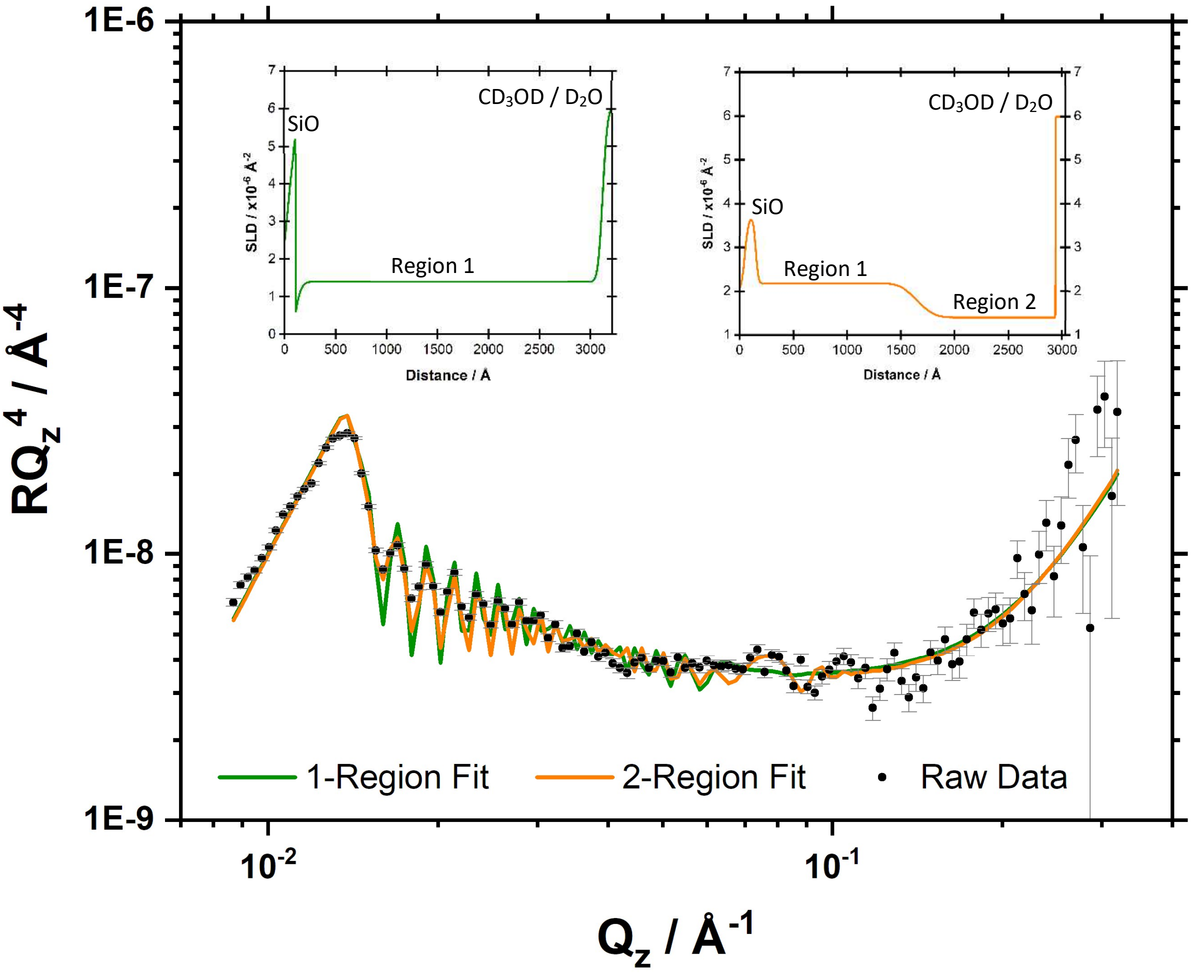

Figure 6.43: Neutron reflectivity profile (raw data), fitting lines, 1-region, and 2-region SLD model of a 100% stoichiometry system cured at 25 °C with a 4-day overcoating interval.

Figure 6.43 displays the neutron reflectivity data (black dots), as well as the 1-region (green line) and 2-region (orange line) fits to allow for comparison. The application of the 2-region SLD model displayed in Figure 6.43 provided a more accurate fit than the 1-region model, decreasing χ^2 from 17.10 to 11.13. Moreover, the SLD of the silicon oxide in the 2-region model is more realistic than that of the 1-region model. The 1-region depth profile corresponds to the silicon substrate, followed by a peak caused by the silicon oxide layer, and then a single homogenous epoxy layer. In this model the SLD of the SiO_2 is much higher than could be accounted for with a reasonable physical density, and so is unrealistic. The 2-region depth profile corresponds to the silicon substrate, followed by a silicon oxide layer peak, and then two plateaus which are the first and second layers of epoxy coating. The 2-region profile surprisingly suggests that the second layer allowed for decreased solvent accumulation, indicated by a decrease in SLD, thus indicating that the second layer attained a greater crosslink density than the first layer.

While the 2-region fit accuracy appears adequate, it could be improved; peak and trough height of the Kiessig fringes between ~ 0.015 and 0.04 Å^{-1} are overexaggerated. In addition, as the SLD of pure 100% stoichiometry system is around 1.2×10^{-6} Å^{-2}, it surprisingly appears that there is relatively little CD_3OD in this layer compared to the other. The application of an additional region of increased or decreased saturation, applied at varying intervals throughout the 2-layer system, such as that described in Figure 6.42 - C, did not reduce χ^2. However, as shown in Figure 6.44, the application of a region of decreased saturation at the film surface dramatically improved the fit.

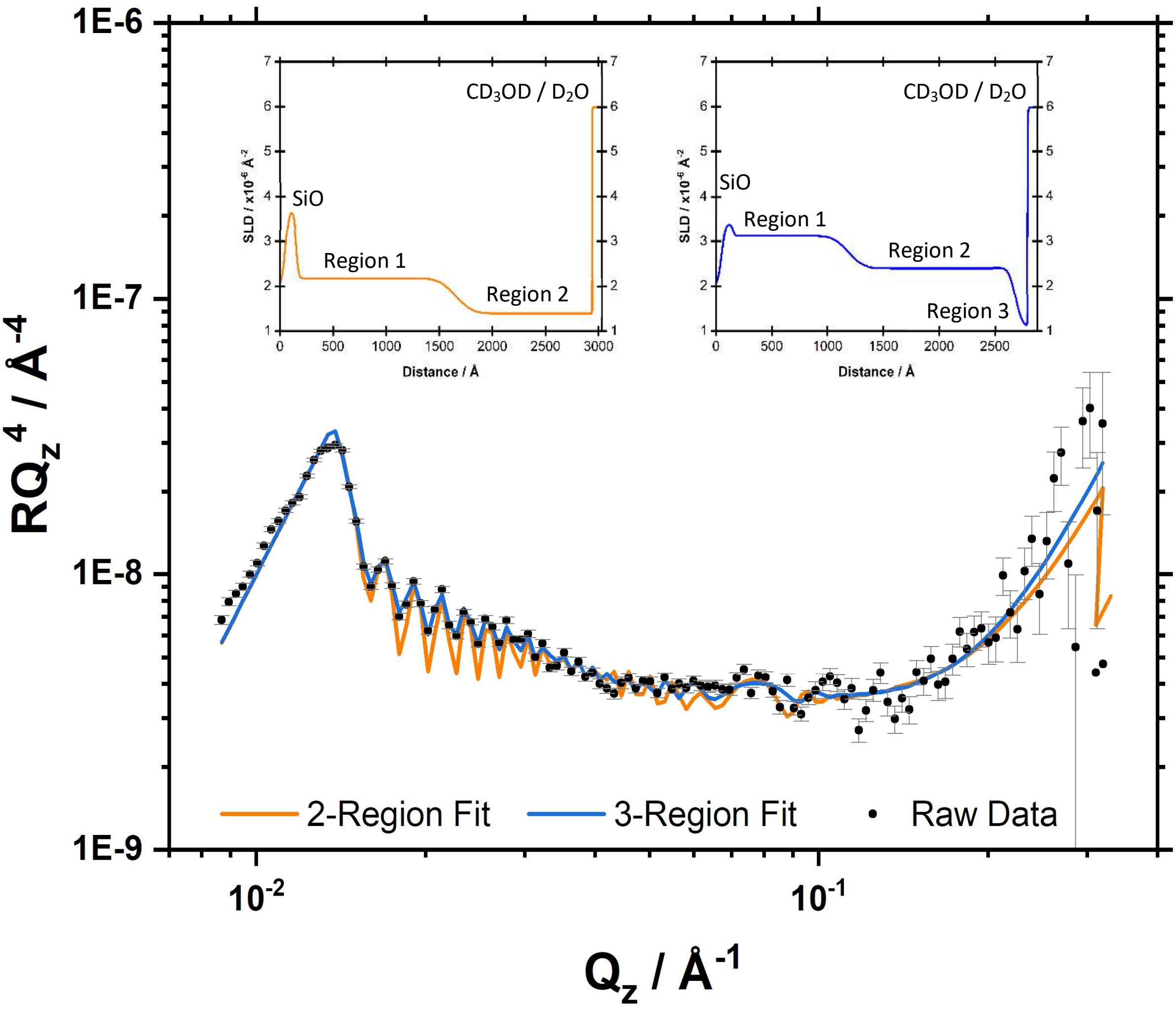

Figure 6.44: Neutron reflectivity profile (raw data), fitting lines, 2-region, and 3-region SLD model of a 100% stoichiometry system cured at 25 °C with a 4-day overcoating interval.

Figure 6.44 displays the neutron reflectivity data (black points), as well as the 2-region (orange line) and 3-region (blue line) fits to allow for comparison. Visually it is clear that the 3-region model, achieved a more satisfactory fit, evidenced by the amplitude of the Kiessig fringes between ~ 0.015 and 0.04 $Å^{-1}$. This observation is statistically-backed, as the 3-region fit significantly reduced χ^2 from 11.13 to 5.12. The overall trend of the 3-region model is like that of the 2-region model suggesting that crosslink density is lower in the first coat allowing for greater solvent accumulation. However, the 3-region model also suggests that there is a ~ 11 nm region of heightened crosslink density near the sample surface indicated by a sharp decrease in solvent accumulation / SLD. The position and size of this region of decreased saturation was optimized by systematically varying these parameters and applying Rascal’s simplex fitting algorithm to reduce fit χ^2. It is not obvious why the area close to the film surface attained an increased crosslink density, although it may be because this region is the furthest point from the initiation centre of interdiffusion and so was less likely to experience stoichiometric imbalance attributed to the interdiffusion of unreacted material. Previously epoxy excess imbalances, in the absence of accelerators, have been shown to reduce crosslink density.[182] Alternatively, this region of the fit may be evidence of a ~ 10 nm carbamate layer at the sample surface. While previously carbamate was not identified in this system using gravimetric or FTIR analysis (Table 5.1; Figure 5.8), a 10 nm layer would not be detectable using these techniques.

We now consider a sample of same composition (100% stoichiometry) cured at an elevated temperature of 35 °C and overcoated after 3 days. The reflectivity plot, fitting line and SLD model is shown in Figure 6.45. By comparing the reflectivity plots displayed in Figure 6.44 and Figure 6.45, the impact of variation in cure conditions on the nanometre scale resolved crosslink density of systems utilising predominantly amine addition polymerisation can be determined.

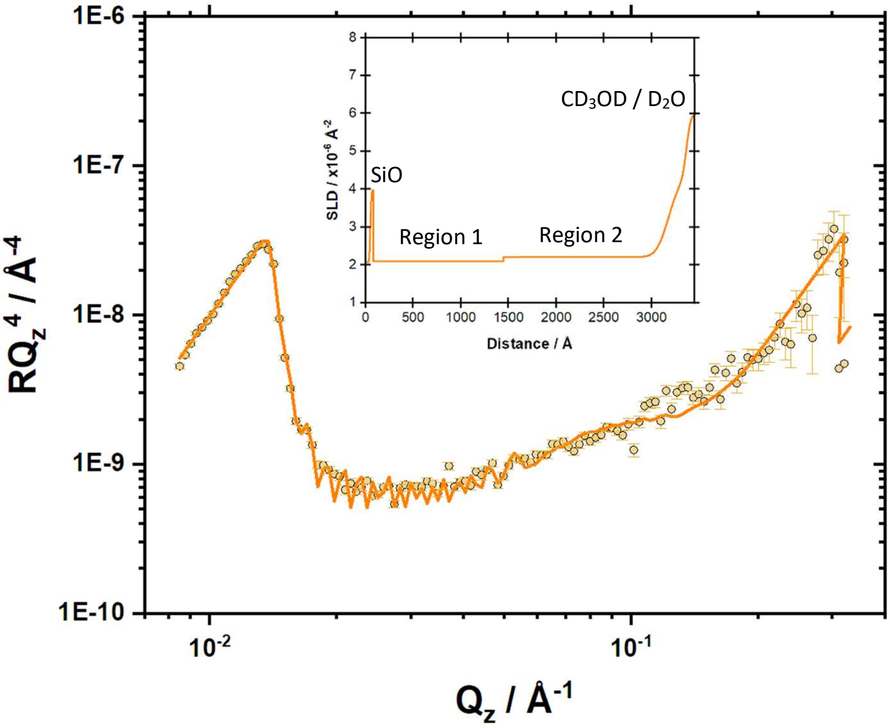

Figure 6.45: Neutron reflectivity profile, fitting line, and 2-region SLD model of a 100% stoichiometry system cured at 35 °C with a 3-day overcoating interval.

The Kiessig fringes displayed in Figure 6.45 are less resolved than those in Figure 6.44, making fitting more challenging. This may be connected to a greater interfacial width at the epoxy-solvent interface and a lower contrast between the epoxy and the solvent. This is likely attributed to comparatively greater solvent uptake into this system, which is also indicated by the relatively high overall SLD. Increased solvent uptake would also increase film thickness; decreased fringe resolution is inevitable with increased film thickness because the instrumental resolution in Q_z is fixed while the spacing varies with inverse film thickness. This was exemplified by Fong, who showed that fringe resolution decreased as spin cast solution concentration, and therefore film thickness, increased.[115,183] Regardless, an accurate fit was produced using the simple 2-region SLD model, producing a relatively low χ^2 of 7.59. It can be noted from the accompanying SLD model, that the variation in saturation between the two regions was minimal indicating a homogeneous crosslink density throughout the 2-layer film at the nanometre scale. The imposition of greater contrast between regions 1 and 2, such as that found in 100% stoichiometry, 25 °C, 4-days OC film (Figure 6.44), reduced the goodness of fit. Therefore, it can be concluded that for this system, at nanometre resolution, there were no signs of variation in crosslink density throughout the film. Unlike with the 25 °C system, this is consistent with that observed on the micron scale. It is interesting that a region of decreased solvent accumulation at the film surface, and so increased crosslink density, is observed in the 25 °C system but not in the

35 °C system. If this region is evidence of carbamation (like suggested above), one may ask the question: why is this feature (proposed to be carbamate) only observed in the NR profile relating to the 25 °C cure sample and not also in the 35 °C cure sample? It may be that 25 °C is more thermodynamically favourable than 35 °C regarding carbamate formation, as previously lower temperatures have generally achieved greater CO_2/amine loading.[184,185] Additional information regarding the thermal kinetics of carbamation would be required to better understand this.

The impact of variation in cure temperature on film crosslink density was also explored in the 35% stoichiometry systems. Figure 6.46 shows the neutron reflectivity plot of a 35% stoichiometry system cured at 25 °C with a 4-day overcoating interval, as well as a 2-region and 3-region based data fit and corresponding SLD models.

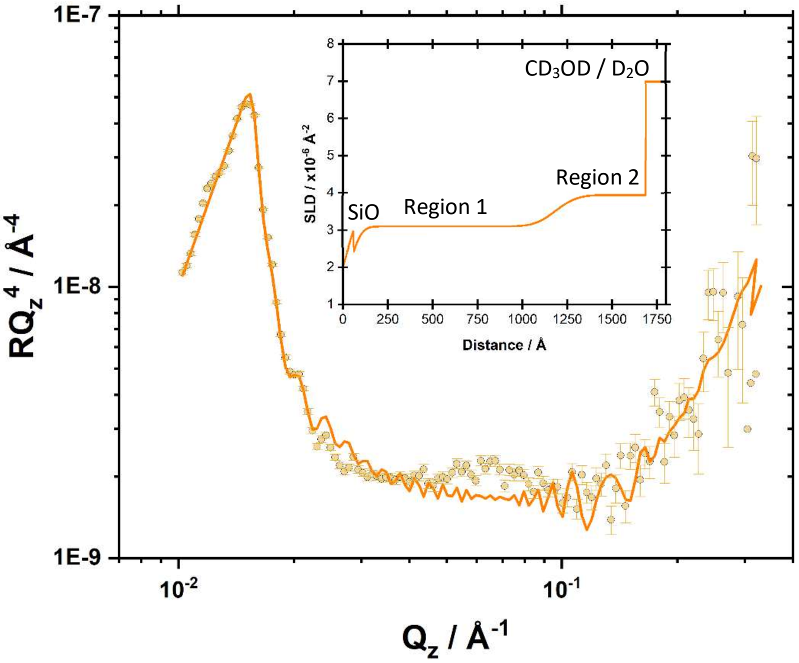

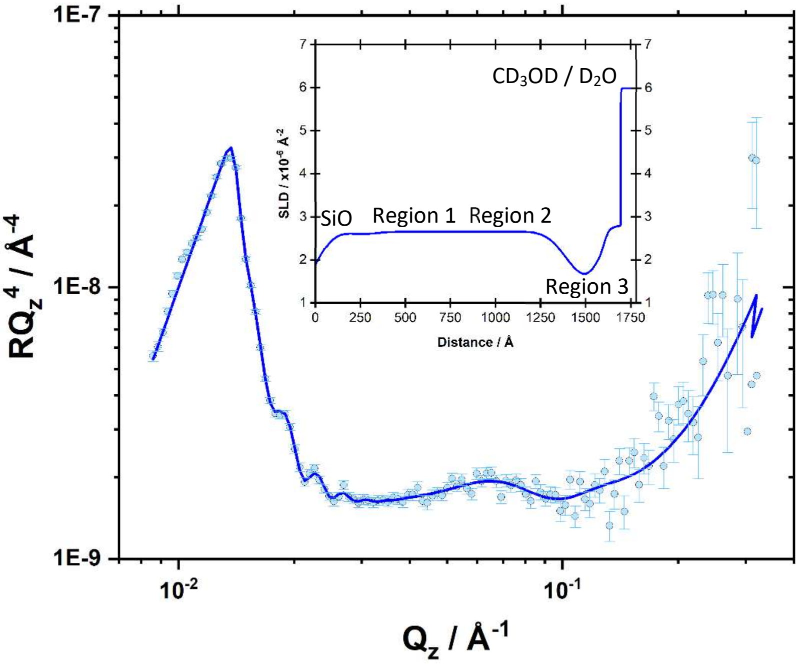

Figure 6.46: Neutron reflectivity profile, fitting lines, 2-region (orange) and 3-region (blue) SLD model of a 35% stoichiometry system cured at 25 °C with a 4-day overcoating interval.

The simple 2-region fit (orange) shown in Figure 6.46 was poor (χ^2 = 17.30). This is visible in the corresponding fitting line whereby fit accuracy decreases particularly between 0.02 – 0.09 Å^{-1}. The inclusion of a region of increased saturation at the 2-layer interface did not improve the goodness of fit. Instead, the 3-region model shown in Figure 6.46, which achieved superior fit accuracy (χ^2 = 8.06.), describes a relatively consistent solvent accumulation throughout the film with a ~ 17 nm area of decreased saturation near the sample surface. This trend was similar to that seen in the 25 °C, 100% stoichiometry system (Figure 6.44), which suggested that there was a region of increased crosslink density near the sample surface. However, the 35% stoichiometry system attained a more homogeneous CD_3OD saturation prior to the region of decreased accumulation near the sample surface.

In addition to the samples discussed above where 3- or 4-day OC intervals were applied, samples were also produced utilizing a 7-day OC interval. The following section presents the reflectivity profiles of these 7-day OC interval samples, comparing the trends observed to those seen in the 3- or 4-day OC systems to determine the impact of OC duration on crosslink density. Figure 6.47 shows the neutron reflectivity plot of a 100% stoichiometry system cured at 25 °C with a 7-day overcoating interval, as well as a 2-, 3-, and 4-layer fit with corresponding SLD models.

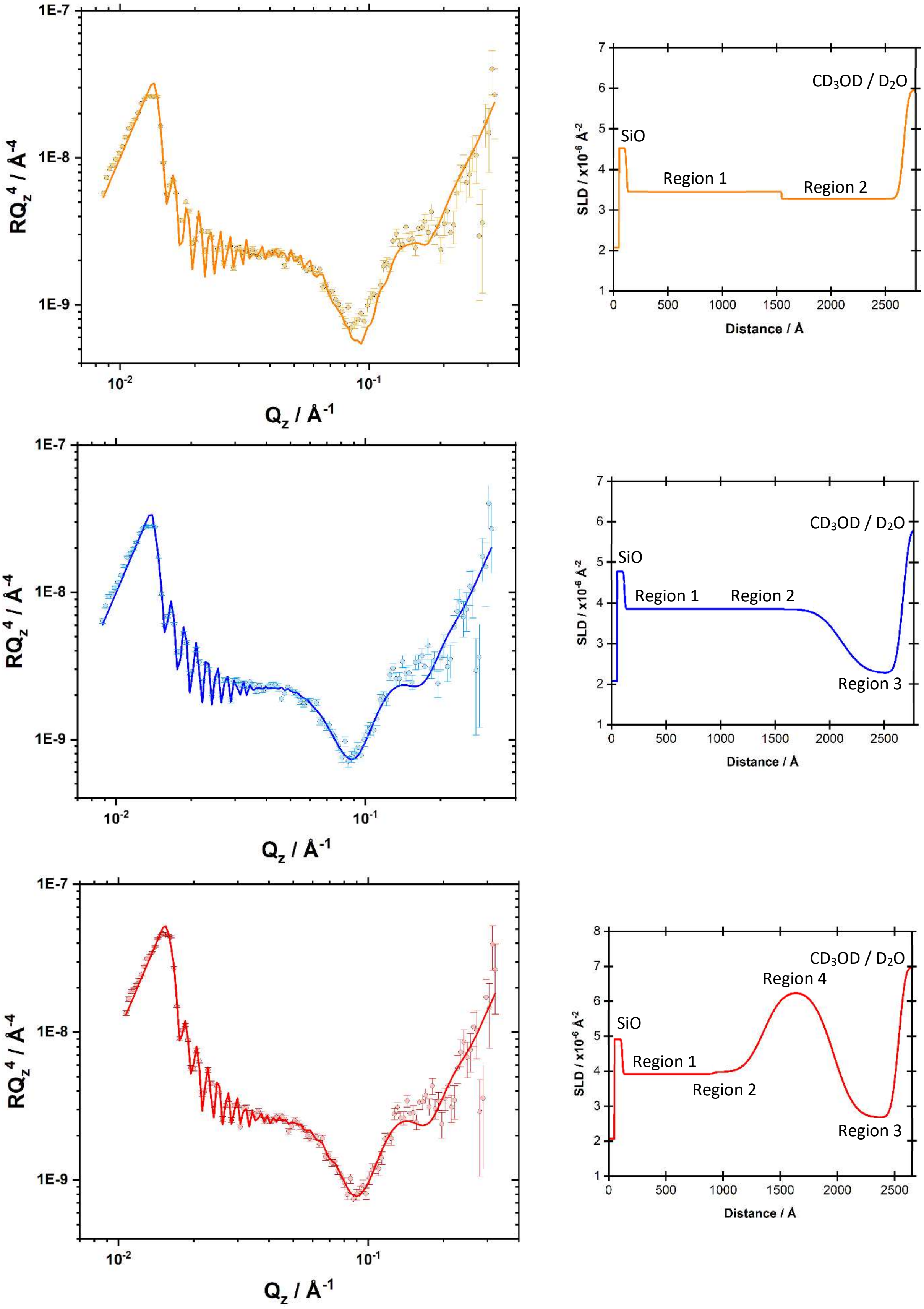

Figure 6.47: Neutron reflectivity profile, fitting lines, 2-region (orange), 3-region (blue), and 4-region SLD model of a 100% stoichiometry system cured at 25 °C with a 7-day overcoating interval.

The reflectivity data for the 7-day OC system (Figure 6.47) is unique compared to all the other figures discussed as there is a trough in RQ_z^4 at Q_z ~ 0.09 Å^{-1}. This trough is indicative of a structure with a distinctive length scale for this film that is absent for all of the other samples. Typically, for a feature with a length scale, *d*, it can be possible to see a peak at a Q_z value of $2\pi/d$ (Equation 6.1). Therefore, it would be expected that the feature observed at 0.09 Å^{-1} in Figure 6.47 would have a length scale of ~ 70 Å.

Like with the other data sets, initially the simple 2-region model was applied (orange) but resulted in an inadequate fit (χ^2 = 14.82). However, while the overall fit required refinement, the feature observed at *0.9* Å^{-1} could be accounted for by applying a SiO layer of 69 Å, much thicker than what is typically observed (≤ 25 Å). However, this perceived thick layer could instead be due to some excess solvent accumulation at the SiO-epoxy interface, which would explain the elevated SiO SLD of nearly 5e-6 Å^{-2}. Therefore, based on this interpretation, it is possible that this feature is not linked to decreased film crosslink density and early signs of adhesion failure. Next, a 3-region model (blue) was applied decreasing χ^2 to 11.49. This indicated an additional region of decreased solvent accumulation near the film surface, consistent with the most similar previously discussed system, 25 °C, 100% stoichiometry, 4-day OC. However, χ^2 was still relatively high compared to all samples discussed and so indicated that goodness of fit could be further improved. Therefore, an additional fourth region (red) was added using the same method by which the third region was identified: systematically defining the region location, saturation, and thickness, then applying Rascal's simplex fitting algorithm to minimise χ^2. It was determined that an additional region of lower solvent saturation did not improve χ^2, however a region of increased saturation encompassing the sample centre reduced χ^2 to 8.00. Locally increased solvent accumulation is indicative of decreased crosslink density within this region and so may be evidence of a weak interface that is likely to fail. However, while this was statistically the best fit achieved, the SLD of region 4 was close to that of pure solvent (CD_3OD and D_2O), thus implying that there would be approximately 10% epoxy and 90% solvent within this region, which is unrealistic. Therefore, it was concluded that the three-region fit was the more credible, and the 4-region fit could be rejected.

By comparing the samples cured under the same conditions and stoichiometries, but varying the OC interval, for 25 °C, 100% stoichiometry systems, increasing the OC interval from 4 days (Figure 6.44) to 7 days (Figure 6.47) decreased solvent homogeneity throughout the film on the nanometre scale, increasing the size of the region of reduced solvent accumulation near the sample surface. If this region is associated with carbamate formation, this would imply that the elevated overcoating interval increased carbamate formation.

35% stoichiometry samples were also produced utilising a 7-day OC interval to determine the impact of OC interval on the crosslink density of films which polymerise by both amine addition and epoxy homopolymerisation. Figure 6.48 shows the neutron reflectivity plot of a 35% stoichiometry system cured at 25 °C with a 7-day overcoating interval, as well as a 2-region and 3-region based data fit with corresponding SLD models.

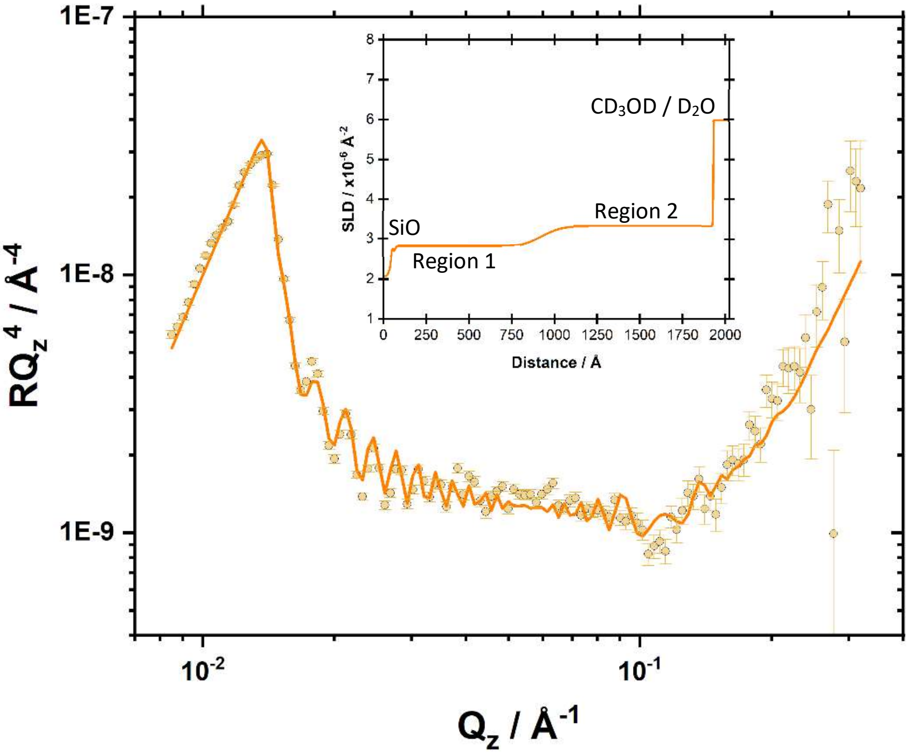

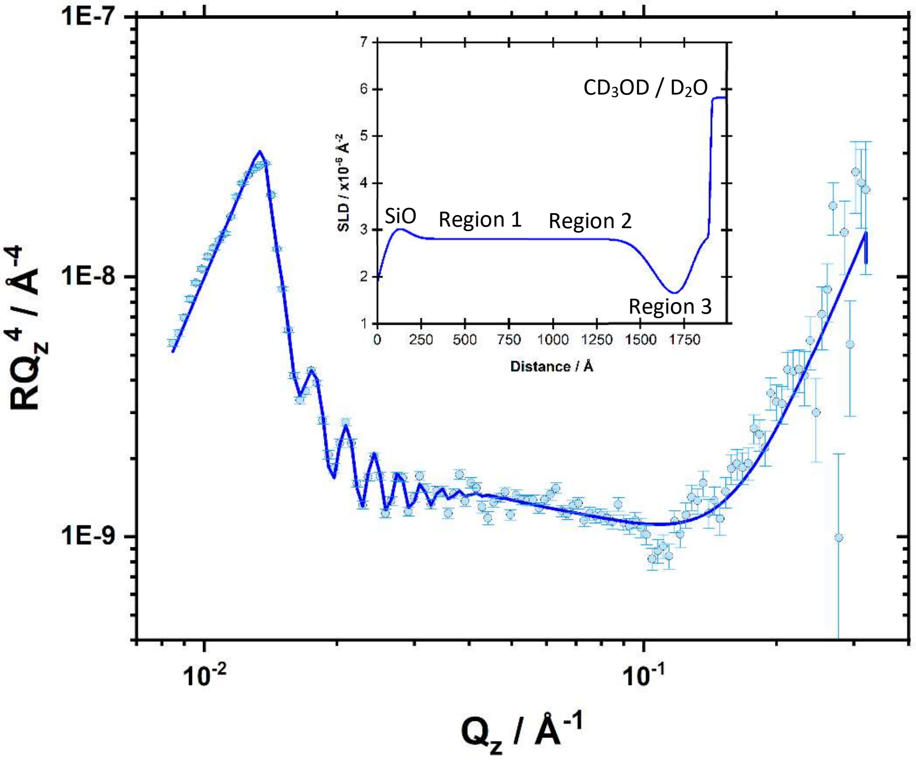

Figure 6.48: Neutron reflectivity profile, fitting lines, 2-region (orange) and 3-region (blue) SLD model of a 35% stoichiometry system cured at 25 °C with a 7-day overcoating interval.

Like with most of the other systems characterised using neutron reflectometry within this work, a 3-region model (blue) provided a significantly superior fit to the simple 2-region model (orange), decreasing χ^2 from 11.92 to 6.93. The 3-region model applied here described a relatively homogenous solvent saturation through the film except for a region of decreased saturation near the sample surface. This is near identical to the model applied for the corresponding system (25 °C, 35% stoichiometry) cured with a shorter 4-day OC interval. This therefore implies that increasing the overcoating interval from 4 to 7 days did not significantly alter the crosslink density throughout the 25 °C, 35% stoichiometry systems.

The final system investigated was the 35 °C, 35% stoichiometry, 7-day OC interval film. Figure 6.49 shows the neutron reflectivity plot of this system, as well as a 2-region based data fit and corresponding SLD model.

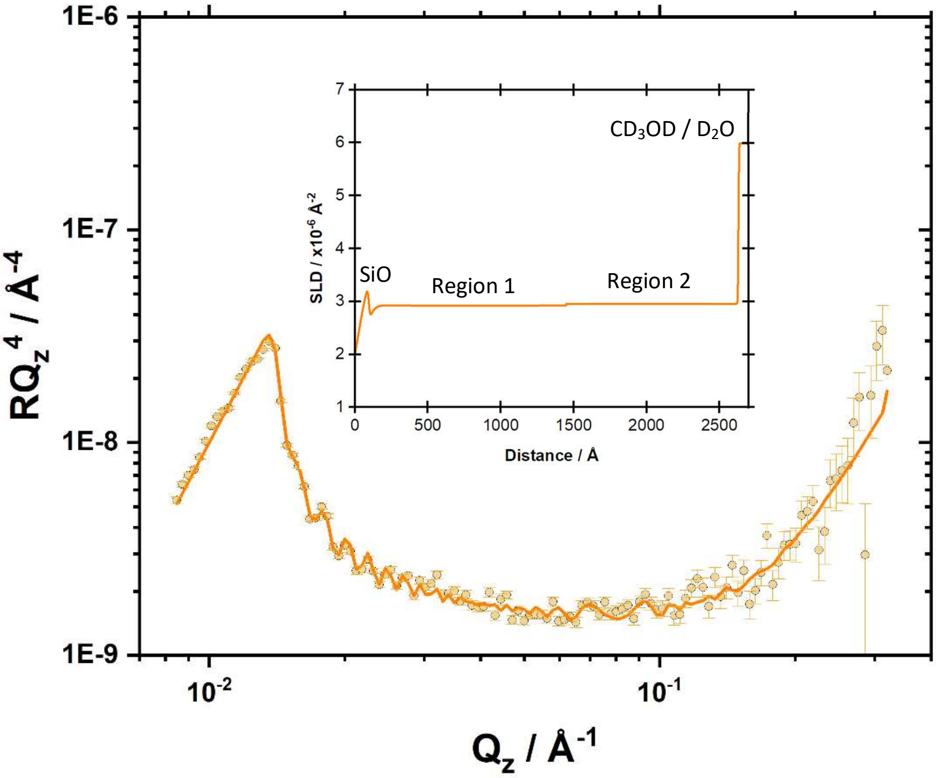

Figure 6.49: Neutron reflectivity profile, fitting line, and 2-region SLD model of a 35% stoichiometry system cured at 35 °C with a 7-day overcoating interval.

Figure 6.49 shows that the 35 °C, 35% stoichiometry, 7-day OC interval system could be successfully fit using the simple 2-region model ($\chi^2 = 5.55$), as was the case with the 35 °C, 100% stoichiometry, 3-day OC interval system. This is interesting as the similar 25 °C, 35% stoichiometry, 7-day OC interval system required a third region for optimal fitting and throughout the entirety of these neutron reflectometry experiments, only the 35 °C systems could be successfully fit using 2-region models. This therefore indicates that generally, at nanometre resolution, more homogeneous crosslink density is achieved *via* curing at 35 °C. Future experiments carried out over a greater range of ambient-cure temperatures (thus increasing the number of data points) may be required to ensure the validity of this trend.

To date, no academic literature could be found that characterised 2+ layer epoxy resin crosslink density using neutron reflectometry, and this is a promising new approach to investigate epoxy resins interfaces that are otherwise quite intractable. Based on the neutron reflectometry studies, the following can be concluded.

- NR reveals that the crosslink density within films varies as a function of depth.
- Stoichiometry, ambient-cure temperature, and OC interval all affected system crosslink density at the nanometre scale.
- Increasing cure temperature from 25 °C to 35 °C increased crosslink density homogeneity, at both stoichiometries studied.
- Increasing the OC interval from 3- or 4- to 7-days may have influenced crosslink density in the 100% stoichiometry film but had no significant impact on the 35% stoichiometry film.
- No compelling signs of early-stage adhesion failure, such as a region of abnormally low crosslink density, were reliably observed.

6.3 Chapter Conclusions

Bilayer cured epoxy interfaces are challenging to study because of their insolubility and the lack of variation in chemistry between layers. In this work, it was shown using Raman spectroscopic mapping that significant diffusion of molecules that mimic the size and solubility of epoxy components is possible into ambient-cured epoxy resins, occurring over tens of microns during a 3-day period. On this basis, it is therefore concluded that interdiffusion in bilayer epoxy interfaces is likely to be a significant part of interphase formation, similarly to that previously reported in epoxy-thermoplastic interphase formation.[57–63] The presence of carbamate on the surface of the first coat had a significant inhibiting effect on small molecule diffusion into the first coat, as did the application of a post-cure. It was also shown that increasing the ambient cure temperature, OC interval, and RH all significantly decreased extent of interdiffusion.

Following on from this, novel approaches to probe apparent variation in crosslink density using spatially resolved solvent ingress measurements were developed to determine the impact of variation in stoichiometry, ambient cure temperature, and OC interval on system crosslink density. Using Raman spectroscopic mapping and PIXE analysis, on the micron scale, it was shown that the crosslink density homogeneity of films polymerised using predominantly amine addition (100% stoichiometry) was increased when the cure temperature was increased from 25 °C to 35 °C. However, little difference was observed between bulk and interphase crosslink densities.

Neutron reflectometry was then utilised for the first time to indirectly characterise interphase crosslink density on the nanometre scale in films cured utilising both amine addition polymerisation (100% stoichiometry systems), and a combination of amine addition and epoxy homopolymerisation (35% stoichiometry systems). Previously, only the nanostructure of single-layer, cured epoxy resin systems has been characterised (using neutron reflectometry).[179] Here, it was shown that cure temperature, stoichiometry and overcoating interval all affected film crosslink density at the nanometre scale. At both stoichiometries, increasing the cure temperature from 25 to 35 °C generally increased crosslink density homogeneity, as regions of increased crosslink density were observed near the surface of films cured at 25 °C. Increasing the overcoating interval from 3- or 4- to 7 days did not significantly impact the crosslink density of the 35% stoichiometry films but had some impact in the 100% stoichiometry systems. Throughout all films, no obvious signs of early-stage adhesion failure were observed. As adhesion failure is a fatigue associated issue, perhaps further loading and unloading of solvents from these systems could lead to areas of suppressed crosslink density that are not initially obvious. However, further work would be required to investigate this hypothesis.

Chapter 7

Solvent Ingress and Egress Studies in Cured Amine Epoxy Networks

7.1 Chapter Introduction

Ingress and egress can be defined as the act of entering and leaving, respectively. During amine-cured epoxy-solvent interactions, ingress and egress of solvent within the cured epoxy networks occurs *via* absorption, the diffusion of liquid (or gas) molecules into a solid (or liquid) material, and its counterpart, desorption. The ingress of compatible liquid cargo into cured epoxy resin coatings is inevitable as in many instances solvent molecular volume is smaller than epoxy void volume.[96,105,106,186–190] Often, to meet client demands and ensure economic viability, a range of chemically diverse cargoes are transported by a single ship whereby cargo scheduling is dictated by ship location, target destination and transport deadlines.[191] Subsequently, coatings can be exposed to a variety of different cargoes in relatively short amounts of time,[1,4] and knowledge of the rate and extent of egress is essential for negating leaching into subsequent loads. For example, high purity compounds, such as mono ethylene glycol (MEG), could only require as little as several ppm of aromatic contamination to be deemed off-specification;[192] contamination can be estimated at ~ 10 ppm (0.3 mm film, 30 m^3 tank, 6 surfaces, 10% saturation), before the impact of swelling and blistering (which leads to increased liquid retention) are even considered. Equally, while a sufficient interval must be observed to prevent leaching, time allocated to egress, whereby a ship is docked and therefore not transporting cargo, represents loss of earnings and so a balance must be struck to ensure economic viability. Therefore, as the rate and extent of ingress dictates the total volume of solvent required to be egressed, knowledge of these properties is crucial, and an elevated rate of egress can be seen as favourable.

The previous two chapters showed how variation in cure conditions and stoichiometry significantly impacted the physicochemical properties of the film and focused on how this may contribute towards adhesion failure. This chapter will instead explore how variation in stoichiometry and cure condition impacts film function as a physical and chemical barrier to ingress by quantifying solvent uptake over time.

7.2 Results & Discussion

7.2.1 Gravimetric Analysis

Gravimetric analysis can be used to quantify coating chemical performance by measuring the rate and total extent of solvent ingress and egress over time.[187] This is particularly relevant when considering solvent-resistant coatings as their impact on chemical performance can be identified *via* systematic variation of coating parameters. Several studies have previously shown how variation in morphology can significantly impact solvent ingress.[10,96,187,190] Jackson *et al.* systematically varied epoxy and curing agent configuration, reporting variation in AVV between films, and a linear correlation between AVV and solvent ingress.[96] Knox *et al*. showed that methanol uptake was slower and lower in epoxy systems cured from aromatic amines compared to their aliphatic analogues attributed to denser, better performing networks.[187] Didsbury showed that slight variation in epoxy structure, associated with differing bisepoxide monomer building blocks, influenced rate and extent of methanol ingress.[10] Sahlin *et al.* showed that rate of uptake into TGDDM-DDS (tetraglycidyl diaminodiphenylmethane-diaminodiphenyl sulfone) epoxy systems was significantly affected by the curing agent weight percentage.[190] Unthank *et al.* reported that the introduction of triethylborate into epoxy-amine formulations significantly reduced solvent ingress and hypothesised that this was due to reduced affinity between the new hybrid material and the ingressing solvent. Unthank *et* al. attributed this to reduced OH and NR_3 groups present in the hybrid material due to the formation of boron-tertiary amino complexes during curing.[105]

In this thesis, gravimetric analysis was used to determine the impact of stoichiometry and ambient cure temperature on the chemical performance of epoxy resin coatings. 35% and 100% stoichiometry films, cured at 25 °C and 35 °C were cast and post-cured according to Section 3.2.3, producing 2-layer films (150 µm / layer) with a solvent reservoir attached. Methanol sorption and desorption was then measured over a 60-day period, as described in Section 3.6.2. Methanol was chosen as a probe molecule because its low molecular volume and polarity (Section 2.5.3) make it relatively compatible with epoxy resin coatings. This compatibility and tendency to cause swelling places a stress on coatings that could lead to failure.

Figure 7.1 displays the sorption and desorption of methanol into different epoxy systems over time, 3 repeats per system. Figure 7.2 shows the average of these 3 repeats.

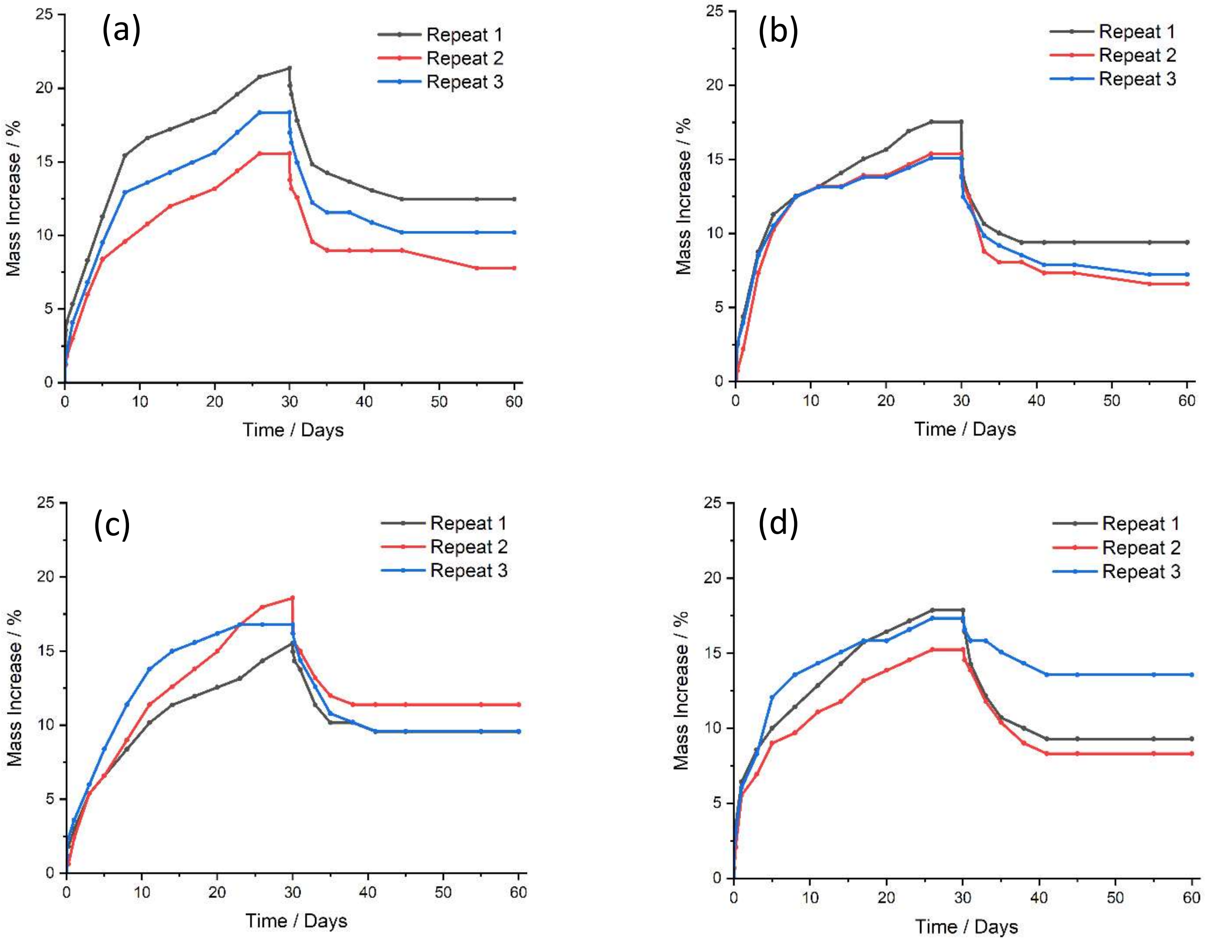

Figure 7.1: Sorption and desorption of methanol in different 2-layer epoxy systems over time (a) 100% stoichiometry, 25 °C (b) 100% stoichiometry, 35 °C (c) 35% stoichiometry, 25 °C (d) 35% stoichiometry, 35 °C.

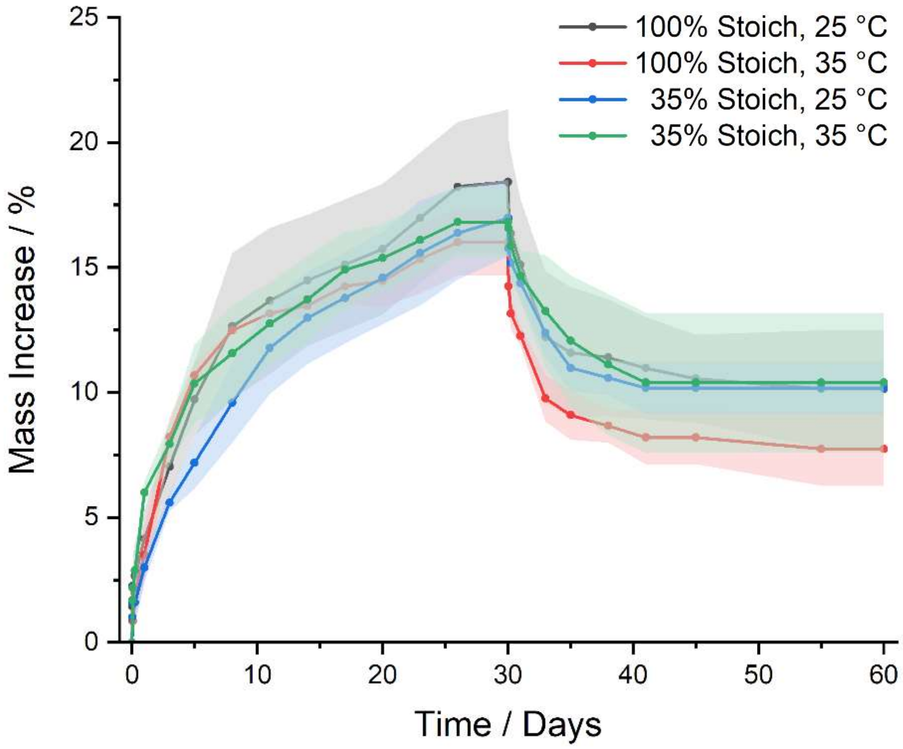

Figure 7.2: The average sorption and desorption of methanol in different 2-layer epoxy systems over time. Ingress method: via topcoat.

As is shown in Figure 7.2, in all 4 systems studied, there was an initial elevated rate of ingress in the first 3 days which then decreased until mass appeared to reach plateau at around day 26 - 30, at which point the films were fully saturated (ultimate ingress). This coincided with the work of Korkees *et al.* who also reported an initial elevated rate of ingress followed by a period of reduced rate of ingress.[186] The values of ultimate ingress observed in Figure 7.2 were in line with previous ingress / egress studies of chemically similar systems.[10,190]

Somewhat surprisingly, the data in Figure 7.2 indicate that there was no statistically significant difference in the sorption and desorption of methanol into systems cured at different stoichiometries and cure temperatures. This is particularly surprising when comparing the two stoichiometries as they utilise a different distribution of reaction mechanisms leading to different structure and final composition, and so could hypothetically attain varying crosslink densities, and thus varying sorption / desorption behaviour. While it is perhaps surprising that films of different compositions have such similar sorption characteristics, this suggests that the final post-cure step is the dominant factor in determining the network properties. For practical purposes, this result suggests that coatings based on these materials could tolerate some variation in formulation. However, it can be noted that the standard error associated with each data point is quite large, which may be related to the experimental technique. As the overall mass of the solvent-reservoir setup was ~ 230 g, and the mass of the coating area exposed to solvent *via* the reservoir was ~ 1.5 g, a 20% increase in sample mass (~ 0.3 g) as shown in Figure 7.2 represents only an overall change in mass of ~ 0.1%, which could explain the observed error. In addition, as the solvent-reservoir was chemically bound to the sample surface, and so could not be removed without damaging the sample, ensuring thorough drying prior to each measurement was challenging and likely led to a decreased accuracy in data acquisition. Subsequently, a second experiment that alleviated this error was carried out whereby 2-layer samples (150 µm / layer) were produced as above, but the solvent-reservoir was not attached. The film was then detached from the substrate *via* snapping and prying to produce a freestanding film. This was then cut down to a 5 cm by 5 cm sample to fit inside a 500 ml Thermo Fisher Scientific, Wide-mouth jar, containing methanol. Figure 7.3 shows the average (3 repeats per system) sorption and desorption of methanol into different epoxy films over time using the updated data collection protocol.

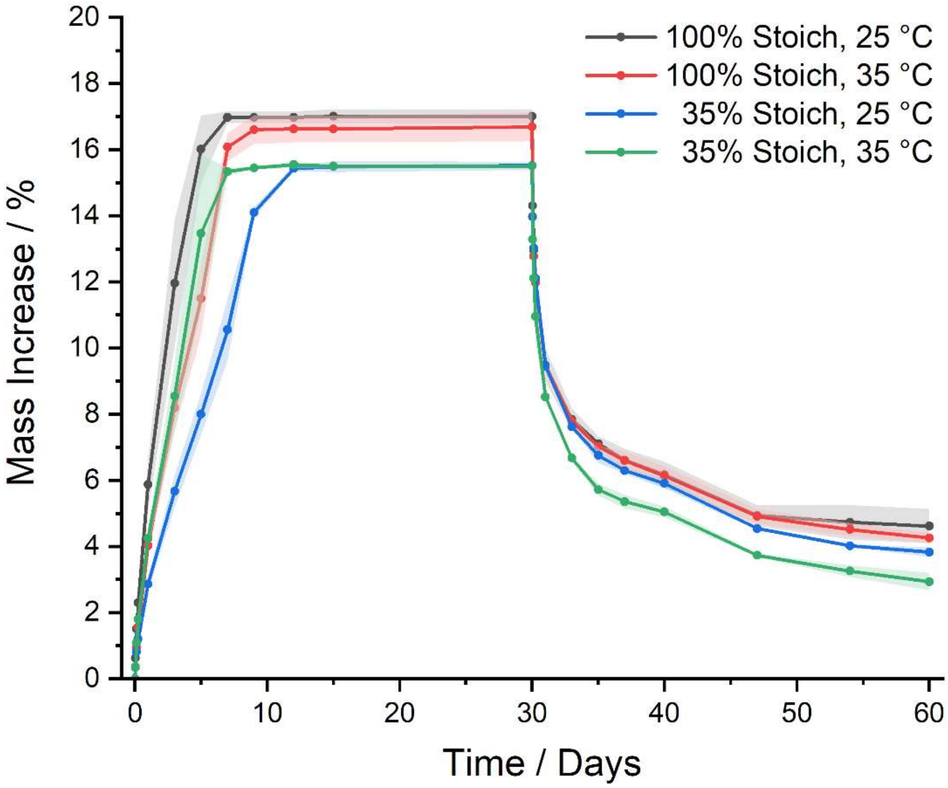

Figure 7.3: Sorption and desorption of methanol in different 2-layer epoxy systems over time. Ingress method: full submersion.

It can be noted that the rate of ingress observed from the data in Figure 7.3 was ~ 4 times quicker than that observed in Figure 7.2. This is because the samples analysed in Figure 7.2 were substrate bound, whereas the Figure 7.3 samples were free standing, thus increasing the surface area available for ingress / egress. Through utilising free-standing films and therefore doubling the surface area, which was exposed to solvent ingress, the maximum distance required to be travelled by the solvent to saturate the film was essentially halved, resulting in a 4-fould impact (Figure 7.4). Therefore, the updated protocol is arguably less true to industrial application, while being consistent with the original observation that ~ 16% uptake is typical. However, it is clear that the accuracy of the data presented in Figure 7.3 is far superior to that shown in the data in Figure 7.2 indicated by the comparatively lower standard error. This therefore indicates that the cause of the error observed in Figure 7.2 was likely due to the protocol used. Therefore, while the updated protocol is less true to industrial application, it allows the impact of variation in stoichiometry and cure condition on methanol sorption and desorption to be more accurately compared. Upon initial observation, it might seem that the ingress/egress kinetics of each individual sample varies depending on the chosen method of data collection (substrate-bound sample v free-standing sample, Figure 7.4). However, it is important to recognise that this perceived variation in kinetics is primarily attributed to the significant error associated with the data presented in Figure 7.2 (substrate-bound sample). In reality, accurate data collection methods should not theoretically impact diffusion kinetics, emphasizing the importance of considering measurement accuracy in the interpretation of experimental results. On this basis, only the data presented in Figure 7.3 (free-standing sample) will be used to comparatively evaluate the ingress/egress kinetics of the different investigated systems.

As shown by Figure 7.3, the ultimate ingress was consistently lower in the 35% stoichiometry systems compared to the 100% stoichiometry systems. The 100% stoichiometry systems utilise mainly step-growth amine polymerisation, whereas the 35% stoichiometry systems utilise a combination of step-growth amine addition polymerisation and anionic chain-growth homopolymerisation of epoxy yielding polyethers. Moller *et al.* investigated the impact of stoichiometry on crosslink density amongst other physicochemical properties (on diglycidyl ether of bisphenol A - diamino diphenyl sulfone systems) and reported elevated crosslink density in excess epoxide systems compared to on-stoichiometry systems when a post cure was applied to promote etherification.[193] Therefore, in this work it is hypothesised that the 35% stoichiometry system (epoxide excess) recorded decreased ultimate ingress due to an increased overall crosslink density. Alternatively, it is possible that the less polar polyethers produced by homopolymerisation, compared to the β-hydroxy amines produced in the amine-epoxy step addition reaction, thermodynamically limit methanol ingress. The ultimate ingress was not significantly impacted by ambient cure temperature at either stoichiometry.

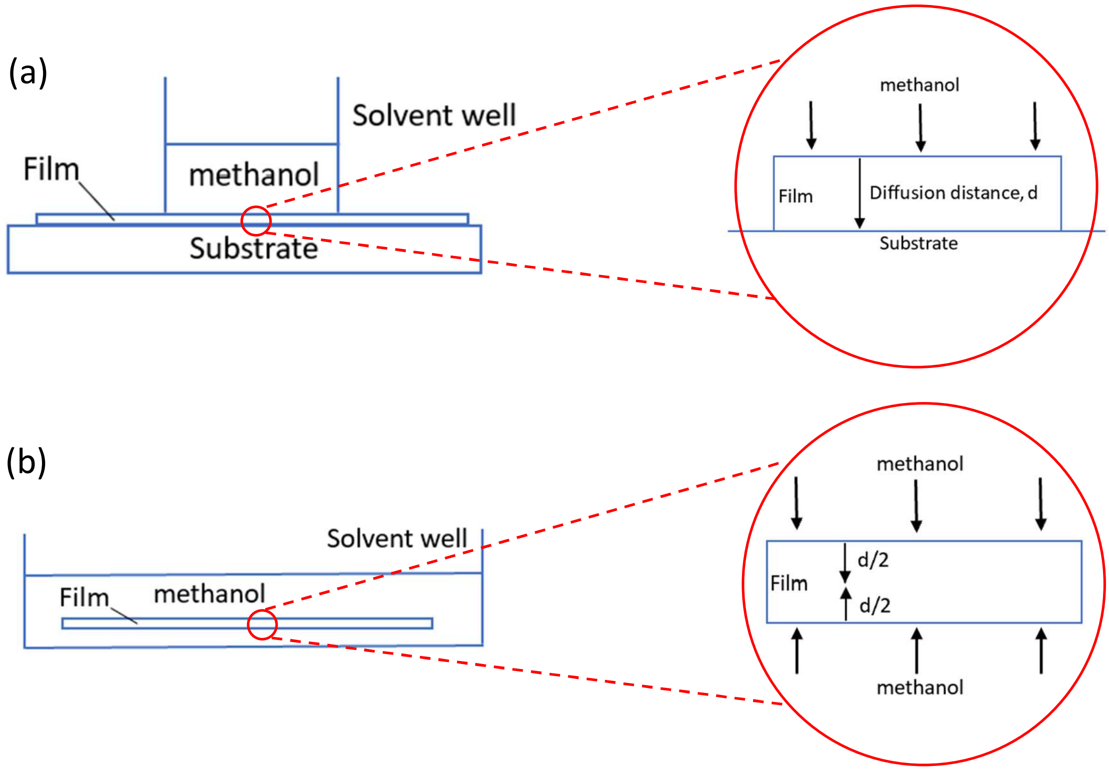

Figure 7.4: Schematic diagram (not to scale) displaying the ingress surface area and diffusion depth into a (a) substrate bound film and (b) free-standing film.

Interestingly, from the data in both Figure 7.2 and Figure 7.3, while desorption was advancing towards zero, full methanol egress was not attained within the timescale of the experiment, suggesting a few possibilities. The first possibility is that full methanol desorption from the system will eventually be achieved but cannot be observed within the experimental timescale utilised.[194,195] It is possible that while in contact with the solvent, the epoxy may be somewhat plasticised,[196] which would allow relatively faster movement at high concentrations. Under drier conditions, the opposite can occur, which may explain why egress is slower than ingress. Alternatively, it is possible that the surface dries faster than the bulk of the film, forming a more glassy region at the surface, termed the 'crust' by de Gennes.[197] Consequently, the diffusion coefficient of the remaining solvent in the film is reduced, decreasing the rate of egress. The final possibility instead suggests that methanol is retained by the polymer network *via* interactions with the polymer chains.[198] Wang *et al.* stated that methanol can interact with epoxy networks in two ways: either by forming a single hydrogen bond with the epoxy network, such as with an epoxy hydroxyl group (Type I), or by forming 2 hydrogen bonds between different chains, thus acting as a physical crosslinker (Type II).[199] They go onto state that Type I bound methanol can egress and evaporate spontaneously at room temperature, whereas Type II bound methanol requires elevated temperature for disassociation, speculated to be due to a comparatively higher activation energy.[199] Therefore, if Type II methanol-epoxy interactions occur, temperatures above RT would be required to achieve full methanol egress. This would also accelerate solvent egress from the first mechanism, but probably with a different temperature dependence. However, it is worth noting, that Type II methanol interactions and their consequences have not yet been widely accepted by the polymer community. An example of type I and II methanol-epoxy polymer chain interactions are shown in Figure 7.5.

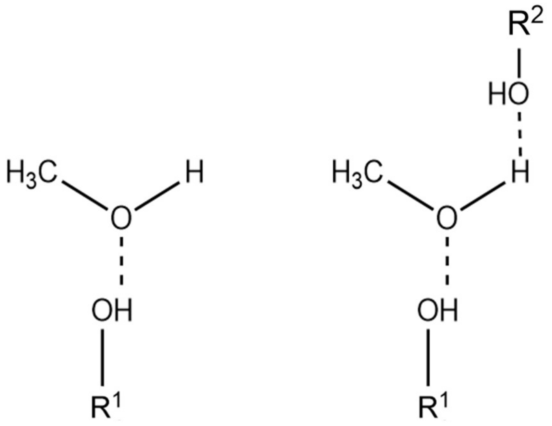

Figure 7.5: An example of Type I (left) and Type II (right) methanol interactions with epoxy polymer chains. R^1 and R^2 notations refer to polymer chains.

Single layer samples, cured under the same conditions and stoichiometries as those discussed above were also subjected to methanol ingress analysis, the results of which can be seen in Figure 7.6. As the two-layer samples contains an epoxy-epoxy interface between the layers but the single-layer samples do not, by comparing the methanol ingress and egress profiles of each corresponding 1- and 2-layer sample, the impact of interphase crosslink density on the overall film saturation can be determined.

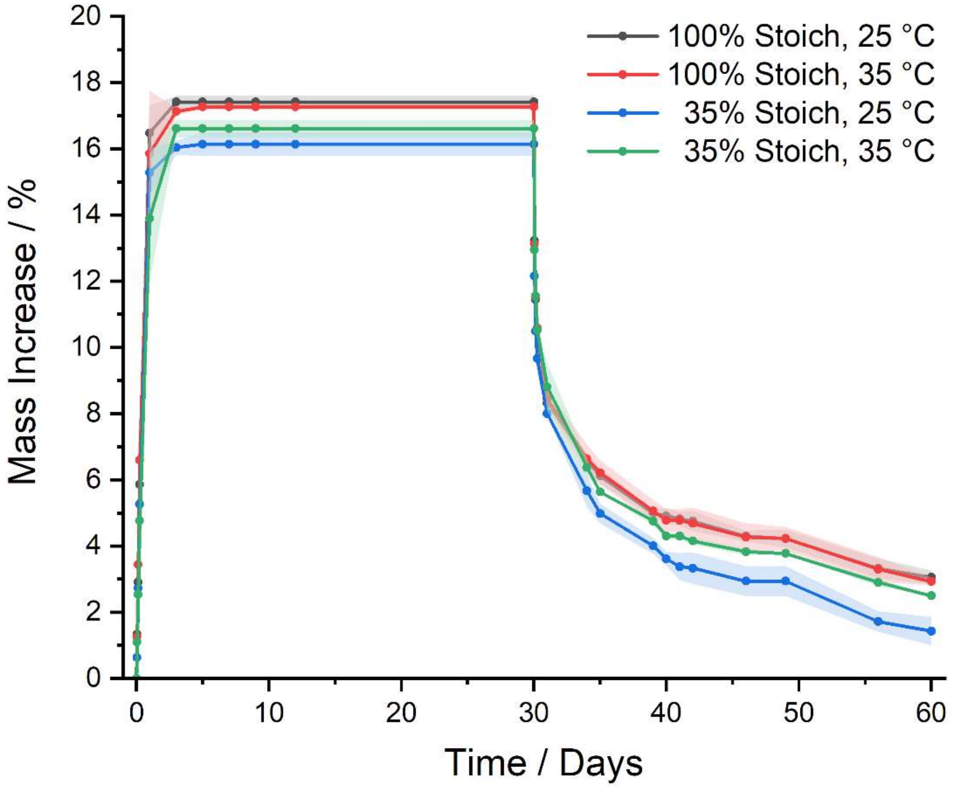

Figure 7.6: Sorption and desorption of methanol in different 1-layer epoxy systems over time. Ingress method: full submersion.

Based on the Raman mapping and PIXE spectroscopy reported in Section 6.2.2 and 6.2.3, respectively, it is expected that the overall film saturation will not be significantly affected by removal of the interfacial region as variation in crosslink density between interphase and bulk was insignificant on the micron scale. This proved to be the case as by comparing Figure 7.3 and Figure 7.6 it can be seen that ultimate ingress is unaffected by the presence of an interfacial region, Table 7.1.

Table 7.1: Ultimate ingress of methanol into different 1- and 2-layer epoxy systems.

System	1-Layer System Ultimate Ingress ± error	2-Layer System Ultimate Ingress ± error
100% stoichiometry, 25 °C	17.4 ± 0.2	17.0 ± 0.2
100% stoichiometry, 35 °C	17.3 ± 0.1	16.7 ± 0.4
35% stoichiometry, 25 °C	16.1 ± 0.4	15.5 ± 0.2
35% stoichiometry, 35 °C	16.6 ± 0.3	15.5 ± 0.1

7.2.2 Solvent Diffusion Mechanism into Post-Cured Epoxy Resins

When considering the ingress of methanol into epoxy resins, Fickian and Case II (non-Fickian) diffusion models are convenient to characterise behaviour. Fickian diffusion implies diffusion is independent of concentration, whereas Case II states that there is a dramatic change in diffusive mobility above a critical concentration.[200] Corresponding equations were previously listed in Chapter 2 (Equation 2.6 - 2.7). The type of diffusion that is observed can be determined by its time dependence, denoted by t^n where n is a constant. Fickian diffusion has a time dependence where $n = 1/2$, whereas for Case II, $n = 1$. Using this information, methanol uptake data of the systems studied can be plotted against idealised, straight-line Fickian and Case II diffusion plots derived from the corresponding data set. These idealised plots are produced by calculating the line statistics using the least squares method. By comparing the idealised fits to the raw methanol uptake data, it can be determined if a system follows a specific diffusion mechanism regarding solvent uptake. A Case II mechanism would support the idea that methanol may plasticize the film, allowing relatively faster movement at high concentrations. Conversely, if the mobility of methanol in the epoxy does not depend on its concentration (Fickian), then this barrier to complete egress does not exist.

In the free-standing films presented in Figure 7.1, solvent ingress was most rapid during the initial 24 hours. After this initial period, the ingress scaling behaviour changed due to the converging solvent fronts migrating from the different film faces. To determine the diffusion mechanism, the log of mass uptake was plotted against the log of time for the initial 24-hour period and compared to idealised Fickian and Case II plots (Figure 7.7).

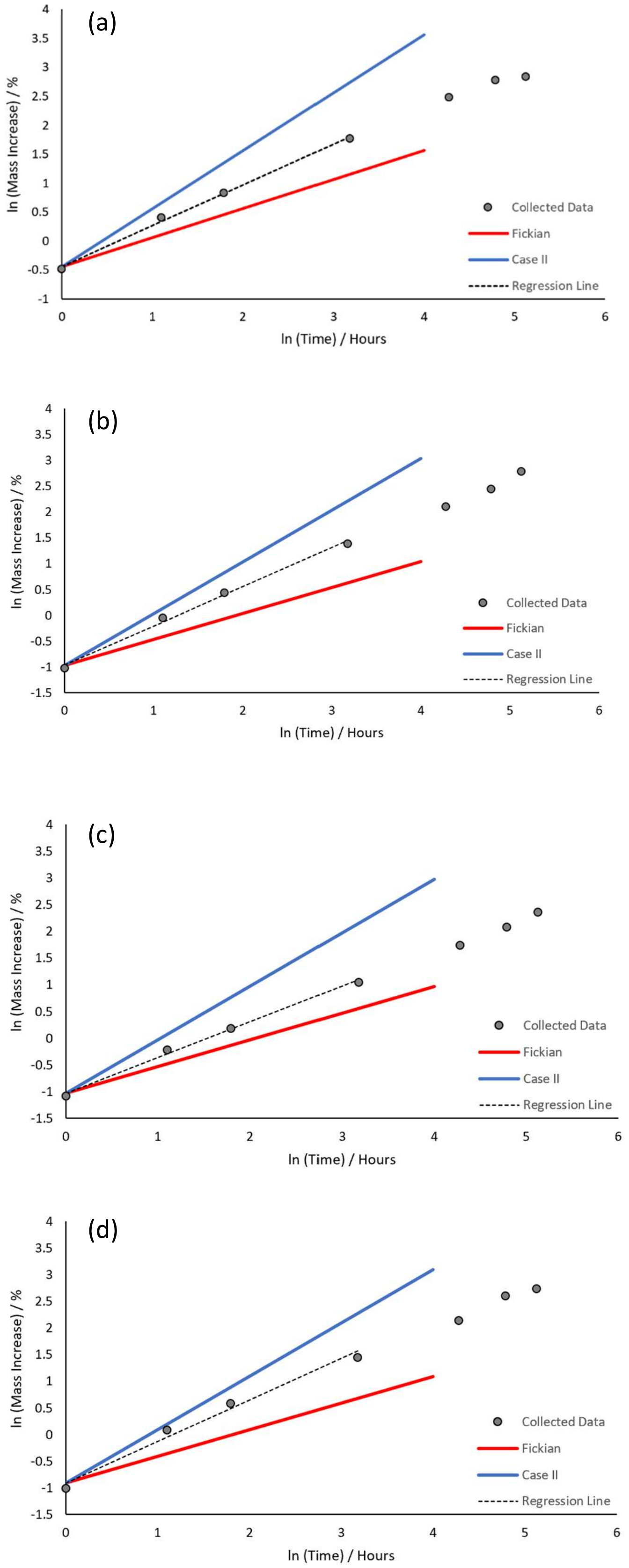

Figure 7.7: The log of percentage uptake of methanol against time, associated regression line, Fickian plot, and Case II plot. Systems: (a) 100%, 25 °C; (b) 100%, 35 °C; (c) 35%, 25 °C; (d) 35%, 35 °C.

As shown in Figure 7.7, the diffusion behaviour of methanol within the systems is neither Fickian or Case II, and instead behaves somewhere between the two. This is not entirely surprising given the models describe ideal cases, which is unlikely in practical application. The diffusion mechanism of organic solvents into epoxy resins has not been reported often in literature. Unlike what is shown here, Kaplan reported Fickian or near-Fickian diffusion of methanol into a range of bisphenol A diglycidyl epoxies cured with different curing agents.[201] The discrepancies between the findings presented here and Kaplan's study may be attributed to variations in the structure of the epoxies and/or curing agents used. Even subtle structural differences can influence the overall material behavior, including its response to solvent ingress.[201]

7.2.3 Epoxy Resin System Swell Analysis

As shown above, methanol is capable of penetrating into epoxy resins during contact. It is hypothesised that methanol can diffuse into the space between the polymer chains of the insoluble crosslinked network and cause the material to swell.[202,203] Polymer-solvent swell has been related to reduced physical and mechanical material properties, and in turn system failure, attributed to increased stress within the network.[186,187] Adamson observed swelling of up to 6% in water-saturated epoxy systems, stating that the polar water molecules are capable of forming hydrogen bonds with the hydroxyl groups of the polymer chains, thereby disrupting interchain hydrogen bonding leading to increased intersegmental hydrogen bond length.[198] While methanol is less polar than water, methanol (like other organic solvents) has a higher affinity to epoxy resins and consequently greater film swelling after absorption is expected.[199]

35% and 100% stoichiometry films were drawn down onto glass substrates using a cube applicator, cured at 25 °C or 35 °C, overcoated, and then post cured at 80 °C. Film thickness was then measured using a claw micrometer (resolution: 5 µm) over a 60-day period, as described in Section 3.6.2, whereby the film was immersed in methanol for the first 30 days and left in ambient conditions for the subsequent 30 days. Figure 7.8 shows the average film swell attributed to methanol ingress and egress into different epoxy films over time.

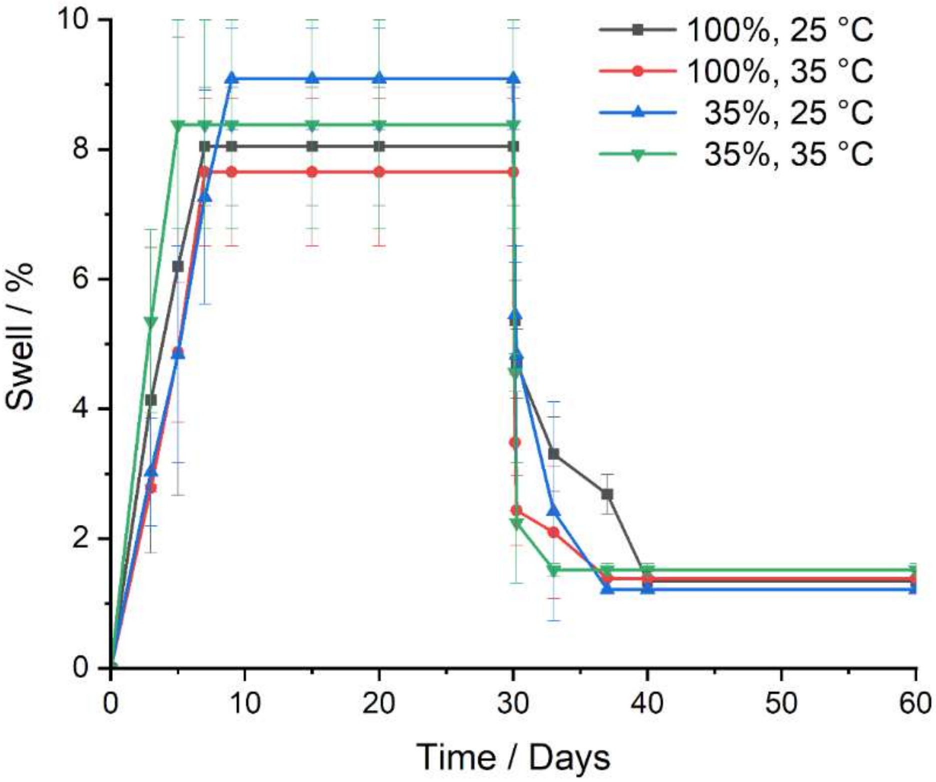

Figure 7.8: Percentage swell of each 2-layer epoxy system (~ 150 µm / layer) attributed to methanol ingress, over time.

Figure 7.8 shows that in all systems studied, methanol ingress led to film swelling, and that swelling (~ 8%) was significantly less than the mass increase previously found in this work (~ 16%). Given that the density of methanol (~ 790 kg/m^3 at 25 °C)[204] is lower than that of amine-cured epoxy resin (~ 1100 kg/m^3),[205] this indicates that at least half the ingressing solvent is occupying voids and adding to the density of the epoxy coating, rather than simply causing the network to stretch. The results of this study coincide with Sahlin and Peppas who reported an increase in TGDDM-DDS epoxy system volume attributed to methanol ingress. They hypothesised that this observed network swell could have been caused by the interactions between methanol hydroxy groups and epoxy hydroxy groups *via* hydrogen bonding. This could cause disruption of the intramolecular hydrogen bonding within the resin matrix itself, potentially causing the resin's network to expand.[190]

Figure 7.8 indicated that variation in cure temperature and stoichiometry had no significant impact on extent of swell. As initial sample thickness was ~ 350 µm, and maximum swell was less than 10%, change in film thickness did not exceed 35 µm. Given only 5 µm resolution could be accurately achieved using a claw micrometer, individual data point accuracy was less than desirable, and so to more accurately determine the impact of cure temperature and stoichiometry on the extent of swell, another technique, with greater precision was attempted. This involved using spin cast films on the thickness scale of hundreds of nanometres and measuring their change in sample thickness associated with solvent exposure using ellipsometry. The thickness of the spin cast samples was ~ 200 nm and based on Figure 7.8, a 20 nm increase in film thickness could be expected. Given ellipsometry allows sub nanometre resolution, this technique provides a relatively more accurate measure of film thickness compared to the previously discussed.

100% and 35% stoichiometry films were spin-cast and cured at 25 °C or 35 °C before overcoating with spin casting after 3 or 4 days and post curing. Prior to immersion in methanol, film thickness was determined. Samples were then immersed in methanol and thickness measured at predetermined intervals, until saturation. Samples were then removed from the methanol and again thickness was measured until sample thickness plateaued. Figure 7.9 shows the average film swell attributed to methanol ingress and egress into different spin cast epoxy films over time.

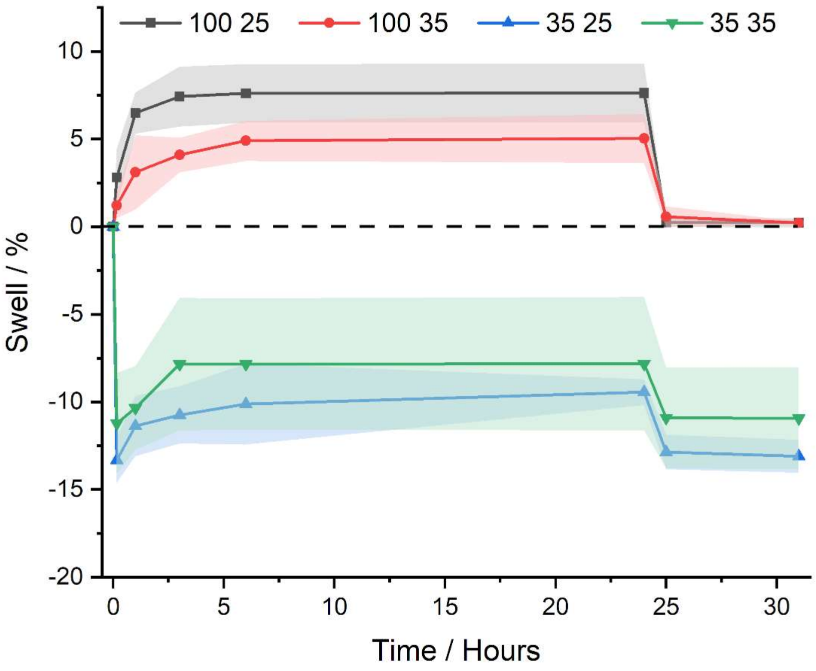

Figure 7.9: Percentage swell of each 2-layer epoxy system (~ 1000 Å / layer) attributed to methanol ingress, over time.

Figure 7.9 shows that in the 100% stoichiometry systems, there is a slight increase in swell in the 25 °C system compared to the 35 °C system. This correlates with Figure 7.3 whereby a greater ingress was seen in the 25 °C system compared to the 35 °C system. In both figures, this slight difference observed between the two systems falls just within the standard error of the curves, either indicating statistical insignificance or simply that the difference is valid but too small to be resolved.

In the 35% stoichiometry systems, there is initially a sharp decrease in the film thickness. A decrease in film thickness associated with solvent exposure is indicative of the removal of unreacted material from the polymer matrix. Wang *et al*. discussed methanol-epoxy interaction mechanisms of novolac epoxy coatings stating that leaching of coating ingredients was related to increased epoxy segmental chain mobility caused by methanol absorption, contributing to the migration of non-immobilised substances from the coating bulk to the adjacent methanol solution.[199] The data shown here suggests that even with a post cure at 80 °C, the epoxide excess system still has a proportion of unreacted material present in the system which is greater than that of the 100% stoichiometry systems. Figure 7.10 displays the DSC thermograms, detailing T_g, of the 35% stoichiometry systems, before and after heating at high temperature to determine if material remains unreacted within the 35% stoichiometry systems even after post curing at 80 °C. This was achieved by carrying out a heat, cool, heat cycle from 50 – 220 °C with a 10 °C / minute heating rate. In cycle 1, as the sample moved through T_g, the sample immediately began to react, evident by the clear exotherm. This indicates that even with a 16 hour, 80 °C post cure, there was still some residual reaction remaining in the 35% stoichiometry system. This led to the increase in T_g observed in cycle 2 of 108.8 °C compared to 106.8 °C in cycle 1. However, this difference may not be significant when compared to the breath of the transition. Regardless, the difference in T_g is relatively small, and may explain why no reduction in film thickness is observed in the micron-scale samples (Figure 7.8). Alternatively, as this initial decrease in film thickness was only observed in the 35% stoichiometry systems, and accelerators were only utilised in the 35% stoichiometry systems, it proposes the question: is a proportion of the accelerators in the 35% stoichiometry system enriched at the surface and subsequently stripped from the film upon contact with methanol? Alternatively, the higher proportion of RDGE and D.E.N. 431 to PAC-M in the 35% stoichiometry system, compared to the 100% stoichiometry system, may allow for greater extraction of unreacted RDGE or D.E.N. 431 from the 35% stoichiometry system. These theories will not be addressed here but provides scope for future work, perhaps through analysing the contents of the adjacent methanol solution *via* NMR, or instead by curing epoxy systems using deuterated accelerators and then applying neutron reflectometry to produce vertical composition profiles of these samples, thus characterising accelerator distribution throughout the film.

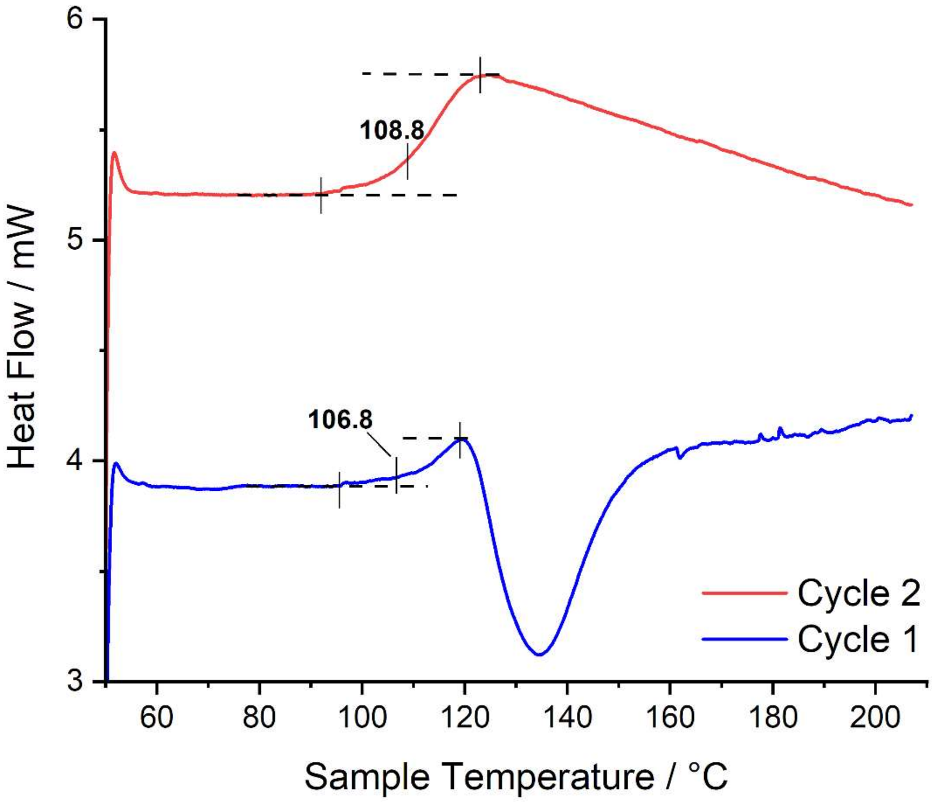

Figure 7.10: DSC thermogram of the 35% stoichiometry system (80 °C post cure) indicating T_g (Cycle 1) and T_g after heating at a elevated temperature (Cycle 2).

7.3 Chapter Conclusions

Epoxy coatings are used to line chemical tankers which transport methanol and other small molecule cargoes. While solvent ingress into epoxy resins has been previously characterised, [10,96,187,190] the impact of cure conditions and stoichiometry on the rate and extent of solvent uptake into the resultant resin systems required further investigation. In this work, it was shown that methanol was capable of diffusing into epoxy resin coatings and that ultimate ingress was significantly impacted by system stoichiometry. It was observed that films cured utilising a combination of step-growth amine addition polymerisation and anionic chain-growth homopolymerisation had decreased ultimate ingress compared to those cured using mainly step-growth amine addition polymerisation. This indicated two possibilities: (i) that anionic chain-growth homopolymerisation led to increased crosslink density compared to step-growth amine addition polymerisation, thus decreasing methanol uptake, or (ii) that the significantly less polar polyethers produced by homopolymerisation (compared to the β-hydroxy amines produced in the amine-epoxy step addition reaction) decreased methanol ingress, i.e., there is a thermodynamic element to saturation level. It was shown that the mechanism in which methanol diffused into the resin systems was not purely Fickian or Case II diffusion, indicating that a combination of the two was a more accurate description. It was also shown that the diffusion of methanol into these films resulted in swelling causing film thickness to increase by 7 – 10 % in ~ 350-micron samples. Ambient cure temperature less significantly impacted extent of methanol ingress, with only a slight increase in ultimate ingress observed in 100%, 25 °C films compared to 100%, 35 °C films. This coincided with nanometre scale swell analysis as the 100%, 25 °C films recorded higher swell than its 35 °C analogue.

Overall, the rate of ingress was quicker than the rate of egress. While the initial rate of egress over the first 24 hours was high, this quickly decreased, and subsequently total egress was not observed within the 30-day experimental egress interval. This indicated that either more time was required to achieve total egress due to slow diffusion, or that methanol was retained by the system due to Type II methanol-epoxy interactions and that elevated temperatures (above RT) would be required for total egress. To test either hypothesis, future work, involving egress data collected over a longer timescale and greater range of temperatures, would be required.

Chapter 8

Conclusions and Future Directions

8.1 Conclusions

Amine-cured, ≥2-layer, epoxy coatings are used to line chemical tankers, which transport methanol and other small molecule cargoes, but can undergo interlayer adhesion failure or delamination over time. Throughout this thesis, the surface, bulk, and interface properties of bilayer, amine-cured epoxy systems have been probed as a function of stoichiometry and cure condition (cure temperature, RH, OC interval) to better understand the surface and interfacial properties that are expected to be critical to interlayer adhesion. This research was loosely split into four aspects: first coat properties, interface formation mechanism, interface properties, and solvent studies.

Initially, first coat surface properties were analysed after the ambient cure phase but prior to post-cure and overcoating with the second coat, as factors affecting amine cured resin surfaces (such as carbamation) are known to influence their performance as substrates for adhesion. It was found that for a variety of controlled conditions, and their combinations, it was possible to detect early stages of carbamation using AFM and contact angle analysis; the most important single parameter appears to be RH, and its impact is most noticeable in formulations with high amine content. Increasing the cure RH also significantly increased surface roughness, surface layer formation, and wettability. While apparent SFE was little affected by variation in stoichiometry, WCA results indicated that the low amine content resin systems were, perhaps surprisingly, more hydrophilic than stoichiometrically balanced systems. Since these resins have T_g values higher than room temperature, and low roughness, it appears unlikely that the difference in wettability can be attributed to either reorientation of surface molecules or to surface topography; therefore, surface chemistry is most likely responsible for the greater wettability.

Following on from this, first coat bulk material properties (R_q, rugosity, wettability, T_g, AVV, FFV) were also characterised as these were hypothesised to be influential regarding intercoat adhesion. Variation in the ambient cure conditions and stoichiometry caused significant variation in the first coat bulk properties. In particular, cure temperature more significantly affected the bulk properties compared to RH, with increasing cure temperature increasing extent of cure and FFV while decreasing AVV.

Investigating the mechanism of interface formation between layers of epoxy resin systems proved challenging due to the insolubility of cured materials and the lack of variation in chemistry between layers. However, in this work, using Raman mapping, it was shown that significant diffusion of molecules that mimic the size and solubility of epoxy components is possible into ambient-cured epoxy resins, occurring over tens of microns during a 3-day period. On this basis, it was concluded that interdiffusion in bilayer epoxy interfaces is likely to be a significant part of interphase formation, similarly to that previously reported in epoxy-thermoplastic interphase formation.[57–63] The presence of carbamate on the surface of the first coat had a significant inhibiting effect on small molecule diffusion into the first coat, as did the application of a post-cure. It was also shown that increasing the ambient cure temperature, OC interval, and RH all significantly decreased extent of interdiffusion. Interestingly, of the first coat properties, which were characterised, T_g, extent of conversion (and system rigidity) seemed to be more influential regarding extent of ingress than the others, including AVV. In contrast to previous studies of AVV on fully cured epoxies,[96] there was no evidence for a sharp cut-off in the size of molecule that could penetrate a partially cured structure.

Novel approaches were developed to probe bulk and interphase crosslink density of the 2-layer systems using spatially resolved solvent ingress measurements. This allowed for the characterisation of system crosslink density as a function of stoichiometry, ambient cure temperature, and OC interval. Using Raman mapping and PIXE analysis, on the micron scale, it was shown that the crosslink density homogeneity of films polymerised using predominantly amine addition (100% stoichiometry) was slightly increased when the cure temperature was increased from 25 °C to 35 °C. However, little difference was observed between bulk and interphase crosslink densities. Neutron reflectometry was then utilised for the first time to indirectly characterise interphase crosslink density on the nanometre scale in films cured utilising both amine addition polymerisation (100% stoichiometry systems), and a combination of amine addition and epoxy homopolymerisation (35% stoichiometry systems). Previously, only the nanostructure of single-layer, cured epoxy resin systems has been characterised (using neutron reflectometry).[179] Here, it was shown that cure temperature, stoichiometry and overcoating interval all affected film crosslink density at the nanometre scale. At both stoichiometries, increasing the cure temperature from 25 °C to 35 °C generally increased crosslink density homogeneity, as regions of increased crosslink density were indicated by low solvent ingress near the surface of films cured at 25 °C. Increasing the overcoating interval from 3- or 4- to 7-days did not significantly impact the crosslink density of the 35% stoichiometry films, but had some impact in the 100% stoichiometry systems. Throughout all films, no obvious signs of early-stage adhesion failure were observed. Given delamination is a fatigue associated issue, this result may imply that obvious signs of delamination are not intrinsically present in the film from synthesis, and instead are caused by the repetitive cycles of solvent exposure, followed by film drying, in industrial application.

While solvent ingress into epoxy resins has been previously characterised, [10,96,187,190] the impact of cure conditions and stoichiometry on the rate and extent of solvent uptake into the resultant resin systems required further investigation. In this work, it was shown that methanol was capable of diffusing into the 2-layer, post cured epoxy resin coatings and that ultimate ingress was significantly impacted by system stoichiometry. It was observed that films cured utilising a combination of step-growth amine addition polymerisation and anionic chain-growth homopolymerisation had decreased ultimate ingress compared to those cured using mainly step-growth amine addition polymerisation. This indicated that anionic chain-growth homopolymerisation led to increased crosslink density compared to step-growth amine addition polymerisation. The mechanism by which methanol diffused into the resin systems was shown to be not purely Fickian or Case II diffusion, indicating that a combination of the two was a more accurate description. It was also shown that the diffusion of methanol into these films resulted in swelling causing film thickness to increase by 7 – 10 % in ~ 350-micron samples. Ambient cure temperature less significantly impacted the extent of methanol ingress, with only a slight increase in ultimate ingress observed in 100%, 25 °C films compared to 100%, 35 °C films. This coincided with nanometre scale swell analysis as the 100%, 25 °C films recorded higher swell than its 35 °C analogue.

In summary, the main outcomes of this work were the following:

- Interlayer diffusion, and the formation of an interphase, was shown to occur in bilayer ambient cured epoxy resin systems. This is likely to be significant regarding the interlayer adhesion.

- Extent of interlayer diffusion was significantly increased by decreasing ambient cure temperature and overcoating interval. This was attributed to reduced conversion and crosslink density in the first coat, as the application of a post-cure to the first coat inhibited ingress.
- High carbamate formation, attributed to elevated cure RH, almost completely suppressed second coat ingress suggesting that carbamate contributes to adhesion failure by inhibiting the interdiffusion of sequential layers.
- No obvious signs of early-stage adhesion failure, such as a sharp decrease in interfacial crosslink density, were observed in samples studied using Raman, PIXE or NR. This may imply that obvious signs of delamination are not intrinsically present in the film from synthesis, and instead may be caused by the repetitive cycling of solvent exposure, followed by film drying, in industrial application.

8.2 Future Directions

The original project aims were:

1. To provide insight into the impact of stoichiometry, cure conditions and the interplay of cure conditions on the surface and bulk properties of the first coat prior to overcoating, to determine the likely impact on interface formation.
2. To determine if the diffusion of sequential layers is possible, thus leading to an area of bonding between the topcoat and basecoat, termed the interphase.
3. To gain understanding of the dimensions and physicochemical properties of the interphase region, as well as the factors which govern this.

Aim 2 was comprehensively addressed, whereas further scope is still available for aim 1. Throughout this thesis, the impact of stoichiometry on system properties was explored by comparing two stoichiometric extremes; 100% stoichiometry, which utilised mainly step-growth amine addition polymerisation, and 35% stoichiometry, which utilised a combination of step-growth amine addition polymerisation and epoxide homopolymerisation. In the future it would be beneficial to carry out these experiments over a greater range of stoichiometries, producing a data series and thus enabling the competing roles of these polymerisation mechanisms to be isolated more clearly. Similarly, system properties could be investigated over a greater range of ambient cure temperatures as opposed to just the two applied in this research (25 °C and 35 °C). This is particularly relevant at temperatures above 35 °C, given the expected continued rise in ambient global temperatures attributed to global warming. Given the different polymerisation mechanisms it would be interesting to establish how these vary with temperature since this could provide a means of modifying coating properties without changing a formulation.

In addition, by building upon the work of this thesis, future scope may be available for aim 3. Further understanding as to the interface formation mechanism could also be built upon from this work. In section 6.2.1.1, it was shown that interdiffusion of the second coat into the first coat is possible, and two hypotheses were proposed as to the mechanism of interface formation and subsequent interlayer adhesion: (1) the reaction of the infusing species with the first layer network and propagation back to the second layer to form a continuous network. (2) Dangling ends of the first layer reaching into, and reacting with, the second layer. This may be attributed to either the removal of first coat sol into the second layer, thus exposing the dangling ends, or a region of decreased T_g at the first coat surface, caused by the diffusion front of the penetrating second coat, thus allowing diffusion of the first coat dangling chains into the second coat. While it is possible that both processes occur to some extent, focus should now be directed towards determining which mechanism is dominant and therefore more significant for interlayer adhesion; greater understanding of the formation mechanism may uncover insight into the likely causes of adhesion failure. However, this may be tricky to achieve using current analytical techniques, perhaps impossible, as it is challenging to independently track the movement of small (sol) and larger (dangling chains) molecules within a system. As a starting point, it would be first interesting to determine if interdiffusion between layers is bidirectional, as in this work only the movement from second coat into first coat was considered. This could be achieved by adapting the method utilised in Section 6.2.1.1, which was originally used to confirm first layer penetration by the second layer: produce the first coat using a component, which contains an elementally unique functional group, and then overcoat with a second coat component, which does not contain this. After the predetermined OC interval, the second coat component, which should still be in liquid form (residue), can be removed from the surface *via* wiping, and compositionally analysed using NMR. The presence or absence, of the unique functional group in this residue would determine if unanchored first layer sol has been able to migrate into the second layer and thus show if the process is bidirectional. Additional analytical approaches might be required to determine the migration of larger, first coat-tethered molecules if these are not sensitively detected by solution state NMR. Perhaps by attaining (or synthesising) deuterated epoxy components, Raman mapping experiments or NR could also be used to further resolve what happens at the interphase.

In addition, further neutron reflectometry experiments could uncover more details regarding the relationship between crosslink density and adhesion failure. While the neutron reflectivity data in this research showed interesting trends regarding crosslink density as a function of cure condition and stoichiometry, our interpretations indicated few if any signs of early-stage adhesion failure. This may be linked to the idea that epoxy coating adhesion failure is a fatigue associated issue, manifesting over longer time periods, and linked to repetitive cycles of exposure to solvent followed by film drying. Therefore, it would be interesting to carry out the same neutron reflectometry experiment again (*i.e.,* samples cured at the same stoichiometries, under the same conditions), but prior to analysis, the samples could undergo repetitive solvent cycling thus mimicking their industrial application where adhesion failure is observed. The results of these experiments could then be compared to those reported in this thesis and the impact of repetitive solvent cycling on system crosslink density determined. This could even be taken a step further by producing a series of samples with a differing number of cycles (independent variable: no. of cycles).

In Chapter 7, it was shown that methanol-saturated epoxy systems could not attain complete methanol egress within 30 days of removal from methanol immersion. This indicated that either more time was required to achieve total-egress, or that methanol was retained by the system due to Type II methanol-epoxy interactions and thus elevated temperatures (above RT) would be required for total egress. By carrying out the same experiment, but over a longer period (*e.g.*, 60 days), it could be determined which hypothesis is true. The results of this would be important for industrial applications of transporting solvent cargoes.

Bibliography

1 Special Projects Team - Safinah Group, *Insurance Market Coating Claims: Focus on Tank Linings*, 2020.

2 S. Sirimanne, R. Asariotis, G. Ayala, M. Assaf, C. Bacrot, H. Benamara, D. Chantrel, A. Cournoyer, M. Fugazza, P. Hansen, J. Hoffmann, T. Kulaga, A. Premti, L. Rodríguez, B. Salo, K. Tahiri, H. Tokuda, P. Ugaz and F. Youssef, *Review of Maritime Transport 2021*, United Nations Conference on Trade and Development (UNCTAD), 2021.

3 B. P. Mallik, in *High-Performance Organic Coatings*, Woodhead Publishing, Cambridge, 2008, pp. 97–122.

4 M. Aamodt, Cargo Tank Coatings: What can go wrong (and how to avoid it), https://iumi.com/education/webinars/webinar-recordings-and-slides/cargo-tank-coatings-what-can-go-wrong-and-how-to-avoid-it_1639400177, (accessed 3 September 2023).

5 G. Poynton, PhD Thesis, The University of Manchester, 2014

6 J. L. Massingill Jr and R. S. Bauer, *Epoxy Resin*, Elsevier, 2000.

7 I. K. Varma and V. B. Gupta, in *Comprehensive Composite Materials*, Pergamon Press, Oxford, 2000, vol. 2, pp. 1–56.

8 J.-P. Pascault and R. J. J. Williams, in *Epoxy Polymers*, Wiley-VCH Verlag GmbH & Co. KGaA, Weinheim, Germany, 2010, pp. 1–12.

9 G. Emmerson, PhD Thesis, Durham University, 2003.

10 M. P. Didsbury, PhD Thesis, Durham University, 2014

11 O. Hara, *Curing Agents for Epoxy Resin*, Three Bond Technical News, Tokyo, 1990.

12 F.-L. Jin, X. Li and S.-J. Park, *Journal of Industrial and Engineering Chemistry*, 2015, **29**, 1–11.

13 W.-F. A. Su, K. C. Chen and S. Y. Tseng, *J Appl Polym Sci*, 2000, **78**, 446–451.

14 G. S. Nolan, L. J. Saethre, M. R. Siggel, T. D. Thomas and L. Ungier, *J Am Chem Soc*, 1985, **107**, 6463–6467.

15 J.-E. Ehlers, N. G. Rondan, L. K. Huynh, H. Pham, M. Marks and T. N. Truong, *Macromolecules*, 2007, **40**, 4370–4377.

16 T. Takeichi and N. Furukawa, in *Polymer Science: A Comprehensive Reference*, 2012, vol. 5, pp. 723–751.

17 M. Dornbusch, U. Christ and R. Rasing, in *Epoxy Resins*, Vincentz Network, 2019, pp. 11–20.

18 C. Jubsilp, T. Takeichi and S. Rimdusit, in *Handbook of Benzoxazine Resins*, Elsevier, 2011, pp. 157–174.

19 S. K. Ooi, W. D. Cook, G. P. Simon and C. H. Such, *Polymer (Guildf)*, 2000, **41**, 3639–3649.

20 M. Döring and U. Arnold, *Polym Int*, 2009, **58**, 976–988.

21 T. Vidil, F. Tournilhac, S. Musso, A. Robisson and L. Leibler, *Prog Polym Sci*, 2016, **62**, 126–179.

22 A. Farkas and P. F. Strohm, *J Appl Polym Sci*, 1968, **12**, 159–168.

23 J. M. Barton and P. M. Shepherd, *Die Makromolekulare Chemie*, 1975, **176**, 919–930.

24 T. Liu, B. Han, L. Zhang, M. Wu, A. Xing, X. Miao, Y. Meng and X. Li, *RSC Advances*, 2016, **6**, 14211–14221.

25 M. J. Marks and R. V. Snelgrove, *ACS Appl Mater Interfaces*, 2009, **1**, 921–926.

26 P.-Y. Kuo, M. Sain and N. Yan, *Green Chem.*, 2014, **16**, 3483–3493.

27 X. M. Chen and B. Ellis, in *Chemistry and Technology of Epoxy Resins*, Springer Netherlands, Dordrecht, 1993, pp. 303–325.

28 C. Yi, P. Rostron, N. Vahdati, E. Gunister and A. Alfantazi, *Prog Org Coat*, 2018, **124**, 165–174.

29 G. Zhang, Q. Xie, C. Ma and G. Zhang, *Prog Org Coat*, 2018, **117**, 29–34.

30 J. Trinidad, L. Chen, A. Lian and B. Zhao, *Int J Adhes Adhes*, 2017, **78**, 102–110.

31 A. Shackleford, PhD Thesis, University of Sheffield, 2019.

32 Y. Li, F. Xiao and C. P. Wong, *J Polym Sci A Polym Chem*, 2007, **45**, 181–190.

33 Z. Wang, P. Gnanasekar, S. S. Nair, S. Yi and N. Yan, *Polymers (Basel)*, 2021, **13**, 2891.

34 F. Meyer, G. Sanz, A. Eceiza, I. Mondragon and J. Mijović, *Polymer (Guildf)*, 1995, **36**, 1407–1414.

35 H. Li, G. Chen, H. Su, D. Li, L. Sun and J. Yang, *Eur Polym J*, 2019, **112**, 792–798.

36 B. Ashrafi, Y. Martinez-Rubi, L. Khoun, M. Yourdkhani, P. Hubert, C. Kingston, A. Johnston and B. Simard, in *ECCM 2012 - Composites at Venice, Proceedings of the 15th European Conference on Composite Materials*, 2012.

37 N. Saleh, A. Razak, M. Tooma and M. Aziz, *Engineering and Technology Journal*, 2011, **29**, 1804–1818.

38 A. P. Gupta, S. Ahmad and A. Dev, *Polym Plast Technol Eng*, 2010, **49**, 657–661.

39 C. Bannister, A. Guy, R. Mihaylova, J. Orgill, S. L. Burg, A. Parnell and R. L. Thompson, *RSC Adv*, 2022, **12**, 28746–28754.

40 F. Lapique and K. Redford, *Int J Adhes Adhes*, 2002, **22**, 337–346.

41 I. A. Saeedi, A. S. Vaughan, T. Andritsch and S. Virtanen, in *2016 IEEE Conference on Electrical Insulation and Dielectric Phenomena (CEIDP)*, IEEE, 2016, pp. 461–464.

42 D. R. Miller and C. W. Macosko, *J Polym Sci B Polym Phys*, 1988, **26**, 1–54.

43 A. Herczeg, G. Ronay and W. Simpson, in *National SAMPE Technical Conference Proceedings*, Azusa, 1970, pp. 221–231.

44 B. L. Burton, Amine-Blushing Problem? No Sweat!, *presented at the Epoxy Resin Formulators' meeting, The Society of the Plastics Industry*, Huntsman Corporation, Texas, 2001.

45 J. R. Davis, *Corrosion: Understanding the Basics*, ASM International, Ohio, 2000.

46 Sean Crow, *Epoxy Coating Blush Explanation & Prevention Recommendations*, TRiiSO, USA, 2018.

47 J. P. Bell, J. A. Reffner and S. Petrie, *J Appl Polym Sci*, 1977, **21**, 1095–1102.

48 N. Mills and M. Jenkins, *Plastics: Microstructure and Engineering Applications*, Elsevier, 3rd edn., 2005.

49 C. Austen Angell and S. Sivarajan, in *Reference Module in Materials Science and Materials Engineering*, Elsevier, 2017.

50 G. Wisanrakkit and J. K. Gillham, *J Appl Polym Sci*, 1990, **41**, 2885–2929.

51 J. Bouchet and A.-A. Roche, *J Adhes*, 2002, **78**, 799–830.

52 W. Possart, J. K. Krüger, C. Wehlack, U. Müller, C. Petersen, R. Bactavatchalou and A. Meiser, *Comptes Rendus Chimie*, 2006, **9**, 60–79.

53 K. Anand, T. Duguet, J. Esvan and C. Lacaze-Dufaure, *ACS Appl Mater Interfaces*, 2020, **12**, 57649–57665.

54 A. A. Roche, J. Bouchet and S. Bentadjine, *Int J Adhes Adhes*, 2002, **22**, 431–441.

55 J. Kanzow, P. S. Horn, M. Kirschmann, V. Zaporojtchenko, K. Dolgner, F. Faupel, C. Wehlack and W. Possart, *Appl Surf Sci*, 2005, **239**, 227–236.

56 S. Morsch, Y. Liu, M. Malanin, P. Formanek and K.-J. Eichhorn, *ACS Appl Nano Mater*, 2019, **2**, 2494–2502.

57 M. Munz, *J Adhes*, 2008, **84**, 445–482.

58 L. Vandi, M. Hou, M. Veidt, R. Truss, M. Heitzmann and R. Paton, in *Proceedings of 28th International Congress of the Aeronautical Sciences*, 2012, pp. 1–9.

59 S. Deng, L. Djukic, R. Paton and L. Ye, *Compos Part A Appl Sci Manuf*, 2015, **68**, 121–132.

60 U. Farooq, S. Heuer, J. Teuwen and C. Dransfeld, *ACS Appl Polym Mater*, 2021, **3**, 6111–6119.

61 O. Erartsın, J. S. M. Zanjani and I. Baran, *Polymers (Basel)*, 2022, **14**, 1493.

62 L. Zweifel and C. Brauner, *Compos Part A Appl Sci Manuf*, 2020, **139**, 106120.

63 H. T. Oyama, J. J. Lesko and J. P. Wightman, *J Polym Sci B Polym Phys*, 1997, **35**, 331–346.

64 A. Karim and S. Kumar, *Polymer Surfaces, Interfaces and Thin Films*, World Scientific, Singapore, 2000.

65 R. P. Wool, *Macromolecules*, 1993, **26**, 1564–1569.

66 C. McIlroy and P. D. Olmsted, *Polymer (Guildf)*, 2017, **123**, 376–391.

67 J. W. Strutton, N. H. Moser, E. J. Garboczi, A. R. Jennings, B. Runnels and J. M. McCollum, *ACS Appl Polym Mater*, 2022, **4**, 1535–1542.

68 C. Villevieille, *Advanced Materials Interfaces, 2022,* ***9****, 2101865.*

69 T. Nguyen, X. Gu, M. R. VanLandingham, D. Nguyen and M. Giraud, in *Proceedings of the 9th International Conference on Durability of Building Materials and Components*, 2002, pp. 1–8.

70 Y. Zhang, PhD Thesis, University of Wollongong, 1995.

71 R. A. L. Jones and R. W. Richards, *Polymers at Surfaces and Interfaces*, Cambridge University Press, Cambridge, 1999.

72 D. De Kee, Q. Liu and J. Hinestroza, *Can J Chem Eng*, 2008, **83**, 913–929.

73 R. L. Thompson, M. T. McDonald, J. T. Lenthall and L. R. Hutchings, *Macromolecules*, 2005, **38**, 4339–4344.

74 J. Comyn, *Adhesion Science*, Royal Society of Chemistry, Cambridge, 2007.

75 J.A. Baghdachi, in *Adhesive Aspects of Polymeric Coatings*, The Federation of Societies of Coating Technology, Blue Bell, 1996.

76 V. E. Basin, *Prog Org Coat*, 1984, **12**, 213–250.

77 N. Balabanava, R. Wierzbicki, M. Zielecka and Z. Rymuza, *Microelectron Eng*, 2007, **84**, 1227–1230.

78 S. A. Page, J. C. Berg and J.-A. E. Månson, *J Adhes Sci Technol*, 2001, **15**, 153–170.

79 K. Kendall, *Molecular Adhesion and Its Applications: The Sticky Universe*, Kluwer Academic/Plenum Publishers, New York, 2001.

80 S. Abbott, *Adhesion science: principles and practice*, DEStech Publications Inc., Lancaster, 2015.

81 J. P. B. van Dam, S. T. Abrahami, A. Yilmaz, Y. Gonzalez-Garcia, H. Terryn and J. M. C. Mol, *Int J Adhes Adhes*, 2020, **96**, 102450.

82 D. Zhang and Y. Huang, *Prog Org Coat*, 2021, **153**, 106135.

83 B. Minisini, S. Rolère, J.-F. Coulon and F. Poncin-Epaillard, *Eur Polym J*, 2019, **112**, 452–460.

84 D. Quan and A. Ivankovic, *Polymer (Guildf)*, 2015, **66**, 16–28.

85 A. Rudawska and E. Jacniacka, *Int J Adhes Adhes*, 2009, **29**, 451–457.

86 D. E. Packham, *Int J Adhes Adhes*, 2003, **23**, 437–448.

87 V. V. Arslanov and V. A. Ogarev, *Problems of Polymeric Composite Materials,* Naukova Dumka, Kiev, 1979, 76.

88 V. Neela and N. von Solms, *Journal of Polymer Research*, 2014, **21**, 401.

89 G. S. Park, *Polymer (Guildf)*, 1975, **16**, 855.

90 Elizabeth Ann Stanley, PhD Thesis, California Institute of Technology, 1985.

91 G. S. Park, *British Polymer Journal*, 1986, **18**, 209–210.

92 D. G. Bucknall, J. S. Higgins and S. A. Butler, *J Polym Sci B Polym Phys*, 2004, **42**, 3267–3281.

93 B. Narasimhan and N. A. Peppas, *Macromolecules*, 1996, **29**, 3283–3291.

94 A. S. Argon, R. E. Cohen and A. C. Patel, *Polymer (Guildf)*, 1999, **40**, 6991–7012.

95 K. Frank and J. Wiggins, *J Appl Polym Sci*, 2013, **130**, 264–276.

96 Jackson Matthew, Kaushik Mukul, Nazarenko Sergei, Ward Steve, Maskell Rob and Wiggins Jeffrey, *Polymer (Guildf)*, 2011, **52**, 4528–4535.

97 K. L. Perry, P. J. McDonald, E. W. Randall and K. Zick, 1994, **35**, 2744–2748.

98 P. J. Flory, *J Chem Phys*, 1942, **10**, 51–61.

99 M. L. Huggins, *J Chem Phys*, 1941, **9**, 440–440.

100 K. te Nijenhuis and D. W. van Krevelen, *Thermal Decomposition*, Elsevier, Amsterdam, 2009.

101 C. M. Hansen, PhD Thesis, Technical University of Denmark, 1967.

102 W. Zeng, du Y, Xue Y and H. L. Frisch, in *Physical Properties of Polymers Handbook*, Springer, New York, 2nd edn., 2007, pp. 289–303.

103 P. J. Flory and J. Rehner, *J Chem Phys*, 1943, **11**, 512–520.

104 S. S. Velankar, V. Lai and R. A. Vaia, *ACS Appl Mater Interfaces*, 2012, **4**, 24–29.

105 M. G. Unthank, C. Cameron, A. Wright, D. Hughes, M. Ashraf Alam and M. R. Probert, *Polym Chem*, 2019, **10**, 4920–4929.

106 K. Frank, C. Childers, D. Dutta, D. Gidley, M. Jackson, S. Ward, R. Maskell and J. Wiggins, *Polymer (Guildf)*, 2013, **54**, 403–410.

107 International Paint Ltd, *Interline 9001 Part B*, Interline 9001 Part B, TCA902, United Kingdom, 2017.

108 World Intellectual Property Organization, WO 2012/119968 A1, 2012, 1–21.

109 G. D. Mills, *Materials Performance*, George Mills and Associates International Inc., Tennessee, 2008, 52–55.

110 J. G. Dorsey, G. F. Dorsey, A. C. Rutenberg and L. A. Green, *Anal Chem*, 1977, **49**, 1144–1145.

111 S. T. Knox, A. Wright, C. Cameron, J. Patrick and A. Fairclough, *Macromolecules*, 2019, **52**, 6861–6867.

112 M. K. Singh and A. Singh, in *Characterization of Polymers and Fibres*, Woodhead Publishing, Sawston, 2022, pp. 321–339.

113 G. W. H. Höhne, W. F. Hemminger and H.-J. Flammersheim, *Differential Scanning Calorimetry*, Springer Berlin Heidelberg, Berlin, Heidelberg, 2003.

114 G. Lomboy, S. Sundararajan, K. Wang and S. Subramaniam, *Cem Concr Res*, 2011, **41**, 1157–1166.

115 R. Fong, PhD Thesis, Durham University, 2020.

116 B. Kelechava, *Surface Texture (Surface Roughness, Waviness, and Lay)*, ASME, New York, 2020.

117 C. P. Gibson, M. A. Litwinowicz, J. P. Tellam, R. J. L. Welbourn, M. W. A. Skoda, J. Claussen and R. L. Thompson, *Polymers (Basel)*, 2021, **13**, 3407.

118 P. G. de Gennes, *Rev Mod Phys*, 1985, **57**, 827–863.

119 R. N. Wenzel, *Ind Eng Chem*, 1936, **28**, 988–994.

120 A. F. Stalder, G. Kulik, D. Sage, L. Barbieri and P. Hoffmann, *Colloids Surf A Physicochem Eng Asp*, 2006, **286**, 92–103.

121 D. K. Owens and R. C. Wendt, *J Appl Polym Sci*, 1969, **13**, 1741–1747.

122 T. Mezger, *The Rheology Handbook*, Vincentz Network, Hanover, 3rd edn., 2011.

123 S. J. Tao, *J Chem Phys*, 1972, **56**, 5499–5510.

124 M. Eldrup, D. Lightbody and J. N. Sherwood, *Chem Phys*, 1981, **63**, 51–58.

125 R. J. Fong, A. Robertson, P. E. Mallon and Richard. Thompson, *Polymers (Basel)*, 2018, **10**, 1036.

126 J. M. de Jesus, C. Costa, A. Burton, V. Palitsin, R. Webb, A. Taylor, C. Nikula, A. Dexter, F. Kaya, M. Chambers, V. Dartois, R. J. A. Goodwin, J. Bunch and M. J. Bailey, *Anal Chem*, 2021, **93**, 13450–13458.

127 P. Dewhurst, PhD Thesis, Durham University, 1998.

128 I. Gomez-Morilla, A. Simon, R. Simon, C. T. Williams, Á. Z. Kiss and G. W. Grime, *Nucl Instrum Methods Phys Res B*, 2006, **249**, 897–902.

129 T. Chatterji, in *Neutron Scattering from Magnetic Materials*, Elsevier, France, 2006.

130 A. Jackson, *Introduction to Small-Angle Neutron Scattering and Neutron Reflectometry*, NIST Center for Neutron Research, Gaithersburg, 2008.

131 M. C. Weidner, Z. Evenson, M. Zamponi and W. Possart, *Macromol Chem Phys*, 2019, **220**, 1–11.

132 D. S. Sivia, *Elementary Scattering Theory*, Oxford University Press, Oxford, 2011.

133 J. Penfold and R. K. Thomas, *Journal of Physics: Condensed Matter*, 1990, **2**, 1369–1412.

134 H. C. Benoit and J. S. Higgins, *Polymers and neutron scattering*, Oxford University Press, Oxford, 1994.

135 H. Wang, J. Mo, B. Shentu and Z. Weng, *Polym Eng Sci*, 2014, **54**, 2595–2604.

136 S. Zhao, G. Zhang, R. Sun and C. Wong, *J Appl Polym Sci*, 2014, **131**, 1–9.

137 H. Nouailhas, C. Aouf, C. le Guerneve, S. Caillol, B. Boutevin and H. Fulcrand, *J Polym Sci A Polym Chem*, 2011, **49**, 2261–2270.

138 M. Suckow, M. Lang, H. Komber, D. Pospiech, M. Wagner, F. Weinelt, F.-E. Baumann and F. Böhme, *Polym Chem*, 2019, **10**, 1930–1937.

139 Olin, Epoxy Novolac Resins, https://olinepoxy.com/products/epoxy-novolac-resins/, (accessed 6 August 2023).

140 A. Kinloch, G. Kodokian and J. Watts, *Philosophical Transactions of the Royal Society of London. Series A: Physical and Engineering Sciences*, 1992, **338**, 83–112.

141 J. L. Kardos, *J Adhes*, 1973, **5**, 119–138.

142 J. Hughes, *Compos Sci Technol*, 1991, **41**, 13–45.

143 V. Safavi-Ardebili, A. N. Sinclair and J. K. Spelt, *J Adhes*, 1997, **62**, 93–111.

144 G. R. Palmese and R. L. McCullough, *J Appl Polym Sci*, 1992, **46**, 1863–1873.

145 I. Dinnissen, *Amine Blushing and Blooming of Epoxy*, Dow Deutschland GmbH & Co. OHG, Germany, 2005.

146 S. A. Didas, M. A. Sakwa-Novak, G. S. Foo, C. Sievers and C. W. Jones, *J Phys Chem Lett*, 2014, **5**, 4194–200.

147 R. W. Flaig, T. M. Osborn Popp, A. M. Fracaroli, E. A. Kapustin, M. J. Kalmutzki, R. M. Altamimi, F. Fathieh, J. A. Reimer and O. M. Yaghi, *J Am Chem Soc*, 2017, **139**, 12125–12128.

148 C. Cantarutti, R. Dinu and A. Mija, *Biomacromolecules*, 2020, **21**, 517–533.

149 C. Sun and P. K. Dutta, *Ind Eng Chem Res*, 2016, **55**, 6276–6283.

150 J.-B. Bossa, F. Borget, F. Duvernay, P. Theulé and T. Chiavassa, *J Phys Chem A*, 2008, **112**, 5113–5120.

151 Gougeon Brothers Inc, *Technical Data TLG-625-R, TLG-625-H*, Bay City, 2015.

152 A. B. D. Cassie and S. Baxter, *Transactions of the Faraday Society*, 1944, **40**, 546.

153 J. S. K. Lim, C. L. Gan and X. M. Hu, *ACS Omega*, 2019, **4**, 10799–10808.

154 C. Rulison, *So You Want to Measure Surface Energy?*, KRÜSS GmbH, Hamburg, 1999.

155 C.-H. CHIOU, PhD Thesis, Texas A&M University, 2016.

156 J. M. Schuster, C. E. Schvezov and M. R. Rosenberger, *Procedia Materials Science*, 2015, **8**, 732–741.

157 H. H. Winter, *Polym Eng Sci*, 1987, **27**, 1698–1702.

158 L. Xu and J. R. Schlup, *J Appl Polym Sci*, 1998, **67**, 895–901.

159 C. M. Sahagun and S. E. Morgan, *ACS Appl Mater Interfaces*, 2012, **4**, 564–572.

160 B. E. F. Ekbrant, A. L. Skov and A. E. Daugaard, *Macromolecules*, 2021, **54**, 4280–4287.

161 M. Michel and E. Ferrier, *Constr Build Mater*, 2020, **231**, 117206.

162 B. Bilyeu, W. Brostow and K. Menard, *Journal of Materials Education*, 2000, **22**, 107–129.

163 H. M. Curry, PhD Thesis, Boston University, 1950.

164 R. J. C. Carbas, E. A. S. Marques, L. F. M. da Silva and A. M. Lopes, *J Adhes*, 2014, **90**, 104–119.

165 A. C. de Luca, G. Rusciano, G. Pesce, S. Caserta, S. Guido and A. Sasso, *Macromolecules*, 2008, **41**, 5512–5514.

166 Z. Sobhani, M. Al Amin, R. Naidu, M. Megharaj and C. Fang, *Anal Chim Acta*, 2019, **1077**, 191–199.

167 E. Perret, O. Braun, K. Sharma, S. Tritsch, R. Muff and R. Hufenus, *Polymer (Guildf)*, 2021, **229**, 124011.

168 Horiba Scientific, Raman analysis, https://www.horiba.com/int/scientific/technologies/raman-imaging-and-spectroscopy/raman-analysis/, (accessed 9 September 2023).

169 P. J. Flory, in *Macromolecular Science Retrospect and Prospect*, Academic Press, New York, 1953.

170 W. H. Stockmayer, *J Chem Phys*, 1943, **11**, 45–55.

171 K. Abiko, Y. Kato, H. Hohjo, Y. Kishida and E. Sudo, *Journal of Raman Spectroscopy*, 2020, **51**, 193–200.

172 International Paint Ltd, *Interline 9001*, AkzoNobel, 2017.

173 T. S. Weeks, D. Adolf and J. D. McCoy, *Macromolecules*, 1999, **32**, 1918–1922.

174 M. Sharifi, K. A. Ghorpade, V. I. Raman and G. R. Palmese, *ACS Omega*, 2020, **5**, 31011–31018.

175 J. M. de Jesus, C. Costa, A. Burton, V. Palitsin, R. Webb, A. Taylor, C. Nikula, A. Dexter, F. Kaya, M. Chambers, V. Dartois, R. J. A. Goodwin, J. Bunch and M. J. Bailey, *Anal Chem*, 2021, **93**, 13450–13458.

176 G. W. Grime, O. B. Zeldin, M. E. Snell, E. D. Lowe, J. F. Hunt, G. T. Montelione, L. Tong, E. H. Snell and E. F. Garman, *J Am Chem Soc*, 2020, **142**, 185–197.

177 K. Kunz and M. Stamm, *Macromolecules*, 1996, **29**, 2548–2554.

178 A. Karim, A. Mansour and G. P. Felcher, *MRS Proceedings*, 1989, **171**, 329.

179 H. Yim, M. Kent, W. F. McNamara, R. Ivkov, S. Satija and J. Majewski, *Macromolecules*, 1999, **32**, 7932–7938.

180 J. Bowers, A. Zarbakhsh, J. R. P. Webster, L. R. Hutchings and R. W. Richards, *Langmuir*, 2001, **17**, 131–139.

181 P. J. Baker, S. C. L. Hall, S. Mukhopadhyay, S. P. Cottrell and A. D. Hillier, *J Phys Conf Ser*, 2023, **2462**, 1–10.

182 K. Frank and J. Wiggins, *J Appl Polym Sci*, 2013, **130**, 264–276.

183 L. R. Hutchings, R. W. Richards, R. L. Thompson and D. G. Bucknall, *The European Physical Journal E*, 2002, **8**, 121–128.

184 P. Singh, D. W. F. (Wim) Brilman and M. J. Groeneveld, *International Journal of Greenhouse Gas Control*, 2011, **5**, 61–68.

185 T. M. Shenk, K. M. Benjamin and R. M. Winter, *Polym Eng Sci*, 2023, **63**, 1347–1358.

186 F. Korkees, R. Swart and I. Barsoum, *Polym Eng Sci*, 2022, **62**, 1582–1592.

187 S. T. Knox, A. Wright, C. Cameron and J. P. A. Fairclough, *ACS Appl Polym Mater*, 2021, **3**, 3438–3445.

188 S.-Y. Zhang, Y.-F. Ding, S.-J. Li, X.-W. Luo and W.-F. Zhou, *Corros Sci*, 2002, **44**, 861–869.

189 C. L. Soles, F. T. Chang, B. A. Bolan, H. A. Hristov, D. W. Gidley and A. F. Yee, *J Polym Sci B Polym Phys*, 1998, **36**, 3035–3048.

190 J. J. Sahlin and N. A. Peppas, *Ind Eng Chem Res*, 1991, **30**, 211–217.

191 M. Stopford, *Maritime Economics*, Routledge, London, 2nd edn., 1997.

192 The Swedish Club, *Cargo in focus: Hazardous chemical cargoes*, 2022.

193 J. C. Moller, R. J. Berry and H. A. Foster, *Polymers (Basel)*, 2020, **12**, 466.

194 G. Singer, G. Sinn, K. Schwendtner, H. C. Lichtenegger and R. Wan-Wendner, *Compos Struct*, 2018, **196**, 155–162.

195 B. K. McConnell and R. A. Pethrick, *Polym Int*, 2008, **57**, 689–699.

196 Y. Shudo, A. Izumi, K. Hagita, T. Yamada, K. Shibata and M. Shibayama, *Macromolecules*, 2018, **51**, 6334–6343.

197 P. G. de Gennes, *The European Physical Journal E*, 2002, **7**, 31–34.

198 M. J. Adamson, *J Mater Sci*, 1980, **15**, 1736–1745.

199 T. Wang, S. Luo, C. Wang, J. Wang, C. E. Weinell, K. Dam-Johansen, J. J. Segura, E. Graversen and S. Kiil, *J Coat Technol Res*, 2021, **18**, 831–842.

200 N. L. Thomas and A. H. Windle, *Polymer (Guildf)*, 1982, **23**, 529–542.

201 M. L. Kaplan, *Polym Eng Sci*, 1991, **31**, 689–698.

202 K. Tsuda, *Journal of Japan Petroleum Institute*, 2007, **50**, 240–248.

203 B. Duncan and W. Broughton, *Absorption and Diffusion of Moisture In Polymeric Materials*, The National Physical Laboratory, Middlesex, 2007.

204 C. Carr and J. Riccick, *Ind Eng Chem*, 1951, **43**, 692–696.

205 M. R. Vanlandingham, R. F. Eduljee and J. W. Gillespie Jr., *J Appl Polym Sci*, 1999, **71**, 699–712.

206 J. Yu and S. S. C. Chuang, *Ind Eng Chem Res*, 2017, **56**, 6337–6347.

Appendix

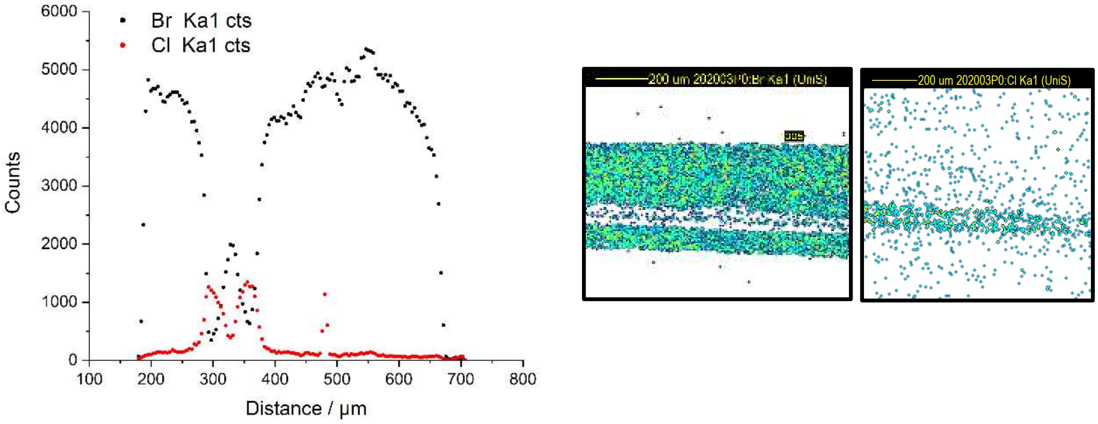

Figure A. 1: Br and Cl signal intensity as a function of film depth and accompanying PIXE maps (System: 35% stoichiometry, 35 °C cure temperature – Repeat 1).

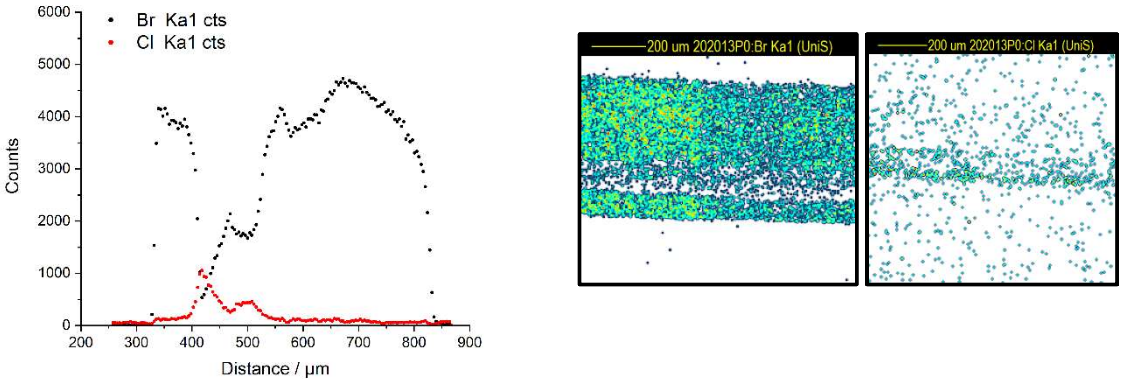

Figure A. 2: Br and Cl signal intensity as a function of film depth and accompanying PIXE maps (System: 35% stoichiometry, 35 °C cure temperature – Repeat 2).

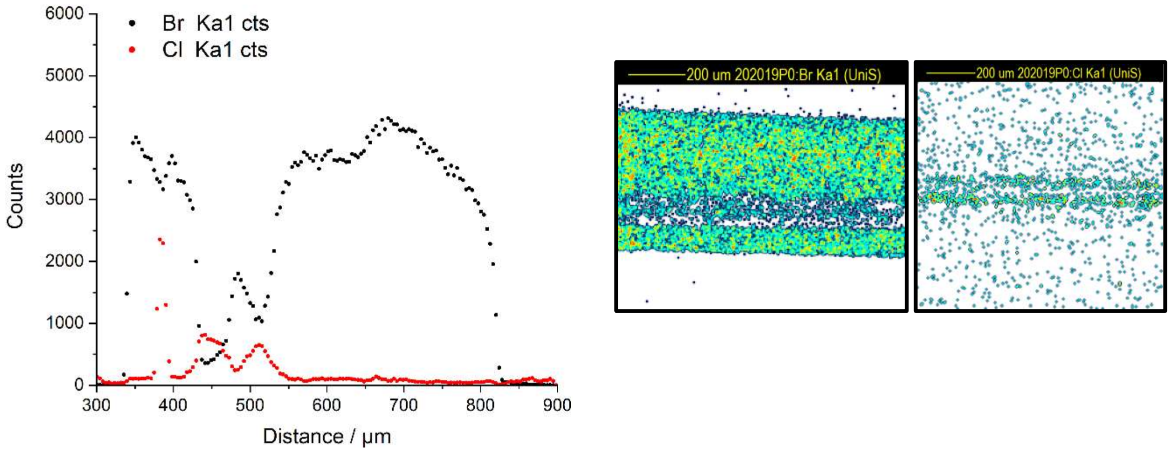

Figure A. 3: Br and Cl signal intensity as a function of film depth and accompanying PIXE maps (System: 35% stoichiometry, 35 °C cure temperature – Repeat 3).

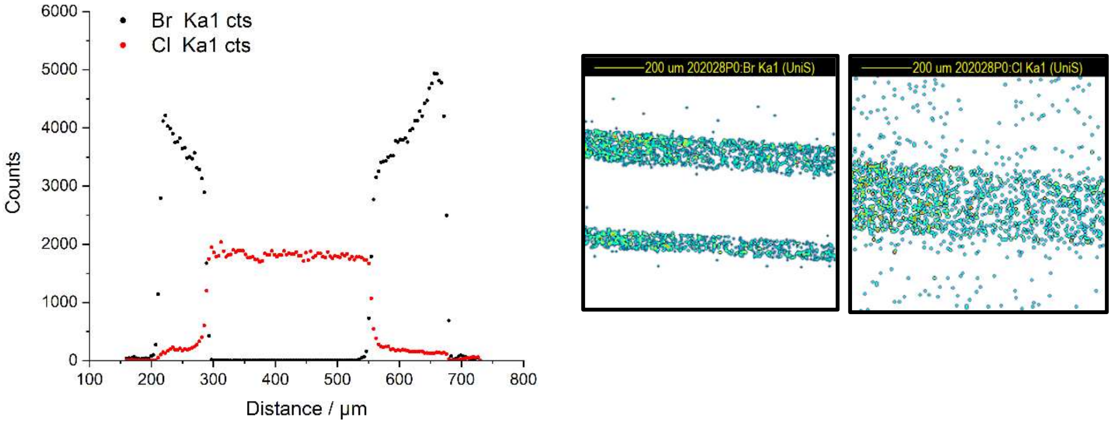

Figure A. 4: Br and Cl signal intensity as a function of film depth and accompanying PIXE maps (System: 35% stoichiometry, 25 °C cure temperature – Repeat 1).

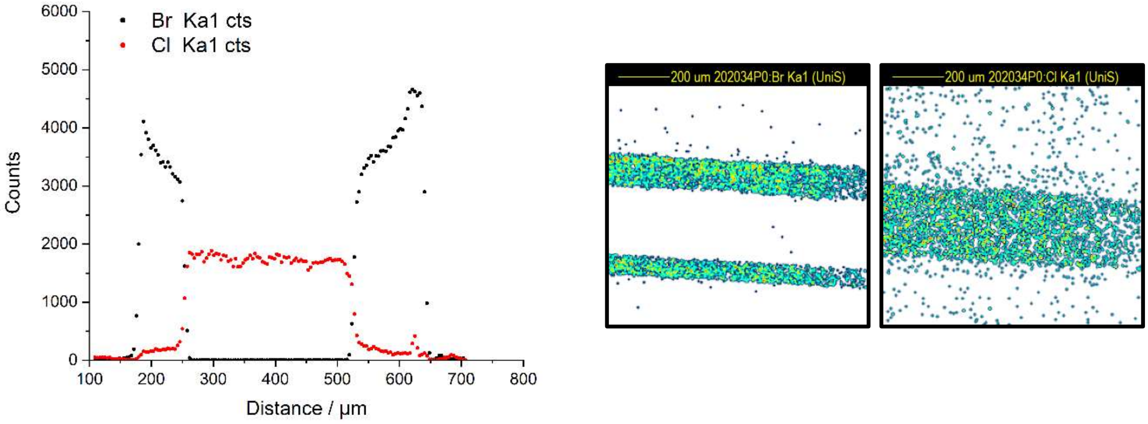

Figure A. 5: Br and Cl signal intensity as a function of film depth and accompanying PIXE maps (System: 35% stoichiometry, 25 °C cure temperature – Repeat 2).

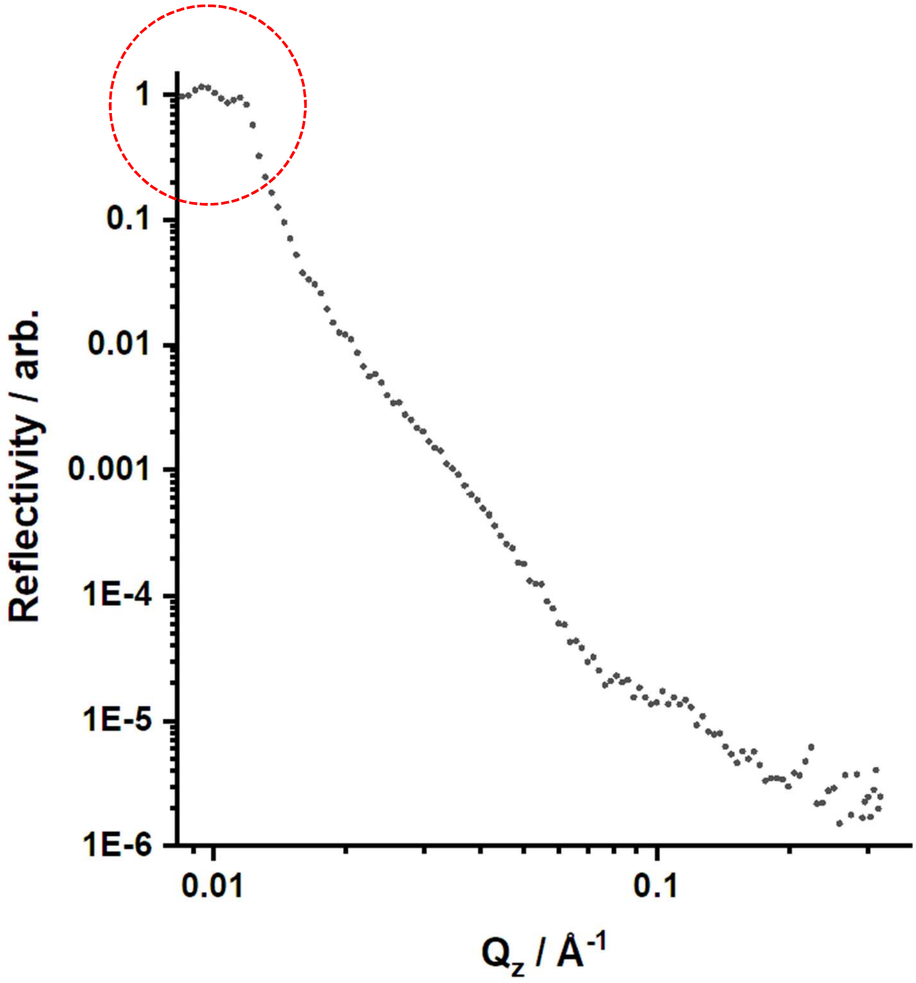

Figure A. 6: Example of unusable neutron data due to a non-flat critical edge (circled).